

Universit degli Studi di Pisa
von Karman Institute for Fluid Dynamics
Aeronautics and Aerospace Department

PhD. Dissertation

**Physical models for nonequilibrium
plasma flow simulations at high
speed re-entry conditions**

Marco Panesi

February 5, 2009

Contact information:

Marco Panesi
von Karman Institute for Fluid Dynamics
72 Chaussée de Waterloo
1640 Rhode-St-Genèse
BELGIUM

email: `marco.panesi@vki.ac.be`

This manuscript was typeset on L^AT_EX with KOMA-Script.

All the research work was done with the GNU/Linux operating system.

A mia madre.

”The purpose of computing is insight, not numbers.”

Richard Hamming

Contents

1	Introduction	3
1.1	Background	3
1.2	Modeling of nonequilibrium flows	6
1.3	Scope and overview of the thesis	11
1.4	Publications related to the thesis	13
I	Multitemperature models	15
2	Governing equations	17
2.1	Multitemperature model: set of equations	19
2.1.1	Species continuity equations	20
2.1.2	Momentum equation	22
2.1.3	Total energy equation	22
2.1.4	Vibrational energy equation	23
2.1.5	Free electron-electronic energy equation	23
2.2	Transport properties	24
2.2.1	Diffusion fluxes	26
2.2.2	Viscous stress and heat flux	26
2.3	Simplified flow equations	27
2.3.1	Onedimensional shock tube: governing equations . . .	28
2.3.2	Quasi-onedimensional nozzle: governing equations . .	28
3	Thermodynamics	31
3.1	Simplified models	32
3.1.1	Simplified models: results	35
3.2	Advanced models for thermodynamics	37
3.2.1	Maximum vibration quantum number	38
3.2.2	Maximum rotational quantum number	39
3.3	Thermal-nonequilibrium thermodynamic model of Jaffe . .	42
3.3.1	Two ways of splitting the ro-vibrational internal energy	43
3.3.2	Two temperature partition function	44
3.4	Results	45

3.4.1	Nonequilibrium thermodynamic properties	46
3.4.2	Influence of the splitting on the results	48
3.4.3	Comparison between the accurate and simplified approaches	49
4	Chemistry and energy exchanges	57
4.1	Chemical nonequilibrium model	58
4.1.1	Influence of nonequilibrium on the kinetic processes .	59
4.2	Energy exchanges among energy modes	65
4.2.1	Vibrational Translational exchanges	66
4.2.2	Vibrational vibrational exchange	67
4.2.3	Elastic energy exchange: free electrons - heavy particle	68
4.2.4	Free-electron vibrational coupling	68
4.2.5	Coupling Chemistry internal energy modes	68
4.2.6	Vibration-Chemistry-Vibration coupling	69
4.3	Comparison preferential dissociation and non-preferential dissociation models	71
5	Multitemperature models: results	79
5.1	Shock code: comparison with literature	79
5.2	Nozzle code: comparison with literature	84
5.2.1	Comparison with NOZNT code	84
5.2.2	Analysis of the TT1 arcjet-facility	86
II	Electronic collisional radiative models	91
6	Collisional Radiative models: atoms	93
6.1	Physical models	95
6.1.1	Air mixture	95
6.1.2	Elementary processes	97
6.1.3	Master equation	109
6.2	Analysis of the FIRE II flight experiment by means of a Collisional Radiative model	110
6.2.1	Physico-chemical modeling	111
6.2.2	Atomic elementary processes	112
6.2.3	Shock-Tube flow solver	114
6.2.4	Results	117
6.2.5	Analysis of the Fire II 1634 s case	118
6.2.6	Analysis of the Fire II 1636 s case	130

6.2.7	Analysis of the Fire II 1643 s case	133
6.3	Comparison with EAST experiments	137
6.3.1	Physico-Chemical modeling	138
6.3.2	Radiative properties prediction	140
6.3.3	Results	142
7	Collisional radiative model: atoms and molecules	163
7.1	Collisional Radiative model: molecules	163
7.1.1	Shock-Tube flow solver	171
7.2	Results	172
7.2.1	Flowfield results: comparison with atomic CR model .	173
7.2.2	Results: molecules	176
7.2.3	Dissociation of the excited states of O ₂	180
7.3	Park's model	181
7.3.1	Atomic and molecular population distributions: comparison against Park 2008	182
7.3.2	Detailed physico-chemical analysis	184
8	Detailed chemistry in expanding flows	197
8.1	Analysis of the VKI Minitorch	198
8.1.1	Model description	199
8.1.2	Flowfield characterization	201
8.1.3	Analysis of the atomic distribution function	203
8.1.4	Analysis of the electronic states of the molecules	205
8.1.5	Influence of the optical thickness on the results	208
9	Toward a simplified model	215
9.1	Lumping of the states of the atomic species	216
9.2	Elementary processes of grouped levels	217
9.3	Comparison approximate and accurate CR models	219
III	Application to CFD: COOLFluiD Hypersonic	223
10	Computational Fluid Dynamics	225
10.1	Numerical methods	226
10.1.1	Numerical discretization	226
10.2	Multitemperature model: 1636 s case	228
10.3	Simplified Collisional-Radiative model: COOLFLUID hypersonic	232

10.3.1 Detailed analysis: atomic nitrogen	233
10.4 3D simulations: Expert vehicle	238
11 Conclusions and future research	245
A Collisional Radiative model: data	257
A.1 Electronic levels	257
A.2 Einstein coefficients	259
A.3 Rate coefficients	261
Bibliography	263
List of Tables	281
List of Figures	283

Acknowledgements

I am very grateful to my adviser and friend Professor Olivier Chazot for his constant support, encouragement and his enlightening guidance. He was a reference point for research and private life. While I have enjoyed the freedom which he allowed me to conduct my research, I am appreciative of the directions given when needed.

Many thanks to Dr. Thierry Magin, the *Lord of Kinetic Theory*, who helped me enormously, during the long and sometimes stressing years of the PhD. Thanks for all the fruitful discussions and the practical help.

I acknowledge Dr. Anne Bourdon and Professor Arnaud Bultel for providing me the necessary insight on the physical modeling, which made this dissertation possible. It was a pleasure to work with them, for their infinite patience, ideas and their theoretical support.

I would like to thank my promoter Prof. Maria Vittoria Salvetti and Prof. Guido Buresti. Although at distance, I could always count on their help and financial support.

I would also like to thank Dr. Winifred Huo, Dr. David Schwenke, Dr. Richard Jaffe, Dr. Galina Chaban for the incredible summer spent studying dissociation with their 22.383.000 elementary kinetic rate constants. The work was performed during the 2008 Summer Program at the Center for Turbulence Research with financial support from Stanford University and NASA Ames Research Center. The author would like to thank Prof. P. Moin and Prof. G. Iaccarino for their hospitality.

Thanks to Professor Douglas Fletcher and Professor Hermann Deconick, always ready to answer my questions and support me all along my thesis work. This help is greatly appreciated.

A special thank goes to Dr. Gianpiero Colonna and Dr. Domenico Giordanano for their help in learning the subject of hypersonics. It was essential

in completing this dissertation.

Thanks to Professor Patrick Rambaud the rising star of the AR department, for the continuous encouragements.

A special thank goes to Dr Andrea Lani for accepting me as COOLFluiD developer and for the fruitful collaboration. It was a real honor and pleasure to code with you on COOLFluiD Hypersonic. Thanks also to Dr. Tiago Quintino the guru of COOLFluiD.

Thanks to Alessandro Munafó anvalueable assistant and excellent student. I wish you all the best for your Diploma Course and I expect nothing less than the von Karman prize.

Thanks to Dr. Mickael Playez for the introducing me to the wonderful world of spectroscopic measurements.

Thanks to "the German" Jan Thömel, for being a good friend and a wonderful officemate.

Thanks to Raimondo for *the wind of change* he brought to the computer center and to Mike Bilka for the continous support and suggestions.

I want to acknowledge the faculty, all my fellow PHD students, who are still fighting to get their degree and all the VKI people in general:

IT WAS AN HONOR TO BE PART OF THE VKI FAMILY.

Finally I would like to thank my family and my girlfriend Kelly; they provided me with all the support and love that I needed.

Chapter 1

Introduction

1.1 Background

In the last few years, there has been considerable effort in understanding the chemistry of shock heated air, which is justified by the renewed interest of NASA and ESA for the space exploration, aiming at transporting humans to the Moon and eventually Mars. Indeed, one of the most important phases, common to all the manned mission, is the re-entry into Earth's atmosphere.

The space vehicles, interacting with the atmosphere at near-orbital or super-orbital speeds, are subjected to a strong deceleration. Typical entry velocities, higher than 10 km/s, in the case of lunar return, exceed the speed of sound in the atmosphere and Mach numbers larger than 40 are encountered. Thus, a strong bow shock is formed in front of the vehicle, which converts the massive amount of the free stream kinetic energy into translational energy of the gas. A rough estimation of the total energy per unit mass of gas can be obtained considering as example a typical Apollo lunar return mission. If we assume a re-entry speed of 11 km/s, the resulting specific kinetic energy $V_\infty^2/2$ exceed 50 MJ/kg. Thus the conversion of such energy into translational energy of the fluid particles yields to chemical reactions (dissociation, ionization) in the gas behind the shock, owing to the strong molecular collisions.

Also, the inter-particle collisions, besides producing chemical changes in the gas, promote energy exchanges among the various internal modes of atoms and molecules. Generally speaking, the re-distribution of energies among internal states and chemistry in the gas is a function of the *collisional history*, being the characteristic collision time scale comparable to the convective time scale. Such physico-chemical state of the gas, usually referred to as *nonequilibrium state*, constitutes the focus of this analysis. Furthermore, if the number of collisions that the gas experiences, while

crossing the shock-layer¹, is negligibly small or in contrast it is overwhelmingly large, two thermochemical regimes referred to as *frozen* or *equilibrium* flows respectively, can be defined.

Near the surface, the boundary layer, developed as a consequence of the viscous dissipation, induces a high energy flux, which strongly depends on the thermochemical state of the gas within the shock-layer. Furthermore at high re-entry speeds, a significant portion of the heating experienced by the spacecraft can be due to thermal radiation. Indeed, the spontaneous de-excitation of the internal (electronic, vibrational and rotational) quantum states of molecules and atoms, yields to emission of energy in the form of electromagnetic radiation, which is highly influenced by the distribution of atoms and molecules among their internal energy levels. Thus, the prediction of the heat fluxes strongly depends on the completeness and accuracy of the physical model used to describe nonequilibrium phenomena. Hence, in order to design the Thermal Protection Systems (TPS), which is designed to prevent the excessive heating of the vehicle, an accurate modeling of the thermochemical state of the gas is required.

The characterization of the re-entry flows often relies on a combined approach, based on numerical simulation as well as ground testing [44]. Ground test facilities, such as shock tunnels, arc-jets or inductively coupled plasma torches, are designed to generate high enthalpy flows to reproduce, at least in part, the flow conditions experienced by the space vehicles during the re-entry phase. The high enthalpy flows, produced by means of electromagnetic discharge (in arc-jets or plasmatrons) or resorting to impulse heating (in shock tunnels) are often accelerated using nozzles to meet the desired test conditions. Sometimes, however, within the nozzle, the thermodynamic conditions change so rapidly that nonequilibrium effects may develop and cause several undesirable effects in the testing of models [132]. Only the knowledge of the nature and extent of the nonequilibrium phenomena in an expansion, allows to predict those effects and correct them.

The state of the gas, i.e. the concentration of the gas species and distribution of their internal energy level populations, can be estimated by means of either *multitemperature* models [33, 69, 138], or *collisional radiative* (CR) models [20, 38, 107, 138].

¹The part of the physical and computational domain bounded by the bow-shock and the wall of the vehicle. See Figure 1.1

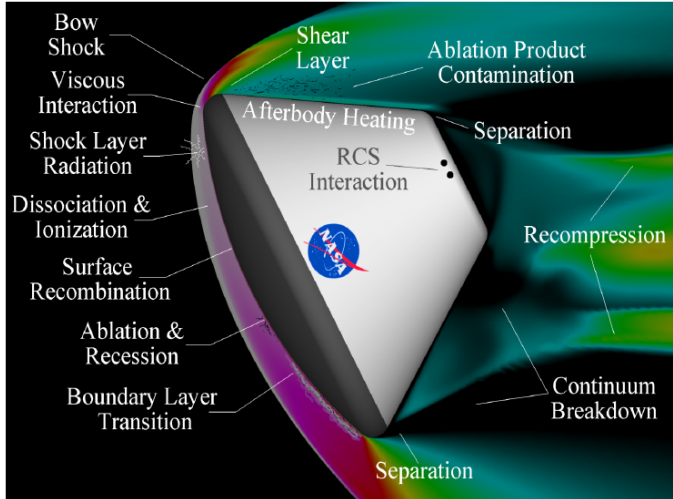


Figure 1.1: Schematic of the flowfield surrounding a capsule during the (re-)entry phase in a planetary atmosphere: (red line) recombination, (black line) ionization (courtesy of NASA).

In the case of multitemperature models, extensively discussed in [138], statistical mechanics provides an expression for the most probable distribution among the energy levels, i.e. the *Maxwell-Boltzmann distribution*. Hence, the physico-chemical properties of the air flow are obtained by assuming that the population of each internal energy mode follows a Maxwell-Boltzmann distribution at a specific temperature. In order to calculate these temperatures and the energy exchanged between all the energy modes (i.e. translational, rotational, vibrational, and electronic), conservation equations for the internal energy modes in thermo-chemical nonequilibrium are added to the classical set of conservation equations for mass, momentum and total energy. It is important to mention that multitemperature models are easy to implement in multidimensional flow codes and have been used extensively in the literature so far [24, 95, 138, 158, 166, 167].

However, at high re-entry speeds and low pressure conditions, nonequi-

librium processes (e.g. nonequilibrium ionization, as discussed in the next section), are expected to affect the internal distribution function, which may significantly depart from Maxwell-Boltzmann distribution, thus making the multitemperature models not applicable. The same is true for the gas rapidly expanding in ground test facilities [47] or the plasma generated by means of electromagnetic discharges, where although the typology of nonequilibrium may be significantly different from the one occurring in re-entry flow, the distribution still deviates from Maxwell-Boltzmann [150–152]. Hence, in contrast to the near equilibrium situations, where the notion of one or more temperatures controls everything, an accurate description of flows, in strong nonequilibrium, is much more complicated. Thus, the use of Collisional-Radiative (CR) models, originally developed by Bates *et al.* [8], is required. The CR models take into account all relevant collisional and radiative mechanisms between the internal energy levels of the different species present in the flow. They constitute a valid alternative to the multitemperature models in that they account for deviations from the Maxwell-Boltzmann distribution, thus exhibiting a larger range of applicability. By increasing order of complexity and computational time, three kinds of CR models can be distinguished for air: *electronic* [27, 28, 30, 93, 138, 159, 171], *vibrational* [29, 31, 35, 38, 43, 47, 139, 150–152], and *rovibrational* state-to-state models. In electronic state-to-state models, transitions between the electronic states are considered and the rovibrational levels of the molecules are populated according to Maxwell-Boltzmann distributions at temperatures T_v and T_r . In vibrational state-to-state models, transitions between the vibrational states of the molecules are also considered and only a rotational temperature is defined. For both types of models, intensive requirements in terms of computational power do not allow for efficient implementation in multidimensional codes, most calculations are thus performed by means of 0D and 1D flow solvers. Finally, in rovibrational state-to-state models, no internal temperature is required. It is interesting to note that rovibrational models have not been proposed so far, due to the computational power limitations and lack of knowledge of the reaction rates.

1.2 Modeling of nonequilibrium flows

The chemical constituents of a gas mixture, referred to as *species*, consist of atoms, molecules and possibly charged particles, which can be subdivided in free-electrons and ions.

Owing to the large number of particles (atoms and molecules) present in the mixture of gases under investigation, a microscopical description of the gas, in terms of velocity, position and internal state of every particle is unattainable. This justifies the use of a statistical approach, which gives the average behavior of the system under investigation. Furthermore, considering that, in our gas model, the internal state of any atom or molecule is independent on the translational velocity, owing to the separability of the Hamiltonian operator in the Schrödinger's equation [68], it is possible to adopt a separate description for the fraction of gas energy ², linked to the translational motion (ϵ_i^T) and the energy due to excitation of internal structure of the particles, (ϵ_i^{Int}).

Thus, following a statistical approach, we define, $f_i(\vec{r}, \vec{c}_i, t)$ as the velocity distribution function [60, 176], which yields the probability of finding an i -particle at a certain location \vec{r} , with a certain velocity \vec{c}_i at the time t in the phase space. In other words, the quantity $f_i d\vec{r} d\vec{c}_i$ represents the number of i -particles, enclosed in a volume $d\vec{r}$ located at \vec{r} , whose velocity is contained in the element $d\vec{c}_i$ about velocity \vec{c}_i at time t .

The evolution of the distribution function is provided by the solution of the Boltzmann equation [60, 113, 176] and its expression for a gas in equilibrium state, with no gradients in composition, velocity and temperature, is given by the well-known Maxwellian distribution f_i^M , which reads

$$f_i^M = N_i \left(\frac{m_i}{2\pi k_B T_i} \right)^{3/2} \exp \left(-\frac{m_i C_i^2}{k_B T_i} \right) \quad (1.1)$$

where N_i is the number density of the species i , m_i and T_i indicates the mass and the temperature of the i^{th} particle respectively, k_B is the Boltzmann constant, \vec{C}_i is the peculiar velocity, linked to the thermal motion of the molecules, and it is given by difference between the i^{th} species particle velocity, \vec{c}_i , and the mixture average velocity \vec{u} .

Thus, the assumption of Maxwellian distribution allows for the definition of the translational temperature of the species in the gas. In general, with the only exception of free electrons, the temperatures of the different species in the mixture thermalize rather quickly (i.e. $T_i = T$), owing to the efficient

²In literature the sum of the kinetic (translational motion of the molecules) and the internal (rotational, vibrational and electronic energy) contribution of the energy of molecules and atoms is referred as internal energy. In this manuscript we keep the separation among kinetic and internal energy.

energy exchanges among particles having comparable masses.

On the contrary, free electrons, whose mass is about 10 000 smaller than the other species, may be found in thermal nonequilibrium (i.e. $T_i = T_e \neq T$), being governed by a Maxwellian distribution at a different temperature. Although not considered in this work, it is important to mention that, nonequilibrium effects in the *electron energy distribution function* may arise, when electric fields are present in the flow or in expanding gases, as a result of deactivation transitions among the vibronic-states [34]. The non-Maxwellian description of the kinetics of the free-electrons requires, in this case, the solution of the Boltzmann equation, as proposed by Capitelli *et al.* in Ref. [35].

When coming to the description of the internal structure of the gas, we have the choice, of assuming a normal distribution among the internal levels, or we can refrain from the use of equilibrium distribution, resorting to a kinetic approach.

In the case of Maxwell-Boltzmann equilibrium from statistical mechanics, the fraction of particles, f_i^α , of the chemical species i in the quantum state α , is given by:

$$f_i^\alpha = \frac{N_i^\alpha}{N_i} = g_i^\alpha \frac{\exp\left(-\frac{\epsilon_{\text{Int}}^\alpha}{k_B T_{\text{Int}}}\right)}{Q_{\text{Int } i}} \quad (1.2)$$

where N_i is the number density of the species i and $Q_{\text{Int } i}$ indicates the partition function [176]. Thus, the knowledge of the chemical composition (molar or mass fractions) of the i species is sufficient to characterize the internal state of the gas, provided that the pressure and internal temperature (or temperatures), (T_{Int}) are known.

If the internal state of the gas deviates from the equilibrium distribution, a kinetic approach is to be adopted. To this end, since each of the internal states of a chemical constituent can be distinguished from the others using the notion of quantum number, we may extend the idea of chemical species to include, not only the true chemical nature of the constituent, but also its internal state. In other words, indicating the internal quantum number with α , the chemical species in the quantum state α is considered as a separate chemical species, referred to as *pseudo-species* in the following. In this case the internal distribution is a result of the detailed kinetic processes occurring among the pseudo-species.

Owing to the large number of levels, which characterize the internal structure of atoms and molecules, a detailed treatment of each single quantum state is not feasible because of the computational cost and the lack of an adequate kinetic database. Hence, adopting a hybrid model, we rely on the Maxwell-Boltzmann distribution to describe rotational and vibrational structures of the molecules, as opposed to the electronic states, which are considered as pseudo-species and assumed to be governed by detailed kinetics.

To this end, we divide the internal energy of the molecules in three contributions: electronic, vibrational and rotational, indicating the quantum numbers of each energy level with e , v and J . Furthermore, the assumption of equilibrium distribution within the rotational and vibrational energy levels allows us to indicate the fraction of particles in the $\epsilon_i(v, J)$ energy state of the electronic level e , as follows:

$$f_i^e(V, J) = \frac{N_i(v, J)}{N_{i,e}} = g_J \frac{\exp\left(-\frac{\epsilon_v}{k_B T_V}\right)}{Q_V} \frac{\exp\left(-\frac{\epsilon_J}{k_B T_R}\right)}{Q_R} \quad (1.3)$$

where i indicates the species or the pseudo-species, T_V , and T_R are (respectively) the vibrational and the rotational temperatures and Q indicates the partition function [176]. Furthermore, we indicate with $N_{i,e}$ the number density of the electronic state e of the species i and with ϵ_v and ϵ_J the vibrational and rotational energy of the particle. Thus, the knowledge of the species composition, pressure and temperatures T , T_V , T_R , becomes sufficient to determine the state of the gas, provided that the population of the pseudo-species is calculated resorting to a detailed kinetic approach. The atomic species, in contrast to the molecules, do not have rotational and vibrational internal modes, therefore the determination of their internal energy does not require the definition of any internal temperature.

The main difference in the two approaches briefly outlined lies in the definition of the mixture and kinetic processes of the gas, which are restricted to the chemical constituents in multitemperature models and extended to the internal states in Collisional Radiative models. Indeed, while multitemperature models require no information concerning the detailed chemistry describing the internal excitation, being the repartition among the internal quantum states provided by the Maxwell-Boltzmann distribution, Collisional Radiative methods directly provide some information on the population of the internal quantum states as a result of detailed kinetics.

Illustrative example

An illustrative example of the typical nonequilibrium population distribution of the electronic states of the atoms is depicted in Figure 1.2. In the sketch, the number density of the population of the excited states divided by the degeneracy ($\log_{10} (N_e/g_e)$), (indicated as normalized population), is plotted against energy levels. The energy distribution is depicted for two

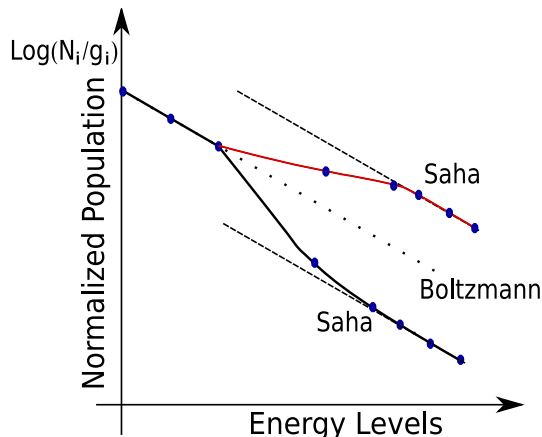


Figure 1.2: Electronic population distribution in ionizing (black curve) and recombining plasmas (red curve).

nonequilibrium conditions: the lower curve (black curve) is characteristic of compressing flows as opposed to the upper curve (red curve), which represents the distribution in recombining situation such as boundary layer flow or expanding flow. The CR model, in both cases, predicts strong departures from the Maxwell-Boltzmann distribution for the high-lying excited states, which are distributed according to the Saha-Boltzmann distribution. However, while the ionizational nonequilibrium leads to a strong depletion of the excited states of the atomic species, the recombining situation induces an overpopulation of the high-lying excited states. Owing to the high efficiency of the ionization (recombination) processes involving the high-lying states, with respect to the excitation (de-excitation) and ionization (recombination) processes involving low lying states, the upper excited states, close to the ionization limit, first tend to reach Saha equilibrium with the free electron, before reaching Maxwell-Boltzmann equilibrium with the lower

states [86, 106].

1.3 Scope and overview of the thesis

This research project addresses the modeling of high temperature non equilibrium flows such as those obtained behind a strong shock wave or generated in high enthalpy ground test facilities. The knowledge gained during former aerospace missions allows for the key role of CFD simulations, in the development of hypersonic applications, to be highlighted in strong interaction with ground testing. The relevance of these simulations is linked to aerothermochemistry features such as high-temperature gas effects in hypersonic flows, in particular in the boundary layer. For instance, the design of the heat shield used to protect spacecraft is based on the estimation of the heat fluxes to the vehicle surface by means of experimental and numerical resources. CFD predictions of these quantities strongly rely upon the accuracy of the model used to describe the flow.

The model, developed within this project will be employed to study the behavior of the electronically excited states of atoms and molecules in post shock condition and in expanding flows. The aim of this project is to develop a reduced mechanism for CFD applications, allowing accurate predictions of the nonequilibrium plasma flows by combining the computational efficiency of the multitemperature models and the accuracy of the more sophisticated CR models.

The manuscript is divided into three parts:

The first part of the manuscript discusses the multitemperature methods for the simulation of the nonequilibrium flows. Chapter 2 describes the governing equations used in CFD and the two simplified one-dimensional flow-solvers employed in the simulation of the flowfield behind a normal shock and within nozzles. Chapter 3 discusses the thermodynamic models, commonly used in literature, which are based on the simplifying assumption of harmonic oscillator and rigid rotator. A detailed comparison of such approximated models with the more sophisticated and innovative model of Jaffe [91], facilitates the discussion of their limits of applicability. The models used to account for chemistry and energy exchange terms within the

internal energy modes are given in Chapter 4. Chapter 5 closes this part of the manuscript describing the validation of multitemperature models, by means of the simplified shock code and the quasi-one dimensional nozzle code. One of the main purposes of the chapter is to demonstrate how simplified models can give a reasonable representation of the flowfield in compressing or expanding situations.

The second part of the manuscript describes the modeling of the nonequilibrium flows of molecules and atoms, by means of Collisional Radiative models. In Chapter 6 the populations of the electronic states of the atomic species is obtained modeling the population and depletion of the atomic states, through collisional and radiative processes. Generalities concerning elementary processes, grouping of the levels and the formulation of the master equation are given in details in the first part of the chapter.

Next, the investigation of the behavior of the excited electronic states of atoms in the relaxation zone of one dimensional air flows is presented. The model employed for the analysis was developed by Dr. A. Bultel and Dr. A. Bourdon and it is referred to in the following as ABBA model [27, 136]. The last part of the chapter is devoted to the analysis of the shock tube experiments carried out in the EAST shock tube. The comparison to experimental data allows for a validation of the Collisional Radiative model for the atomic species. Chapter 7 addresses the modeling of the post shock relaxation of atomic and molecular species by means of an electronically specific collisional radiative model. Furthermore the same model is used to investigate the deviations from the Maxwell-Boltzmann distribution occurring in the expanding flow of the VKI minitorch facility. In Chapter 9 the use of the accurate CR model allows to develop a simplified model with a reduced number of levels to be applied to multidimensional CFD solver.

The third part of the manuscript is devoted to application of the multitemperature and CR models developed in the first two parts to an unstructured Navier-Stokes solver extended to the chemically reacting flows in the framework of this project in collaboration with Dr. A. Lani, responsible for the development of the numerical methods.

1.4 Publications related to the thesis

The theoretical findings and the results presented in the dissertation have led to the following publications in international journals [132, 135, 136]:

- M. Panesi, P. Rini, G. Degrez, and O. Chazot. *Analysis of chemical non-equilibrium and elemental demixing in the VKI plasmatron.* Journal Thermophysics and Heat Transfer, 21(1):57-66, 2007.
- M. Panesi, T. Magin, A. Bourdon, A. Bultel, and O. Chazot. *Analysis of the Fire II flight experiment by means of a collisional radiative model.* Journal of Thermophysics and Heat Transfer, 2009. Accepted for publication.
- M. Panesi, T. Magin, A. Bourdon, A. Bultel, and O. Chazot. *Behavior of the molecular species predicted by a Collisional-Radiative model in the case of the Fire II experiment.* Journal of Thermophysics and Heat Transfer, 2009. Under submission.
- M. Panesi, T. Magin, A. Bourdon, A. Bultel, and O. Chazot. Collisional radiative modeling in flow simulation. RTO-EN-AVT-162 VKI lecture series, 1(1), 2008.

The work carried out at Stanford University in the framework of the *CTR Summer program 2008* in collaboration with the researchers of NASA Ames research center has led to the following publication:

- A. Bourdon, M. Panesi, A. Brandis, T. Magin, G. Chaban, W. Huo, R. Jaffe, and D. W. Schwenke. *Simulation of flows in shock-tube facilities by means of a detailed chemical mechanism for nitrogen excitation and dissociation.* Center for Turbulence Research, Proceedings of the Summer Program 2008.

Further published material includes several contributions to conference proceedings [53, 129–131, 133, 134, 155]. In addition, as a result of the research conducted during this thesis, several articles are under preparation concerning additional results and theoretical findings presented in this manuscript:

- M. Panesi, Y. Babou, and O. Chazot. *Predictions of nonequilibrium radiation: analysis and comparison with EAST experiments.* Presented at 40th Thermophysics Conference, pages AIAA-2008-3812, Seattle, Washington, June 23-26

- M. Panesi, A. Munafo, O. Chazot. *Modeling of the supersonic plasma flows in the VKI Minitorch by means of a Collisional Radiative model.* Presented at 6th European Symposium on Aerothermodynamics for Space Vehicles, France. 3-6 November 2008

Part I

Multitemperature models

Chapter 2

Governing equations

In this chapter, we present the governing equations used to describe multicomponent, multitemperature, chemically reacting, relaxing and emitting flows. The detailed derivation of the equations used in this work is omitted, limiting ourselves to a brief analysis of the fundamental assumptions underlying the mathematical construct employed. Further information concerning the derivation can be found in Ref. [67, 69, 74, 108, 176].

The chapter is arranged in the following manner. The governing equations, describing the behavior of plasma flows, are detailed in Section 2.1, whereas a brief review of the models used to estimate the transport fluxes is provided in Section 2.2. The last part of the chapter is devoted to discussion of the one dimensional models and describing the thermo-chemical relaxation of the plasma behind a normal shock or within a nozzle (Section 2.3).

Throughout the analysis to be presented, the gas is considered a continuum medium and hence it is described using the Navier-Stokes model, complemented by additional equations to account for the effects induced by chemical reactions and internal energy relaxation. The continuum Navier-Stokes equation model can be applied only when the gradients of the macroscopic variables have much larger characteristic length than the mean free path λ . We define the gradient-length local Knudsen number as

$$(Kn)_{GLL} = \frac{\lambda}{\rho} \left\| \frac{\partial \rho}{\partial \ell} \right\| \quad (2.1)$$

where $\vec{\ell}$ is the direction of the steepest density gradient. Ref. [164] shows Navier-Stokes equations are limited to flows with a Knudsen number of 0.05 or less. The most popular numerical method for simulating high-speed, high Knudsen number (rarefied) flows is the Direct Simulation Monte Carlo (DSMC) particle method developed by Bird [12]. Furthermore, when only

parts of the computational domain exhibit large Knudsen numbers, hybrid methods, based on both a kinetic and continuum approach can be used [160].

The modified set of Navier-Stokes equations, often referred to in literature as *multitemperature model* [24, 95, 138, 158, 166, 167], is not mathematically closed since it requires the modeling of the transport fluxes (shear viscosity, heat-flux and diffusion fluxes), a proper definition of the internal energy and the characterization of the source terms accounting for chemical reactions and energy relaxation in the fluid. Thus the physical description incorporates various physical and mathematical models, discussed in the next chapters: transport properties, thermodynamics and thermo-chemistry.

The modeling of the transport of momentum, energy, and mass in high-temperature gases (described in Chapter 2.2) is obtained with the method of Chapman and Enskog [85] and it is based on the work of Magin [114]. An alternative approach is given by the *irreversible thermodynamics* [67] which provides phenomenological relations avoiding the overwhelming mathematical cumbersomeness and complexity of kinetic theory. However this formalism, because of its lack of description of the microscopic physics, does not allow for the determination of the transport coefficients, needed in the final expression of the fluxes.

Semi-classical statistical mechanics, using quantized energy levels and Boltzmann statistics allows us to define the *thermodynamic properties*, describing the energy of the different internal energy modes, i.e. translational, electronic, rotational, vibrational¹. Thus, in the multitemperature models, the physico-chemical properties of the gas are obtained by assuming that, for all the species, the population of each internal (rotational, vibrational, or electronic) mode follows a Boltzmann distribution at a specific temperature (T_r rotational, T_v vibrational, or T_e electronic temperature, respectively). Also, high temperature gases, in the range of pressure and temperature we are interested in, are composed of different chemical species, which can be divided in two categories: *neutral* and *ionized* species. Among the ionized species we can distinguish between electrons and ions. Owing to their weak mass, the electrons are often referred in the manuscript as *light particles* as opposed to the other species in the mixture often termed *heavy particles*. Each component of mixture behaves with good approximation as a *perfect gas*, given the high temperatures and low pressures conditions that charac-

¹Note that the internal energy of the atoms is restricted to translational and electronic.

terize the flow around a space vehicle during the (re-)entry phase.

Thermo-chemistry provides the mass production terms, modeled according to the *Law of mass action* [176], where macroscopic rate coefficients are assumed to depend on an empirical temperature, function of the different temperatures in the flow, and energy exchange terms are often based on very simplified physical model (e.g. harmonic-oscillator).

2.1 Multitemperature model: set of equations

A numerical model to simulate high temperature gases for re-entry application is presented in this section. The model includes a continuity equation for each species included in the mixture, the momentum equation, the total energy conservation, a vibrational energy conservation for each molecule², as well as a separate equation for the free-electron electronic energy.

In literature the TT_V model of Park [138] is widely used owing to its simplicity and computational efficiency. Such model can be considered a particular case of multitemperature model and can be obtained summing up the vibrational energy equations and the free-electron electronic energy equation. As a result the relaxation of the internal energy modes, with the exclusion of the rotational energy, is described only by one additional energy equation.

Mixture parameters

The characterization of the thermodynamic state of chemically reacting gases requires the knowledge of pressure, temperatures (kinetic and internal) and composition. In this section we introduce the physical quantities used throughout the manuscript to express the composition in a gas mixture.

The *mass fraction* of the i^{th} component, y_i , in the mixture and is given by the ratio of the species mass density ρ_i and the mixture mass density $\rho = \sum_{i \in \mathcal{S}} \rho_i$.

$$y_i = \frac{\rho_i}{\rho}, \quad i \in \mathcal{S} \quad (2.2)$$

²Usually the set of equation for the different molecules is restricted to the neutral molecules in the mixture, i.e. N₂, NO, O₂

where \mathcal{S} indicates the set of indices of the species present in the mixture.

Furthermore in equation 2.3, we define the *molar fraction*, x_i :

$$x_i = \frac{n_i}{n} = \frac{N_i}{N} \quad (2.3)$$

where n_i indicates the number of moles of species i and n the total number of moles. N_i is the number density and it is easily obtained knowing that $N_i = n_i N_A$ where N_A is Avogadro's number.

By definition mass and molar fraction respect the following constraint

$$\sum_{i \in \mathcal{S}} x_i = 1 \quad \text{and} \quad \sum_{i \in \mathcal{S}} y_i = 1 \quad (2.4)$$

and they are related by the following expression

$$y_i = \frac{M_i}{M} x_i \quad (2.5)$$

where M_i is the molar mass of the i^{th} species and $M = \sum_{i \in \mathcal{S}} x_i M_i$ is the mixture molar mass.

2.1.1 Species continuity equations

In order to describe the evolution of the gas composition, the set of Navier-Stokes equations is complemented by additional equations expressing the conservation of the species present in the gas mixture:

$$\frac{\partial \rho_i}{\partial t} + \nabla \cdot (\rho_i \vec{u} + \vec{J}_i) = \dot{\omega}_i, \quad i \in \mathcal{S} \quad (2.6)$$

where ρ_i is the species mass density and $\dot{\omega}_i$ is the mass production term (described in Chapter 4), i.e. it describes the rate of production or depletion of the i^{th} species due to chemical reactions and \vec{J}_i is the diffusion flux (see Chapter 2.2). Summing up all the species continuity equations, we retrieve the global mass conservation equation, since the sum of the mass production terms as well as the sum of the diffusive fluxes is zero:

$$\sum_{i \in \mathcal{S}} \dot{\omega}_i = 0 \quad (2.7)$$

$$\sum_{i \in \mathcal{S}} \vec{J}_i = \sum_{i \in \mathcal{S}} \rho_i \vec{V}_i = 0 \quad (2.8)$$

where \vec{V}_i indicates the diffusion velocity. Equation 2.7 enforces the physical fact that there is no net destruction or production of matter inside the mixture. Equation 2.8 means that the total mass does not diffuse, i.e. there are only $(N_S - 1 : \mathcal{S} = \{1, \dots, N_S\})$ independent diffusive fluxes.

The global mass conservation equation expresses the global conservation of mass in the system

$$\frac{\partial \rho}{\partial t} + \nabla \cdot (\rho \vec{u}) = 0 \quad (2.9)$$

where ρ is the global density and \vec{u} is the mean velocity of the mixture.

Equations of state

Each heavy component of the mixture is governed by the perfect gas law

$$p_i = \rho_i \frac{\mathcal{R}}{M_i} T, \quad i \in \mathcal{H} \quad (2.10)$$

where \mathcal{H} indicates the set of indices of the heavy particles, M_i is the molar mass of the i^{th} species in the mixture, \mathcal{R} is the universal gas constant and with $R_i = \mathcal{R}/M_i$ we refer to the specific gas constant. When electrons are present in the mixture we have

$$p_e = \rho_e \frac{\mathcal{R}}{M_e} T_e \text{ with } T_e \neq T \quad (2.11)$$

where p_e is the partial pressure of the free electrons assumed to be out of equilibrium with the kinetic temperature of the heavy particles. The pressure of the mixture can be easily retrieved from the Dalton's law ($p = \sum_{i \in \mathcal{S}} p_i$) which yields the perfect gas equation

$$p = \sum_{j \in \mathcal{H}} \rho_j \frac{\mathcal{R}}{M_j} T + \rho_e \frac{\mathcal{R}}{M_e} T_e \quad (2.12)$$

where p indicates the pressure of the mixture.

2.1.2 Momentum equation

The momentum conservation equation can be written as:

$$\frac{\partial \rho \vec{u}}{\partial t} + \nabla \cdot (\rho \vec{u} \vec{u}) = -\nabla p + \nabla \cdot \bar{\tau} \quad (2.13)$$

where p is the mixture pressure and $\bar{\tau}$ is the viscous stress tensor discussed in Section 2.2. Since we have assumed quasi-neutrality there is no net electrostatic force on the flow, and the momentum equation retains the exact expression as in the basic Navier-Stokes.

2.1.3 Total energy equation

The total energy conservation equation for the mixture is:

$$\frac{\partial \rho E}{\partial t} + \nabla \cdot (\rho H \vec{u}) = \nabla \cdot (\bar{\tau} \cdot \vec{u}) - \nabla \cdot \vec{q} - Q_I^{Rad} \quad (2.14)$$

where H is the total enthalpy and can be expressed as $H = E + p/\rho$ and E is the total energy per unit mass, i.e. the sum of the mixture internal and kinetic energy: $E = e + (\vec{u} \cdot \vec{u})/2$. The mixture energy per unit mass is given by $e = \sum_{i \in \mathcal{S}} y_i e_i$, where the species energy e_i , $i \in \mathcal{S}$, comprises the translational and formation contributions [$e_e = e_e^T(T_e) + e_e^F$] for electrons; the translational, electronic, and formation contributions [$e_i = e_i^T(T) + e_i^E(T_e) + e_i^F$] for the atoms N, O and ions N⁺, O⁺; and the translational, rotational, vibrational, electronic, and formation contributions [$e_i = e_i^T(T) + e_i^R(T) + e_i^V(T_{vi}) + e_i^E(T_e) + e_i^F$] for all the molecules, where T_{vi} is the vibrational temperature of the i molecule.

The first term in the right hand side is the work of the pressure forces p , the second term is the work of the viscous stresses $\bar{\tau}$ and the third term takes into account the heat flux \vec{q}

$$\vec{q} = \overbrace{-\lambda^{TR} \nabla T - \sum_{m \in \mathcal{V}} y_m \lambda_m^V \nabla T_{vm} - (\lambda^e + \lambda^E) \nabla T_e}^{\vec{q}^c} + \overbrace{\sum_{i \in \mathcal{S}} h_i \vec{J}_i}^{\vec{q}^d} \quad (2.15)$$

where $h_i = e_i + p_i/\rho_i$ is the enthalpy of the i^{th} species, λ^{TR} is the sum of the translational and rotational contribution to the thermal conductivity, λ^V is the vibrational thermal conductivity of the species m , λ^e and λ^E are the thermal conductivities of free electrons and electronic levels respectively.

In equation 2.15 the heat flux \vec{q} is divided in the two components: the conductive part indicated by \vec{q}^c and the diffusive part by \vec{q}^d . Furthermore, in the case of radiating medium an additional term Q_I^{Rad} is added to account for the energy losses.

2.1.4 Vibrational energy equation

The vibrational energy equation expresses the conservation of the vibrational energy of a specific molecule.

$$\frac{\partial \rho_m e_m^V}{\partial t} + \nabla \cdot (\rho_m \vec{u} e_m^V) = -\nabla \cdot \vec{q}_v + \dot{\Omega}_m^{CV} + \dot{\Omega}_m^{VT} + \dot{\Omega}_m^{VV} - \dot{\Omega}_m^{EV}, \quad m \in \mathcal{V} \quad (2.16)$$

where \mathcal{V} indicates the set of indices of the N₂, O₂, and NO molecules, e_m^V is the vibrational energy per unit mass. The other molecules are assumed to be in thermal equilibrium with the vibrational temperature of N₂, if not specified otherwise in the text. The first term on the right hand side represents the heat flux of conduction and diffusion of vibrational energy:

$$\vec{q}_{mv} = -y_m \lambda_m^V \nabla T_m^V + h_m^V \vec{J}_m \quad (2.17)$$

and the other terms account for the energy exchanges with the other energy modes and are discussed in greater detail in Chapter 4 . In particular, $\dot{\Omega}^{CV}$ represent the loss/production of vibrational energy due to chemical reaction. The energy exchange with the translational energy modes are described by $\dot{\Omega}_m^{VT}$. The vibrational energy exchanges among the different molecules are accounted for with the term $\dot{\Omega}_m^{VV}$. The last term, $\dot{\Omega}_m^{EV}$, describes the energy exchanges among vibration and free electrons.

2.1.5 Free electron-electronic energy equation

The relaxation of the energy stored in the translational motion of the free electrons and in the electronic levels of atoms and molecules is described by a separate equation.

$$\frac{\partial \rho E_e}{\partial t} + \nabla \cdot (\rho \vec{u} E_e) = -p_e \nabla \cdot (\vec{u}) - \nabla \cdot \vec{q}_e + \sum_{i \in \mathcal{E}} \dot{\omega}_i e_i^E - \dot{\Omega}^I + \dot{\Omega}^{ET} + \dot{\Omega}^{EV} - Q_{II}^{Rad} \quad (2.18)$$

and \mathcal{E} , the set of indices of the N, O, N⁺, O⁺, N₂, O₂, NO, N₂⁺, O₂⁺, and NO⁺ species, whose electronic energy populations are assumed to follow

Boltzmann distributions. $E_e = y_e e_e + \sum_{i \in \mathcal{E}} y_i e_i^E$ is the free-electrons electronic energy per unit mass. The translational energy of free-electrons and the electronic energy are often couple together, since the most favored channel of electronic excitation is the interaction with the electrons.

The first terms account for the heat flux within the electronic-electron energy mode \vec{q}_e and reads:

$$\vec{q}_e = -(\lambda^e + \lambda^E) \nabla T_e + \sum_{i \in \mathcal{S}} h_i^E \vec{J}_i \quad (2.19)$$

The second terms represent the work done on the electrons by the electric field induced by the pressure gradient. The other terms represent respectively: the influence of the electronic excitation on the electronic energy mode, the influence of the ionization losses $\dot{\Omega}^I$, the elastic exchanges with the heavy particles $\dot{\Omega}^{ET}$, the exchanges with the vibrational energy modes $\dot{\Omega}^{EV}$ and the energy losses due to radiation Q_{II}^{Rad} .

2.2 Transport properties

Transport fluxes constitute the closure of the system of equations governing the dynamics of high enthalpy flows, when dissipative effects are accounted for. Indeed Navier-Stokes equations, presented in Chapter 2, require the knowledge of diffusion fluxes \vec{J}_i , stress tensor $\hat{\tau}$, and heat flux \vec{q} in order to be solved. In this work the transport fluxes have been evaluated using MUTATION library, written by Magin [114], which provides the transport properties for air and CO₂ mixtures of high temperature, weakly ionized gases. This section summarizes the method employed for the evaluation of the transport properties using kinetic theory. The interested reader can find the detailed derivations in Ref. [113, 114].

The kinetic theory of gases is based on the Boltzmann equation, which describes the behavior of atoms and molecules in dilute gases using a statistical approach. In this work the internal structure of the gas has been neglected, disregarding the changes of the internal states of atoms and molecules, during the interaction among the particles. In order to account for the contribution of the internal structure to the transport phenomena, we have used the Eucken correction [60].

The expression of the transport fluxes requires the knowledge of the velocity *distribution function* $f_i(\vec{r}, \vec{c}_i, t)$ [60, 176], whose behavior is governed

by the solution of the Boltzmann equation, written as follows:

$$\frac{\partial f_i}{\partial t} + \vec{c}_i \cdot \nabla_{\vec{r}} f_i + \vec{F}_i \cdot \nabla_{c_i} f_i = \sum_{j \in \mathcal{S}} J_{ij}(f_i, f_j) \quad (2.20)$$

where F_i the external force acting on the particle and J_{ij} is the collisional operator and accounts for the effects due to the collisions.

A particular solution of the Boltzmann equation was obtained by Maxwell for a gas in an equilibrium state with no gradients in composition, velocity and temperature. Hence, by multiplying the Boltzmann equation by the *collision invariants*, integrating over velocity, summing over all the species and assuming a Maxwellian distribution [113], the Euler equations, can be obtained.

In order to retrieve the dissipative effects, we must solve the Boltzmann equation for a system out of equilibrium, where gradients in temperature, velocity and species composition are present. An approximate solution for this problem was proposed separately by Chapman and Enskog, and it linearizes the Boltzmann equations about the equilibrium state. The method of Chapman and Enskog is based on the expansion of the Maxwellian distribution with respect to a small perturbation parameter, which is assumed to be the Knudsen number.

$$f_i = f_i^M (1 + \phi_i) \quad (2.21)$$

Such expansion leads to a set of integral equations which can be solved using a spectral Galerkin method. An approximate solution of the perturbation function ϕ_i is found using a truncated series of Sonine polynomials. The accuracy of the approximation depends on the number of terms retained in the expansion. Furthermore projecting the Boltzmann equation on the collision invariants and using Equation 2.21, we retrieve the set of Navier-Stokes equations and the definition for the transport fluxes.

Transport coefficients are expressed as the solution of linear systems in terms of the so called *collision integrals*. The collision integral may be interpreted as generalized cross sections, i.e. an averaged cross section over all the possible relative energies. The kinetic data used throughout this investigation were compiled by Vanden Abeele [174] for an air mixture.

The evaluation of the transport coefficients can be done using direct methods, iterative methods or resorting to the so called *mixture rules*. The accuracy of the approximate mixture rules is not adequate for dissociating and

ionizing gases and have been discarded in the present work. Furthermore the iterative methods have proven their efficiency, allowing to obtain the same accuracy of the direct methods at a reduced cost [114].

2.2.1 Diffusion fluxes

The solution of the Stefan-Maxwell system of equations is used to retrieve the diffusive fluxes. The method is completely equivalent to the complete diffusion equations derived by means of Chapman-Enskog theory, and it was preferred due to its computational efficiency. The diffusion fluxes may be written as

$$\frac{M}{\rho} \sum_{i \in \mathcal{H}} \left(\frac{x_s \vec{J}_i}{M_i \mathcal{D}_{si}} - \frac{x_i \vec{J}_s}{M_s \mathcal{D}_{si}} \right) = \vec{d}_i \quad (2.22)$$

where \vec{d}_i is the vector of the driving forces and it does not account for thermal and pressure diffusion, which are found to be of negligible importance in our applications [6]. The symbol \mathcal{D}_{si} indicates the binary diffusion coefficients. The diffusion flux of the light particles J_e is retrieved by quasi-neutrality.

2.2.2 Viscous stress and heat flux

The viscous stress tensor as computed by the Chapman Enskog approximation reads

$$\hat{\tau} = \mu (\nabla \vec{u} + \nabla \vec{u}^T) \left(\kappa - \frac{2}{3} \mu \right) (\nabla \cdot \vec{u}) \hat{I} \quad (2.23)$$

where μ is the shear viscosity and κ is the contribution due to the bulk viscosity, the latter being neglected in the present work. Bulk viscosity accounts for the nonequilibrium effects among translation and the internal structure of the particle populations which equilibrates thanks to inelastic collisions. To estimate the shear viscosity we solve the transport system using the conjugate gradient method as explained in Ref. [114]. The contribution to viscosity due to light particles is found negligible due to the mass disparity with respect to the heavy particles.

The heat-flux can be expressed as follows:

$$\vec{q} = -\lambda^T \nabla T - \lambda^e \nabla T_e - \lambda^V \nabla T_V - \lambda^R \nabla T_R - \lambda^E \nabla T_E + \sum_{i \in \mathcal{S}} h_i \vec{J}_i \quad (2.24)$$

The contribution to the transport properties, given by the internal structure of the molecules, have been accounted for by means of the Eucken correction [60], as follows:

$$\lambda^R = \sum_{i \in \mathcal{H}} \frac{\rho_i c_{Pi}^R}{\sum_{j \in \mathcal{H}} x_j / \mathcal{D}_{ij}} \quad (2.25)$$

$$\lambda^V = \sum_{i \in \mathcal{H}} \frac{\rho_i c_{Pi}^V}{\sum_{j \in \mathcal{H}} x_j / \mathcal{D}_{ij}} \quad (2.26)$$

$$\lambda^E = \sum_{i \in \mathcal{H}} \frac{\rho_i c_{Pi}^E}{\sum_{j \in \mathcal{H}} x_j / \mathcal{D}_{ij}} \quad (2.27)$$

where c_{Pi}^R , c_{Pi}^V , c_{Pi}^E are the rotational, vibrational, and electronic species specific heats per unit mass. The translational thermal conductivity is obtained as done for the viscosity solving the system of equations using an iterative method.

2.3 Simplified flow equations

The accurate simulation of high enthalpy flows requires the solution of the Navier-Stokes equations. To this end, the governing equations described in the preceding section are implemented into three dimensional solvers, which although able to reproduce all the flow features, they are computationally expensive and are not suitable for fundamental studies of detailed kinetics.

In this section we present two approximate Eulerian set of equations used to test multitemperature models. Although based on an approximate one dimensional flow model, which neglect dissipative effects, SHOCKING and the nozzle code are able to reproduce the main features of the flow of interest and are extremely efficient in terms of computational time.

SHOCKING simulates the flow behind a strong normal shock and it is used to study the thermal and chemical relaxation in a compressing flow situation. The nozzle code reproduces the flow along the axis of a nozzle and it is based on a quasi one-dimensional assumption. The nozzle code allow us to study the thermal and chemical relaxation in expanding flows which may be substantially different from the one taking place in a compressing flow situation.

2.3.1 Onedimensional shock tube: governing equations

Post-shock conditions are derived from jump relations assuming frozen gas composition and vibrational and electronic energy modes, the rotational mode being in equilibrium with the translational mode. Then, the downstream flowfield is determined by solving conservation equations of mass, momentum, global energy, vibrational energy of the N₂, O₂, and NO molecules, respectively, and a separate energy equation for the free electrons and species with electronic energy level populations assumed to follow Boltzmann distributions:

$$\frac{\partial}{\partial x} (\rho_i u) = \dot{\omega}_i, \quad i \in \mathcal{S} \quad (2.28)$$

$$\frac{\partial}{\partial x} (\rho u^2 + p) = 0 \quad (2.29)$$

$$\frac{\partial}{\partial x} [\rho u (h + \frac{1}{2} u^2)] = 0 \quad (2.30)$$

$$\begin{aligned} \frac{\partial}{\partial x} (\rho u y_m e_m^V) &= \dot{\omega}_m e_m^V + \Omega_m^{VT} + \Omega_m^{VV} - \Omega_m^{EV}, \quad m \in \mathcal{V} \\ \frac{\partial}{\partial x} [\rho u (y_e e_e + \sum_{i \in \mathcal{E}} y_i e_i^E)] &= -p_e \frac{\partial u}{\partial x} + \dot{\omega}_e e_e + \sum_{i \in \mathcal{E}} \dot{\omega}_i e_i^E \\ &\quad - \Omega^I - \Omega^E + \Omega^{ET} + \Omega^{EV} \end{aligned} \quad (2.31)$$

where x is the stagnation line coordinate and the other symbols have been previously defined. Following the derivation of Thivet [173], the conservative system of Eqs. (2.28)-(2.31) is transformed into a system of ordinary differential equations easily solved by means of the LSODE [153] library.

2.3.2 Quasi-onedimensional nozzle: governing equations

In this paragraph, we briefly describe the general model, for a reacting flow through a converging-diverging nozzle in the quasi-onedimensional approximation and in stationary conditions. Viscous effects are neglected and the resulting set of equations is complemented by additional conservation equations for the relaxation of the internal energy modes. The set of governing equations to be solved are written in 2.28-2.31, with the additional constraint:

$$\rho u A = \dot{m} \quad (2.32)$$

where \dot{m} is the mass flow $\dot{m} = \rho u A$ and $A = A(x)$ indicates the cross-section. In the quasi-onedimensional nozzle code, the cross sectional area

is dependent on x as opposed to the previous case where the area was assumed to be constant and hence was dropped when writing the system of equations. In this sense the nozzle code is more general and can reproduce the results in the post shock relaxation area for given the initial conditions (e.g. Rankine-Hugoniot).

Fixing temperature, pressure and gas composition in the reservoir, the nozzle flow features are determined by the inlet flow speed. For a particular value of the inlet velocity u_c , the flow passes from the subsonic regime in the inlet to a supersonic regime in the outlet. For an inlet speed u_{in} lower than u_c the gas enthalpy is not high enough to let the flow expand and the flow is subject to a re-compression in the diverging part of the nozzle. The value of the critical speed can be found only by a trial error problem, which makes the procedure quite tedious.

The system of equations describing the relaxation of a gas inside a nozzle as written in 2.28-2.32 can be rearranged and directly solved with a ODE package, as in the case of the shock tube code. In this case however, the momentum equation presents a singularity in correspondence of the throat, where the Mach number becomes one. Hence a direct integration of the system of ODEs results in a large number of spatial-steps required since the error monotonically increases as we approach the sonic point. To circumvent this issue, a discontinuous solution procedure is usually adopted. The calculations are interrupted right before the sonic point and are restarted a few cells after the singularity, by extrapolating the solution. As we can see, the problems can be resolved only using tricks, but difficulties in the approach still remain and often the solution near the throat exhibits a physical spurious oscillations.

The new method described in Ref. [48] eliminates these difficulties. The main advantage is that it eliminates the discontinuity in the model using a different approach to manipulate the Euler equations. Such a method leads to a hybrid system of equations composed of algebraic and ordinary differential equations, which although computationally less efficient than the classical approach, allows the elimination of the singularity in the equations. The details of the solution procedure can be found in Ref. [48, 122].

Chapter 3

Thermodynamics

The set of equations, governing the dynamics of high temperature gases presented in the preceding chapter, requires the characterization of the thermodynamic properties of the gas. When dealing with systems in equilibrium (or partial equilibrium, such as in the multitemperature models), the thermodynamic properties can be obtained rather easily using statistical mechanics.

A gas consists of a large number of atoms and molecules, moving throughout the space with a certain amount of *translational* energy. Besides the kinetic energy related to the translational motion, atoms and molecules possess a certain amount of *internal* energy, which is linked to electronic excitation, i.e. to the relative position of the bound electrons with respect to the nucleus. In addition, the molecular species exhibit *two additional degrees of freedom*: rotation and vibration. The rotational and vibrational energy modes of the molecules are intrinsically coupled to each other, owing to the influence that the change in the relative position of the nuclei has on the inertia of the molecule. In the presence of thermal nonequilibrium effects, internal energy modes relax according to different time scales, hence requiring the separation of the internal contributions to the global energy of the gas (e.g. vibration-rotation).

In the present chapter we distinguish among *simplified* or *accurate* thermodynamic models. Thus, depending on the model chosen to describe the rotational and vibrational motion of the molecules, we can distinguish among:

- simplified approaches, which are based on the rigid rotator and harmonic oscillator model (to describe respectively rotational and vibrational motion), allowing for a the complete separation of the internal energy modes;
- accurate models, which preserve the vibrational-rotational coupling and are based on the more realistic model of non-rigid rotator and an-harmonic oscillator.

The approximate model, described in Section 3.1 allows for the estimation of the thermodynamic properties of the gas in thermal equilibrium as well as thermal nonequilibrium conditions. On the contrary the validity of the accurate model, discussed in Section 3.2, is restricted to thermal equilibrium conditions. Indeed, the extension of such a model to nonequilibrium cases requires the definition of the *interaction* energy, as prescribed in Jaffe's model [91] and thoroughly described in Section 3.3.

The aim of this study is to use the more complex and physically consistent model of Jaffe to define the limits of validity of the simplified model and assess its accuracy in different flow conditions. To this end the specific heats at constant pressure and the enthalpy are compared, using the two thermodynamic models for equilibrium and nonequilibrium conditions.

In the last part of the chapter the two models are applied to the one dimensional shock-tube solver described in Section 2.3.1. The results produced are compared in order to directly assess their influence on the flowfield calculation.

REMARK: The legitimacy of the separation of the internal energy modes, universally used in aerothermodynamics, as a result of the extrapolation of microscopic partitioning among rotational, vibrational and electronic levels, originated from a *re-interpretation* of the Born-Oppenheimer approximation, and has been subject to strong criticism in literature [68]. Nevertheless in this work we decided to retain the separation of the internal energy modes owing to lack of data concerning the thermal relaxation as well as the kinetic processes needed for a more consistent model.

3.1 Simplified models

The separation of the internal energy modes is very appealing for CFD applications, owing to its computational efficiency. Hereafter we briefly discuss the assumptions made and the main results obtained with simplified thermodynamics models, comparing our predictions against literature.

Quasi-classical statistical mechanics allows us to express the equilibrium thermodynamic properties of any atom or molecule, using the construct called the partition function [176]. The separability of electronic, rotational and vibrational energy modes, which is linked to the possibility of factorizing

the partition function, becomes possible if:

- firstly, assuming an infinite number of ro-vibrational levels, we describe the rotational and the vibrational motion of the molecules with the simplified models of the rigid rotator and harmonic oscillator.
- Secondly, we require that each electronic level of a particular species is characterized by the same "type" of rotator and harmonic oscillator. In other words, the second constraint requires the use of the same spectroscopic constants for excited and ground electronic states.

The derivation of thermodynamic properties, can be found in Ref. [18, 19, 84, 128, 176] and it is therefore omitted. Hereafter we limit ourselves to provide the final expressions of the thermodynamic properties, as given by simplified models.

Translational energy, enthalpy and entropy The expressions of the translational energy, enthalpy and entropy per unit mass are:

$$e_i^T = \frac{3}{2}R_i T \quad (3.1)$$

$$h_i^T = e_i^T + R_i T \quad (3.2)$$

$$s_i^T = \frac{h_i^T}{T} + R_i \ln \left[\left(\frac{2\pi m_i}{h^2} \right)^{\frac{3}{2}} k^{\frac{5}{2}} \right] + \frac{5}{2} R_i \ln T - R_i \ln p \quad (3.3)$$

where $R_i = \mathcal{R}/M_i$, m_i is the mass of the i^{th} species.

Rotational energy, enthalpy and entropy Within the approximation of rigid rotator, the rotational energy and enthalpy per unit mass is:

$$e_i^R = h_i^R = R_i T_R \quad (3.4)$$

$$s_i^R = \frac{h^R}{T_R} + R_i \ln \left[\frac{1}{\sigma} \left(\frac{T_R}{\theta_i^R} + \frac{1}{3} \right) \right] \quad (3.5)$$

Where θ_i^R stands for the rotational characteristic temperature. The symmetry number $\sigma_i = 1$ or 2 depends on whether the molecule is heteronuclear (NO , NO^+) or homonuclear (N_2 , O_2).

Vibrational energy and enthalpy Within the approximation of the harmonic oscillator, the vibrational energy and enthalpy per unit mass reads:

$$e_i^V = h_i^V = \frac{R_i \theta_i^V}{\exp\left(\frac{\theta_i^V}{T_V}\right) - 1} \quad (3.6)$$

$$s_i^V = \frac{h_i^V}{T_V} - R_i \ln \left[1 - \exp\left(\frac{\theta_i^V}{T_V}\right) \right] \quad (3.7)$$

where θ_i^V is the characteristical vibrational temperature of the i species.

Electronic energy, enthalpy and entropy The electronic energy per unit mass reads:

$$e_i^E = h_i^E = R_i \frac{\sum_e g_{ie} \theta_{ie}^E \exp(-\theta_{ie}^E/T_E)}{\sum_e g_{ie} \exp(-\theta_{ie}^E/T_E)} \quad (3.8)$$

$$s_i^E = \frac{h_i^E}{T_E} + R_i \sum_e g_{ie} \exp(-\theta_{ie}^E/T_E) \quad (3.9)$$

where g_{ie} is the degeneracy of the electronic level e and θ_{ie}^E is its characteristic temperature. Since the series diverges, a simple cut off criteria is applied, selecting the number of electronic energy levels in order to match the results of more accurate calculations.

The energy, enthalpy and entropy of the atoms are:

$$e_i = e_i^T(T) + e_i^E(T_E) + e_i^F \quad (3.10)$$

$$h_i = e_i + R_i T \quad (3.11)$$

$$s_i = s_i^T(T) + s_i^E(T_E) \quad (3.12)$$

where e_i^F is the formation energy and it is computed from the heat of formation at 0 K.

The molecules exhibit additional degrees of freedom and their expression for the energy and the enthalpy reads:

$$e_i(T, T_E, T_V, T_R) = e_i^T + e_i^E(T_E) + e_i^V(T_V) + e_i^R(T_R) + e_i^F \quad (3.13)$$

$$h_i = e_i + R_i T \quad (3.14)$$

$$s_i(T, T_E, T_V, T_R) = s_i^T + s_i^E(T_E) + s_i^V(T_V) + s_i^R(T_R) \quad (3.15)$$

This simple formula states that the overall contribution of the internal energy is a function of the separate contributions of each of the internal energy modes. Even more interesting, the energy of each energy mode depends on its own temperature.

The electrons do not have internal structure hence their energy, enthalpy and entropy read:

$$e_e(T_e) = e_e^T + e_e^F \quad (3.16)$$

$$h_i = e_i + R_i T_e \quad (3.17)$$

$$s_e(T_e) = s_e^T + R_e \ln 2 \quad (3.18)$$

The mixture thermodynamic properties are given by:

$$e = \sum_{i \in S} y_i e_i \text{ and } h = \sum_{i \in S} y_i h_i \quad (3.19)$$

$$s = \sum_{i \in S} y_i s_i + k_B \sum_{j \in S} n_j (1/x_j) \quad (3.20)$$

where the contribution of the entropy of mixing is accounted for to evaluate the mixture entropy. Furthermore, species Gibbs free energies used to estimate the equilibrium constants are given by the relation $g_i = h_i - T s_i$.

3.1.1 Simplified models: results

The non-dimensional specific heat of N₂ calculated with the simplified model is compared in Figure 3.3 with the results of Capitelli [36], carried out considering a more realistic thermodynamic model. Both the predicted specific heats at constant pressure start at 3.5 ($5/2\mathcal{R} + \mathcal{R}$), since at low temperature only the translational and the rotational energy modes are excited. As the temperature rises the first mode to be excited is vibration, which increases the specific heat up to 4.5 ($5/2\mathcal{R} + \mathcal{R} + \mathcal{R}$), and a further increase in the temperature brings about the excitation of the electronic energy levels of the molecule, responsible for the maximum in the evolution of the specific heat. The discrepancies among the two results are mostly due to the infinite number of levels considered for the simplified models, which leads to an overestimation of the specific heat in correspondence of the maximum. This can be artificially compensated reducing the number of electronic levels considered. The influence of cut off is shown in the figure and the different

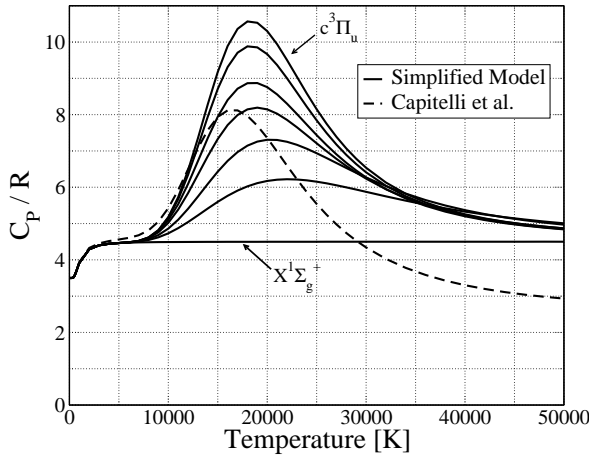


Figure 3.1: N_2 . Non-dimensional specific heat at constant pressure. The broken line refers to the calculation of Capitelli *et al* [36]. The unbroken lines represent the results obtained with the simplified models, for increasing number of electronic levels considered.

curves account for an increasing number of electronic states considered.

For increasing temperatures, the specific heat converges to the value of $(5/2 \mathcal{R})$, as the internal degrees of freedom become saturated and the only additional contribution comes from the translational energy mode. The reason of such behavior is due to the finite number of levels considered in the system.

Since the simplified model considers an infinite number of ro-vibrational levels, rotation and vibration keep contributing to the specific heat, and the asymptote is displaced accordingly to $(5/2 \mathcal{R} + 2\mathcal{R})$.

As we can observe from the specific heat curve the error of the so called simplified model becomes relevant for temperatures exceeding $10\,000 [K]$. However at such high temperatures, if the flow is not too far from the equilibrium conditions, the molecules are completely dissociated. Hence, the use of such simplified models is justified at least for equilibrium conditions for CFD applications.

3.2 Advanced models for thermodynamics

A validation of the accurate model for thermodynamic properties under thermal equilibrium [36, 57, 63] is seen as a necessary step before presenting the results using the nonequilibrium thermodynamic model of Jaffe, which is an extension of such model to thermal nonequilibrium. The method employed for the determination of the equilibrium thermodynamic properties of diatomic molecules, based on a more realistic physical model than the harmonic oscillator and rigid rotator, is discussed hereafter.

The starting point is the definition of the ro-vibronic energy levels, here expressed as follows:

$$\epsilon(e, v, J) = \epsilon_e(e) + \epsilon_v(e, v) + \epsilon_J(e, v, J) \quad (3.21)$$

where e, v, J are respectively the electronic, vibrational and rotational quantum number. $\epsilon(e, v, J)$ is the ro-vibronic state, $\epsilon_e(e)$ is the electronic contribution to the "total" energy, $\epsilon_v(e, v)$ is the vibrational energy and $\epsilon_J(e, v, J)$ accounts for the rotational part. In equation 3.21 rotation is considered as a perturbation of vibration, since vibrational energy does not depend on the rotational motion, as opposed to rotation which depends on the vibrational quantum number. The problem of the energy splitting and the impact that the adopted partitioning method has on the results is discussed later on in section 3.3, within the nonequilibrium thermodynamics. In the case of an equilibrium calculation, one temperature is assigned to the internal and kinetic part of the energy and the problem of partitioning does not affect the results.

The formulation of the partition function requires the solution of the triple summation over the electronic, vibrational and rotational energy levels of the molecules. The expression of the internal partition function is given here:

$$Q_{INT}(T) = \sum_e^{e_{Max}} g_e \exp\left(\frac{-\epsilon_e(e)}{k_B T}\right) \sum_v^{V_{Max}(e)} \exp\left(\frac{-\epsilon_v(e, v)}{k_B T}\right) \sum_J^{J_{Max}(e, v)} (2J+1) \exp\left(\frac{-\epsilon_J(e, v, J)}{k_B T}\right) \quad (3.22)$$

The extrema of the summations depend on the electronic quantum number and in particular the maximum rotational quantum number J_{max} depends

on the vibrational quantum number as we shall see in the next sections. In order to be able to retrieve the internal partition function, $V_{Max}(e)$ as well as $J_{Max}(e, v)$ have to be determined for each electronic level.

3.2.1 Maximum vibration quantum number

If we consider a non-rotating molecule, the maximum vibrational quantum number can be easily estimated, provided that the dissociation energy is known. Thus we seek for the value of vibronic state characterized by vibrational energy equal to the dissociation energy of the considered electronic state. This is done imposing

$$\epsilon_v(e, v) = D_e \quad (3.23)$$

where D_e is the dissociation energy of the electronic state. Solving for the vibrational quantum number, we find the desired value of maximum vibrational quantum number. An analytical expression of the vibrational energy levels is given by the Dunham expansion [84] and leads to the following expression

$$\epsilon_v(e, v) = \omega_e \left(v + \frac{1}{2} \right) - \omega_e x_e \left(v + \frac{1}{2} \right)^2 = \frac{D_e}{hc} \quad (3.24)$$

where ω_e , $\omega_e x_e$ are the spectroscopic constants and are listed in many references, Ref. [36, 80]; we indicate Planck's constant with h and the speed of light with c . High order terms in the expression have been neglected for two reasons. Not all the necessary spectroscopic data are known for all the molecules and more importantly, the effects of the higher order terms are usually negligible considering the focus of this work, being the definition of the thermodynamic properties.

The solution of the equation 3.24 has two real roots, the smaller one is the one to be chosen. In some cases, however, the solution is a complex number. Such solutions have no physical meaning and are due to approximations in the determination of the vibrational quantum state.

In the case of complex roots, instead of solving the equation (3.24), we consider the maximum of the curve. The error committed in this case is relatively small, being the maximum of the parabola (given by equation 3.24) very close to the dissociation energy. The value of the v_{max} for some electronic state of the molecular nitrogen and the comparison with literature is shown in Table 3.1. Discrepancies between the maximum number of levels are mainly due to different models for the potential curve. All the data

Electronic State	v_{max}	Present Work	Gurvich	Bacri
$X^1\Sigma_g^+$	48	56	48	
$a^3\Sigma_u^+$	26	33	26	
$b^3\Pi_g$	29	35	32	
$w^3\Delta_u$	37	-	-	
$b'^3\Sigma_u^-$	40	46	-	
$A'^1\Sigma_u^-$	63	58	-	
$A^1\Pi_g$	45	50	46	
$W^1\Delta_u$	43	51	-	
Σ_g^+	6	6	-	
$g^3\Delta_g$	22	-	-	
$c^3\Pi_u$	5	-	-	

Table 3.1: v_{max} for different excited state of molecular nitrogen.

concerning the maximum number of vibrational levels have been included in Ref. [128].

REMARK: Our calculations have been performed by taking as a reference for the energy levels the minimum of the potential curve. Other results were obtained taking as a reference the first vibrational level of the an-harmonic oscillator. This determines a difference in the internal partition function and energy at low temperature.

3.2.2 Maximum rotational quantum number

The determination of the maximum permissible rotational quantum number J_{max} could proceed, in analogy with what was done for the vibrational quantum number, comparing the vibrational-rotational energy with the dissociation energy relative to the electronic level considered. This however represents a crude approximation since it neglects the influence of rotation on the dissociation energy. Indeed, as the rotational quantum number increases it affects the shape of the potential increasing the value of D_e .

If we consider a rotating molecule on the basis of the classical mechanics, we must introduce an additional term in the expression of the potential to account for the effects due to centrifugal forces. The effective potential energy becomes:

$$U_J(r) = V(r) + \frac{J(J+1)h^2}{4\pi\mu_{A-B}r^2} \quad (3.25)$$

where r is the inter-nuclear separation of the generic AB molecule, U_J is the potential of the rotating molecule, V is the rotationless potential and μ is the equivalent mass $\mu = m_A m_B / (m_A + m_B)$. Introducing the expression of Morse potential in the equation we have:

$$\begin{aligned} U_J(r, J, v, T_e) &= \epsilon_e + \epsilon_v(e, v) + (D_e - \epsilon_v(e, v)) \\ &\quad [1 - \exp(-\beta_e(r - r_e))]^2 + \frac{J(J+1)h^2}{4\pi\mu_{A-B}r^2} \end{aligned} \quad (3.26)$$

A series of potential curves can be constructed for different values of the rotational quantum number.

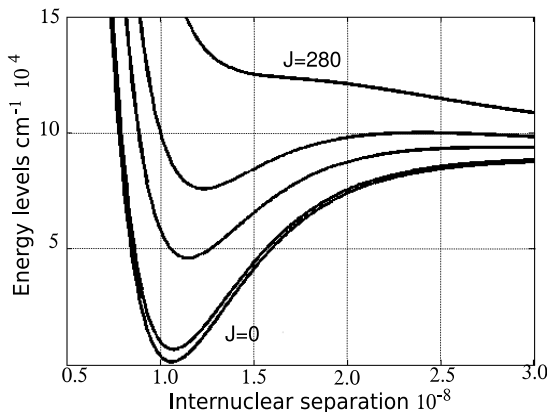


Figure 3.2: Potential curve (Morse) for N_2 ground state for different centrifugal distortions

For $J = 0$ no centrifugal distortion occurs and we retrieve the rotationless potential. As the quantum number increases, the minimum in the curves is displaced respect to the equilibrium distance and the dimensions of the potential well decrease. When the J reaches the value of J_{Max} , the potential does not exhibit a minimum and the molecule is torn apart. This means that for $J = 0$ all vibrational states with energy lower than the dissociation limit are present, while there are no stable states with J larger than J_{max} .

Hence, the existence of *quasi-bound* states above the dissociation limit of the molecule is determined by the centrifugal distortion of the potential energy due to rotation. In order to evaluate the maximum number of rotational states we have to find, for each vibrational quantum number, the *limit potential curves*, which are characterized by a negative derivative with respect to the radius. So we change the rotational quantum number until we reach this condition:

$$\frac{\partial U}{\partial r} < 0 \quad (3.27)$$

This potential is compared with the energy as calculated from the coupled vibrational-rotational energy expression for any assumed v and J is varied until these two energies are equal. When this point is reached, one has a compatible v, J combination.

$$\epsilon_m = \frac{\epsilon_v(e, 0)}{hc} + \omega_0 v - \omega_0 x_0 v^2 + B_v J(J+1) - D_v J^2(J+1)^2 \quad (3.28)$$

where B_v and D_v are the spectroscopic constants for rotation and can be found in Ref. [36, 80].

Once the maximum number of vibrational levels for each electronic state and the maximum number of rotational states for each vibrational state have been determined, the internal partition function can be calculated using equation 3.22.

In this work, the spectroscopic constants have been taken from Gurvich in Ref. [80] and Morse potential was used to estimate the maximum number of rotational levels for each vibrational quantum number. The details of the calculation are given in [128].

A comparison in terms of non-dimensional enthalpy for the molecular nitrogen is presented in Figure 3.3. Our results agree with the calculation of Capitelli *et al* in Ref. [36]. The contribution of the quasi-bound states have been considered in the calculations as it was shown to have an influence on the thermodynamic properties in Ref. [36]. In the same figure a comparison of the results obtained using simplified models shows once more how the validity of the simplified models is restricted to low temperatures regimes.

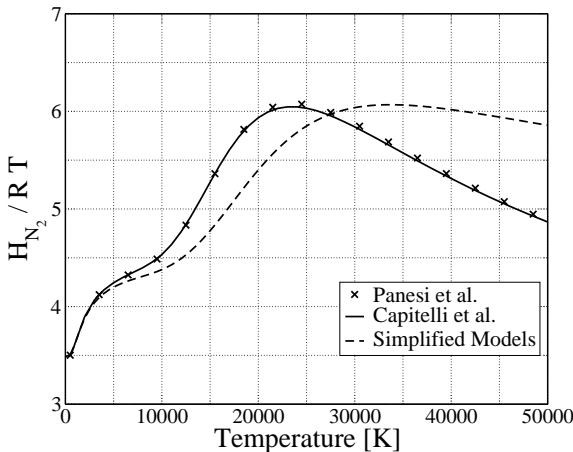


Figure 3.3: N_2 . Non dimensional enthalpy. (x) refers to the calculation performed by Panesi et al. [128]. The unbroken line refers to the work of Capitelli *et al* [36] and the broken line represents the results obtained with the simplified models.

3.3 Thermal-nonequilibrium thermodynamic model of Jaffe

The calculation of the partition function and the estimation of the thermodynamic properties of equilibrium gases have been extensively described in literature [57, 128]. Problems arise in nonequilibrium conditions since the thermodynamic state of the gas cannot be described making use of one temperature. The correct approach in the latter case is to consider each individual ro-vibronic state as a separate species and perform a detailed calculation accounting for all the elementary kinetic processes.

The enormous number of levels and kinetic processes to be accounted for makes this mathematical problem impossible to solve. Engineering models such as the TT_V model of Park have been created to overcome these difficulties. Such models postulate the existence of separate temperatures for different modes drastically reducing the number of equations to be solved and the number of kinetic processes to be modeled.

The separation of the internal energy modes is done in these approaches

in artificial way assuming that rotation is fully developed¹ and lumping the rest of the internal energy with a single temperature often called T_V . Since experimental measurements showed that often rotation and translation equilibrate rather quickly (at least at moderate temperatures [138]), the population of the rotational levels is assumed to be governed by translational temperature, i.e. $T = T_R$.

Jaffe in Ref. [91], keeping the idea of two different temperatures $T_T V$, proposes a more consistent model for thermodynamics, which preserves the coupling among rotational and translational energy modes.

3.3.1 Two ways of splitting the ro-vibrational internal energy

If we consider a molecule in a generic electronic state and we indicate the vibrational quantum number with v and the rotational quantum number with J , the energy of each ro-vibrational state can be indicated as $\epsilon(v, J)$. However if we want to partition such energy into rotational and vibrational part, problems arise due to the so called *interaction energy*. The classical model of non-rigid oscillator gives an idea of the interaction among vibration and rotation. Because of the oscillations, the inertia of the molecules changes affecting their rotational motion (classical mechanics). The interaction energy originates from the coupling among the two energy modes. In order to separate these, we have the choice to include the interaction energy in the rotational energy, considering only the perturbation effects of vibration on rotation, or we can include the interaction energy in the vibrational energy mode leaving rotation unchanged. Considering rotation as a perturbation of the vibrational energy we write:

$$\epsilon(v, J) = \epsilon(v, 0) + \underbrace{\epsilon(v, J) - \epsilon(v, 0)}_{\Delta^I \epsilon(v, J)} \quad (3.29)$$

The other possibility is:

$$\epsilon(v, J) = \epsilon(0, J) + \underbrace{\epsilon(v, J) - \epsilon(0, J)}_{\Delta^{II} \epsilon(v, J)} \quad (3.30)$$

In nonequilibrium conditions, the two cases lead to different results in terms of the partition function and thus in terms of thermodynamic properties,

¹The rotational specific heat is assumed to be equal to \mathcal{R} , which correspond to the asymptotic value of the specific heat in the case of rigid rotator.

whereas in equilibrium the separation of rotation and vibration is only formal and the results are not dependent on the type of energy splitting.

3.3.2 Two temperature partition function

The concept of partition function is generalized to multitemperature approach if the summation over each internal mode is performed for the respective internal temperature. Using the first of the two possible energy splitting described in Section 3.3.1, we obtain:

$$Q_{INT}^I(T_V, T) = \sum_e^{e_{Max}} g_k \exp\left(\frac{-\epsilon_e(e)}{k_B T_V}\right) \sum_v^{V_{Max}(e)} \exp\left(\frac{-\epsilon_{v,0}(e, v)}{k_B T_V}\right) \\ \sum_J^{J_{Max}(e, v)} (2J+1) \exp\left(\frac{-\Delta^I \epsilon_J(e, v, J)}{k_B T}\right) \quad (3.31)$$

The other splitting leads to a different expression of the nonequilibrium partition function:

$$Q_{INT}^{II}(T_V, T) = \sum_e^{e_{Max}} g_k \exp\left(\frac{-\epsilon_e(e)}{k_B T_V}\right) \sum_J^{J_{Max}(e)} (2J+1) \exp\left(\frac{-\epsilon_{0,J}(e, J)}{k_B T}\right) \\ \sum_v^{V_{Max}(e, J)} \exp\left(\frac{-\Delta^{II} \epsilon_V(e, v, J)}{k_B T_V}\right) \quad (3.32)$$

The non uniqueness of the partition function affects all the thermodynamic properties, since they depend on the choice made at the moment of the splitting of the energy levels. The internal energy can be expressed in the following two forms:

$$E_{Ave}^I(T_V, T) = Q_{INT}^{I-1} \sum_e^{e_{Max}} g_e \exp\left(\frac{-\epsilon_e(e)}{k_B T_V}\right) \sum_v^{V_{Max}(e)} \exp\left(\frac{-\epsilon_{v,0}(e, v)}{k_B T_V}\right) \\ \sum_J^{J_{Max}(e)} (2J+1) \epsilon_{v,J}(e, v, J) \exp\left(\frac{-\Delta^I \epsilon_J(e, v, J)}{k_B T}\right)$$

$$E_{Ave}^{II}(T_V, T) = Q_{INT}^{II-1} \sum_e^{e_{Max}} g_e \exp\left(\frac{-\epsilon_e(e)}{k_B T_V}\right) \sum_J^{J_{Max}(e)} (2J+1) \exp\left(\frac{-\epsilon_{0,J}(e, J)}{k_B T}\right) \\ \sum_v^{V_{Max}(e)} \epsilon_{v,J}(e, J, v) \exp\left(\frac{-\Delta^{II}\epsilon_V(e, v, J)}{k_B T_V}\right)$$

The vibrational and rotational contributions to the internal specific heat are:

$$C_P^V(T_V, T) = \left(\frac{\partial E_{Ave}}{\partial T_V} \right)_T$$

$$C_P^R(T_V, T) = \left(\frac{\partial E_{Ave}}{\partial T} \right)_{T_V}$$

Each component of the specific heat is still a function of both T_V and T . Furthermore, when $T_V=T$:

$$C_P^{INT} = C_P^V + C_P^R$$

The three quantities $E_{ave}(T_V, T)$, $C_P^V(T_V, T)$ and $C_P^R(T_V, T)$ fed to the system of equations, described in Chapter 2, allow us to determine T_V and T in flowfield calculations.

3.4 Results

In order to gain further insight in the understanding of the importance of the partitioning of rotational-vibrational energy, its effect on the thermodynamic properties is investigated, using nonequilibrium maps for the specific heats at constant pressure (Section 3.4.1). Furthermore, the impact of the modeling on the state of the gas is addressed by means of simplified flow solvers, which allow to assess the influence of the energy splitting in Jaffe's model (Section 3.4.2) comparing the results given by the simplified model with the ones obtained using the accurate model (Section 3.4.3).

3.4.1 Nonequilibrium thermodynamic properties

In this study, we propose an analysis of the vibrational and rotational components of specific heats at constant pressure as a function of the two temperatures T_V and T , aiming to quantify the influence of the partitioning criteria under nonequilibrium conditions. Although the analysis that follows is limited to molecular nitrogen, the same conclusions can be extended to the other diatomic molecules belonging to the air mixture. The forthcoming results will show how the internal energy is weakly affected by the partitioning method adopted, confirming Jaffe's conclusions in Ref. [91], as opposed to the behavior of the specific heats, which are expected to be more sensitive, since they are defined as a derivative of the internal energy.

The non dimensional specific heat at constant pressure of N_2 , shown in Figures 3.4, was obtained adopting the first method of partitioning, i.e. including the interaction energy in the rotational energy. The results appear to be qualitatively similar to the ones obtained adopting the second partition scheme, shown in Figure 3.5. Both plots present the peak due to the excitation of the electronic energy levels as seen in the equilibrium case and they both tend to the asymptotic value of $5/2$ as the temperature increases. On the diagonal the two temperatures are equal and the equilibrium results are retrieved in both cases.

The differences are restricted to the lower part of the contour plot, characterized by low vibrational temperature and high rotational temperature. The reasons of such discrepancies are to be sought in the definition of the specific heat of vibration and in the relative importance of vibrational and interaction energy. The vibrational and rotational specific heats depend on both vibrational and rotational temperature as previously discussed. However the dependence of the specific heats on their corresponding temperatures is stronger than the dependence on the other temperature², (the C_P^V strongly depends on T_V but it only weakly depends on T). Generally speaking, the interaction energy is indeed smaller than the vibrational and the rotational contributions. Therefore in the region of the diagram where the vibrational temperature (or T for C_P^R) is significant its contribution dominates and the influence of the interaction energy is weak. However as we move to lower T_V and higher T , the importance of the interaction energy increases, thanks to the rotational temperature. In such situations the in-

²Usually each specific heat depends on its own temperature since the internal rotation and vibration are separated without accounting for the interaction energy, which is assumed negligible.

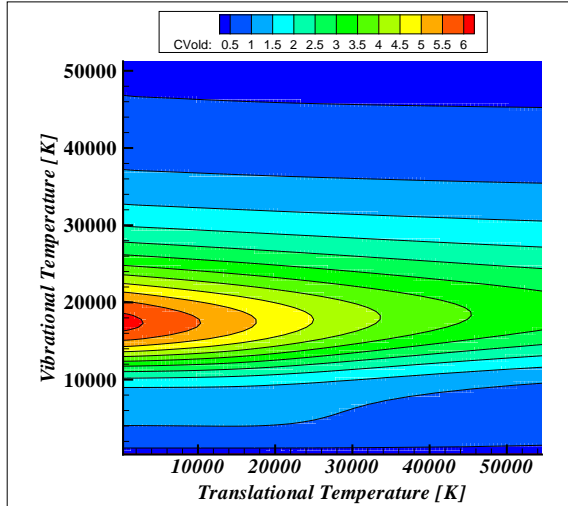


Figure 3.4: N_2 first partition method. Nonequilibrium specific heat at constant pressure as a function of T_V and T . The values of the specific heat have been non-dimensionalized dividing by \mathcal{R} .

teraction energy becomes comparable with the vibrational energy and the choice of the partitioning method may lead to differences in the results. Figure 3.6 shows the difference in terms of vibrational heat specific for the two partitioning methods. The differences are small everywhere except in a narrow region close to the T axis where the vibrational temperature approaches zero. In such area the discrepancies can be very large.

Figures 3.7-3.8 show the specific heat of rotation for the two possible splitting. Since the rotational heat specific depends mainly on the rotational temperature, we should expect differences in the part of the contour map where the rotational temperature is small and the vibrational temperature is high. The results in Figure 3.9 confirm this tendency, even if the influences of the partitioning method on the results are found to be smaller than in the previous case.

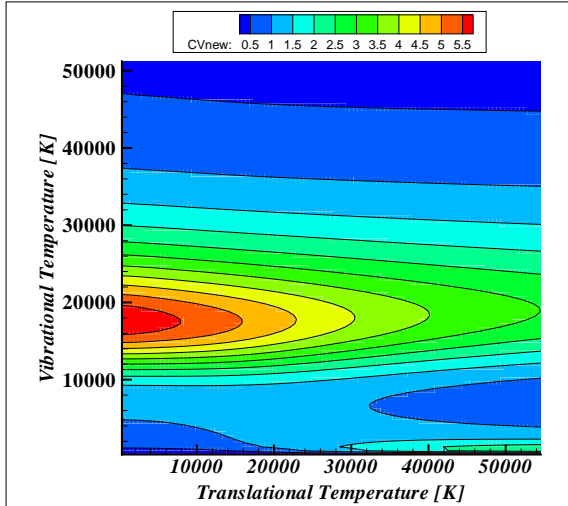


Figure 3.5: N_2 second partition method. Nonequilibrium specific heat of vibration at constant pressure as a function of T_V and T . The values of the specific heat have been non-dimensionalized dividing by \mathcal{R} .

3.4.2 Influence of the splitting on the results

The analysis of the results in the foregoing section showed a certain sensitivity of the C_P^V to the partitioning method employed. The aim of this section is to quantify the impact that such differences may have on the flowfield calculations. For this purpose we simulated the flowfield in the post-shock relaxation area using the one dimensional shock tube code, described in Section 2.3.1. The two different separation methods are employed for all the molecules included in the mixture (N_2 , NO , O_2 , N_2^+ , NO^+ , O_2^+) and the results are compared in terms of temperature and composition profiles. The test conditions are taken from the EAST test campaign, discussed in Section 6.3, and assumed a pre-shock pressure of 13.3 Pa and a shock speed of 10 km/s.

The analysis of the temperature profiles in Figure 3.10 demonstrate the insensitivity of the results to the partitioning method chosen. Small differences in the nonequilibrium part of the curves are possibly due to the difference in the C_P^V discussed in the foregoing section.

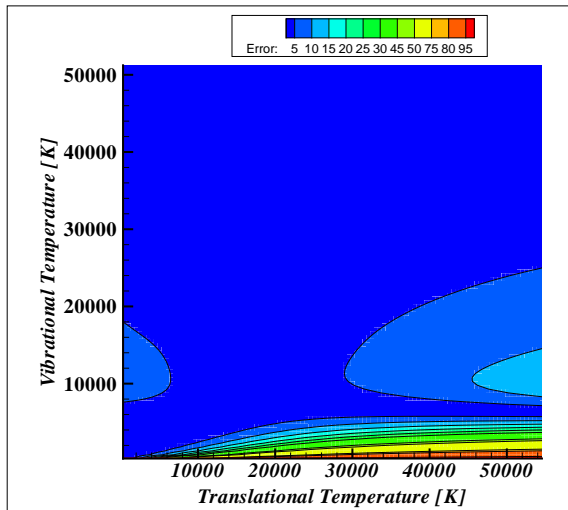


Figure 3.6: N_2 relative error. Nonequilibrium specific heat of vibration at constant pressure as a function of T_V and T . Influence of the partitioning method.

The number densities of the eleven species included in the mixture are depicted in Figure 3.11 and confirm the weak influence of the partitioning method adopted. The differences in the composition are in general less than 10 %.

The analysis of the temperature and composition has led us to the conclusion that the influence of the method used for the separation of rotation and vibration is rather limited, owing to the reduced importance of the interaction energy with respect to the vibrational and rotational energy.

3.4.3 Comparison between the accurate and simplified approaches

The simplified models described in Section 3.1 are often used in CFD due to their computational efficiency, which mainly arises from the separation of the internal energy modes. Hereafter we propose a detailed comparison of

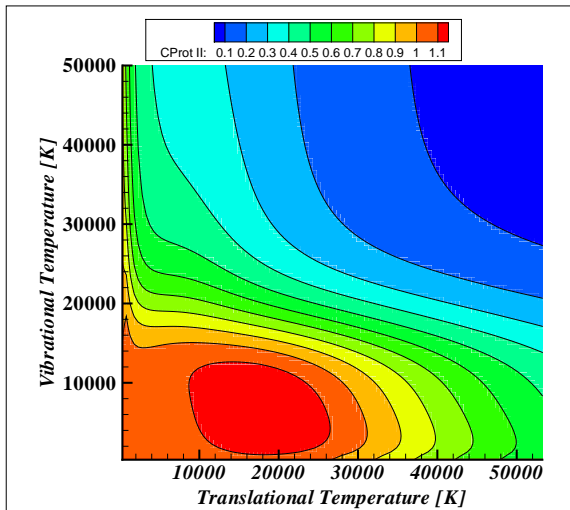


Figure 3.7: N_2 first partition method. Nonequilibrium specific heat of rotation at constant pressure as a function of T_V and T . The values of the specific heat have been non-dimensionalized dividing by \mathcal{R} .

such models against the more physically consistent model of Jaffe to assess its accuracy.

This comparison is carried out using the one dimensional shock tube code described in Section 2.3.1. We simulate the flow behind a normal shock using the two models for thermodynamics and we analyze the differences of the results in terms of temperature and composition along the stagnation line.

It is important to remark that the improved thermodynamic models were not applied to the modeling of the source terms in the vibrational energy equation. Such terms often rely on the Landau Teller formulas (such as vibrational-translational exchanges), which are based on the harmonic oscillator assumption.

Figure 3.12 shows the temperature plots for the FIRE II-1634 testcase. The testcase is thoroughly presented in Section 6.2.4 and the flight conditions are characterized by a re-entry velocity of 11.36 km/s and the free-

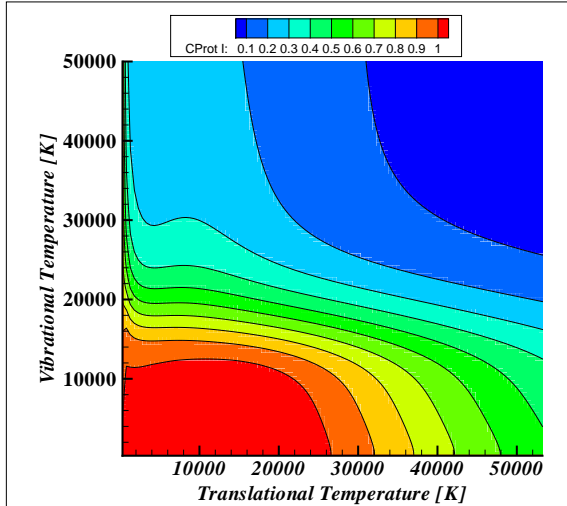


Figure 3.8: N_2 second partition method. Nonequilibrium specific heat of rotation at constant pressure as a function of T_V and T . The values of the specific heat have been non-dimensionalized dividing by \mathcal{R} .

stream pressure of 2 Pa. The flight conditions are similar to those encountered by a space vehicle during the re-entry from the moon and cause strong nonequilibrium effects in the shock layer. The ro-translational and vibrational temperature profiles after a normal shock are compared for the two thermodynamic models. The relaxation of the two models is qualitatively the same even if the simplified model tends to overestimate both temperatures. In the equilibrium plateau region the predictions differ by less than 200 K. Composition profiles are not shown here but we found differences smaller than 10 % for the two models throughout the computational domain.

The predicted electron number density in the plateau region is compared in Table 3.2 against results of Johnston in Ref. [93]. The thermodynamic model used in the reference results is based on the work of McBride *et al* [118]. The separation of the internal energy among rotation and vibration is based on the assumption that the contribution of the rotational part to the global specific heat is R , being that rotation is fully developed at high temperatures [69]. The model indicated as "Modified Jaffe" is based on the

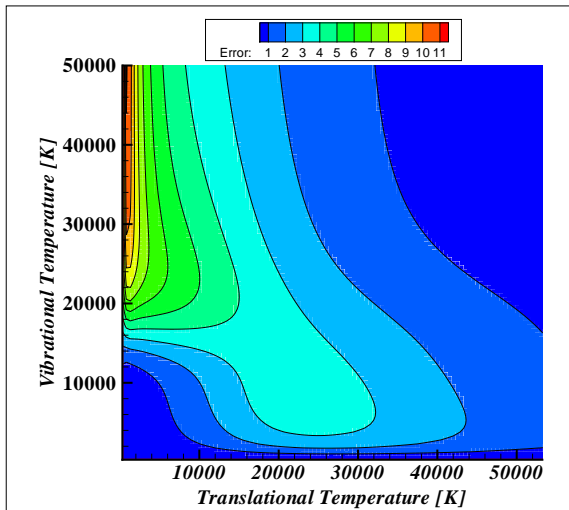


Figure 3.9: N_2 relative error. Nonequilibrium specific heat of rotation at constant pressure as a function of T_V and T . Influence of the partitioning method.

Jaffe model and relies on the same assumptions concerning the rotational specific heat. The Jaffe model predicts the lowest value for the electron density as opposed to the results presented by Johnston which yield the highest prediction. Such differences can be explained when we compare the modified model of Jaffe for the thermodynamics with the results of Johnston. The difference in this case are of the order of few percent suggesting the possibility that the assumption made leads to an increase of the electron density. Differences between the simplified model and the one proposed by Jaffe are about 9 %.

Large differences are found in the computational time required to perform a full simulation with the simplified and with the accurate model. While the simplified thermodynamics allows us to simulate the full domain in less than a second, the simulation with the accurate model takes up to 15 minutes. For this reason, look up tables for the specific heats have been created, fitting the contour maps presented in Section 3.3. Although the computational time was reduced to a few seconds and it is not competitive with the sim-

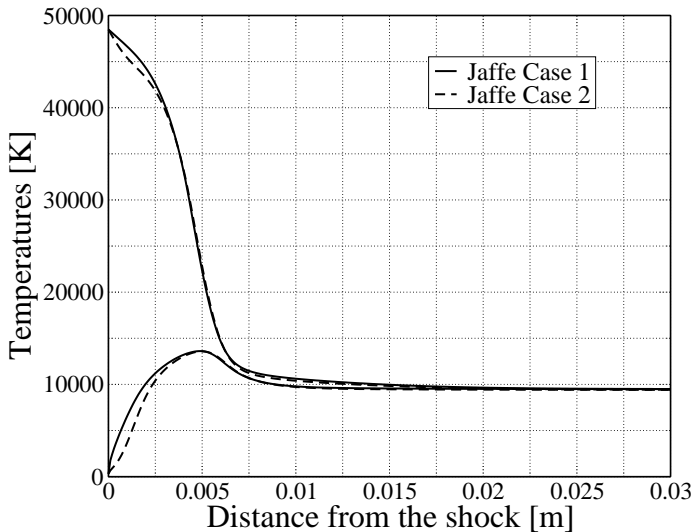


Figure 3.10: EAST case. Temperature profiles. Unbroken lines indicate the first method of partitioning and the broken lines represent the results obtained adopting the second method of partitioning.

Model	$N_e [m^3]$	Difference [%]
Simplified Model	$4.22E + 22$	7 %
Jaffe	$3.84E + 22$	15 %
Johnston	$4.55E + 22$	-
Modified Jaffe	$4.38E + 22$	3 %

Table 3.2: Electron density and influence of the thermodynamic models.

plified model, since the simplified model results are still about 7 times faster.

At lower speeds, up to $7 - 8$ km/s, the predictions given by the simplified and the accurate model are in good agreement and are not presented here. The reason of the agreement is twofold: firstly the flow approaches equilibrium conditions and therefore molecules tend to dissociate as the temperature exceeds the dissociation threshold. Secondly most of the molecules are found close to the bottom of the potential well where the potential of

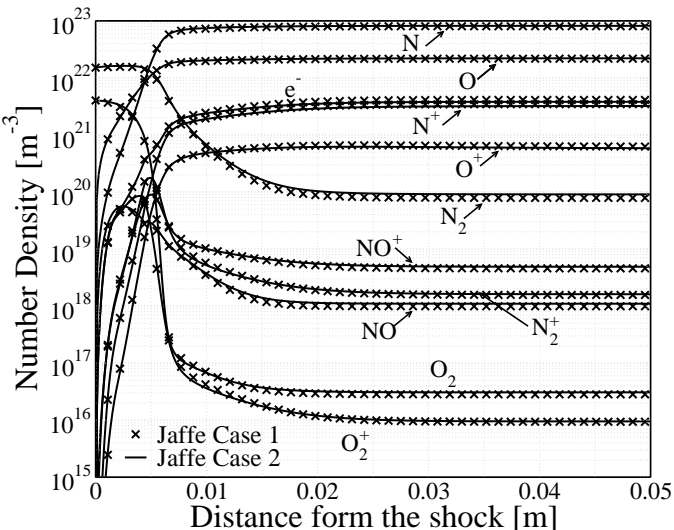


Figure 3.11: EAST case. Composition profiles. (\times) indicate the first method of partitioning and the unbroken lines represent the results obtained adopting the second method of partitioning.

the molecules can be modeled with good approximation by the harmonic oscillator potential.

Summary

The chapter proposes a review of different models used to express the thermodynamic properties of high temperature gases. A comparison among the so called "simplified models" and the more physically consistent model of Jaffe is presented. The approximate methods based on the simplifying assumption of rigid rotor and harmonic oscillator (assuming an infinite number of ro-vibrational levels), is found to give a reasonable estimate of the thermodynamic properties of the diatomic molecules in air. Such accuracy is enhanced with an artificial selection of the electronic states of the diatoms in order to reproduce the results given by the more accurate models. Furthermore, a comparison of the results obtained by means of a shock tube solver with the two models for thermodynamics confirms a weak dependence of the results on the model chosen.

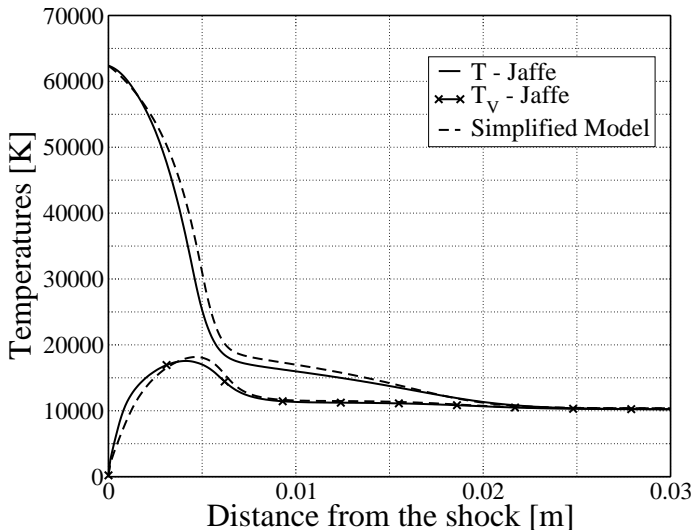


Figure 3.12: 1634 s. Comparison of the temperature profiles along the stagnation line. Unbroken lines refer to results obtained with the accurate model for thermodynamics. Dashed lines refer to the simplified model.

Also, the separation of rotation and vibration leads to a non unique definition of the partition function, which depends on the hypotheses made at the moment of separation. We investigate the influences of the partitioning of rotational and vibrational energy, using nonequilibrium maps of specific heat and comparing the results obtained with different assumptions. The results have shown to be rather insensitive to the separation method selected. This conclusion is confirmed by the one dimensional analysis presented using the one dimensional shock tube code.

The analysis performed has led us to the conclusion that the simplified models presented in this chapter give a reasonable estimation of the thermodynamic properties of high temperature air. Differences with the accurate model of Jaffe for a strong nonequilibrium test case are found in the composition profiles. Such differences do not exceed the 10 % throughout the computational domain and it is considered acceptable given the strong nonlinear behavior of the composition.

Chapter 4

Chemistry and energy exchanges

Chemistry and energy exchange source terms are the key parameters in the set of equations governing the behavior of high enthalpy gases; they allow to account for changes in the mixture due to chemical reactions as well as the exchanges of energy among the internal energy modes. Also, chemistry and internal excitation are closely correlated and they influence each other. Thermal nonequilibrium models are distinguished by the way they describe the interaction among the excitation of the internal energy modes and the macroscopic kinetic mechanisms employed. A more accurate and most physical description of the reciprocal influence of the internal structure and chemistry is given in Chapter 6-7 using a state-to-state approach for electronic levels of atoms and molecules. Hereafter we propose a brief overview of the models used in literature to account for nonequilibrium effects in the framework of the multitemperature philosophy.

The present chapter is divided in three parts:

- The first part describes the physical models used in the species conservation equations (Section 2.1.1) to account for the production and destruction of the species due to chemical reactions. Also, the effects of vibrational nonequilibrium on dissociation are detailed, describing the different models found in literature to account for such effects.
- The second part deals with the modeling of energy exchange terms among the internal energy modes of the gas. Particular attention is devoted to the coupling of the vibrational energy and chemistry due to the influence of such physical phenomena on the state of the plasma.
- The last part of the chapter is devoted to the comparison of the different multitemperature models introduced. The use of the one dimensional shock tube code allows us to analyze the influence of the thermochemical models on the results.

4.1 Chemical nonequilibrium model

The chemical reactions taking place in a gas can be expressed as:

$$\sum_{i=1}^{Ns} \nu'_{ir} X_i \rightleftharpoons \sum_{i=1}^{Ns} \nu''_{ir} X_i \quad (4.1)$$

where X_i indicates the species subjected to the chemical reaction and the symbols ν'_{ir} and ν''_{ir} indicates the stoichiometric coefficients for the i^{th} reactant and product respectively. Notice that an elementary reaction can proceed in both directions and when a perfect balance between forward and backward reaction is achieved, the process is in chemical equilibrium.

In accordance with the *Law of Mass Action* [176], the net rate of production of species i by Nr elementary reactions of the kind (4.1) is:

$$\dot{\omega}_i = \sum_{r=1}^{Nr} \dot{\omega}_{ir} \quad (4.2)$$

$$\dot{\omega}_{ir} = M_i (\nu''_{ir} - \nu'_{ir}) \left\{ k_{fr} \prod_{j=1}^{Ns} \left(\frac{\rho_j}{M_j} \right)^{\nu'_{jr}} - k_{br} \prod_{j=1}^{Ns} \left(\frac{\rho_j}{M_j} \right)^{\nu''_{jr}} \right\}$$

where $\dot{\omega}_{ir}$ is the mass production term of species i due to the r^{th} elementary reaction and $\dot{\omega}_i = (d\rho_i/dt)_{chem}$ is the global *mass production term* for species i (Sec. 2.1.1). In Equation (4.2) k_{fr} is the forward reaction rate constant for the r^{th} reaction and k_{br} is the backward reaction rate constant. A semi-empirical formulation, known as *Arrhenius Law*, is used to express the reaction rate constants:

$$k_{fr} = A_r T^{\eta_r} e^{-\frac{\Theta_r}{T}} \quad (4.3)$$

where A_r and η_r are constant coefficients and Θ_r is the activation temperature for the r^{th} reaction. The forward reaction rate is usually computed by fitting experimental data, which is often affected by large uncertainties. The backward rates are usually estimated using the detailed balance, provided that the equilibrium constant is known. Since Equation 4.2 does hold in equilibrium conditions ($\dot{\omega}_i = 0$), the two reaction rates can be related by the following expression:

$$\frac{k_{fr}}{k_{br}} = \prod_{j=1}^{Ns} \left(\frac{\rho_j}{M_j} \right)^{\nu''_{jr} - \nu'_{jr}} = K_{cr} \quad (4.4)$$

where K_{cr} is the equilibrium constant for r^{th} reaction. The equilibrium constant can be expressed with the *Gibbs free energy*. Referring to the r^{th} elementary reaction, K_{cr} reads:

$$\log K_{cr}(T) = - \sum_{i=1}^{Ns} \frac{(\nu''_{ir} - \nu'_{ir}) \hat{g}_i(T)}{\mathcal{R}T} - \log(\mathcal{R}T) \sum_{i=1}^{Ns} (\nu''_{ir} - \nu'_{ir}) \quad (4.5)$$

where \hat{g}_i is the Gibbs free energy per unit mole of species i . The statistical mechanics methods described in [176] are used to compute the Gibbs free energy.

4.1.1 Influence of nonequilibrium on the kinetic processes

The foregoing section deals with the modeling of the mass production terms due to chemical reactions, assuming equilibrium among the internal energy modes. We now discuss the influence of vibrational nonequilibrium on the chemistry, in the framework of the multitemperature approach. In particular, the first part of the section discusses the dissociation, whereas the second part is devoted to the analysis of the remaining reactions. To this end the most relevant models available in literature are reviewed and discussed.

Multitemperature models were developed to extend the validity of the rates to nonequilibrium conditions, assuming Boltzmann equilibrium within the energy modes. The nonequilibrium rates, indicated by k_f^r , are obtained by multiplying the correspondent equilibrium value by the so-called *nonequilibrium factor*, as follows:

$$k_f^r = Z(T, T_I) k_f^{r, eq} \quad (4.6)$$

The nonequilibrium factor $Z(T, T_I)$ introduces the dependence of the rate constant on the internal temperature. T_I represents the temperature, relevant for the reaction under analysis, e.g. T_I in the case of dissociation is T_V , owing to the influence of vibration on dissociation.

Dissociation reactions

Although the most rigorous approach, to model dissociation consists in considering the state-to-state vibrational kinetics, using a state specific method [25, 50], simplified approaches such as multitemperature methods are often used. Hence, the use of a nonequilibrium factor, which is a function of the vibrational excitation (T_V), modifies the equilibrium rate coefficients, considering that endothermic processes are faster for vibrationally

excited molecules, requiring less translational energy to dissociate. Thus, in post shock situations, where the vibrational temperature is relatively low, $Z(T, T_V)$ is much lower than one and the dissociation rates become very small, until a sufficient degree of vibrational excitation has taken place¹. The nonequilibrium factor has different analytical expression depending on the model chosen, so in order to reproduce measured nonequilibrium dissociation rates, adjustable parameters are often introduced in the analytical expression. In the following we discuss three different models characterized by different expressions for the nonequilibrium factor: Park's model, Treanor and Marrones' model and Macheret-Fridmans' model.

Park's model

Park's model can be considered as the simplest model to account for vibrational effects on the dissociation rates. The temperature T in Equation 4.3 is replaced by the averaged temperature $T^q T_V^{1-q}$ with $q = 0.5$ or $q = 0.7$. Thus the equilibrium factor becomes:

$$Z(T, T_V) = (T_{Ave} T^{-1})^n \exp\left(\frac{-\theta_d}{T_{Ave}} + \frac{\theta_d}{T}\right) \quad (4.7)$$

where T_{Ave} represents the averaged temperature, and θ_d is the characteristic dissociation temperature of the molecule.

Park's model is found to give reasonable results except for condition of strong nonequilibrium ($T \gg T_V$ and $T_V \gg T$) where large errors in the dissociation rates are present. When using shock fitting techniques to model the shock, such discrepancies can be reduced by artificially increasing the post-shock vibrational temperature, which is usually assumed to be frozen across the shock. Precursor effects due to radiation and diffusion can at least in part justify such changes from a physical point of view [138].

¹Such effects were observed in experiments carried out in shock tubes for intermediate shock speed (6 – 8 km/s). However at higher speeds the chemistry and vibrational excitation can occur in the pre-shock region because of precursor effects. This may lead to a drastic reduction of the incubation period.

Treanor's model

The model of Treanor and Marrone [116] can be considered as an extension of the work of Hammerling [81]. The main innovation is due to the introduction of a distribution of dissociation probabilities. The dissociation probabilities among the vibrational levels depend on the vibrational quantum number by means of a parameter (U).

$$P(v) \propto \exp [-(D - \epsilon_v)/k_B U] \quad (4.8)$$

The parameter U has the dimension of a temperature and generally takes on values of:

$$\frac{\epsilon_{d,s}}{6k_B} \leq U \leq \frac{\epsilon_{d,s}}{3k_B} \quad (4.9)$$

For an infinite value of U the model becomes equivalent to the model of Hammerling. Treanor's model relies on the Boltzmann distribution to describe the population of the vibrational levels and assumes that during the dissociation processes such distribution is negligibly affected by chemistry.

The nonequilibrium factor has the following expression

$$Z(T, T_V) = \frac{Q(T)Q(T_F)}{Q(T_V)Q(-U)} \quad (4.10)$$

where with Q we indicate the partition function for a truncated harmonic oscillator and T_F is an average temperature defined as follows:

$$T_F = \left(\frac{1}{T_V} - \frac{1}{T} - \frac{1}{U} \right)^{-1} \quad (4.11)$$

Da Silva in Ref. [51] compares the dissociation rates obtained with multitemperature models against the ones given by a state to state approach. According to this analysis, Treanor's model nicely predicts the dissociation rates for molecule-molecule collisions at high temperatures, where the error in the predictions does not exceed one order of magnitude. However at low temperatures (of the orders of few thousands of degrees) the model tends to over-predict the rate of dissociation. The interaction atom-molecule is predicted rather well by the model over all the range of interest for hypersonic applications. In conclusion Treanor's model gives a good representation of the dissociation rates in compressing or expanding flows, although the good agreement found in Ref. [51] for expanding flow seems to be coincidental.

Knab's model

Knab *et al* [96] extended Treanor's model to other reactions, adopting the same philosophy used by Treanor and Marrone and assuming that the chemical reactions do not affect the vibrational distribution function. Knab's model, disregarding anharmonicity effects, uses the well known trunked harmonic oscillator model. Thus, indicating with $Q_{V_m}^{\theta_m^D}(T_V)$ the vibrational partition function (trunked oscillator) of molecule m at the temperature T_V , we have:

$$Q_{V_m}^{\theta_m^D}(T_V) = \frac{1 - \exp\left(-\frac{\theta_m^D}{T_V}\right)}{1 - \exp\left(-\frac{\theta_m^V}{T_V}\right)} \quad (4.12)$$

where θ_m^D is the characteristic dissociation temperature and θ_m^V is the characteristic vibrational temperature. For dissociation-recombination reactions the forward reaction rate constant is given by:

$$k_f = Z(T, T_V) CT^\eta e^{-\theta_m^D/T} \quad (4.13)$$

where:

$$Z(T, T_V) = \frac{Q_{V_m}^{\theta_m^D}(T)}{Q_{V_m}^{\theta_m^D}(T_{vm})} \left[\frac{e^{-\alpha\theta_m^D/T} Q_{V_m}^{\alpha\theta_m^D}(\Gamma_m) + Q_{V_m}^{\theta_m^D}(T_m^0) - Q_{V_m}^{\alpha\theta_m^D}(T_m^0)}{e^{-\alpha\theta_m^D/T} Q_{V_m}^{\alpha\theta_m^D}(-U) + Q_{V_m}^{\theta_m^D}(T^*) - Q_{V_m}^{\alpha\theta_m^D}(T^*)} \right] \quad (4.14)$$

and

$$\begin{cases} \Gamma_m = \left(\frac{1}{T_{vm}} - \frac{1}{T} - \frac{1}{U} \right)^{-1} \\ T^* = \left(\frac{1}{T} - \frac{1}{U} \right)^{-1} \\ T_m^0 = \left(\frac{1}{T_{vm}} - \frac{1}{U} \right)^{-1} \end{cases} \quad (4.15)$$

Usually U and α are set equal to $\theta_m^D/3$ and 0.7, respectively.

Macheret's model

Macheret *et al* in Ref. [111] describes the dissociation process using the simplifying assumption of rigid rotor and harmonic oscillator, modeling the collision within the impulsive approximation. The model acknowledges the existence of two dissociation regimes: the dissociation from the upper levels, which strongly depends on the vibrational temperature as opposed to the dissociation of the lower levels that depends on the translational temperature.

The nonequilibrium factor of Macheret's model is given by

$$Z(T, T_V) = \frac{1 - \exp(-\theta_V/T_V)}{1 - \exp(-\theta_V/T)} (1 - L) \exp \left[-\theta_d \left(\frac{1}{T_V} - \frac{1}{T} \right) \right] + \\ L \exp \left[-\theta_d \left(\frac{1}{T_a} - \frac{1}{T} \right) \right] \quad (4.16)$$

where the expression of L depends on the species involved in the collision. If the collision takes place among an atom and a molecule

$$L = \frac{9\sqrt{\pi(1-\alpha)}}{64} \left(\frac{T}{\theta_d} \right)^{1-n} \left[1 - \frac{5(1-\alpha)T}{2\theta_d} \right] \quad (4.17)$$

For molecule-molecule collisions:

$$L = \frac{2\sqrt{\pi(1-\alpha)}}{\pi^2 \alpha^{3/4}} \left(\frac{T}{\theta_d} \right)^{3/2-n} \left[1 + \frac{7(1-\alpha)(1+\sqrt{\alpha})T}{2\theta_d} \right] \quad (4.18)$$

Figure 4.1 shows the reaction rate constants of N_2 due to the interaction with N atoms, using the different models described. In addition, we plot the value estimated in Ref. [25], and based on the accurate quantum mechanical calculations presented in Ref. [40, 90]. As we can observe, Macheret's model is found to give the best agreement with dissociation rates and it has the great advantage of not requiring any adjustable semi-empirical parameter. Reasonable agreement is shown for the predictions based on the model of Treanor and Knab as opposed to Park's model predictions, which strongly underestimate the rate of dissociation.

REMARK: The backward rate constants are computed by means of the *detailed balance* in all the models presented:

$$k_b = \frac{k_{f_{eq}}}{K_c(T)} = \frac{CT^n e^{-\theta_m^D/T}}{K_c(T)} \quad (4.19)$$

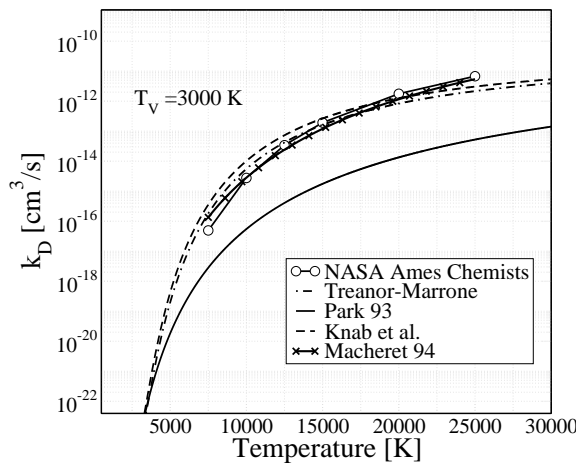


Figure 4.1: $\text{N}_2 - \text{N}$. Comparison of the dissociation reaction rate constants in thermal nonequilibrium: (○) NASA Ames chemists Ref. [25]; (dash-dotted line) Treanor and Marrones' model; (unbroken line) Park TT_V model; (dashed line) Knab's model; (×) Macheret's model.

Other reactions

The influence of the internal excitation on the chemistry, usually limited to the introduction of a correction factor for the dissociation, is extended by Knab *et al* to exchange, associative ionization and electron impact dissociation reactions.

For *exchange reactions* the formulation is similar to dissociation. The rate constant is given by:

$$k_f = Z_3 C T^\eta e^{-\theta_a/T} \quad (4.20)$$

where θ_a is the activation energy in K:

$$Z_3 = \frac{Q_{V_m}^{\theta_m^D}(T)}{Q_{V_m}^{\theta_m^D}(T_{vm})} \left[\frac{e^{-\alpha\theta_a/T} Q_{V_m}^{\alpha\theta_a}(\Gamma_m) + Q_{V_m}^{\theta_m^D}(T_m^0) - Q_{V_m}^{\alpha\theta_a}(T_m^0)}{e^{-\alpha\theta_a/T} Q_{V_m}^{\alpha\theta_a}(-U) + Q_{V_m}^{\theta_a}(T^*) - Q_{V_m}^{\alpha\theta_m^D}(T^*)} \right] \quad (4.21)$$

The definition of the "temperatures" T^* and T_m^0 is the same as before. In this case m indicates the molecule being destroyed. The expression for the

backward rate constant is slightly different from the previous case, taking into account the nonequilibrium effects, as follows:

$$k_b = Z_5 \frac{k_{f_{eq}}}{K_c(T)} = Z_5 \frac{CT^\eta e^{-\theta_a/T}}{K_c(T)} \quad (4.22)$$

where:

$$Z_5 = \frac{Q_{V_m}^{\theta_m^D}(T)}{Q_{V_m}^{\theta_m^D}(T_{vm})} \left[\frac{Q_{V_m}^{\theta_m^D}(T_m^0)}{Q_{V_m}^{\theta_a}(T^*)} \right] \quad (4.23)$$

In Equation 4.23 m refers now to the molecule being created.

For *electron impact dissociation* reactions the equations to be used are the same given for dissociation from heavy particle impact. The only difference is that the free electron temperature T_e replaces T in all expressions.

For *associative ionization* reactions the backward rate constant reads:

$$k_f = CT^\eta e^{-\theta_a/T} \quad (4.24)$$

while for the backward rate we have:

$$k_b = Z_5 \frac{CT^\eta e^{-\theta_a/T_e}}{K_c(T_e)} \quad (4.25)$$

Finally for *electron impact ionization*:

$$k_f = CT_e^\eta e^{-\theta_a/T_e} \text{ and } k_b = \frac{CT_e^\eta e^{-\theta_a/T_e}}{K_c(T_e)} \quad (4.26)$$

When Knab's model is not employed, the expression used for forward and backward rate constants, with emphasis on the temperature dependence can be found in Table 4.1.

4.2 Energy exchanges among energy modes

The second part of the chapter deals with the modeling of the source terms in the relaxation energy equations discussed in Chapter 2. A correct representation of these terms is extremely important, since they allow for the determination of the vibrational and electronic temperatures², which are used in the modeling of the reaction rate constants discussed in the foregoing sections.

²We refer to the temperature of the electronic levels and the free electron energy that are assumed to be in equilibrium.

Reaction	k_f^r	k_b^r
Exchange	$k_f = CT^\eta e^{-\theta_a/T}$	$k_b = \frac{CT^\eta e^{-\theta_a/T}}{K_c(T)}$
Associative ionization	$k_f = CT^\eta e^{-\theta_a/T}$	$k_b = \frac{CT_e^\eta e^{-\theta_a/T_e}}{K_c(T_e)}$
Electron impact ionization	$k_f = CT_e^\eta e^{-\theta_a/T_e}$	$k_b = \frac{CT_e^\eta e^{-\theta_a/T_e}}{K_c(T_e)}$

Table 4.1: Recommendation for multiple temperature rate constants for different types of reactions.

4.2.1 Vibrational Translational exchanges

The rate of vibrational-translational energy transfer follows a Landau-Teller formula:

$$\Omega_m^{VT} = \rho_m \frac{e_m^V(T) - e_m^V(T_{vm})}{\tau_m^{VT}(T)}, \quad m \in \mathcal{V}. \quad (4.27)$$

Equation 4.27 is valid for harmonic oscillators and it relies on the following three assumptions:

- the transitions occur only among neighboring states.
- the rate constants for such transitions are proportional to the quantum number.
- the levels are populated according to the Maxwell-Boltzmann distribution.

The average relaxation time is given by the quantity:

$$\tau_m^{VT} = \sum_{j \in \mathcal{H}} (\rho_j / M_j) / \sum_{j \in \mathcal{H}} [\rho_j / (M_j \tau_{mj}^{VT})] \quad (4.28)$$

where the species relaxation time τ_{mj}^{VT} is based on Millikan-White's formula including Park's correction [146] to avoid that the relaxation times become smaller than the time required for a collision to take place.

The Landau-Teller formula nicely reproduces the behavior of diatoms at low temperatures ($< 5000 K$). However, as the temperature rises, the relaxation tends to follow a diffusion type equation as explained in [138]. To account for the slower relaxation at high temperature, Park introduced a correction factor which simply multiplies the Landau-Teller formula as follows:

$$\Omega_m^{VT} = \rho_m \frac{e_m^V(T) - e_m^V(T_{vm})}{\tau_m^{VT}(T)} \left\| \frac{T_{sh} - T_V}{T_{sh} - T_{Vsh}} \right\|^{s-1}, \quad m \in \mathcal{V}. \quad (4.29)$$

where with the index sh we indicate the post shock conditions and $s = 3.5 \exp(-5000/T_s)$.

The use of such a correction, although straightforward for one dimensional analysis where the shock is considered as a discontinuity, is not immediate when using CFD solvers with shock capturing, owing to the obvious difficulties in defining the post shock conditions. Therefore Park's correction is not used in the manuscript if not indicated otherwise.

4.2.2 Vibrational vibrational exchange

When using a multitemperature approach the energy exchanges among the vibrational energy modes of the different molecules must be accounted for. For the vibrational-vibrational energy exchange, different formulations have been tested. The one proposed by Candler [33] is inconsistent in the sense that at thermal equilibrium, it differs from zero. Hence, the modified version of Knab *et al* [95] has been chosen:

$$\Omega_m^{VV} = \sum_{l \in \mathcal{V}} \mathcal{N}_A \sigma_{ml} P_{ml} \sqrt{\frac{8RT}{\pi \mu_{ml} M_l}} \rho_l \rho_m \left(e_m^V(T) \frac{e_l^V(T_{vl})}{e_l^V(T)} - e_m^V(T_{vm}) \right) \quad (4.30)$$

where the exchange probability P_{ml} is assumed to be equal to 10^{-2} , as suggested in Ref. [33]. Symbol μ_{ml} denotes the reduced molar mass, and \mathcal{N}_A , the Avogadro's number. In the flow conditions analyzed the vibrational vibrational exchange terms have been found of secondary importance with respect to the other energy exchange processes.

4.2.3 Elastic energy exchange: free electrons - heavy particle

The energy lost by electrons through elastic collisions with heavy particles is written as follows:

$$\Omega^{ET} = \frac{\frac{3}{2}n_e k_B (T - T_e)}{\tau_e^{ET}(T_e)}. \quad (4.31)$$

The relaxation time is obtained from kinetic theory, $1/\tau_e^{ET} = \sum_{j \neq e} (m_e/m_j) \nu_{ej}$, where the collision frequencies read $\nu_{ej} = (8/3)v_e n_j \bar{\Omega}_{ej}^{11}$. The value of the $\bar{\Omega}_{ej}^{11}$ needed to evaluate the collision frequency can be found in [174].

4.2.4 Free-electron vibrational coupling

To model the exchange between the vibrational energy and the free-electron energy, we only consider molecular nitrogen, since this molecule is more efficient than O₂ and NO for this kind of process. This rate is assumed to follow a Landau-Teller formula:

$$\Omega^{EV} = \rho_{N_2} \frac{e_{N_2}^V(T_{v_{N_2}}) - e_{N_2}^V(T_e)}{\tau_e^{EV}(T_e)}. \quad (4.32)$$

The relaxation time taken from Ref. [21] is preferred to the analytical form of Lee [108], which overestimates the relaxation time by a factor of 2-3 [21].

4.2.5 Coupling Chemistry internal energy modes

At high speeds, it is important to account for the energy lost by the free electrons during ionization of the atoms and molecules, as already stressed in Ref. [146]-[157]. Otherwise, electron impact ionization reactions, and in general all the reactions involving free electrons, produce a large amount of free electrons without depleting their kinetic energy, thus enhancing their production. This phenomenon may lead to an avalanche ionization with consequential related numerical problems, especially for high speed conditions. Here is an expression for the related source terms for electron-impact ionization reactions:

$$\Omega^I = \sum_{r \in \mathcal{R}^I} \dot{\omega}_{e,r} \mathcal{U}^r, \quad (4.33)$$

where \mathcal{U}^r is the reaction enthalpy of the r reaction, and $\dot{\omega}_{e,r}$, the electron chemical production term of the r reaction. Symbol \mathcal{R}^I denotes the set of indices of the electron-impact ionization reactions. The term Ω^I accounts for the energy removed by electron-impact ionization reactions.

4.2.6 Vibration-Chemistry-Vibration coupling

The chemical reactions depleting or producing molecules affect the average vibrational energy in the gas. Hence the presence of chemistry in the flow imposes the introduction of an additional energy source term into the vibrational energy equations.

The source term Ω_m^{CV} is given by the following expression:

$$\Omega_m^{CV} = G_{app_{rm}} \dot{\omega}_m^f + G_{var_{rm}} \dot{\omega}_m^b \quad (4.34)$$

where $G_{app_{rm}}$ indicates the average vibrational energy lost due to chemistry and $G_{var_{rm}}$ represents the average vibrational energy gained thanks to chemistry. The terms $\dot{\omega}_m^f$ and $\dot{\omega}_m^b$ are the terms of destruction and production of the molecule m due to chemistry.

The determination of the exact amount of energy depleted by a specific chemical reaction is a challenging task, which can be accomplished rigorously in the framework of a state-to-state (or collisional radiative models, Chapter 6) approach [40, 59]. However the applicability of such approaches to CFD is restricted due to the large number of equations to be solved and to the huge number of kinetic processes to be modeled.

In literature different models have been created to correctly account for the vibrational energy losses due to dissociation reactions. Among them it is common to distinguish between *preferential* and *non-preferential* dissociation models. The non-preferential models prescribe an equal probability of dissociation from all the quantum levels of the molecules as opposed to the preferential dissociation model based on the assumption that dissociation takes place from the upper vibrationally excited states. Hence the molecules in the lower vibrationally excited states must *ladder climb* to the higher states before dissociating.

The most commonly used models based on the preferential-dissociation concept in the literature are now briefly outlined, highlighting the hypotheses

on which each of them rely.

Treanor and Marrone

The main hypotheses of this model were outlined in Section 4.1.1, when discussing the effects of the vibration on chemistry. This leads to the following expression for the the mean energy lost ($G_{app_{rm}}$) or gained ($G_{va_{rm}}$)

$$\begin{cases} G_{app_{rm}} = \frac{R_i \theta_m^v}{e^{-\theta_m^v/U} - 1} - \frac{R_i \theta_m^D}{e^{-\theta_m^D/U} - 1} \\ G_{va_{rm}} = \frac{R_i \theta_m^v}{e^{\theta_m^v/T_F} - 1} - \frac{R_i \theta_m^D}{e^{\theta_m^D/T_F} - 1} \end{cases} \quad (4.35)$$

where θ_m is the dissociation energy in K and the averaged temperature has the following expression:

$$T_F = \left(\frac{1}{T_V} - \frac{1}{T} - \frac{1}{U} \right)^{-1} \quad (4.36)$$

Since U characterize the distribution of the dissociation probabilities the energy loss or gained is strongly affected by its definition. Experimentally was observed that behind a shock wave the energy lost due to dissociation corresponds to about 30 % of the dissociation energy.

Knab's model [96] is a preferential dissociation model which extends the work of Treanor and Marrone to exchange and associative ionization reaction.

Macheret's model

The energy loss due to chemistry for Macheret's model are briefly outlined hereafter:

$$G_{app_{rm}} = \frac{e^{V^*}(k_f^r(T, T_V))_l + R_i \theta_d(k_f^r(T, T_V))_h}{Z(T, T_V) k_f^{eq}} \quad (4.37)$$

with $e^{V^*} = \alpha R_i \theta_d \left(\frac{T}{T_a} \right)^2$. The symbols $(k_f^r(T, T_V))_l$ and $(k_f^r(T, T_V))_h$ represent the dissociation rate coefficient for the low and high vibrational levels respectively. The formula for the rate coefficient from low vibrational levels is:

$$(k_f^r(T, T_V))_l = (1 - L) A_r T^\eta \exp\left[-\frac{\theta_d}{T_a}\right] \quad (4.38)$$

The expression of the rate coefficient for the higher levels is:

$$(k_f^r(T, T_V))_h = \frac{1 - \exp(-\theta_V/T_V)}{1 - \exp(-\theta_V/T)} L A_r T^\eta \exp\left[-\frac{\theta_d}{T_V}\right] \quad (4.39)$$

The energy gained reads:

$$G_{varm} = R_i \theta_d [\alpha(1 - L) + L] \quad (4.40)$$

Non-preferential models

As the free-stream kinetic energy becomes much larger than the dissociation energy of the molecules, dissociation tends to occur with equal probability from all the levels and the ladder climbing process is not required to dissociate. The simplest of the models which does not account for the preferential dissociation is due to Candler [33] and the energy loss is given by ($\Omega_m^{CV} = c_1 e_m^V \dot{\omega}$). The constant introduced (c_1) is equal to one for non-preferential models and it assumes values larger than one when preferential dissociation is accounted for.

REMARK: The influence of the chemistry on vibration is already in part accounted for in the V-T terms previously discussed. The relaxation time τ_m^{VT} in Equation 4.27 is an average of the individual relaxation times of the single species and therefore it depends on the composition [173].

4.3 Comparison preferential dissociation and non-preferential dissociation models

The models described in the preceding sections are now applied to the relaxing flow behind a strong normal shock wave. The thermal and chemical relaxation of the gas is governed by the system of equations presented in Section 2.3.1.

The test conditions are indicated in Table 4.2, where the free stream characteristic quantities are denoted by the subscript $_1$, and the post-shock characteristic quantities by the subscript $_2$. Symbols u stands for the shock

p_1 [Pa]	15.0
T_1 [K]	205
u_1 [m/s]	7198
p_2 [Pa]	10 960
T_2 [K]	25 162
u_2 [m/s]	1209

Table 4.2: Shock-tube flow characteristic quantities.

velocity. The mole fractions of nitrogen and oxygen are assumed to be constant through the shock ($x_{N_2} = 0.79$ and $x_{O_2} = 0.21$). We recall that, after the shock, the rotational temperature is equal to the post-shock gas temperature T_2 , whereas the vibrational and electron temperatures are still equal to the free stream gas temperature T_1 .

The air mixture used to perform the simulation accounts for neutral species N_2 , O_2 , NO , N , O , and for charged species N_2^+ , O_2^+ , NO^+ , N^+ , O^+ , and e^- . The kinetic mechanism used, was compiled by Park and described in Ref. [146].

The results obtained with the preferential dissociation model of Treanor (assuming ($U = \theta_d/3$)), are compared to the ones obtained with Park model (coupled with the non preferential model of Candler) in Figure 4.2. A first difference can be observed in the vibrational relaxation process: Park's results in dashed line present a maximum in the vibrational temperature when $T = T_V$, as opposed to all the other models, for which the vibrational temperature does not overshoot the translational one. This is due to the weaker value of the Ω_m^{CV} source term for the non-preferential models, which is about 10 times smaller than the corresponding term in the preferential dissociation models [69]. Hence the derivative of the vibrational temperature is governed by the Landau Teller expression of the VT source term and becomes zero when $T = T_V$. Different is the behavior of Knab (in Figure 4.3), Macheret (in Figure 4.4) and Treanor's model (in Figure 4.5) which exhibit in general lower vibrational temperatures (especially for O_2). Dissociation in these models removes in general a large amount of energy, if compared to the non-preferential dissociation models. Hence the vibrational temperature in the post shock regions tends to be lower. Furthermore we can notice a minimum in the vibrational temperature of O_2 which is due to a strong dis-

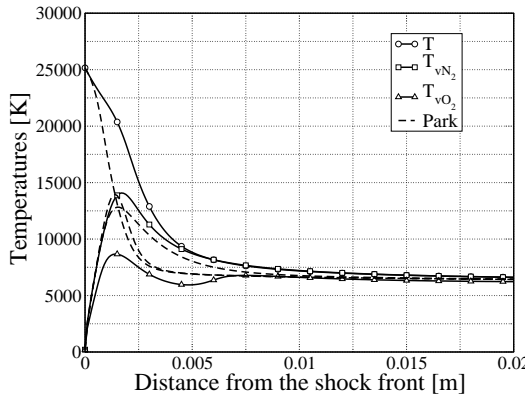


Figure 4.2: Temperature profiles. Comparison among the preferential dissociation model of Treanor and Marrone (unbroken lines) and the non-preferential dissociation model of Park-Candler (dashed lines).

sociation coming from the upper vibrational levels of this molecule. When dissociation is almost completed the quick energy exchanges with the atoms restore the thermal equilibrium.

Since the preferential dissociation models require a sufficient vibrational excitation to promote the onset of dissociation, the chemical reactions and in particular the dissociation is slowed down (Figures 4.7-4.6).

The evolution of the composition in Figure 4.6 compares the three preferential models previously discussed. We can observe that Knab model predicts larger dissociation rates which leads to larger fall off rates for the molecular species followed by a sharper reduction of the translational temperature³. Knab in Ref. [97] introduces an additional parameter with respect to Treanor (α parameter in Ref. [97]) which gives a stronger dependence of the dissociation rate to the translational temperature. Hence the dissociation is enhanced and the results are closer to the non preferential dissociation models. Opposite is the behavior of Macheret's model which predicts a slower dissociation rate.

The evolution of the N_2 and O_2 in Figure (4.7) confirms the typical behavior of the Park model: at the beginning of the relation when the two

³The dissociation is an endothermic reaction and removes energy from the flow causing a reduction in temperature and an increase of the density of the gas.

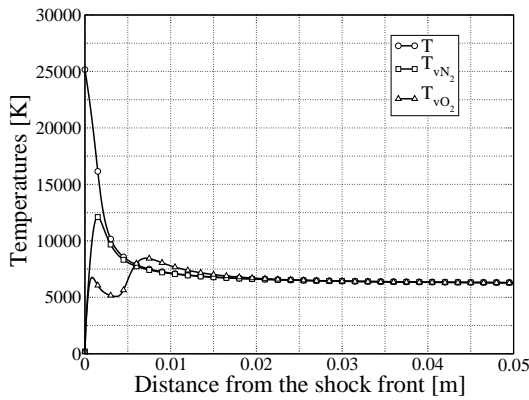


Figure 4.3: Temperature profiles. The preferential dissociation model of Knab is used in this figure. The symbol (\square) represents the vibrational temperature of N_2 ; we indicate the vibrational temperature of O_2 with the symbol (\triangle). Translational temperature is indicated with the symbol (\circ) in the figure.

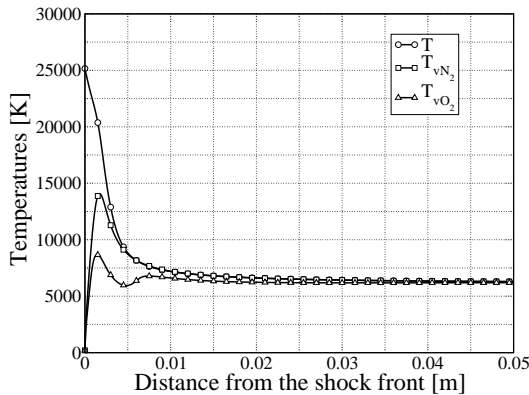


Figure 4.4: Temperature profiles. The preferential dissociation model of Macheret is used in this figure. The symbol (\square) represents the vibrational temperature of N_2 ; we indicate the vibrational temperature of O_2 with the symbol (\triangle). Translational temperature is indicated with the symbol (\circ) in the figure.

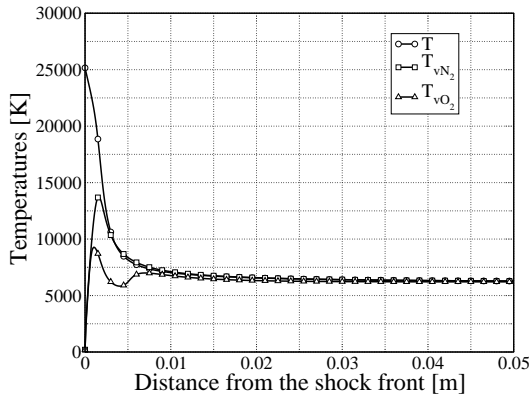


Figure 4.5: Temperature profiles. The preferential dissociation model of Treanor is used in this figure. The symbol (\square) represents the vibrational temperature of N_2 ; we indicate the vibrational temperature of O_2 with the symbol (\triangle). Translational temperature is indicated with the symbol (\circ) in the figure.

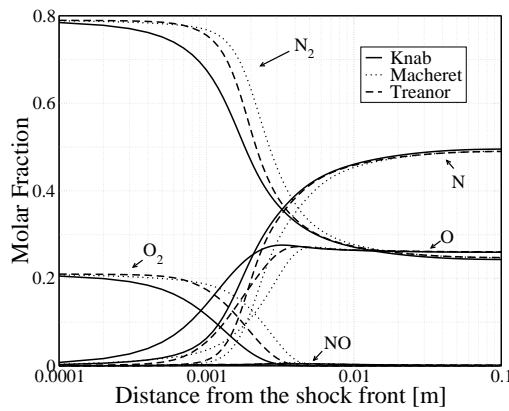


Figure 4.6: Composition profiles for preferential dissociation methods. Unbroken line indicates Knab's model; dashed lines represent Treanor's model and the dotted lines indicate the results obtained with Macheret's model.

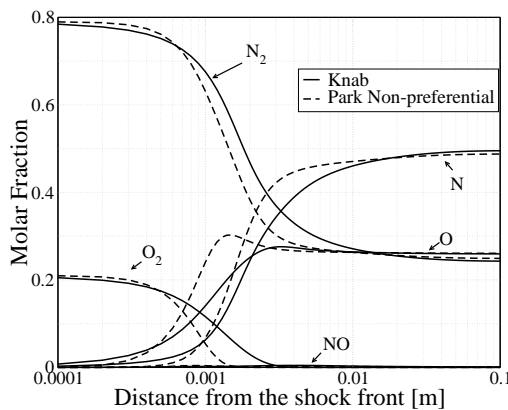


Figure 4.7: Comparison of the composition profiles obtained with Knab's model (unbroken lines) and the non-preferential model of Park-Candler (dashed lines).

temperatures are very different the dissociation rates are underestimated respect to preferential dissociation models [111]. As the vibrational temperature increases, the dissociation rates obtained using the Park model quickly becomes larger than the ones obtained with Knab's model and the Park model dissociate more.

Summary

This chapter briefly outlines the models used to express the mass production terms and the energy exchange terms in the set of equations introduced in Chapter 2. Particular emphasis is given to the interaction among chemistry and the relaxation of the internal energy modes: vibration-dissociation, ionization-free electron energy.

In literature we can distinguish two different classes of models for the coupling of vibration and dissociation: *preferential* and *non-preferential* dissociation models. The models of Treanor, Knab, Macheret and the model of Park coupled with the non-preferential dissociation model of Candler are presented and analyzed. The analysis has led us to the conclusion that the

interaction vibration-chemistry based on the preferential dissociation model causes a reduction of the thermal and chemical relaxation rate. Also, among the different models analyzed Macheret's model predicts the slowest chemical and relaxation among all the models under investigation as opposed to Knab's model, which exhibits a behavior closer to the non-preferential dissociation models and dissociates more than the others.

Chapter 5

Multitemperature models: results

The forthcoming results present an analysis of the nonequilibrium flows in compressing and expanding conditions by means of a one dimensional shock tube code and a quasi one dimensional nozzle code respectively. The internal energy of shocked gases, mostly stored in the translational energy, is transferred to the other energy modes and to the chemistry, thanks to inelastic processes. The thermo-chemical state of the expanding gas, such as the flows occurring in the off-stagnation point region in shock layers or within the nozzles of ground test facilities, exhibit a substantially different form of nonequilibrium. Owing to the high cooling rates and the high accelerations imposed to the flow, the energy is mainly extracted by the translational energy mode, whereas the internal structure of the gas tends to freeze, inducing strong nonequilibrium effects. The objective of this chapter, besides highlighting the thermo-physical characteristics of the flows, is the validation of the models previously discussed, before introducing the state specific model, which, in part, relies on the multitemperature models.

The first section presents an analysis of the FIRE II testcase using the one dimensional shock tube code within the multitemperature approach.

The second section is devoted to a validation of the nozzle code against the model presented by Park in Ref. [147] and the multidimensional, multi-temperature Navier-Stokes model of Bourdon [24].

5.1 Shock code: comparison with literature

We investigate the flow along the stagnation line of the FIRE II flight vehicle for two points of its re-entry trajectory (Table 5.1), comparing the results obtained with the one dimensional shock code with results provided by Johnston in Ref. [93].

The non-preferential model of Candler, coupled with the TT_V model of

Time [s]	1634	1636
p_1 [Pa]	2.0	5.25
T_1 [K]	195	210
u_1 [m/s]	11 360	11 310
p_2 [Pa]	3827	9229
T_2 [K]	62 377	61 884
u_2 [m/s]	1899	1891

Table 5.1: Shock-tube flow characteristic quantities.

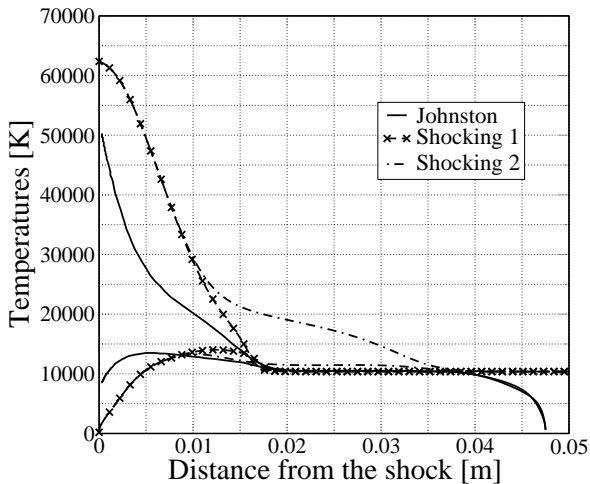


Figure 5.1: 1634 s. Temperature profiles comparison with Ref. [93] (unbroken lines). (\times) results obtained with assuming a prescribed value of Ω^I . The dash-dot lines refers to the classical expression for Ω^I .

Park to account for the influence of vibration on the chemistry, has been used. The choice of this model is partially justified by the main objective of this chapter, which is the "validation" of the simplified codes. To this end we chose to make use of the same model used by Johnston during its investigation [93]. Nevertheless, owing to the high speed conditions simulated, we feel that the use of a non preferential model better reproduces mechanisms of dissociation of the molecules, which have sufficient energy to dissociate directly from the lower states of the energetic ladder.

The temperature profiles for the first flight condition are shown in Figure 5.1. The shock, located on the left at $x = 0$, was fitted using the Ranking-Hugoniot (R-H) equations and assuming that the chemistry and the internal energy modes are frozen across the shock. Different is the approach of Johnston, which makes use of the shock slip equation [93], accounting for the dissipative effects across the shock. As a result the post-shock vibrational temperature is higher than the free-stream value and the translational temperature is lower than the value given by R-H. As we shall see, the difference in the model used to account for the presence of the shock is responsible for the differences in the flowfield in the region close to the shock.

The results were obtained using two different models for the source term indicated as Ω^I in the vibrational energy equation. Such a term is physically responsible for the depletion of the kinetic energy of the translational energy of the free-electrons, due to the ionization processes by electron impact. In the same figure, predictions indicated in figure as "Shocking 1" and "Shocking 2" differ dramatically. The curves indicated as Shocking 2 refer to the case where this term is modeled using the expression of Chapter 4 as opposed to the other curves (Shocking 1), which uses a preselected amount of energy removed by each reaction involving free-electrons, computed based the expression suggested in Ref. [93]

$$\Omega^I = -\omega_{N+} I^{N+} - \omega_{O+} I^{O+} \quad (5.1)$$

where $I^{N+} = 4.05 \times 10^8 \text{ J/(kg mol)}$ and $I^{O+} = 4.30 \times 10^8 \text{ J/(kg mol)}$, respectively. We found roughly an order of magnitude difference in the Ω^I term using the two different models, the one prescribed by Johnston being smaller. As a consequence the rate of electron production is greatly enhanced, since the energy removal is lower, leading to a faster thermal equilibration. Strong is also the effect on the dissociation by electron impact (Figure 5.2), which strongly contributes to the production of atomic species. As we shall see

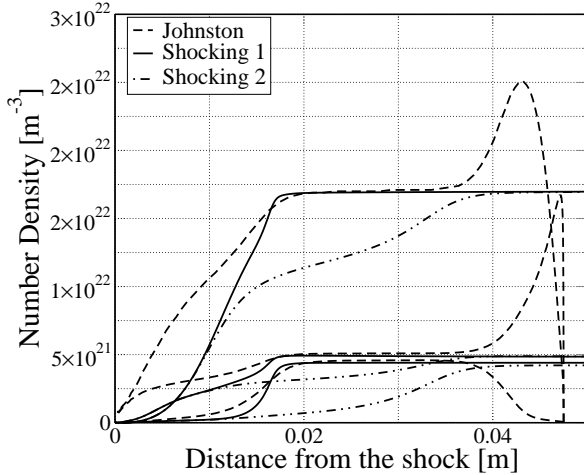


Figure 5.2: FIRE II -1634 s. Number density profiles: Johnston's results (unbroken line);(×) our results obtained with a prescribed value of Ω^I ; (dashed lines) classical approach Ω^I .

in the second part of the manuscript, the collisional radiative model allows us to correctly predict the amount of energy removed by the elementary processes involving light particles, without imposing any prescribed value, which may depend on the condition of the flow. For instance the use of a prescribed source term in expanding flow produces an unphysical overpopulation of the excited states, causing large distortion of the electronic levels distribution [122]. Figure 5.3 presents the analysis of a second point in the trajectory. The calculations have been obtained using the modified value of Johnston for the Ω_I source term. The agreement is qualitatively similar to the one shown previously. The differences are restricted to a narrow region close to the shock where the large differences in the assumed post-shock temperature explain the differences in the evolution of the composition of atomic species and free-electrons shown in Figure 5.4.

In conclusion the analysis of the two points in the trajectory of the FIRE II experiment has shown the importance of the Ω^I term and has given us confidence in the prediction given by the one dimensional shock tube code. The difference shown in the results are a consequence of the difference on the boundary condition (initial condition) used to fit the shock and par-

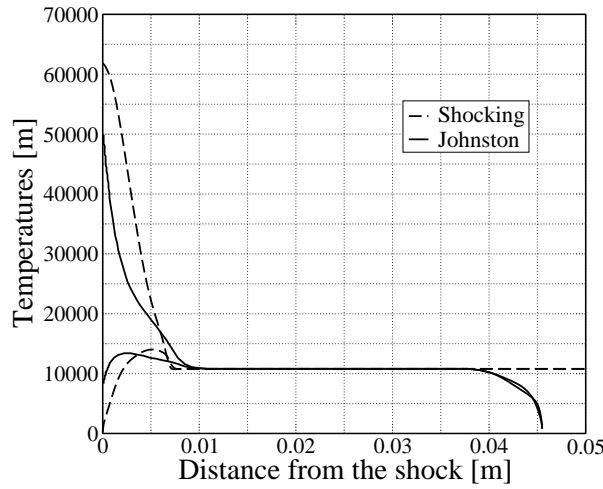


Figure 5.3: 1636 s. Temperature profiles: Johnston's results (unbroken line); results obtained with a prescribed value of Ω^I (dashed lines).

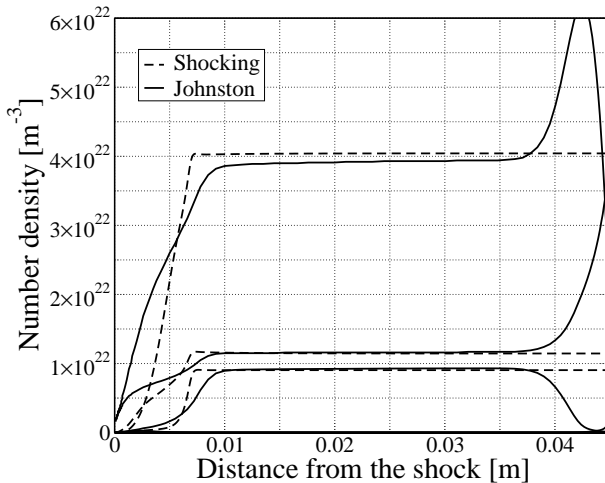


Figure 5.4: 1634 s. Number density profiles (Park-Candler). Johnston's (unbroken line). (dashed lines) results obtained with a prescribed value of Ω^I .

tially due to limits imposed to the temperatures driving the rate constants in Johnston's results.

5.2 Nozzle code: comparison with literature

To validate the nozzle code discussed in Chapter 2, comparisons were made with results available in literature in Ref. [24, 147]. An effort was made to use the same kinetic models and thermo-physical properties in the present nozzle code as are applied in the reference solvers. The temperature and species number densities predicted by quasi-onedimensional method and the two reference results are compared in Figures 5.5-5.8 for the expansion in the nozzle of two arc-jet wind tunnels. The results used for the first of the two validation testcases were obtained using a solver (NOZNT) based on the quasi-one dimensional method allowing us to validate the implementation of our code. The analysis is restricted to the diverging part of the conical nozzle under investigation, since the flow in the converging part is found to be under equilibrium conditions.

The second comparison was made with the two dimensional Navier-Stokes results of Ref. [24] for the expanding flow in the nozzle of the TT1 arcjet-facility. This testcase was chosen to show how the one dimensional flow solver is capable of reproducing the main physico-chemical features of the flow along the symmetry axis of the nozzle.

Both comparisons were carried out assuming a Boltzmann distribution of the electronic energy levels for the atomic and molecular species present in the mixture as prescribed in the reference cases.

5.2.1 Comparison with NOZNT code

In Ref. [147] Park performs an analysis of the flow inside the Low Density Wind Tunnel Nozzle of the H₂ arc-jet facility (at Arnold Engineering Development Center). A series of measurements made in the correspondence of the nozzle outlet allowed for a validation of the NOZNT flow solver. NOZNT, thoroughly described in Ref. [147], is a quasi-one dimensional nozzle solver that solves the Euler equations by means of an implicit space marching technique. Additional equations were added to account for the relaxation of the internal energy modes. The model for air includes eleven species: N₂, N₂⁺, O₂, O₂⁺, NO, NO⁺, N, N⁺, O, O⁺, and e⁻. The kinetic model used for the investigation was compiled by Park, and it is given in the reference used for the comparison. Differences are present in the model for the ther-

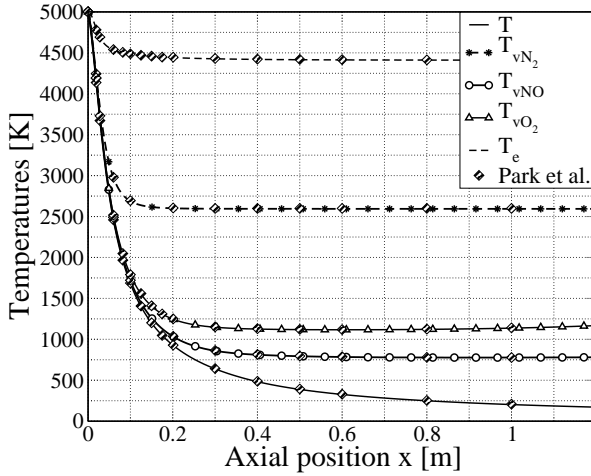


Figure 5.5: Temperature profiles in arc-jet wind tunnel (AEDC): comparison with Ref. [147].

modynamics: we use the simplified models of harmonic oscillator and rigid rotor model as opposed to Park which accounts for anharmonicity effects. The arc-jet can run for reservoir pressures ranging from 5 to 95 atm with enthalpies ranging from 5 to 10 MJ/kg. In our case the reservoir pressure and enthalpy are respectively 5 atm and 9.7 MJ/kg, the flow is considered to be in equilibrium.

Figure 5.5 shows the temperature profiles computed by the VKI nozzle code and the ones obtained with NOZNT. As expected right after the throat the internal energy modes freeze and corresponding temperatures deviate from the ro-translational temperature. In particular the free-electron temperature appears to strongly deviate from the other temperatures followed by the vibrational temperature of molecular nitrogen which is strictly coupled to the free electron temperature by means of electronic vibrational energy exchanges[138].

The predictions of the two codes are in very good agreement for the five temperatures considered in the investigation as depicted in Figure 5.5.

It is important to mention that the elastic exchanges among light and heavy particles have been neglected as suggested in Ref. [147]. The choice

of removing the energy exchange by elastic collision is justified by the comparison with experimental data. The inclusion of the foregoing source term causes a significant lowering of the free-electron energy. In the following sections however, the latter assumption will be discarded and elastic energy exchanges among light and heavy particles will be accounted for.

5.2.2 Analysis of the TT1 arcjet-facility

Our predictions of the thermo-chemical state of the flow in the arc-heated wind tunnel nozzle of the TT1 facility (located at Tsniimach, Moscow), are compared against the calculations presented in Ref. [24]. The analysis presented in literature was carried out by means of a 2D finite volume Navier-Stokes solver that benefits of advanced models for kinetics and energy exchange terms for the internal energy modes.

The air model applied consists of the following 5-species: N₂, O₂, NO, N and O. A different vibrational temperature for each of the molecules present in the mixture was used and the internal energy was modeled by making use of the simplified model of harmonic oscillator and rigid rotator. The forward chemical rates are taken from Park [146], while the backward rates are obtained by applying detailed balancing. The constants required for the energy exchange terms equation were discussed in Chapter 4, and are believed to be consistent with what is applied in the reference case. In particular for the vibrational dissociation coupling the self-consistent model of Knab [96] is applied.

Figure 5.6 shows the evolution of the composition inside the nozzle. The agreement shown is satisfactory, since mass fraction profiles agree to within less than 10% with the literature results. All the graphs (in Figures 5.6, 5.7, 5.8) are characterized by a plateau which is also present in the reference calculation. The reason of such a feature is the geometry of the nozzle in correspondence of the throat. In order to reduce the convective heating, the throat has a constant area section of a few centimeters. As a result composition and temperatures do not change in this part of the nozzle.

The temperature profiles along the axis of the nozzle are depicted in Figures 5.7, 5.8 and they compare well with the Navier-Stokes predictions. The plots representing the evolution of the vibrational temperatures of O₂ and NO compare well with reference results and since the agreement is similar to the one depicted in Figure 5.8 , we do not report them here.

The present section shows that the quasi-one dimensional method gives predictions of the thermo-physical state of the gas along the nozzle axis,

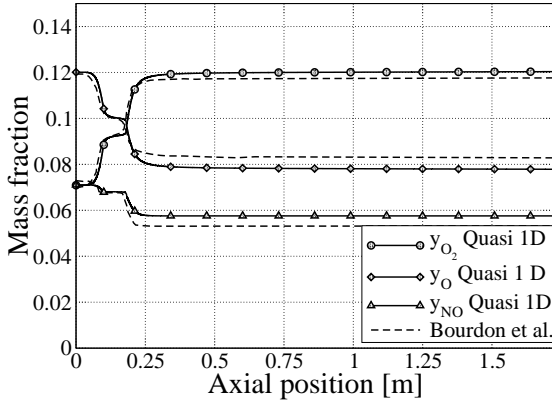


Figure 5.6: Composition evolution in the contoured nozzle of the TT1 arcjet facility: comparison with Ref. [24]

which are in agreement with calculations carried out with a two dimensional Navier-Stokes solver.¹

A validation of the multitemperature model in expanding flows was required before applying the accurate modeling of detailed chemical kinetics and coupling of the detailed kinetics with the flow, which although not included here, is dependent on the energy exchange terms and on the relaxation process in general through the nozzle.

Summary and conclusions

The multitemperature models discussed in the foregoing chapters, have been applied to the analysis of the flow behind a normal shock and in the expansion through a converging-diverging nozzle. The analysis, while introducing the reader to the main features of the nonequilibrium flows in compressing and expanding conditions, aims toward the validation of two simplified flow

¹In case of non-adiabatic expansion the conclusion may be rather different since the total enthalpy of the flow is not conserved; differences in the temperature profiles may appear [122].

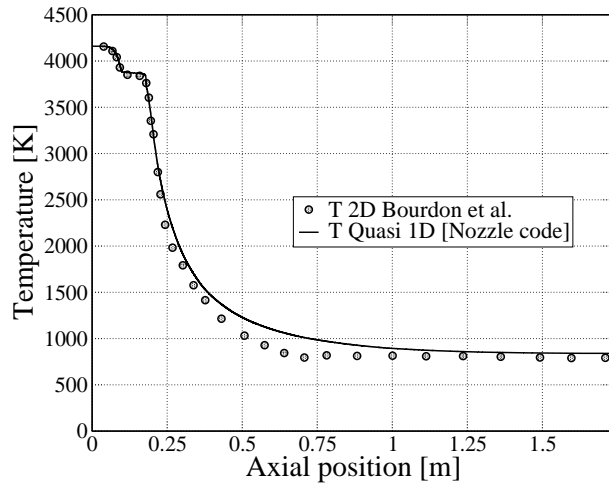


Figure 5.7: Ro-translational temperature in the contoured nozzle of the TT1 arcjet facility: comparison with Ref. [24]

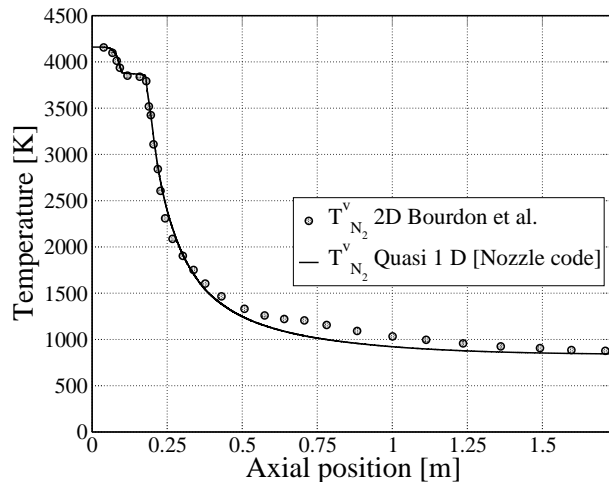


Figure 5.8: Vibrational temperature of N₂ in the contoured nozzle of the TT1 arcjet facility: comparison with Ref. [24]

solver against literature results. To this end our results are compared with the viscous shock layer calculations of Johnston's [93] for the compressing case, and with the calculation of Park [147] and Bourdon [24] for the validation of the nozzle flow. In both cases, our results, show good agreement with the reference results, in terms of composition and temperature profiles, although some discrepancies, owing to the approximation introduced in the fluid model (one dimensional assumption, inviscid flow), still persist.

Furthermore the importance of the correct modeling of the coupling of the chemistry and the translational energy of the free electrons is briefly discussed. The use of the classical formulation of the Ω^I source term leads to higher translational temperatures and lower degree of ionization in the flow. The use of a prescribed source term based on an heuristic estimation suggested by Johnston, allows for a better description of the thermo-physical state of the gas in the shock layer, drastically reducing the extent of nonequilibrium and increasing the degree of ionization. As we shall see in the next chapter the use of Collisional Radiative model allows for an accurate estimation of this term removing the needs for prescribed values which have only a limited range of applicability.

Part II

Electronic collisional radiative models

Chapter 6

Collisional Radiative models: atoms

In first part of this work, the physico-chemical properties of the air flow were obtained through the shock layer by assuming that, for all the species, the population of each internal (rotational, vibrational, or electronic) energy mode follows a Boltzmann distribution at a specific temperature. Park has extensively worked on multitemperature models for air and has also shown that the internal energy level populations may depart from Boltzmann distributions in expanding and compressing flows, for example in Refs. [138, 139]. Therefore, the use of multitemperature models, even if very efficient from a computational point of view, can only be justified when the departure from the Boltzmann population is small, i.e. for low velocity and high pressure reentry conditions.

During high-speed entry, a significant portion of nonequilibrium shock-layer requires a state specific treatment of the *electronic state* populations of atoms and molecules in order to account for non-Boltzmann effects. Thus, the electronic specific Collisional Radiative models, which takes into account all relevant collisional and radiative mechanisms between the electronic energy levels, treated as pseudo-species, have to be employed. To this end conservation equations for the pseudo-species are added to the classical set of conservation equations for mass, momentum and energies, extending the spectrum of applicability of the multitemperature models, to non-Boltzmann distributions for the electronic energy mode.

When using CR models, we distinguish several ways to deal with time integration and coupling with flow solvers. The most widely used approach for time integration is the quasi-steady-state (QSS) approximation [15, 93]. This method is based on the simplifying assumption that the characteristic time of processes involving excited states is extremely fast compared to the one of the flow, therefore, concentrations of the species on excited states adjust almost instantaneously to the flow changes. The QSS assumption can be used either for all excited levels or only for a limited number of them (e.g.

high lying electronic levels). Various QSS CR models have been developed for air [43, 159, 171] and used in 0D. For example, the electronic state-to-state models given in Refs. [43, 159, 171] and the vibrational state-to-state model in Ref. [43] have been developed to study nonequilibrium effects in recombining plasmas at atmospheric pressure characterized by a free electron temperature larger than the heavy-particle temperature.

QSS CR models can be loosely coupled to flow codes [93, 138]; the profiles of the thermodynamic variables (pressure and temperatures) and species mass fractions are derived based on a flow calculation, then, the populations of excited states are obtained at each desired location in the flow by means of a QSS CR model [138]. Johnston [93] has used this approach (QSS electronic state-to-state CR model [137]) to study the influence of the nonequilibrium distribution of the electronic energy levels of atoms and molecules of air after a strong shock. He has shown that nonequilibrium populations strongly affect the radiative heat fluxes.

The second approach for time integration is the so-called time-dependent CR model, in which balance equations are solved simultaneously for all species on ground and excited states without any constraint on the relaxation times of the excited levels. Recently, a time-dependent electronic state-to-state CR model for air has been developed and used in 0D in Ref. [27]. Different typical re-entry flow conditions have been studied and significant differences have been observed between the species concentrations calculated with the CR model and the widely used multitemperature kinetic mechanisms of Dunn and Kang [58], Park [145], and Gupta [79].

Time-dependent CR models can be either loosely, or directly coupled to flow codes. The loosely coupled, or Lagrangian approach, is particularly well adapted when the concentrations of excited states are much lower than those of the ground state. In this method, the profiles of the thermodynamic variables (pressure and temperatures) and the mass fractions of species are also derived based on a flow computation. Then, in a second step, the excited species mass fractions are obtained by following accurately in time a cell of fluid. For example, this method has been used for entries into the atmosphere of Titan [115]; for low pressure conditions, significant deviations of the excited electronic state populations of nitrogen molecules from QSS predictions have been observed in the near-shock region.

In the directly coupled approach, state-to-state equations are solved simultaneously with classical conservation equations of the flow, this approach is the most general one. In Refs. [38, 49], vibrational nonequilibrium has been studied in supersonic air nozzle flows and, in Ref. [139], Park has shown that the populations of upper vibrational levels deviate from a Boltzmann

equilibrium and are strongly affected by the air chemistry, in particular, by the Zel'dovich reaction between molecular nitrogen and atomic oxygen.

The present chapter is organized in the following manner. The analysis begins with a general introduction to the CR modeling, discussing the different models found in literature (in Section 6.1).

We move then to a description of the ABBA model and its application to the analysis of three points in the re-entry trajectory of the FIRE II flight experiment (in Section 6.2).

The last part of the chapter is devoted the simulation of the flow inside the EAST facility comparing the simulated radiative signature with the experimental one (in Section 6.3).

6.1 Physical models

Aiming to a better understanding and a more reliable modeling of strong nonequilibrium flows, we introduce the reader to the Collisional Radiative modeling, discussing the building blocks of the method. In this section, we restrict ourselves to the analysis of the non-Boltzmann description of the electronic states of the atoms, leaving to the next chapter the analysis of the full collisional radiative model including a state to state treatment of the electronic states of the molecular species.

The first step consists in the definition of the electronic states considered in the CR model as pseudo-species. The discussion of the selection of the levels as well as the grouping in macroscopic states is detailed in Section 6.1.1.

The core of the analysis is constituted by the definition of the detailed kinetic, and radiative processes, which are the key points in the modeling rate of production or destruction of each species or pseudo-species. Such processes are discussed individually in Section 6.1.2. The last section (6.1.3) is devoted to the formulation of the master equation, which yields the expression of the mass production terms for the pseudo-species as a results of the contribution of all the kinetic and radiative processes considered.

6.1.1 Air mixture

The air we breath, consists of a mixture of nitrogen, oxygen and their products: argon as the other gas traces are neglected. Due to the wide range of

temperatures and pressure studied, we take into account

- Neutral species: N_2 , O_2 , NO , $\text{N}(1 - 46)$, and $\text{O}(1 - 40)$,
- Charged species: N_2^+ , O_2^+ , NO^+ , N^+ , O^+ , and e^- .

In accordance with the philosophy of the collisional radiative models we considered the electronic levels of nitrogen and oxygen as separate *pseudo-species*. Thus, the coupling of the atom electronic energy levels, through the different elementary processes considered in the following sections, allows for explicit determination of their excitation and the radiative signature of the plasma without using any a priori assumption on their populations.

Nitrogen and oxygen atoms own a large number of electronic states (e.g. nitrogen according to NIST [117] accounts for 381 states) and a detailed treatment of every single level is not practical and above all not needed [31]. The electronic structure of these atoms exhibits some similarities: both of them present a large energy gap between the first two excited states, which are *metastable*, and the other excited levels, which are clustered in a narrow energy region close to the ionization limit. Also, as the principal quantum number increases, the radiative processes become less efficient with respect to collisions in populating and depopulating the states. Hence, the closed spaced high lying states are likely to be in equilibrium with each other and they can be grouped together in pseudo-states, reducing the number of levels to be accounted for¹. In this work, we adopt the same selection of levels and grouped levels, proposed by Bourdon in Ref. [22, 23].

Forty-six electronic energy levels for N and forty levels for O are accounted for in Table A.1 found in appendix. They allow to accurately calculate: 1) Ionization of the N and O atoms by electron impact; 2) The net population of the metastable states $\text{N}(2) = \text{N}({}^2\text{D}^0)$, $\text{N}(3) = \text{N}({}^2\text{P}^0)$, $\text{O}(2) = \text{O}({}^1\text{D})$, and $\text{O}(3) = \text{O}({}^1\text{S})$ resulting from electron induced processes.

Although the O_2^- and O^- species can also be formed, their contribution to chemistry can be considered to be negligible, as a result of the high temperature level reached behind the shock wave and of the high rate coefficient for detachment processes which follows.

¹Such grouping is suitable to model kinetics but it is not adequate when modeling the radiation spectrum. This can be resolved using a more detailed radiation transport code in post processing.

6.1.2 Elementary processes

The highly energetic particles in the plasma, interacting during a collision with an atom or a molecule, can bring about a change of the quantum state (*excitation*) or a chemical transformation (e.g. *ionization*). Also, the excited species can transit spontaneously to lower quantum states loosing some energy in the form of electromagnetic radiation.

Such processes are often referred in literature as *elementary processes*. All the elementary processes can be divided in two main categories: *radiative* and *kinetic* processes. Among the kinetic processes we can distinguish the processes induced by the interaction with electrons and processes involving heavy particles.

The atoms and molecules are efficiently excited and ionized by electron impact reactions; due to their weak mass, free electrons very easily change occupation of the attached electrons of atoms. The free electrons are much lighter than heavy particle, therefore their average collision frequency is also larger (about 100 times). Such difference becomes very important at low pressure conditions, where the nonequilibrium effects are strong, since under these conditions the probability of reaction is governed by the collision frequency [86]. Also, the interaction potential among electrons (charged) and neutral particles is a long range type of interaction, as opposed to the one involving neutral particles, which has a reduced range of influence. The type of interaction strongly affects the cross sections which as a consequence are large for processes involving electrons and relatively small for kinetic processes among neutral particles.

The collisions among heavy particles may become important in situations where the electron density is low, such as the flow behind a shock wave, especially for atomic gases (e.g. argon). In this case, the heavy particles are responsible for the creation of the *prime electrons* in the flow and for the excitation of the other particles as well. The importance of such type of collisions is discussed in greater detail in Chapter 7.

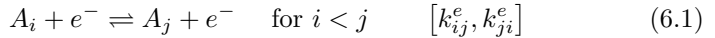
A review of the electron induced collisional processes is given in Section 6.1.2.1, where the different models found in literature are described. The comparison of the different kinetic mechanisms is provided in Section 6.1.2.2, whereas the discussion of the collisional processes due to the heavy particles are given in Section 6.1.2.3. We close this part of the chapter with

a brief discussion of the radiative processes due to atomic transitions (Section 6.1.2.4). Further information concerning the elementary processes can be found in Ref. [35, 46, 86, 165, 178].

6.1.2.1 Electron induced collisional processes

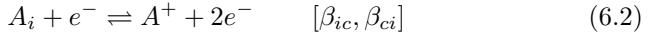
During the entry into a planetary atmosphere the gas in the shock layer may become partially ionized. In such case the collisions of the free-electrons with atoms and molecules strongly enhance the production of excited states.

In plasma flows, the excitation of a generic atom A induced by interaction with light particles can be expressed as:



where k_{ij}^e ($\text{cm}^3 \text{ s}^{-1}$) and k_{ji}^e ($\text{cm}^3 \text{ s}^{-1}$) are the electron-impact excitation rate coefficient and the de-excitation rate coefficient from the two quantum states i and j .

Also, if the energy of the colliding electron is sufficient enough, the interaction with an atom can result in ionization, which can be expressed as:



where β_{ic} ($\text{cm}^3 \text{ s}^{-1}$) and β_{ci} ($\text{cm}^6 \text{ s}^{-1}$) are, respectively, the electron impact ionization rate coefficient from the level i and the three-body recombination rate coefficient on the same level.

Owing to the lack of experimental data or accurate quantum mechanical calculations for many important electronic transitions, the estimation of the rate coefficients (k_{ij}^e, β_{ic}) is often based on approximate models. Those models are often created for simpler atoms (e.g. hydrogen) and are empirically extended to the more complicated atoms. In view of the analysis in the following sections it appears appropriate to briefly describe the basic features of the models used throughout our investigation.

High-lying levels: Drawin's Model

Drawin cross sections [54, 55] are widely used to describe excitation processes in noble gases [26] and can be used to model the inelastic processes for other species [27]. The semi-empirical formulas of Drawin are derived

from quantum mechanics and contain adjustable parameters, which are corrected to match experimental data.

We have expressed the rate coefficients under an analytical form derived from integration of these cross sections over a Boltzmann distribution at the electron temperature T_e . For an electronic transition from the i to j level, where $j > i$, the rate coefficient $k_{i \rightarrow j}^e$ is a function of the secondary quantum number l of each level involved

- For an optically allowed transition ($l_i \neq l_j$):

$$k_{i \rightarrow j} = 4 \pi v_e a_0^2 \alpha \left(\frac{E_H}{k_B T_e} \right)^2 I_1(a), \quad (6.3)$$

where quantity $v_e = [8 \mathcal{R} T_e / (\pi M_e)]^{1/2}$ is the electron thermal speed; \mathcal{R} , the universal gas constant; M_e , the electron molar mass; $a_0 = 0.529 \times 10^{-10}$ m, the first Bohr radius; $E_H = 13.6$ eV, the ionization energy of the hydrogen atom; $\alpha = 0.05$; and $I_1(a) = 0.63255 a^{-1.6454} \exp(-a)$, with the reduced energy $a = (\epsilon_j - \epsilon_i)/(k_B T_e)$.

- For an optically forbidden transition ($l_i = l_j$):

$$k_{i \rightarrow j} = 4 \pi v_e a_0^2 \alpha \left(\frac{\epsilon_j - \epsilon_i}{k_B T_e} \right)^2 I_2(a)$$

with the same notations and where quantity $I_2(a) = 0.23933 a^{-1.4933} \exp(-a)$.

The reverse processes are based on the micro-reversibility principle, the reverse rate is calculated from the equilibrium constant $K_{eq}(T_e) = (g_j/g_i) \exp(-a)$.

For ionization of an atom under electron impact, Eq. (6.3) is used with $\alpha = 1$ and a reduced energy $a = (\mathcal{I}_i - \epsilon_i)/(k_B T_e)$, where \mathcal{I}_i is the energy of the ground state of the ion related to that of the ground state of the atom.

Gryzinski's Model

Gryzinski's model [77] describes the interaction of electrons with the atomic shell using classical mechanics with several ad hoc assumptions. In this sense, the nature of his cross-section can be seen as semi-empirical, as are Drawin's formulas 6.3.

The expression of the cross section for the excitation from the electronic level i to the electronic level j reads
if $(\mathcal{U} + \mathcal{I} - \epsilon_i \leq \epsilon)$

$$\sigma_{i,j}(\epsilon) = \frac{\sigma_0}{\mathcal{U}^2} \left(\frac{\epsilon}{\mathcal{I} - \epsilon_i + \epsilon} \right)^{\frac{3}{2}} \left[\frac{2}{3} \frac{\mathcal{I} - \epsilon_i}{\epsilon} \frac{\mathcal{U}}{\epsilon} \left(1 - \frac{\mathcal{I} - \epsilon_i}{\epsilon} \right) - \left(\frac{\mathcal{U}}{\epsilon} \right)^2 \right] \quad (6.4)$$

if $(\mathcal{U} + \mathcal{I} - \epsilon_i > \epsilon)$ then

$$\begin{aligned} \sigma_{i,j}(\epsilon) = & \frac{\sigma_0}{\mathcal{U}^2} \left(\frac{\epsilon}{\mathcal{I} - \epsilon_i + \epsilon} \right)^{\frac{3}{2}} \frac{2}{3} \left[\frac{\mathcal{I} - \epsilon_i}{\epsilon} \frac{\mathcal{U}}{\epsilon} \left(1 - \frac{\mathcal{I} - \epsilon_i}{\epsilon} \right) - \left(\frac{\mathcal{U}}{\epsilon} \right)^2 \right] \\ & \left[\left(1 + \frac{\mathcal{U}}{\mathcal{I} - \epsilon_i} \right) \left(1 - \frac{\mathcal{U}}{\epsilon} \right) \right]^{\frac{1}{2}} \end{aligned} \quad (6.5)$$

where $\sigma_0 = 8.4526 \cdot 10^{-29} \text{ cm}^2 \text{J}^2$, \mathcal{I} stands for the ionization potential of the atom considered. ϵ_i indicates the energy of the i levels and the energy of the free electron is indicated with ϵ . The symbol \mathcal{U} indicates the threshold energy, i.e. $\epsilon_j - \epsilon_i$ (with $i < j$).

The cross sections are then integrated over the relative velocity (energy) of the colliding partners assuming a Maxwellian distribution, as explained in [77].

$$\begin{aligned} k_{i \rightarrow j}^e = & \frac{8\pi}{m_e^{1/2}} \left(\frac{1}{2\pi m_e k_B T_e} \right) \left[\int_{\mathcal{U}}^{\infty} \sigma_{i,j} \exp \left(-\frac{\epsilon}{k_B T_e} \right) \epsilon d\epsilon \right. \\ & \left. - \int_{\mathcal{U}^*}^{\infty} \sigma_{i,j+1} \exp \left(-\frac{\epsilon}{k_B T_e} \right) \epsilon d\epsilon \right] \end{aligned} \quad (6.6)$$

where the Boltzmann constant is indicated as k_B . The symbol \mathcal{U}^* stands for $\epsilon_{j+1} - \epsilon_i$.

Park's Model

Park's model [138] was one of the first collisional radiative models compiled for the non-Boltzmann treatment of the atomic species. The excitation cross sections are estimated using the hydrogenic model of Gryzinski [77]. Since the hydrogenic approximation does not hold for the electrons close to the

nuclei, some modifications to the rate constants for the processes involving the two first metastable states have been adopted [142]. In order to differentiate among optically allowed and forbidden transitions ad hoc assumptions have been made (i.e. the rate coefficients for the forbidden transitions are reduced up to 40%). The cross sections adopted for the modeling of ionization processes are taken from Lotz [110] and were derived for hydrogen atoms. However, since ionization comes mostly from the high-lying excited states, which are hydrogenic, their use for nitrogen and oxygen atoms is justified. For the molecules experimental rate coefficients, often measured at low temperatures and extrapolated to higher temperatures are used. The NEQAIR package [137], widely used in the hypersonic community, employs Park's model for the prediction of the nonequilibrium radiation.

Frost's Model

Frost et al. in Ref. [62] compiled a new set of inelastic cross sections for atomic and ionized nitrogen. The data-set was obtained using the R-matrix method and it validated using spectroscopic measurements in the visible and Vacuum Ultra Violet (VUV) wavelength range using low pressure arc plasmas. The inelastic transitions studied involve the excitation from the ground state and two metastable states to the first 23 states of atomic nitrogen.

The values of the *collision strengths* compiled were validated for a range of electron energy from 2 to 12 eV, which is a bit out of our range of interest, since in general the free electron energy, for our application, is below 2 eV. However the use of such cross sections improves the agreement with the experimental results as discussed in Section 6.3.

The rate constants provided by Frost have been fitted in Arrhenius form using a least squared method and are available in appendix, in Table A.3.

6.1.2.2 Comparison of the different models: excitation and ionization

The rate constants for inelastic processes of atomic nitrogen and oxygen were reviewed by Johnston in Ref. [93]. The present analysis aims at comparing Drawin's model, extensively used in the next sections, against more sophisticated models available in literature.

Generally speaking, the use of universal formulas (e.g. Drawin, Gryzinski) is particularly adapted to describe the transitions among the high lying states close to the ionization limit, since their behavior is almost hydrogenic. Moreover, for such transitions quantum mechanical calculations become more complicated and the use of the approximate formulas becomes necessary. On the contrary the behavior of the lower lying (e.g. metastable states) excited states can and should be reproduced using quantum mechanics. Hereafter we limit ourselves to an analysis of few transition involving excitation and ionization from the lower lying excited states that requires a more accurate modeling.

Figure 6.1 shows a comparison in terms of rate constants among Drawin, Gryzinski, Park and Frost model. While the predictions given by Gryzinski and Drawin agrees within a factor 2, different is the rate predicted by Frost which is larger by 1 order of magnitude. The recent calculations of Huo [86] (not shown in the plot), are lower than the predictions of Frost and shows a better agreement with the simplified models of Drawin and Gryzinski. Park's predictions [138] are several orders of magnitude larger the the other rates.

Figure 6.2 compares Drawin rates against Van Regmoter's model, as formulated in Ref. [93]. In the same figure we report Tayal predictions, which rely on detailed quantum mechanical calculations. Tayal in Ref. [169] gives the values of the inelastic collisions cross sections for transition from the lowest three levels to the first 12 levels. Although the predictions of Frost tend to depart at low temperatures from the two simplified approaches and the detailed calculations of Tayal, all the different models are in reasonable agreement except for the Park's model, which seems to overestimate the rate constant for the process under consideration. Similar conclusions were found by Johnston [93] for this and other transitions.

The rate constants for excitation of oxygen atoms derived by Drawin are now compared against rates obtained using more sophisticated quantum mechanical calculations [11, 70, 177] and other approximate formulas [2, 138].

In Figure 6.3, Drawin model seems to overestimate the rate constant for the excitation from the fundamental state to the tenth excited level. The agreement with the other predictions is acceptable, although for this transition the use of corrections for spin forbidden transitions, proposed by Drawin and neglected in this work, would have improved the quality of the agree-

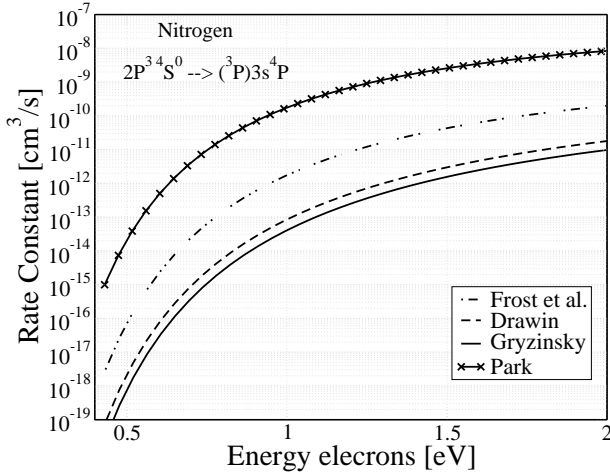


Figure 6.1: Nitrogen. Rate constant electron impact excitation $\text{N}(1) \rightarrow \text{N}(4)$. Comparison among Drawin model (dashed line), Gryzinski (unbroken line), Park (\times) and Frost (dash-dotted line).

ment. In fact the spin forbidden transitions take place by substitution of the bound electron with the free electron, lowering the cross section for inelastic transition.

Figure 6.4 presents a comparison of Drawin model against accurate and approximate calculations. Drawin's rates are estimated using the equation 6.3 for allowed transition. Although we use the formulation of Drawin proposed for the optically allowed transitions, the results are in good agreement with the other approximate models and the calculations of Gordillo Kunc [70]. Furthermore discrepancies are shown among the two more accurate calculations which give lower rates for this transition.

Figure 6.5 shows rate constants for electron impact ionization reactions of the first states of atomic nitrogen, using Drawin formula as in Ref. [93]. Such model will be extensively used in Section 6.3 and was found to underestimate the rate constant for direct ionization of the upper states by one order of magnitude if compared to the model proposed in Section 6.1.2.1. Also, in the same graph, we present the rates as predicted using quantum mechanical

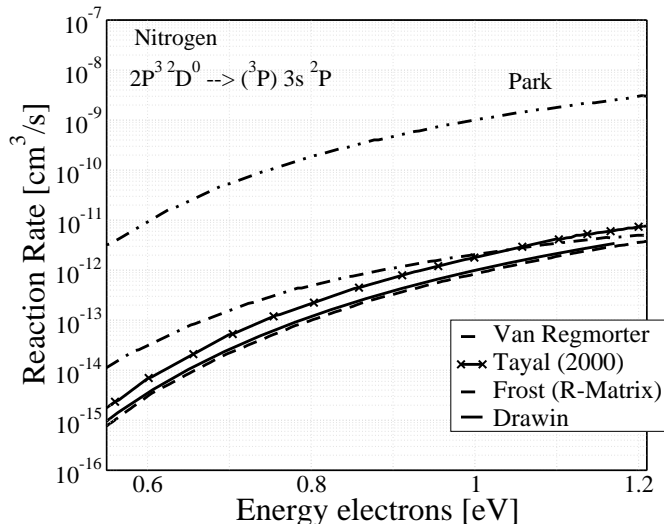


Figure 6.2: Nitrogen. Rate constant electron impact excitation $\text{N}(2) \rightarrow \text{N}(5)$. Comparison among Drawin model (unbroken line), Van Regmoter (dashed line), Park (dashed with two dots) and Frost (dash with one dot). Tayal (x)

calculations in Ref. [86].

The results show a relative good agreement for the lower states as opposed to the higher states for which the two predictions gives different results. Both models however predict a characteristic behavior ionization rate constant for oxygen and nitrogen atoms. The large differences in the ionization rates between the metastable and the high-lying states justifies the possibility discussed in Section 6.2.5.2 that the upper states will reach equilibrium with the free electron before they reach Boltzmann equilibrium with the lower states.

In conclusion we have shown that Drawin formulas and other simplified models gives predictions that are in general with the order of magnitude with the more accurate quantum mechanical estimations. The importance of such differences will be assessed in Section 6.3 where some of the model

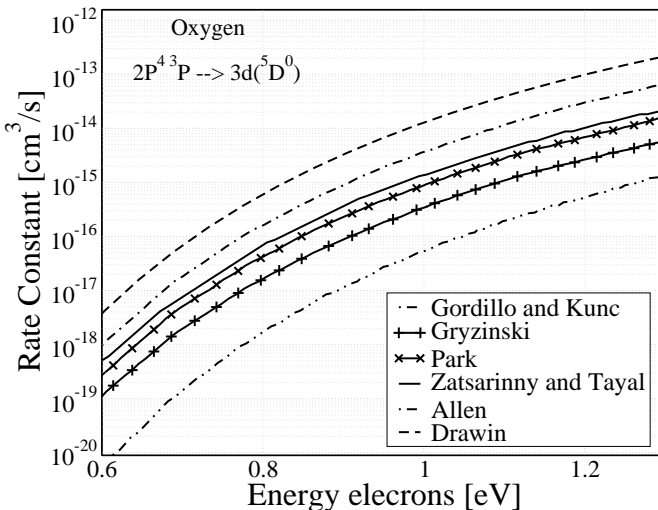


Figure 6.3: Oxygen. Rate constant electron impact excitation $O(1) \rightarrow O(10)$. Comparison among Drawin model (dashed line), Gordillo Kunc [70] (dash and two dots), Park (\times) Gryzinski (+), Zatsarinny and Tayal [177] (unbroken line), Allen (dash-dotted line)

presented have been used to reproduce the flow in a shock tube comparing the synthetic radiative signature with the experimental one.

6.1.2.3 Heavy particles induced collisional processes

The collision between two atoms or between an atom and a molecule can bring about electronic excitation of one of the colliding partner. Hence, these processes have been included in the collisional radiative model. Such elementary processes can be expressed as

$$A_i + M \rightleftharpoons A_j + M \quad \text{for } i < j \quad [k_{ij}^M, k_{ji}^M] \quad (6.7)$$

where k_{ij}^M ($\text{cm}^3 \text{s}^{-1}$) and k_{ji}^M ($\text{cm}^3 \text{s}^{-1}$) are, respectively, the heavy particle-impact excitation rate coefficient for the transition from the level i to the level j and its inverse, the de-excitation rate coefficient. The colliding partner is indicated with M and refers to atoms or molecules.

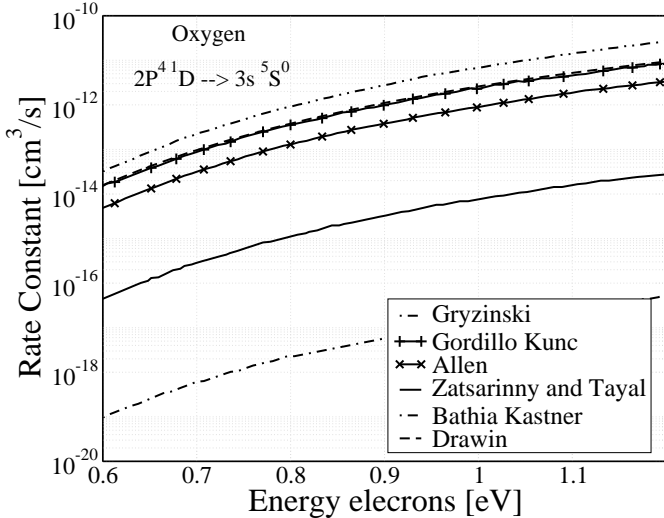


Figure 6.4: Oxygen. Rate constant electron impact excitation $O(1) \rightarrow O(10)$. Comparison among Drawin model (dashed line), Gordillo Kunc [70] (+), Allen (x) Gryzinski (dash-two dots), Zatsarinny and Tayal [177](unbroken line), Bathia and Kastner [11] (dash-dotted line)

The excitation of the ground to the high lying energy levels as well as the excitation among the high lying states have been estimated using Drawin cross section in Ref. [56].

A linear form for the cross section was used σ_{ij}^A for excitation from the ground or the metastable states towards highly excited levels:

$$\sigma_{ij}^{A-A}(\epsilon) = \beta_{ij}^{A-A}(\epsilon - E_{ji}) \quad (6.8)$$

where E_{ji} is the threshold and ϵ is the relative kinetic energy. We have assumed that the cross section can be derived from the case of argon [26] taking the mean value $\beta_{ij}^{A-A} = 3.4 \times 10^{-25} m^2 eV^{-1}$.

For excitation between highly excited levels, we have considered, similarly to argon, that Eq.(6.8) is applicable with $\beta_{ij}^{A-A} = 8.69 \times 10^{-22} E_{ji}^{-2.26} m^2 eV^{-1}$.

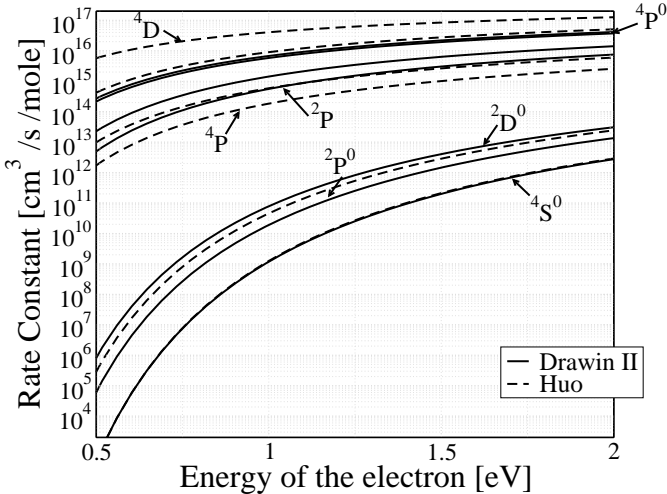


Figure 6.5: Comparison rate constants for electron impact ionization processes of N: (dashed lines) Huo's results Ref. [86]; (unbroken lines) Drawin rate constants Ref. [93].

Capitelli et al in Ref. [35] published rate constants for the excitation of atoms from the ground state to the metastable levels based on experimental data. Such data have been preferred to the rates given by Drawin model, when available.

The excitation cross section of atoms by molecular impact can be approximately written as [110]:

$$\sigma_{ij}^{A-M}(\epsilon) = \sigma_0 \frac{\ln(\epsilon/E_{ji})}{\epsilon/E_{ji}} \quad (6.9)$$

where $\sigma_0 \simeq 10^{-20} \text{ m}^2$.

Excitation by heavy particle impact are usually neglected in literature given the small cross sections associated with these elementary processes [138]. In this work, we prefer to account for such processes in order to verify such hypothesis in conditions where the electron density is relatively scarce (e.g. post shock region).

6.1.2.4 Atomic radiative processes

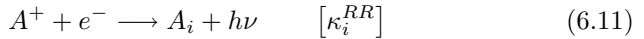
At speeds higher than 10 km/s, the radiative signature of heated N₂ and O₂ mixtures is mainly due to the spontaneous emission of the N and O atoms. The *bound-bound* transition of an atom from an upper electronic state to a lower one followed by emission of energy under the form of a photon can be written as



where \mathcal{A}_{ji} (s^{-1}) is the transition probability (Einstein coefficient) from the level j to the level i . Since our atomic model is based on grouping elementary levels having similar characteristics, the equivalent spontaneous emission probability of each level has to be determined. Related data taken from the NIST (National Institute of Standards and Technology) database Ref. [117] are given in Table A.2. In total, we take into account 45 spontaneous emission lines for N and 24 lines for O.

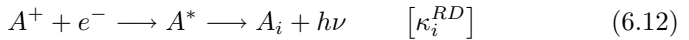
Radiative and dielectronic recombination

Radiative recombination is an interaction among a free electron and an ions that bring about the formation of a neutral (in case of singly ionized ions) atom with a consequent release of energy in the form of electromagnetic radiation. The process can be expressed as



where κ_i^{RR} ($cm^3 s^{-1}$) is recombination rate coefficient on the i^{th} electronic state of the atom. The inverse process is indicated as *photo-ionization* and although it may be important for high speed re-entry, it requires the knowledge of the radiation field and hence the solution of the radiative transport equation [149, 178], which falls out of the scopes of this project.

Dielectronic recombination consists of two phases: firstly a electron interacting with an ion form a metastable state of neutral atom (auto-ionization); secondly the metastable state radiates a photon during the de-excitation process (bound - bound transition). The process can be expressed as



where κ_i^{RD} ($cm^3 s^{-1}$) is the recombination rate coefficients on the level i and A^* represents an auto-ionizing state of the A atom.

The values of the recombination rates coefficients are given in Ref.[20, 22].

6.1.3 Master equation

Taking into account the different elementary processes mentioned above, the rate equations for the production of an excited atom on the level i can be written as

$$\frac{\dot{\omega}_i}{m_i} = \frac{dA_i}{dt} = \sum_{j \neq i} k_{ji}^e A_j n_e + \sum_{j \neq i} k_{ji}^M A_j N_M + \sum_{j > i} \alpha_{ji} \mathcal{A}_{ji} A_j + \alpha_i^{RD} \kappa_i^{RR} n_e A^+ + n_e A^+ [\alpha_i^{RD} \kappa_i^{RD} + n_e \beta_{ci}] - A_i \left[\sum_{j \neq i} k_{ij}^e n_e + \sum_{j \neq i} k_{ij}^M N_M + n_e \beta_{ic} \right] \quad (6.13)$$

where A_i refers to the number density of the i^{th} electronic state of the A atom; n_e is the electron number density; m_i is the species mass ($m_i = M_i/\mathcal{N}_A$). The symbol N_M is the number density of the molecule M and α indicates the escape factors for the radiative processes described, that is : α_{ji} is related to the bound-bound transition from j to i , α^{RD} refers to dielectronic recombination and α^{RR} refers to the radiative recombination. The symbol A^+ refers to the ion created when a bound electron of A is stripped due to kinetic processes. The reverse kinetic processes, i.e. de-excitation and recombination by electron or heavy particle impact have been estimated using the detailed balance, hence reducing the amount of data required.

$$\dot{\omega}_i = \dot{\omega}'_i + \bar{\omega}_i$$

where with $\dot{\omega}_i$ we indicate the production/destruction of pseudo-species of type i . The term $\dot{\omega}'_i$ accounts explicitly for the kinetic and radiative elementary processes (excitation, ionization ..) involving atomic species and the interaction with heavy and light particles. The other reactions, such as dissociation, exchange, associative ionization and their reverse processes contribute to populate the electronic levels of atoms and are accounted implicitly in the term $\bar{\omega}_i$. The expression of $\bar{\omega}_i$ is given by the *law of mass action* described in Chapter 4.

The overall number of kinetic and radiative processes exceeds 30000 and this gives an idea of the complexity of the model if compared with other over-simplified kinetic mechanism present in literature that do not account

for more than 50 kinetic processes [58, 146].

The possible re-absorption of radiation is estimated making use of an escape factors. In the following analysis, we assume that an optically thin medium is described by a value of $\alpha = 1$, whereas for an optically thick medium $\alpha = 0$.

6.2 Analysis of the FIRE II flight experiment by means of a Collisional Radiative model

In the previous sections, the modeling of the kinetic and radiative elementary processes was discussed, comparing different models derived from approximate formulas or accurate quantum mechanical calculations. In the next sections an hybrid CR model, referred in the following as ABBA model, is used to analyze the behavior of the electronically excited states of atomic species behind a strong shock. The model, developed by A. Bourdon and A. Bultel, is thoroughly presented in Ref. [27]. Besides the detailed treatment of the electronic levels of the atomic and molecular species, the original model includes a vibrationally specific CR model for the NO^+ , which is disregarded in this work.

We propose to study FIRE II [39], a reentry flight experiment carried out in 1960s. One of the primary objectives of the Fire Project was to estimate the heating that a capsule experiences at high speed conditions ($\geq 10 \text{ km/s}$). The focus of this project was the estimation of the radiative component of the heat-flux by measuring directly the incident radiation using on-board radiometers. Moreover, the data collected from the experiment can be used for the validation of flow solver and physical models [93, 125, 134].

In the analysis that follows, we focus our attention on three different points in the trajectory: 1634 s, 1636 s, and 1643 s (elapsed time from the launch). The first two points chosen belong to the earlier part of the trajectory where the flow exhibits strong nonequilibrium effects, whereas for the last point under consideration, the gas is close to equilibrium conditions.

The investigation is carried out by means of a hybrid model that combines the use of an electronic state-to-state CR model for the electronic levels of the atoms and describes the thermal nonequilibrium effects of the other energy modes by means of a multitemperature model. The choice of the atoms is justified by the fact that, for the high temperatures reached at high

speeds (≥ 10 km/s), the contribution to the radiative component of the heat flux is dominated by atomic lines and continuum radiation [17, 92, 93], the molecules being almost completely dissociated in this temperature range. The rates of the electronic-specific reactions are based on the data of the electronic state-to-state CR model recently developed by Bultel et al. [27]. A complementary set of reaction rates is taken from Park et al. [148]. In this work, the time-dependent CR model is directly coupled with a one-dimensional flow solver to simulate shock-tube experiments. Then, conservation equations of mass, momentum, global energy, vibrational energy, and free-electron energy are solved simultaneously.

The large number of elementary processes considered in the model will allow for a better understanding of the kinetic mechanisms for air plasmas, enabling us to better reproduce the gas kinetics in the shock layer and also describe the electronic energy level populations used to estimate radiative heat-fluxes. Furthermore, as the state-to-state CR model is directly coupled to the flow solver, a thorough analysis of the validity of the QSS assumption is also carried out.

The physical model is presented in Section 6.2.1, with a description of the CR part and the multitemperature part of the model. Section 6.2.4 is devoted to simulations of shock-tube flows representative of the Fire II flight experiment. A comparison with results from literature [83, 93] is performed. Then, validity of the QSS assumption is discussed, comparing three different formulations with the fully coupled approach described in Section 6.2.5.4.

6.2.1 Physico-chemical modeling

The air mixture, described in Section 6.1.1, comprises 95 species including the electronic energy levels of atomic nitrogen and oxygen. The vibrational energy level populations of the N_2 , O_2 , and NO molecules are assumed to follow Boltzmann distributions at the vibrational temperatures T_{vN_2} , T_{vO_2} , and T_{vNO} , respectively; the vibrational populations of the other molecules are associated with the vibration of the N_2 molecule. The rotational energy level populations are assumed to follow Boltzmann distributions at the translational temperature T of the gas. The CR model yields the electronic state populations of the N and O atoms. Thus, their electronic temperature does not need to be specified. The electronic energy populations of the other species are assumed to follow Boltzmann distributions at the translational temperature T_e of the free electrons.

6.2.2 Atomic elementary processes

The cross sections proposed by Drawin proved to be efficient in similar conditions [54, 55], and are thus adopted here for excitation and ionization processes induced by free electrons. The details are given in Section 6.1.2. Excitation and ionization from the inner core of the nitrogen and oxygen atoms, i.e. from ground and metastable states, is poorly described by approximate models. Hence, the use of accurate quantum mechanical calculations or when available experimental data is required. For the electron impact excitation of atoms from the ground states to the two metastable states, the R-matrix calculations of Berrington [10] were used. The experimental ionization cross sections from the ground states were reviewed by Tawara [168] and are found to be in agreement with the quantum mechanical predictions of Huo [86]. The ionization processes from the metastable states of atomic nitrogen are taken from [94] and we have assumed that the cross section for metastable oxygen has the same form when the shift due to the different threshold is taken into account.

The rate coefficients have been extracted from the experimental cross sections assuming a Maxwellian distribution for the free electrons and fitting them in Arrhenius form [20, 27]

$$k_{i \rightarrow j}(T_e) = A T_e^{-\alpha} e^{-\theta/T_e} \quad (6.14)$$

where A , α and θ are parameters. In Table 6.1 are summed up the parameters A , α and θ hence calculated for $2000 \text{ K} \leq T_e \leq 10000 \text{ K}$.

The excitation processes involving heavy particles (atoms and molecules) have been neglected in the present section. Their influence on the electronic population of the excited states and on the production of free electrons in the post shock region is discussed in Chapter 7.

The bound to bound radiative processes, discussed in the preceding section, have been considered, neglecting the less relevant radiative and dielectronic recombinations. The optical thickness of the medium was accounted for using escape factors which were set to 0 or 1 to model respectively the optically thick and thin case. Within the approximation of optically thin medium, all the radiation leaves the domain without interacting with the gas as opposed to the optically thick case which assumes that all the radiation emitted is immediately re-adsorbed.

i	j	A	α	θ	Ref.
$N(^4S^0)$	$N(^2D)$	1.720×10^{-15}	-0.280	28250	[10]
$N(^4S^0)$	$N(^2P)$	4.004×10^{-16}	-0.324	42860	[10]
$O(^3P)$	$O(^1D)$	1.374×10^{-17}	-0.566	24600	[10]
$O(^3P)$	$O(^1S)$	9.352×10^{-19}	-0.620	50110	[10]
$N(^4S^0)$	$N^+(^3P)$	8.583×10^{-16}	-0.276	166870	[168]
$N(^2D)$	$N^+(^3P)$	7.732×10^{-18}	-0.711	139900	[94]
$N(^2P)$	$N^+(^3P)$	1.026×10^{-17}	-0.677	126310	[94]
$O(^3P)$	$O^+(^4S^0)$	5.393×10^{-18}	-0.750	158330	[168]
$O(^1D)$	$O^+(^4S^0)$	8.571×10^{-18}	-0.695	134190	[94]
$O(^1S)$	$O^+(^4S^0)$	1.397×10^{-17}	-0.647	108800	[94]

Table 6.1: Parameters A , α and θ for the calculation of the rate coefficient (in $m^3 s^{-1}$) given by Eq.(6.14) for the transition $i \rightarrow j$ induced by electron collision. θ is expressed in K . (Taken from Ref. [27])

6.2.2.1 Molecular elementary processes

The kinetic mechanism comprises:

- Dissociation of N_2 , O_2 , and NO by atomic or molecular impact / recombination,
- Dissociation of N_2 by electron impact / recombination,
- Associative ionization / dissociative recombination,
- Radical reactions (including Zel'dovich reactions),
- Charge exchange.

For direct dissociation by molecular impact, the rate coefficients of Park et al. [148] are computed at the average temperature $(T T_{vi})^{1/2}$, where symbol i stands for the index of the molecule being dissociated. The reverse rates are computed at the gas temperature T based on the equilibrium constant. The rate of the nitrogen dissociation reaction by electron impact and of the reverse process is computed at the electron temperature T_e based on the same reference.

Zel'dovich reactions are known to greatly influence the distribution of nitrogen and oxygen between atomic and molecular systems and contribute to the destruction of O_2 and N_2 and the formation of NO. We have used the rate coefficients obtained by Bose and Candler [13, 14] using a quasi classical trajectory method performed starting from an ab initio potential surfaces calculation.

The dissociative recombination of the molecular ions is known to play a important role in the case of recombining plasmas [26, 78, 121]. In addition, the inverse process, associative ionization, allows for formation of the first electrons in many cases, such as in shock-tubes and reentry problems, and consequently, explains many ionizing situations. In our case, since N_2^+ , O_2^+ , NO^+ are present in the plasma described here, dissociative recombination has to be considered.

We have extracted the rate coefficients compiled by Teulet et al. [171], Capitelli et al. [35] and Kossyi et al. [98] those related to charge transfer (with possible re-association of atoms to form a molecule), re-association, excitation transfer, ionization, and dissociation. Due to the pressure levels involved in our CR model, we have also taken into account the previous processes occurring when a third particle interacts. For further details, refer to Ref. [27].

6.2.3 Shock-Tube flow solver

We have developed a one-dimensional flow solver, SHOCKING, to simulate air plasmas obtained in shock-tube facilities, based on the model presented in Section 2.3.1. This model has been modified to simulate reentries at speeds higher than 10 km/s, using a hybrid state to state model. First, a radiative source term Q_{Rad} has been added in the equation that expresses conservation of the total energy. Indeed, radiative transitions tend to deplete the flow energy for an optical thin medium. Second, a separate equation for the electronic levels of the atoms has been considered. These additional equations are solved in fully coupled manner with the momentum, total energy, vibration and free-electron electronic energy conservation equation. Furthermore the electronic energy of the atomic species, which is not governed by a Boltzmann distribution, is not included in the conservation of the total electronic energy. Indeed the conservation of such energy is implicitly imposed through the conservation equations for the pseudo-species.

$$\frac{\partial}{\partial x} (\rho_i u) = \dot{\omega}_i, \quad i \in \mathcal{S} \quad (6.15)$$

$$\frac{\partial}{\partial x} (\rho u^2 + p) = 0 \quad (6.16)$$

$$\frac{\partial}{\partial x} [\rho u (h + \frac{1}{2} u^2)] = -Q^{Rad} \quad (6.17)$$

$$\frac{\partial}{\partial x} (\rho u y_m e_m^V) = \dot{\omega}_m e_m^V + \Omega_m^{VT} + \Omega_m^{VV} - \Omega_m^{EV}, \quad m \in \mathcal{V} \quad (6.18)$$

$$\begin{aligned} \frac{\partial}{\partial x} [\rho u (y_e e_e + \sum_{i \in \mathcal{E}} y_i e_i^E)] &= -p_e \frac{\partial u}{\partial x} + \dot{\omega}_e e_e + \sum_{i \in \mathcal{E}} \dot{\omega}_i e_i^E - \Omega^I \\ &\quad - \Omega^E + \Omega^{ET} + \Omega^{EV} \end{aligned} \quad (6.19)$$

where symbol \mathcal{S} stands for the set of indices of the mixture species, \mathcal{V} , the set of indices of the N_2 , O_2 , and NO molecules, and \mathcal{E} , the set of indices of the N^+ , O^+ , N_2 , O_2 , NO , N_2^+ , O_2^+ , and NO^+ species, whose electronic energy populations are assumed to follow Boltzmann distributions. Symbols \mathcal{N} and \mathcal{O} stand for the set of indices of the electronic energy levels of the N and O atoms. Thus, the set of indices of the heavy particles is given by $\mathcal{H} = \mathcal{N} \cup \mathcal{O} \cup \mathcal{E}$ and the set of the mixture species by $\mathcal{S} = \mathcal{H} \cup \{\text{e}\}$. The species energy e_i , $i \in \mathcal{S}$, comprises the translational and formation contributions [$e_e = e_e^T(T_e) + e_e^F$] for electrons; the translational, electronic, and formation contributions [$e_i = e_i^T(T) + e_i^E + e_i^F$] for the electronic energy states N(i), $i \in \mathcal{N}$, and O(i), $i \in \mathcal{O}$; the translational, electronic, and formation contributions [$e_i = e_i^T(T) + e_i^E(T_e) + e_i^F$] for the N^+ and O^+ ions; and the translational, rotational, vibrational, electronic, and formation contributions [$e_i = e_i^T(T) + e_i^R(T) + e_i^V(T_{vi}) + e_i^E(T_e) + e_i^F$] for all the molecules, where T_{vi} is the vibrational temperature of the i molecule. The number of electronic levels used to compute the energy of the ions and molecules is tuned to yield the best matching agreement between values of the computed energies and the reference tables of Gurvich et al. [80]. Energy of molecules is computed assuming the rigid rotor and harmonic oscillator approximation (see Section 3). Spectroscopic constants are taken from Ref. [80]. Electronic specific data have been used for the vibrational and rotational constants of the molecules.

6.2.3.1 Energy relaxation terms

Most of the energy source terms in the equations have been discussed in the previous sections and stays unchanged. However some terms have been modified to be utilized in the framework of the state to state approach.

Radiative losses are modeled by means of the Q^{Rad} term in the energy equation. This term represents the radiant power emitted per unit volume and is directly given by the expressions

$$Q^{Rad} = \alpha \sum_{\substack{i,j \in \mathcal{N} \\ j < i}} (E_i - E_j) \mathcal{A}_{ij} N_i + \alpha \sum_{\substack{i,j \in \mathcal{O} \\ j < i}} (E_i - E_j) \mathcal{A}_{ij} N_i \quad (6.20)$$

where \mathcal{A}_{ij} is the Einstein coefficient, N_i , the number density of the excited state, and α , the escape factor.

At high speeds, it is important to account for the energy lost by the free electrons during ionization and excitation of the atoms and molecules, as already stressed in Ref. [146]-[157]. Otherwise, electron impact ionization reactions, and in general all the reactions involving free electrons, produce a large amount of free electrons without depleting their kinetic energy, thus enhancing their production. This phenomenon may lead to an avalanche ionization with consequent related numerical problems, especially for high speed conditions. Here is an expression for the related source terms for electron-impact ionization and excitation reactions

$$\Omega^I = \sum_{r \in \mathcal{R}^I} \dot{\omega}_{e,r} \mathcal{U}^r, \quad \Omega^E = \sum_{r \in \mathcal{R}^E} \dot{\omega}_{e,r} \mathcal{U}^r \quad (6.21)$$

where \mathcal{U}^r is the reaction enthalpy of the r reaction, and $\dot{\omega}_{e,r}$, the electron chemical production term of the r reaction. Symbol \mathcal{R}^I denotes the set of indices of the electron-impact ionization reactions, and \mathcal{R}^E , the set of indices of electron-impact excitation reactions. The first term Ω^I accounts for the energy removed by electron-impact ionization reactions, and the second term, Ω^E for the energy removal by electron-impact excitation reactions.

The coupling among vibration and chemistry was modeled using the non-preferential model of Candler [33], which appears to be an appropriate choice, given the high speeds that characterize the flight conditions. Furthermore the vibrational-translational relaxation was modeled using the Landau

Teller formula without using Park correction to account for the diffusive nature of the relaxation.

The final set of equations accounts for over hundred ODEs to be solved simultaneously with the flow. The integration of the set of equations is performed using LSODE package which requires less than 5 minutes to perform one full simulation over the entire shock layer.

6.2.4 Results

In this section, we apply the collisional radiative model previously described to FIRE II, a well-known flight experiment from the 1960's. One of the primary objectives of the Fire project was to define the radiative heating environment associated with the reentry of a large-scale Apollo vehicle at a velocity of 11.4 km/s. During this reentry, a large portion of the overall wall heat flux was due to radiation. Most of the radiation (approximately 90%) comes from atomic lines [93], thus, an accurate prediction of the populations of excited electronic states of the atoms is crucial. The aim of the present work is to test the CR model for different physico-chemical conditions, from electronic energy level populations in strong nonequilibrium to populations following Boltzmann distributions. Starting from the earliest trajectory points, we move to a description of a point approaching peak heating.

The first part of this section is devoted to thermal nonequilibrium effects in the flow. We study the influence of separating the free electron energy from the vibrational energy and compare our results for temperature and ionization degree with literature data. The rest of the section is devoted to a detailed analysis of the physico-chemical state of the plasma for three trajectory points: 1634 s, 1636 s, and 1643 s elapsed time from the launch. The validity of the QSS assumption often used to compute the excited electronic states is investigated for the 1634 s case by comparing the electronic energy level populations of atomic nitrogen obtained with the QSS assumption to the populations obtained by means of the full CR model.

The set of shock-tube operating conditions corresponding to the three trajectory points investigated here can be found in Table 6.2. Free stream characteristic quantities are denoted by the subscript 1 , post-shock characteristic quantities by the subscript 2 . Symbols u stands for the shock velocity. The mole fractions of nitrogen and oxygen are assumed to be con-

Time [s]	1634	1636	1643
p_1 [Pa]	2.0	5.25	21.3
T_1 [K]	195	210	276
u_1 [m/s]	11 360	11 310	10 480
p_2 [Pa]	3827	9229	24 506
T_2 [K]	62 377	61 884	53 191
u_2 [m/s]	1899	1891	1756

Table 6.2: Shock-tube flow characteristic quantities.

stant through the shock ($x_{N_2} = 0.79$ and $x_{O_2} = 0.21$). We recall that, after the shock, the rotational temperature is equal to the post-shock gas temperature T_2 , whereas the vibrational and electron temperatures are still equal to the free stream gas temperature T_1 .

6.2.5 Analysis of the Fire II 1634 s case

We investigate the physico-chemical state of the plasma corresponding to the 1634 s trajectory point. We show that the flow is characterized by strong thermo-chemical nonequilibrium and depleted populations of the upper electronic energy levels of atoms.

6.2.5.1 Thermal relaxation

In this section, we estimate the influence of the assumption of thermal equilibrium between the free electron energy/Boltzmann electronic energy and the vibrational energy of N_2 on the results. Two different assumptions are used: 1) Two separate temperatures: T_{vN_2} , for the vibration of N_2 and, T_e , for the translation of the free electrons and electronic excitation of the species following a Boltzmann distribution; 2) One common temperature $T_{vN_2} = T_e$ for all these energy modes. After the shock, no electrons are present since we have assumed the chemistry to be frozen in the jump relations. Moreover, the electronic populations of molecular nitrogen and oxygen follow Boltzmann distribution at the free stream temperature T_1 . Figure 6.6 shows how thermal nonequilibrium ($T_{vN_2} \neq T_e$) is restricted to a narrow zone after the shock (≤ 0.4 cm) and has a negligible influence on the evolution of the post shock temperatures and electronic energy populations for atomic nitrogen. The populations of the higher energy levels computed

based on $T_{vN_2} = T_e$ are overestimated in this zone, as shown in Figure 6.7. The thermal nonequilibrium zone is associated with a small electron number density (see Figure 6.9). As soon as the electron density becomes significant, thermal relaxation is very fast, via the efficient EV energy exchange processes².

Judging these discrepancies negligible, we have decided to assume that $T_{vN_2} = T_e$ in the remainder of this work and to solve the following equations

$$\begin{aligned} \frac{\partial}{\partial x} [\rho u (y_{N_2} e_{N_2}^V + y_e e_e + \sum_{i \in \mathcal{E}} y_i e_i^E)] &= \dot{\omega}_{N_2} e_{N_2}^V + \Omega_{N_2}^{VT} + \Omega_{N_2}^{VV} - p_e \frac{\partial u}{\partial x} \\ &\quad + \dot{\omega}_e e_e + \sum_{i \in \mathcal{E}} \dot{\omega}_i e_i^E - \Omega^I - \Omega^E + \Omega^{ET} \\ \frac{\partial}{\partial x} (\rho u y_m e_m^V) &= \dot{\omega}_m e_m^V + \Omega_m^{VT} + \Omega_m^{VV}, \quad m \in \{\text{O}_2, \text{NO}\} \end{aligned} \quad (6.22)$$

instead of Eqs. (6.18) and (6.19).

In Figure 6.8, we compare our four-temperature profiles ($T = T_r$, $T_{vN_2} = T_e$, T_{vO_2} , T_{vNO}) with the two-temperature profiles ($T = T_r$, $T_v = T_e$) obtained by Johnston [93]. While the vibrational free-electron temperature results agree quite well, discrepancies are found in the relaxation of the ro-translational temperature.

Figure 6.9 shows the electron number density for different values of the escape factor α (from 0 to 1) and allows for the influence of the optical thickness on the results to be emphasized. We can appreciate how the free-electron number density rises rapidly after a distance of 0.4 cm due to the electron-impact ionization reactions. In the optically thick case ($\alpha = 0$), the electron population reaches an asymptotic value, whereas in the optically thin case ($\alpha = 1$), the curve exhibits a maximum after which the plasma loses energy and recombines due to radiative cooling.

In the same figure, we have also plotted the electron number density obtained by means of the two-temperature model of Park [148] assuming a Boltzmann distribution among the electronic energy levels. The rate of ionization obtained in this case is higher.

²It is worth to notice that thermal nonequilibrium could have been even larger if the relaxation time of Lee had been used instead of the one of Bourdon and Vervisch.

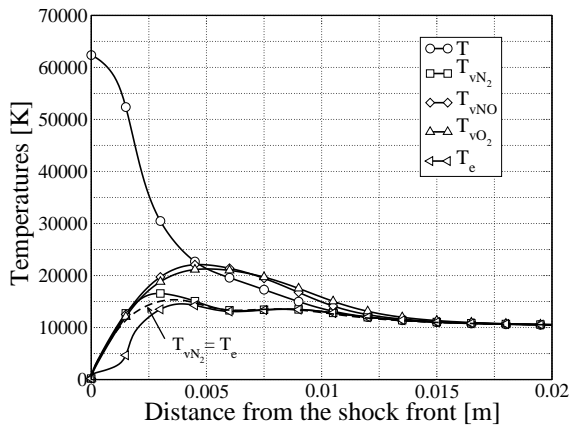


Figure 6.6: 1634 s case. Temperature profiles. Comparison between the five temperature model with $T_{vN_2} \neq T_e$ (unbroken line) and the four temperature model with $T_{vN_2} = T_e$ (dashed line).

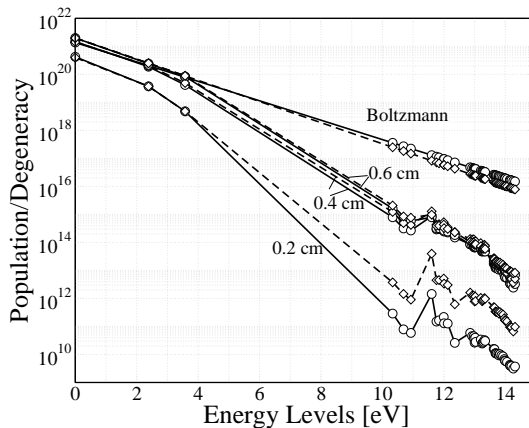


Figure 6.7: Electronic energy level populations for atomic nitrogen [m^{-3}] : CR model at 0.2 cm, 0.4 cm, and 0.6 cm; Boltzmann distribution at 0.4 cm. Comparison between the five temperature model with $T_{vN_2} \neq T_e$ (unbroken line) and the four temperature model with $T_{vN_2} = T_e$ (dashed line).

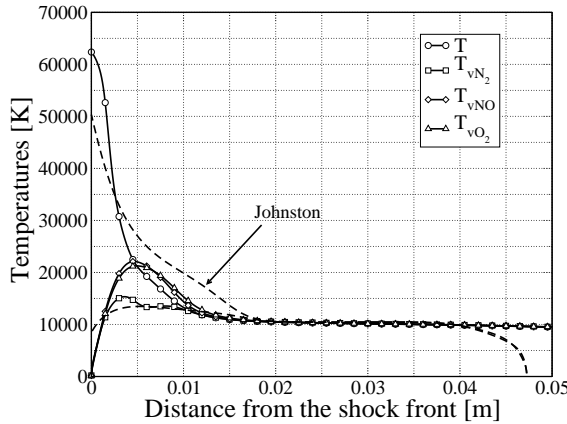


Figure 6.8: 1634 s case. Temperature profiles: CR model (unbroken line); Johnston's results [93] (dashed line).

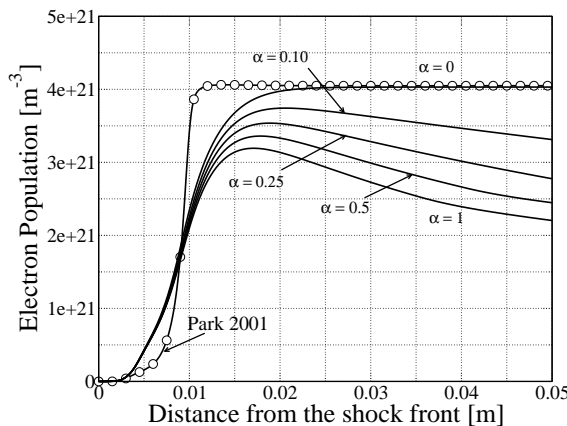


Figure 6.9: 1634 s case. Electron number density profiles: CR model with escape factor values of 0, 0.1, 0.25, 0.5, and 1 (unbroken line); simplified kinetic mechanism of Park et al. [148] (line with circles).

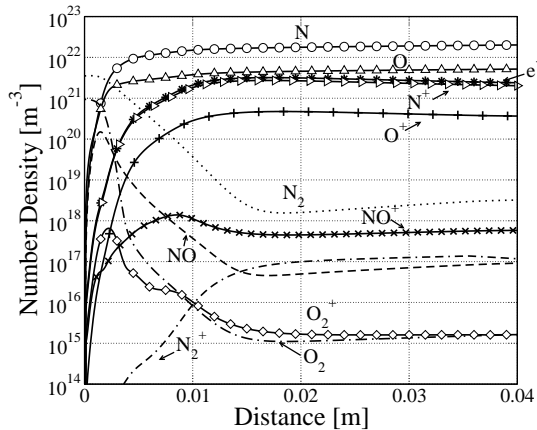


Figure 6.10: 1634 s case, Species number density profiles.

6.2.5.2 Composition and electronic energy populations

Characterization of the physico-chemical state of the plasma in the shock layer requires the knowledge of the chemical composition, as well as the determination of the energy stored into the internal modes. In Figure 6.10, we examine the evolution of the different species concentrations. We recall that only molecular nitrogen and oxygen are present after the shock. These molecules first dissociate, in particular, molecular oxygen tends to completely disappear in favor of atomic oxygen right after the shock, while the full dissociation of molecular nitrogen is delayed. Ionization occurs simultaneously and produces free electrons, nitrogen atom ionization being more efficient than ionization of the other species. Figure 6.11 shows electronic state specific population profiles for atomic nitrogen.

It is interesting to mention that the upper electronic states are more reactive than the ground state and lower (metastable) states. Immediately after the shock, the populations of the excited levels tend to equilibrate with the free electron populations that are in nonequilibrium. Moreover, we can observe how the atom populations are mainly in the ground electronic state at the beginning of the relaxation, consistent with the kinetic mechanism assuming that dissociation of molecular nitrogen and oxygen generates atoms

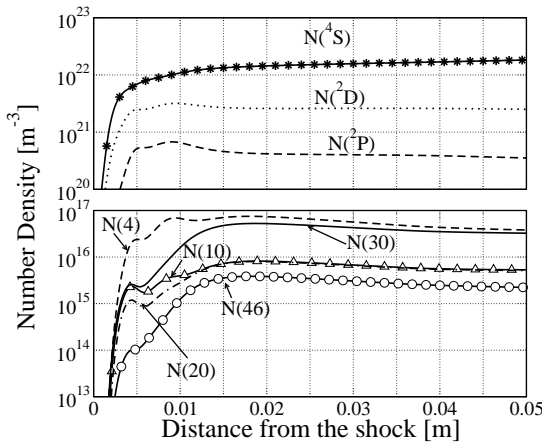
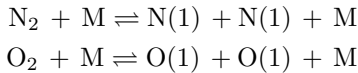
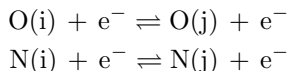


Figure 6.11: 1634 s case, number density profiles: N(1), N(2), N(3), N(4), N(10), N(20), N(30), N(46).

in the ground state:



The same assumption holds for all the other reactions (in particular for the Zel'dovich reaction responsible for the atomic nitrogen formation). This assumption is justified since electronic excitation mainly occurs via electron impacts; the number density of electrons is still low in the post-shock region. After this incubation distance, the number density of electrons significantly increases and the electronic states of atoms thermalize. The electron-impact excitation processes:



are fast and the populations of excited electronic states rapidly increase. The upper states are then depleted, in particular by ionization and spontaneous emission, which explains the maximum found in the population profiles.

In order to characterize nonequilibrium of the populations, the number density of the electronic states of atomic nitrogen is compared in Fig-

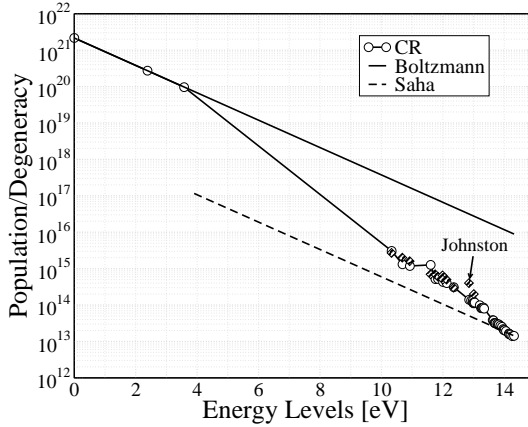


Figure 6.12: 1634 s case. Electronic energy level populations for atomic nitrogen at 0.7 cm from the shock front [m^{-3}]: CR model (line with circles), Boltzmann distribution (unbroken line), Saha distribution (dashed line), and Johnston's results [93] (black diamonds)

ures 6.12- 6.13 with the Boltzmann and Saha distributions at two locations after the shock. Both Boltzmann and Saha distributions are computed based on the electron temperature T_e by keeping the atomic nitrogen concentration constant. In logarithmic scale, they appear as two parallel straight lines of slope proportional to $-1/T_e$.

In Figure 6.12, at 0.7 cm from the shock, the CR model predicts that the ground and metastable states follow the Boltzmann distribution, whereas the number density of the highly excited states is much lower and tend to the Saha distribution, following T_e . This phenomenon is typical of nonequilibrium conditions encountered during high speed reentries. Excellent agreement is found with the results presented in Ref. [93].

Figure 6.13 shows the same quantities at 2.5 cm from the shock. Since we have moved at further distance from the shock front, the flow tends towards equilibrium, and the Saha distribution tends to the Boltzmann distribution. Our model predicts that the high lying excited states are still being depleted by radiative exchange with lower states. We notice that at this location the comparison with literature is not as good. Our results show a higher degree of nonequilibrium than in Ref. [93], closer to the Boltzmann distribution.

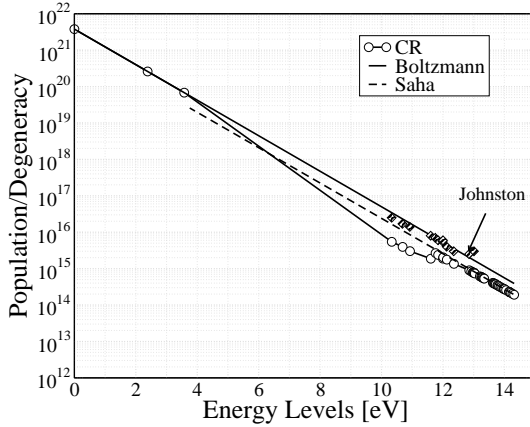


Figure 6.13: 1634 s case. Electronic energy level populations for atomic nitrogen at 2.5 cm from the shock front [m^{-3}]: CR model (line with circles), Boltzmann distribution (unbroken line), Saha distribution (dashed line), and Johnston’s results [93] (black diamonds)

6.2.5.3 Standard QSS approach

Quasi-steady-state models are often used in the literature [93, 138] to study electronic energy level populations in strong nonequilibrium conditions, under which the hypothesis of a Boltzmann distribution does not hold. They constitute a valid alternative to the time-dependent CR model presented in this paper when the characteristic time of the excited state processes is very short with respect to the characteristic time of the flow. As a consequence, the set of mass conservation equations for the electronically excited states given in Eq. (6.15) can be expressed as a set of non linear algebraic equations to be solved separately from the other conservation equations. It is important to emphasize that this operation does not reduce the computational cost if the electronic energy populations are computed everywhere in the flow. The QSS assumption is only desirable when the populations of excited states are probed at some locations of interest, for instance along the stagnation line in multidimensional flow simulations, and therefore, allowing for a drastic reduction of the computational cost versus the time-dependent CR model.

It is well-known that the regime of validity of the QSS assumption is strongly

influenced by a sudden change in the plasma conditions, such as after a strong shock where the electron density is very scarce. Since the collisional processes are responsible of the equilibration of the internal energy states, in particular the processes involving electrons as collision partners, a lack of electrons contributes to the failure of the QSS assumption.

In this section, we compare the results obtained by means of the time-dependent CR model to the standard QSS methods presented in Refs. [93, 138]. First, we compute the profiles of the flow characteristic quantities (pressure, temperatures, and composition) based on the effective reaction rates of Park et al. [148] for air chemistry, widely used in the literature but different from the mechanism given in Section 6.2.1. Then, the QSS populations of excited states are computed at a given location by solving the following system of ordinary differential equations

$$\frac{d}{dt}y_i = \frac{\dot{\omega}_i}{\rho}, \quad i \in \mathcal{N}_1 \cup \mathcal{O}_1 \quad (6.23)$$

where the index i runs over all the excited states of N and O, including the metastable states. Our approach, formally different from the system of nonlinear algebraic equations described by the law of mass action, $\dot{\omega}_i = 0$, $i \in \mathcal{N}_1 \cup \mathcal{O}_1$, has an equivalent solution for $t \rightarrow \infty$. Our method presents the advantage to overcome numerical problems sometimes encountered when using the algebraic formulation [93, 138]. The population of the ground states is retrieved by ensuring that the total number density computed during the flow calculation is conserved in the QSS calculation.

In the following analysis, we examine the first trajectory point at a location of 0.7 cm from the shock front. We compute the electronic energy populations of nitrogen atoms based on three models:

1. Full CR: the time-dependent CR model described in Section 6.2.1,
2. QSS Abba: QSS model with the same data for the atomic and radiative elementary processes as in the full CR model,
3. QSS Park: QSS model with the energy levels and data for the atomic and radiative elementary processes of Park [138].

The main differences between the various models are the coupling method and the sets of data for the reaction rates. For both QSS models, the flow calculations have been performed by clipping the reaction rates of Ref. [148]

in order to avoid using them out of their validity range; the translational temperature driving the rate constants has been limited to the value of 30 000 K. Moreover, the free-electron energy loss term for electron impact ionization given in Eq. (6.22) is computed based on the expression suggested in Ref. [93]

$$\Omega^I = -\omega_{N^+} I^{N^+} - \omega_{O^+} I^{O^+} \quad (6.24)$$

where $I^{N^+} = 4.05 \times 10^8 \text{ J/(kg mol)}$ and $I^{O^+} = 4.30 \times 10^8 \text{ J/(kg mol)}$, respectively. In the full CR model, we recall that this term is directly computed based on Eq. (6.21) from the expressions for the reaction rates intrinsic to the model, without any a priori hypothesis.

Figure 6.14 shows a comparison between the results obtained by means of the three models, the Boltzmann distribution, and Johnston's results. The full CR model and the QSS ABBA model yield electronic energy level populations in rather good agreement with Johnston's results. The QSS ABBA model slightly under-predicts the population of the lower electronic levels. The QSS assumption is a fair approximation at this location. The differences between the QSS ABBA results and the QSS results of Johnston are not well understood, they might be explained by the different data for the electron-impact excitation rates of atoms or for the radiative processes. The differences with respect to the QSS Park model for atomic and radiative processes are significant: up two orders of magnitude for the upper levels above the metastable states.

In conclusion, the standard QSS approach seems to be valid, *at this location*, provided that a correct set of reaction rates is chosen for the model. This choice should be based on a comparison of the computed results with experimental data.

In the flow calculation, the need for a special adjustment for the effective rate constants of Park et al. [148] (maximum temperature) and for the source term responsible for the energy removal from the free electron temperature makes difficult its extrapolation to generic flow conditions.

6.2.5.4 Towards a simplified CR model

In the foregoing section, we have studied the standard QSS approach by comparing QSS results and time-dependent CR results at one location in the flow. In this comparison, the reaction rate data are not identical, for instance the rates of molecular elementary processes used in the full CR model differ from the rates used in the QSS ABBA model. In this section, we

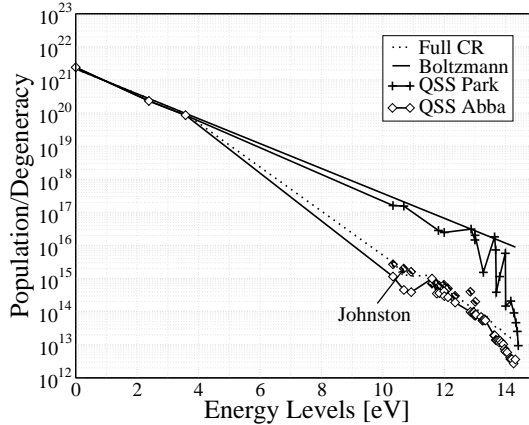


Figure 6.14: 1634 s case, 0.7 cm from the shock front. Electronic energy level populations for atomic nitrogen [m^{-3}]: full CR model (dotted line), QSS ABBA model (line with diamonds), QSS Park et al. model [148] (crosses), Boltzmann distribution (unbroken line), and Johnston’s results [93] (black diamonds)

further investigate the validity of the QSS assumption, based on the same set of reaction rates, at several locations in the flow. This is a preliminary step to derive a simplified CR model for reentries at speeds higher than 10 km/s, typical of Moon returns.

For this purpose, we compute the electronic energy populations of atomic nitrogen for the first trajectory point (1634 s case) by means of the full CR model. From the calculation, we extract the profiles of the flow characteristic quantities (pressure, temperatures, and composition). Then, the QSS populations of excited electronic states are computed at a given location by solving the system of Eqs. (6.23). This approach is called “simplified CR model” in the following.

The QSS distribution of excited states is computed by solving the set of Eqs. (6.23). In the first model (simplified CR metastable) the index runs from $i = 2$ to the total number of electronic levels for the atomic species, whereas in the second model (simplified CR) the metastable states are considered in Boltzmann equilibrium with the ground state and i starts from 4. The latter hypothesis is justified by the small difference in terms of

electronic energy among the ground state and the two metastable states which enhances the excitation due to impacts with light and heavy particles promoting thermalization. At the instant $t = 0$ the initial population is assumed to be Boltzmann at the prescribed pressure and temperature conditions³. A careful analysis of the system (6.23), reveals that the population of the ground state and the one of the two metastable states (for the second model, the simplified CR model) is needed in order to close the system of equations. In the first case the population of the ground state is retrieved summing the population of the excited states and subtracting this value to the total number density given by the flowfield calculation.

The flow is investigated at three locations: 0.3 cm, 0.5 cm, and 1 cm from the shock. The electronic energy level populations for atomic nitrogen are shown in Figure 6.15. At 0.3 cm, the populations obtained by means of the simplified CR model are higher than the populations obtained by means of the full CR model; the QSS assumption is not valid in the near shock region. This difference of populations is much more pronounced for the metastable states that follow a Boltzmann distribution when the QSS assumption is used. At 0.5 cm, all the excited states practically satisfy the QSS condition. After 1cm, no difference is noticed between the results obtained by means of the two models. An explanation is found by examining the characteristic time for the atomic excitation and ionization processes. For instance, we find that this characteristic time for the first metastable state is of the same order of magnitude as the characteristic time of the flow 5×10^{-6} s computed at 1 cm from the shock.

Based on this analysis, we recommend to keep the atomic metastable states as separate species for this trajectory point and compute the upper electronic states by means of a QSS model, in order to reduce the computational cost in multidimensional flow simulations. The CR model could be used as a tool to derive effective reaction rates for the simplified mechanism associated with this mixture of species and also the expressions for the free-electron energy loss term for electron impact ionization and ionization reactions.

³The initial distribution does not have any influence on the results that depend only on temperature, pressure and the total number of atoms

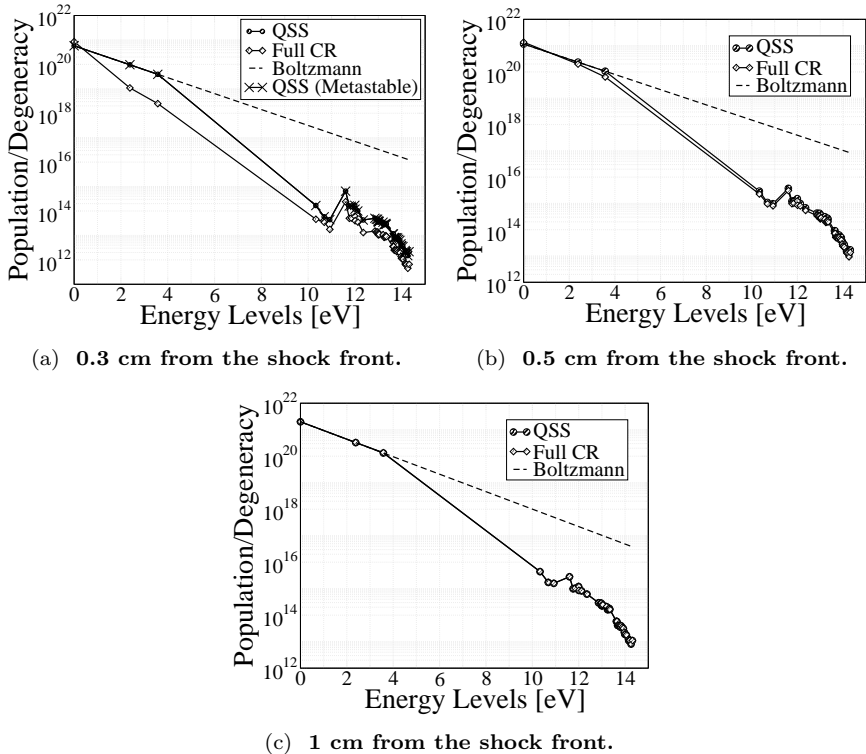


Figure 6.15: 1634 s case. Electronic energy level populations for atomic nitrogen [m^{-3}]: simplified CR model (line with circles), full CR model (line with diamonds), Boltzmann distribution (dashed line).

6.2.6 Analysis of the Fire II 1636 s case

6.2.6.1 Thermal nonequilibrium effects

In order to demonstrate that the one dimensional flow solver SHOCKING is capable of reproducing the main physico-chemical features along the stagnation line of reentry flows, except for the boundary layer region, we compare our results to simulations obtained by means of validated flow solvers: LAURA, DPLR [83] and the viscous shock layer code of Johnston [93]. The

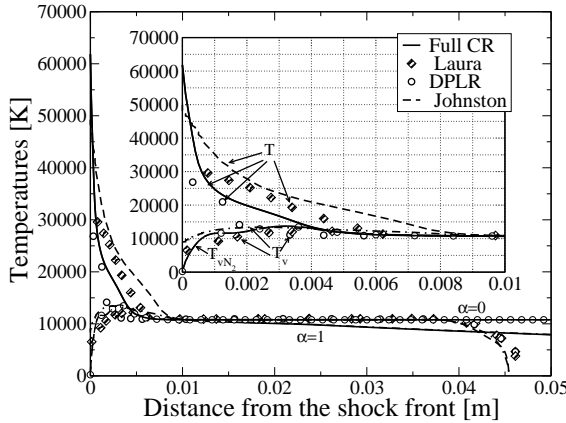


Figure 6.16: 1636 s case. Temperature profiles: comparison with results from literature Refs. [83]-[93]. CR model with escape factor values of 0 and 1 (unbroken line), LAURA code (diamonds), DPLR code [83] (circles), and Johnston’s results [93] (dashed line).

comparison is carried out for the temperature and ionization profiles.

In Figure 6.16, we show profiles of the translational temperature and the molecular nitrogen vibrational temperature obtained by means of our CR model (T and T_{vN_2}) and of the two-temperature reference models (T and T_v). Noticeable differences are found in the thermal relaxation zone. The post-shock translational temperature obtained by means of the SHOCKING code from the Rankine-Hugoniot relations is much higher than the values obtained by the means of the LAURA and DPLR codes and closer to the value obtained by Johnston who used a discrete boundary condition (shock slip condition). Another possible source of discrepancies is the absence of dissipative effects in the CR model. The vibrational temperature obtained by the means of the CFD codes is higher than the frozen value. Fair agreement can be observed among all the results for the vibrational temperature of N_2 . This is very important seeing its close association with radiation, electronic excitation, and electron density [145].

The optical thickness of the medium plays an important role in our simulations. The upper curve (labeled $\alpha = 0$) represents the optically thick

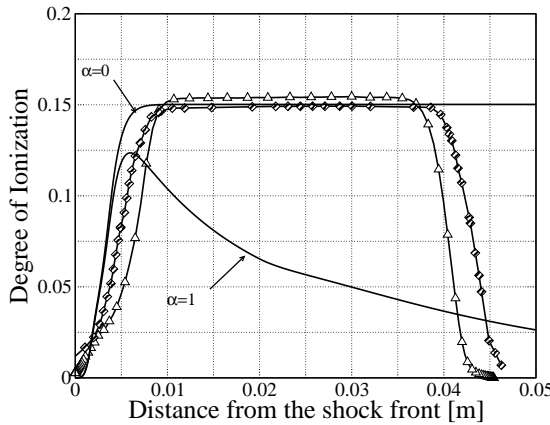


Figure 6.17: 1636 s case. Ionization degree profiles: CR model with escape factor values of 0 and 1 (unbroken line), LAURA code [83] (line with diamonds), and Johnston’s results [93] (line with triangles).

case, and the lower curve (labeled $\alpha = 1$), the optically thin case. A lower temperature is obtained for an optically thin medium since the flow energy is depleted by radiation.

In Figure 6.17, we compare the results obtained for the ionization degree. In the case of an optically thick medium, it reaches a plateau; a fair agreement is found with the literature. Large differences are found when radiative cooling is taken into account since it reduces the degree of ionization. Our model predicts that the ionization process is more rapid than the model implemented into the LAURA code and into the viscous shock layer code.

6.2.6.2 Electronic energy populations

In Figures 6.18-6.19, the electronic energy level populations are shown at 0.5 cm from the shock front, for an electron temperature value of 12 883 K. We clearly see that the low electronic energy levels tend to follow a Boltzmann distribution at the electron temperature, whereas, close to the ionization limit, the excited electronic states approach a Saha distribution at the electron temperature. Since the channels between the low and high lying electronic states exhibit finite ionization rates, a lack of free electrons may

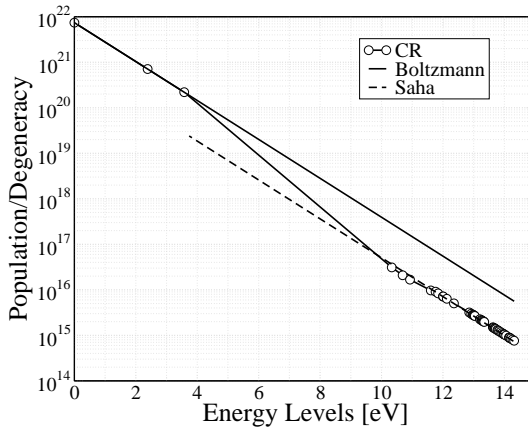


Figure 6.18: 1636 s case, 0.5 cm from the shock front. Electronic energy level populations of atomic nitrogen [m^{-3}]: CR model (line with circles), Boltzmann distribution (unbroken line), and Saha distribution (dashed line).

result in depleted populations for the highly excited states. The distribution is no longer of Boltzmann type and the electronic temperature is no longer defined.

The departures from the Boltzmann distribution, which are of the same order of magnitude for atomic nitrogen and atomic oxygen, tend to reduce the radiative contribution to the overall heat flux in the earlier parts of the trajectory. For this reason, attempts to estimate the radiative flux assuming a Boltzmann distribution among electronic levels might lead to an overestimation of this heat flux.

6.2.7 Analysis of the Fire II 1643 s case

In this section, we analyze a trajectory point close to peak heating. Figure 6.20 shows that the thermal nonequilibrium effects are located in a very narrow region near the shock. The electronic energy level populations of atomic nitrogen at 0.5 cm from the shock are given in Figure 6.21. It is interesting to mention that these populations follow Boltzmann distributions in the entire domain. These results are explained by the values of the post-shock pressure p_2 given in Table 6.2, much higher than for the first two trajectory points. At high pressures, the plasma is dominated by col-

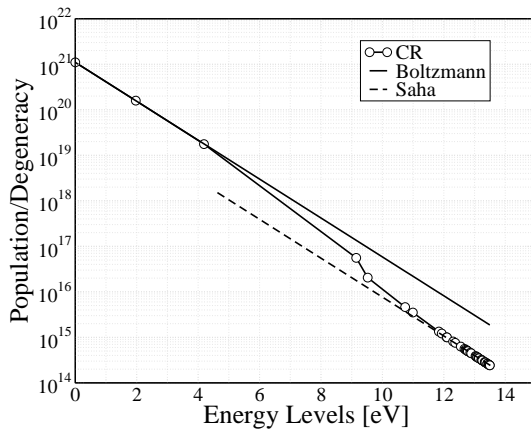


Figure 6.19: 1636 s case, 0.5 cm from the shock front. Electronic energy level populations of atomic oxygen [m^{-3}]: CR model (line with circles), Boltzmann distribution (unbroken line), and Saha distribution (dashed line).

lisional processes; thermal relaxation is enhanced and the electronic state populations tend towards Boltzmann distributions.

Conclusions

We study the behavior of the excited electronic states of atoms in the relaxation zone of one dimensional air flows obtained in shock-tube facilities. A collisional radiative model is developed, accounting for thermal nonequilibrium between the translational energy mode of the gas and the vibrational energy mode of individual molecules. The electronic states of atoms are treated as separate species, allowing for non-Boltzmann distributions of their populations. Relaxation of the free electron energy is also accounted for by using a separate conservation equation. We apply the model to three trajectory points of the FIRE II flight experiment. In the rapidly ionizing regime behind strong shock waves, the electronic energy level populations depart from Boltzmann distributions since the high lying bound electronic states are depleted. In order to quantify the extent of this nonequilibrium effect, we compare the results obtained by means of the collisional radiative model with those based on Boltzmann distributions. For the earliest trajectory point, we show that the quasi-steady-state assumption is only valid

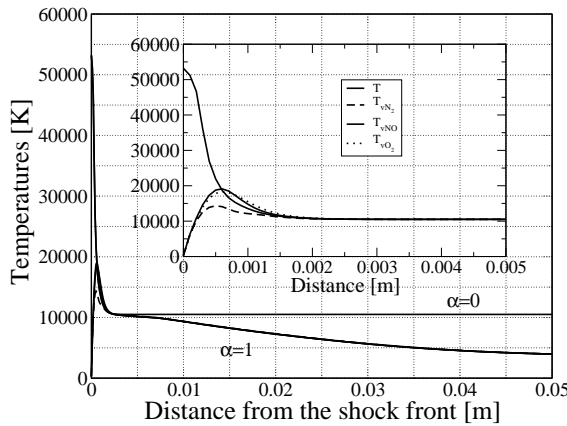


Figure 6.20: 1643 s case. Temperature profiles with escape factor values of 0 and 1.

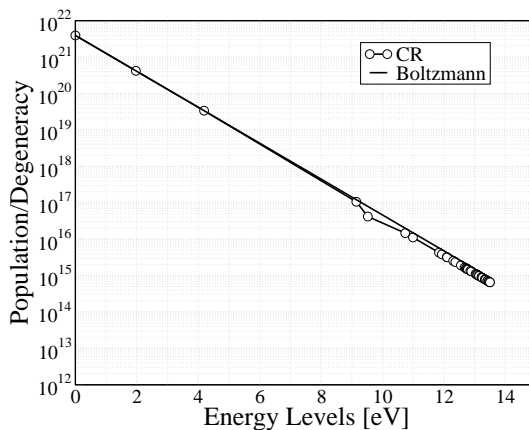


Figure 6.21: 1643 s case. Electronic energy level populations for atomic nitrogen [m^{-3}]: CR model (line with circles) and Boltzmann distribution (unbroken line), 0.5 cm from the shock front.

for the high lying excited states and cannot be extended to the metastable states. In this work, we have studied the departure of the atomic electronic energy populations from Boltzmann distributions for one dimensional air flows obtained in a shock-tube. The operating conditions are taken from three points in the trajectory of the FIRE II flight experiment at 1634 s, 1636 s, and 1643 s elapsed time from the launch. The results have been obtained by means of a multi-temperature fluid model fully coupled with an electronic-specific collisional radiative model. We have compared the flow-field quantities and electronic energy populations with literature [83, 93] and found a good agreement. We have also found that, for the first two points of the trajectory (1634 s and 1636 s), the electronic energy level populations of the N and O atoms depart from Boltzmann distributions since the high lying bound electronic states are depleted. The analysis of the last trajectory point (1643 s) reveals instead a Boltzmann distribution among the electronic levels.

An analysis of the state of the flow for the first flight condition (1634 s) led us to the conclusion that the excited species of atoms satisfy the quasi-steady-state assumption, except for the two metastable states. As a consequence, the global rate coefficients and free electron energy loss terms could be derived in the steady state based on our model, considering however the metastable states as separate pseudo-species governed by their own chemical-kinetic mechanism.

Moreover, the validity of the standard QSS approach widely used by the aerospace community has been tested; the results obtained by means of our full CR model and the standard QSS model are found in good agreement. It is important to mention that the full CR model is more general, since the parameters governing the free-electron energy losses by electron impact ionization are obtained from the expressions for the reaction rates intrinsic to the model, without any *a priori* hypothesis.

Finally, we have shown that the populations of high-lying excited states of atoms obtained by using the rates of Park [138] for electron-impact excitation and ionization reactions are up to two orders of magnitude higher than the populations obtained by using the rates of Bultel et al. [27], consistent with the result of Johnston [93].

6.3 Comparison with east experiments

The present section is committed to the partial validation of the *electronically specific* collisional-radiative model, thoroughly described in Section 6.2, ([27, 131, 134, 136]), against the recent measurements [66], given in Ref. [92] and performed on the EAST shock tube facility. The analysis allows us to extract useful information concerning the accuracy of the collisional and radiative mechanisms used and at the same time to gain some insights on the chemico-physical processes occurring behind strong shock waves.

In Section 6.3.1, we briefly recall the features of the physico-chemical models implemented in the SHOCKING code and we describe the modifications introduced in the ABBA model in order to improve the modeling of the excitation and ionization by electron-impact and to enhance the agreement with the experimental results. The choice to focus our attention on the atomic processes is justified by the fact that, at high temperatures and for high speed re-entry (≥ 10 km/s), the contribution of the radiative component to the heat flux is dominated by atomic lines and continuum radiation [17, 92, 93, 134], the molecules being almost completely dissociated in this temperature range.

The radiative prediction, described in Section 6.3.2, is carried out on the basis of the advanced tools available at the EM2C laboratories (Le laboratoire d’Energetique Moleculaire et Macroscopique, Combustion), based on the spectroscopic database devoted to the study of the radiative transfer for air plasmas under chemical and thermal equilibrium in the temperature range 300 – 25000 K [41, 42, 52]. Atomic lines, which constitute the focus of the present investigation, have been taken from the NIST database [117]. The influence of the velocity and the pressure on the radiative signature of the plasma is analyzed using high resolution spectra and radiative source strength.

The section of results (§6.3.3) is divided in three parts. We first analyze the physico-chemical state of the plasma in the post-shock relaxation zone in terms of temperature profiles and population densities of the electronic levels of the atoms.

We move then to the analysis of the radiative properties of the shock layer, comparing the simulated radiative signature with the experiments. Considerations on the optical properties of the gas are also discussed in this part of the manuscript.

In the last part of the section we focus our attention on the influence of the chemical kinetics on the results. In this part a new set of cross sections for the elementary processes of excitation and ionization are also tested. Moreover the influence of the shock speed on the radiative intensity is investigated, analyzing in detail the influence of the ionizational nonequilibrium on the radiative signature.

6.3.1 Physico-Chemical modeling

Numerical predictions are carried out by making use of two different codes: SHOCKING code [131, 134] for the flowfield calculations and the radiation code solver developed at EM2C for the study of radiative processes.

The first numerical tool is used to model the chemico-physical phenomena taking place in the relaxation zone behind a shock wave, whereas the second code is used to model the radiative signature of the high temperature gases.

SHOCKING describes the post-shock relaxation process by means of 1D Euler equations fully coupled with a set of equations describing the thermal relaxation processes (Section 6.15). In the present contribution only one temperature T_V is used to describe the nonequilibrium relaxation for vibration and electronic excitation processes of the molecules. Hence when equilibrium among the vibrational levels of all the molecules is assumed, the vibrational and electronic conservation equation takes this form:

$$\frac{\partial}{\partial x} \left[\rho u \left(e^V + y_e e_e + \sum_{i \in \mathcal{E}} y_i e_i^E \right) \right] = -p_e \frac{\partial u}{\partial x} + \sum_{i \in \mathcal{E}} \dot{\omega}_i e_i^E - \Omega^I - \Omega^E + \Omega^{ET} + \sum_{m \in \mathcal{V}} \dot{\omega}_m e_m^V + \Omega^{VT} \quad (6.25)$$

The collisional radiative model is coupled with the flowfield model to determine the evolution of the electronic population densities of the atoms. The populations of the internal levels of the atoms are modeled by means of a CR model writing a master equation for each electronic level considering it as separate pseudo-species. Conservation equations of mass, momentum, global energy, vibrational and free-electron-electronic energy are solved simultaneously, as opposed to Lagrangian methods [115] and quasi-steady-state approximations [15, 93] where the electronic populations are

determined subsequently to the flow calculation.

6.3.1.1 Kinetic mechanisms

Behind strong shock waves, the population of the electronically excited states is assumed to depart from the equilibrium distribution and to be governed by finite rate kinetics. A detailed description of the processes that populate and de-populate the electronically excited states, was given in Section 6.1.2. In this work, the rate constants for the radiative and kinetic elementary processes are taken from Ref. [27]. Moreover, in order to assess the influence of the kinetic processes on the results, we decided to modify the kinetic data set, governing the excitation and ionization by electron impact. Since the electronic excitation of atoms directly affects radiation, a direct comparison with the measured intensity diagrams can give an idea of the accuracy of the model used. The importance of the atomic line radiation for high speed entry conditions has been discussed in Ref. [17, 92] and justifies the need for a sensitivity study.

6.3.1.2 Excitation by electron impact

The non-elastic cross sections for ionization and excitation by electron impact exhibit a surprising degree of regularity and have been the subject of considerable theoretical research [120]. Several "universal" formulas for these cross sections have been proposed.

The original set of rate constants implemented in the ABBA model is based on direct integration of Drawin [54, 55] cross sections. In the following different kinetic mechanisms will be tested:

- Gryzinski cross sections [77], (see Section 6.1.2) which were derived on the base of classical calculations within the hydrogenic assumption.
- Frost et al. [62] rate constants, (see Section 6.1.2) based on R-matrix calculations.

6.3.1.3 Ionization by electron impact

Two different formulations Ref. [55] and Ref. [93]) for the electron impact ionization are used in the present contribution, and both are based on the work of Drawin. The first model is used in the baseline ABBA model [27], whereas the second model is used in the CR model of Johnston [93]. It is

important to notice that a direct comparison of the rate constants shows a difference of 1 order of magnitude for the two models.

6.3.1.4 Models used in the investigation

The kinetic models, briefly outlined in the foregoing section, allow us to describe the excitation and ionization processes of the atomic species. In the present section we present the CR models derived using the kinetic model described. We define:

ABBA model: which is the baseline model and has been thoroughly described in Section 6.2.

ABBA TCNQ: which uses different energy exchange source terms among internal energy modes, respect to the ABBA model. In particular preferential dissociation model, discussed by Gnoffo in Ref. [69], was adopted. In such model the vibrational energy removed by dissociation is not the average vibrational energy but the 30% of the dissociation energy. The diffusion model of Park [138] was used for the modeling of the VT relaxation and the electronic energy reactive source term Ω^I was modeled as described in Ref. [93]. The set of kinetic data is unchanged respect to the ABBA model.

MODIFIED ABBA: which uses an updated set of rate constants for the excitation and ionization of atoms by electron impact. In particular, the model of Frost et al. [62] is used for the excitation of the ground state and the two metastable states to the upper states. For the missing reaction we adopt Gryzinski's cross sections [77]. Ionization by electron impact is modeled as described in Ref. [93]

Moreover in order to assess the influences of the each set of reaction, we define the following model ABBA FROST and ABBA *Gryzinski*. In order to clarify the differences among the different tools of the investigation we summarize in Tab. 6.3 all the features of the kinetic models.

6.3.2 Radiative properties prediction

The radiative signature of the plasma is determined on the basis of the advanced tool developed at the EM2C laboratory and presented in various contributions (see [41, 42, 52, 101, 156, 161]). The code allows for calculation high resolution emission and absorption spectra due to bound-bound,

Table 6.3: Kinetic models used in the investigation.

Model	Excitation			Ionization (Drawin)	
	Drawin	Gryzinski	Frost	Ref. [131]	Ref. [93]
ABBA	×			×	
ABBA TCNQ	×			×	
ABBA FROST			×	×	
ABBA Gryzinski		×	×	×	
MODIFIED ABBA	×	×			×

bound-free and free-free transitions over a wide spectral range from the VUV to the far infrared. Furthermore it relies on an accurate spectroscopic data base, described in Refs. [41, 42] for O₂-N₂ mixtures, combined with suitable emission and absorption expressions, presented in Ref. [101] in the frame of a two temperature description of the thermodynamic state of the plasma. For all the radiative mechanisms, except for N and O bound-bound transitions, the radiative properties are calculated using expressions provided by Ref. [101]. According to the state-by-state description considered here for N and O energy level distributions, modification were introduced, for the calculation of radiative properties due to the bound-bound transitions. Similar improvements should also include the photo-ionization⁴, but are not required in the present contribution, since we restrict our analysis to N and O bound-bound transitions.

The emission and absorption coefficients, for the transitions from an upper level i to a lower level j of the atomic species, are obtained using the following expressions:

$$\eta_\sigma = n_i \frac{A_{ij}}{4\pi} h c \sigma_{ij} f(\sigma - \sigma_{ij}) \quad (6.26)$$

$$\kappa_\sigma = (n_j B_{ji} - n_i B_{ij}) h \sigma_{ij} f(\sigma - \sigma_{ij}) \quad (6.27)$$

where n_i (respectively n_j) is the population of the upper (respectively lower) level; A_{ij} , B_{ij} and B_{ji} are the Einstein coefficients respectively for spontaneous emission, induced emission and absorption processes; σ_{ij} is the transition wave number and $f(\sigma - \sigma_{ij})$ is the spectral line profile shape which accounts for collisional and Doppler broadening; h and c are the Planck con-

⁴Detailed absorption cross-sections are available in the TOPBASE databases [172].

stant and the light velocity. Wave number and Einstein coefficient values are taken from the NIST [117] databases. The collisional line width, including van der Waals, resonance and Stark broadening was estimated in the frame of the semi-classical adiabatic approximation (see [156]).

Furthermore in some cases, the CR model provides number densities for grouped electronic levels. Hence the required population n_i for individual levels i , which belong to the grouped level k , is calculated assuming Boltzmann equilibrium at T_V according to:

$$n_i = n_k \frac{g_k}{g_i} \exp\left(-\frac{\epsilon_k - \epsilon_i}{k_B T_V}\right), \quad (6.28)$$

where the population n_k is provided by the CR calculations. The energy ϵ_k of the group (respectively the degeneracy g_k) is related to the corresponding individual energy levels ϵ_i (respectively degeneracy's g_i) through $\epsilon_k = \frac{\sum_i g_i \epsilon_i}{g_k}$ (respectively $g_k = \sum_i g_i$).

For the other levels which are not considered in the ABBA model (energy levels above 14.31962 eV for N and above 13.48156 eV for O), we assumed that they are in Saha-Boltzmann equilibrium with the free electrons, thus the population n_i of the energy level ϵ_i is determined according to :

$$n_i = \frac{g_i n_A^+ n_e}{2Q_A^+} \left(\frac{h^2}{2\pi m_e k_B T_V} \right)^{\frac{3}{2}} \exp\left(\frac{(\mathcal{I} - \epsilon_i)}{k_B T_V}\right) \quad (6.29)$$

where n_e and n_A^+ designate respectively the concentration of the electrons and the ion corresponding to the atomic species A (which is O or N). $Q_A^+(T_V)$ is the partition function of the ion corresponding to the atomic species A ; g_i is the degeneracy of level i ; \mathcal{I} is the ionization energy corrected to account for the Debye ionization lowering and m_e is the mass of the electron.

6.3.3 Results

The investigation of the reliability of the physico-chemical models considered in this study is carried out by comparing the predicted post-shock radiation to the measured post shock radiation for relevant test conditions. To this end the recent experiments carried out on the NASA Ames EAST facility, are used. The EAST facility is a 10.16 cm diameter shock tube with an electric arc-heated driver. The arc in the driver is supported by a capacitor bank which can store up to 1.24 MJ of energy heated at 40kV (see Refs. [162, 163]).

The EAST experiments were committed to measurement of the (absolute) intensity profile behind an air moving shock. The pressure of the driver gas (He/Ar mixtures) was maintained at 0.1 and 0.3 torr, and the velocity was targeted to 10 km/s and measured with an uncertainty of 1.5%. The intensity emitted, in the direction normal to the shock speed, was recorded using optical benches including two 0.3 m imaging spectrographs coupled at the exit focal plane, along with various intensified cameras for measurements in UV, visible and infrared spectral ranges. The spectral resolutions of the cameras ranged from 0.08 to 2 nm and with exposure time ranging from 0.015 to 0.98 μ s. The detailed description of the measurement campaign, including the test matrix and the instrumentation, is documented in Ref. [66], and the calibration procedures and sample error analysis are reported in Ref. [16, 76].

The EAST measurement campaign was very fruitful, and the recorded spatially and spectrally resolved spectra are still under post-processing; therefore only few data are published. The experimental data considered in this study are taken from the literature in a crude manner. We used the intensity profiles measured in the spectral range 700-1020 nm and available in Ref. [92] for the test cases documented in Table 6.4. The experimental analysis revealed that the radiation is mainly due to N and O bound-bound transitions. The measurements are presented in terms of spatial absolute intensity profiles $I_{\Delta\lambda}^{exp}(x)$ spectrally integrated over a suitable wavelength range $\Delta\lambda$ to emphasize the contribution to the emission of well defined electronic levels. The spectral ranges and the corresponding upper levels are detailed in Figure 6.22. For the high pressure cases (0.3 torr), the radiation was found to rapidly reach equilibrium. For the low pressure cases (0.1 torr), the distribution of the observed N and O emitting energy levels was found to depart from the Boltzmann. The measured radiation contains useful information concerning the population of some excited N and O atomic levels, allowing us to assess the reliability of the considered kinetic model (see Section 6.3.1) for the prediction of the non-equilibrium post-shock excitation. The temperature and population profiles, predicted on the basis of the models described in Section 6.3.1, are presented below. Then, comparisons among the radiative predictions and measurements are presented and discussed to suggest some possible improvements for kinetic reactions involving N and O atoms.

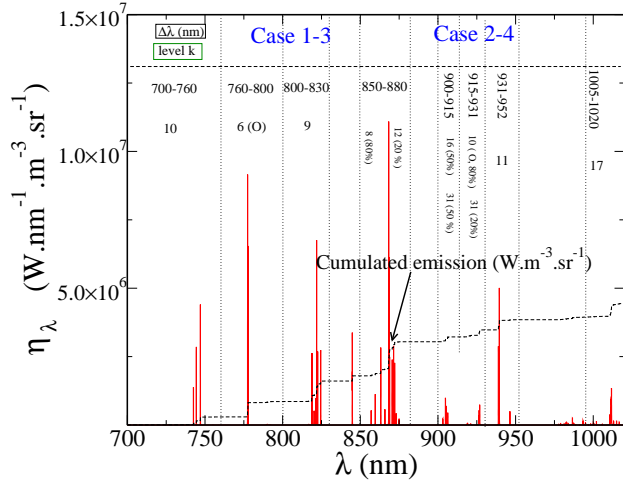


Figure 6.22: High resolution emission coefficient predicted for Case 1 at 4 cm downstream from the shock. The considered spectral ranges $\Delta\lambda$ are detailed. The corresponding main contributing electronic levels are indicated using the nomenclature of Ref. [131, 134].

Table 6.4: Operating conditions for the EAST shock-tube experiments considered here (see Ref. [92])

Case	Shock speed v_s (km/s)	p (torr)	acquisition time τ_{acq}
1	10.340	0.3	0.075
2	9.880	0.3	0.98
3	9.165	0.1	0.5
4	9.989	0.1	0.98

6.3.3.1 Thermo-chemical state and radiative signature predictions

The aim of the present section is to describe the physico-chemical state of the plasma flow in the post shock region for the test conditions corresponding to Case 3 and 4. In the first part of the section, temperature profiles and composition are presented and discussed, whereas the remaining part is devoted to the study of the evolution of the population of excited states

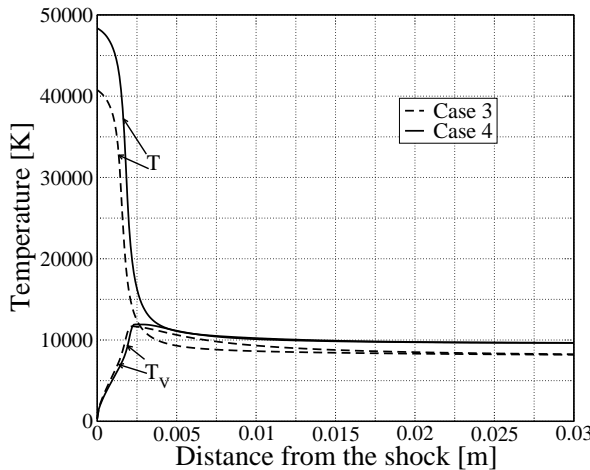


Figure 6.23: Case 3-4. Temperature profiles [K]. Dashed line profiles correspond to flight conditions of case 3. Unbroken lines refer to case 4.

and the influence of the excitation model on the results.

Figure (6.23) shows the evolution of the temperature profiles in the post shock region. Across the shock the internal energy modes are assumed to be frozen as well as the chemistry, whereas we use Rankine-Hugoniot's jump relations to estimate post shock pressure, velocity and translational temperature.

We remind the reader that T_v describes the vibrational and electronic temperature of the molecules and the energy stored in the translational mode of the free electrons. The internal energy stored in the energy modes of the atoms is computed by means of the CR models, which gives directly the populations of the excited states.

In Figure 6.24, we examine the evolution of the different species concentrations. Right after the shock molecular oxygen quickly dissociates, whereas the dissociation of the nitrogen is slower. At higher shock velocities, however dissociation tends to proceed faster than ionization so that the rate equations for ionization may be decoupled from the dissociation reactions assuming that dissociation is complete.

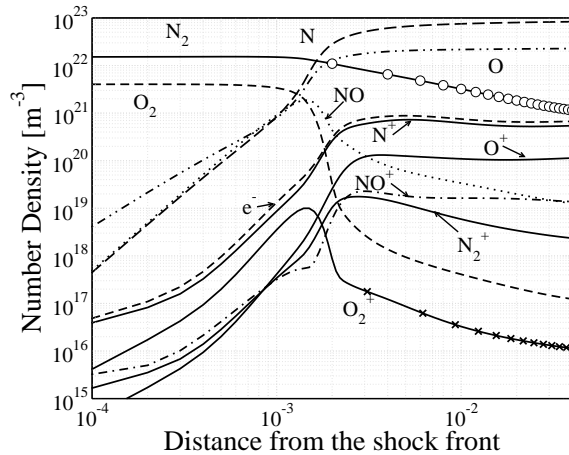


Figure 6.24: Case 3. Evolution of the composition in the post shock area.

Since the concentration of N^+ and free electrons are very close in the diagram we can assume that most of the electrons are created by ionization of the atomic nitrogen.

Figure (6.25) shows the evolution of the electronic states of atomic nitrogen and oxygen. As we shall see in the next sections, those states are responsible for the bound to bound radiation emitted in the spectral range from 700 nm to 880 nm (Case 1-3). Thus, since the foregoing spectral range is believed to be almost completely thin [92], for the flight conditions corresponding to Case 3, we have the possibility to directly access to the population density of the emitting states (with emission measurements) and validate the accuracy of the CR model.

Excitation by electron impact is the main channel of excitation of atoms, hence the electron density has a crucial importance in the evolution of the electronically excited states. Electron impact excitation reactions are fast and the populations of excited electronic states rapidly increase. The upper states are then depleted, by ionization and spontaneous emission, explaining the maximum found in the population profiles. The maximum in the population corresponds to a maximum in the radiation, which exhibits the same peak in the nonequilibrium zone after the shock.

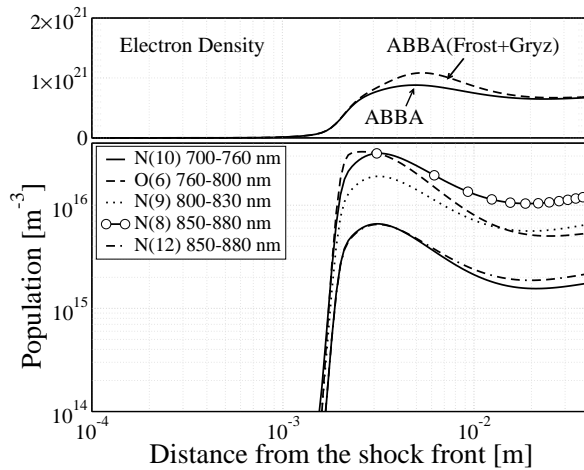


Figure 6.25: Case 3. Populations of electronically excited states of atomic nitrogen. $\text{N}(10)$ (unbroken line), $\text{O}(6)$ (dashed line), $\text{N}(9)$ (dotted line), $\text{N}(8)$ (circle) and $\text{N}(12)$ (dash-dotted line)

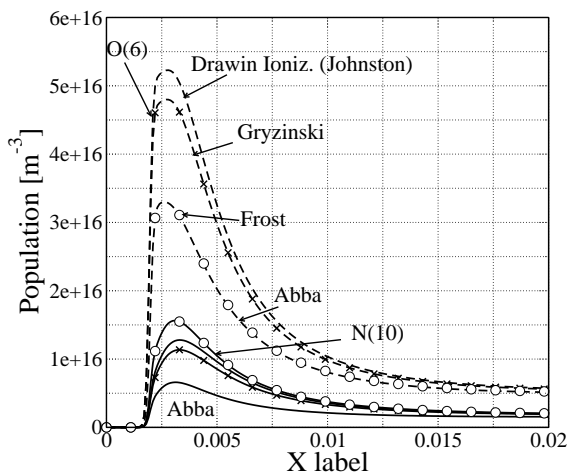


Figure 6.26: Influence of the model on the population densities of $\text{O}(6)$ and $\text{N}(10)$ electronic states.

The population profiles for the atomic oxygen ($O(6)$) and ($N(10)$) are depicted in Figure (6.26). As expected, the use of the Frost's rate constants does not affect the population profile of $O(6)$, since the set of reaction rates proposed by Frost concern the excitation from ground and metastable states to the excited states of nitrogen atoms.

The Gryzinski cross sections instead promote the excitation of $O(6)$ enhancing the overshoot in the population density profile. Also, electron impact ionization reactions do not seem to significantly affect the evolution of the profile in the overshoot region.

6.3.3.2 Comparisons with experiments and analysis

In order to compare our results with the experimental data ($I_{\Delta\lambda}^{exp}(x)$ taken from [92]), the intensity profiles were predicted using the radiative transfer equation, resulting from a constant property line of sight. Assuming that the radiation coming from the wall at the opposite side of the window is negligible (in $\Delta\lambda$), the intensity profile $I_{\lambda}(x)$ for a given location x may be written as :

$$I_{\lambda}(x) = \frac{\eta_{\lambda}(x)}{\kappa_{\lambda}(x)} (1 - e^{-\kappa_{\lambda}(x)D}) \quad (6.30)$$

where the shock diameter D is assumed to be equal to the shock-tube test section diameter 10.16 cm; $\eta_{\lambda}(x)$ and $\kappa_{\lambda}(x)$ are the emission and absorption coefficients at the location x . The intensity $I_{\lambda}(x)$ was then spectrally integrated over well defined narrow wave length ranges $\Delta\lambda$ detailed in Figure 6.22. Moreover in order to account for the spatial smearing, due to the finite acquisition time, intensity profiles were convoluted with a normalized gate function, as follow:

$$I_{\Delta\lambda}^{sim}(x) = \frac{1}{\Delta x} \int_x^{x+\Delta x} \left(\int_{\Delta\lambda} I_{\lambda}(x') d\lambda \right) dx', \quad (6.31)$$

where Δx is equal to the shock velocity v_s multiplied by acquisition time τ_{acq} . $I_{\Delta\lambda}^{sim}(x)$ indicates the integrated intensity used for the comparison against the experiments.

REMARK: Since the radiative code and SHOCKING are used in a decoupled manner, we have the possibility to neglect the adsorption of the gas in the radiation code, while the shock solver assumes an optically thick medium. This is done in order to extract information concerning the amount of radiation which is self-adsorbed and it constitute an *a posteriori* validation of

the assumption made in the flow solver. The case described is indicated in the plot with the label *optically thin*, and it refers to $\alpha \neq 0$ cases. In the following, when considering the medium as optically thick ($\alpha \neq 0$), we shall report in the graphs the corresponding optically thin case.

The overall comparisons, for the four cases investigated, are gathered in Figures (6.27-6.28) and (6.29-6.30) to outline some peculiarities of the predictions. The high pressure cases 1 and 2 are characterized by a fast and abrupt rise of the intensity profile, corresponding to the excitation phase of the post shock flow. Also, we observe that at higher velocity, the equilibrium plateau is reached earlier. For the low pressure Case 3 (see Figure (6.30)), the intensity presents a pronounced peaked shape profile, located at about 0.7 cm, followed by a slightly decreasing plateau, indicating that the flow may be still relaxing at 4 cm for the shock. For the low pressure Case 4, the intensity profile, shown in Figure (6.28) slowly increases, suggesting that, similarly to Case 3, the equilibrium may not yet be reached at 4 cm, possibly due to the reduced collision frequency. The intensity profile presents also a little burst, not present in the simulation and situated at about the same location as the peak observed for Case 3.

The measured intensity profiles for Cases 2 and 4 are compared to the predicted profiles using the ABBA baseline model. The optical thickness of the plasma is varied assuming: ($\alpha = 1$) optically thin medium; ($\alpha = X$) partially optically thick medium, i.e the radiated energy is fully absorbed in the VUV; ($\alpha = 0$) optically thick medium. For $\alpha = 1$, the population of electronic levels is ruled by collisional processes and by radiative de-excitation processes, since the radiated energy is not absorbed and completely escapes the plasma. This leads to the decrease in the population of the emitting levels, owing to the *radiative cooling* phenomena, starting at a distance of about 1 and 2 cm, for cases 2 and 4 respectively. Different is the behavior of the calculations for $\alpha \neq 0$, for which the contribution of the radiative cooling is absent ($\alpha = 0$) or strongly reduced ($\alpha = X$). The importance of radiative process within the VUV spectral range is revealed by the agreement between the $\alpha = 0$ and $\alpha = X$ calculations. The considerably flat shape of the measured profiles far behind the shock is attributed to the negligible radiative energy escaping.

Comparisons with optically thin calculations show that Case 1 and 2 are optically thick, since the intensity profiles are significantly altered, when absorption is accounted for in the radiation code. On the contrary, Cases 3 and 4 can be reasonably considered as thin, except for the spectral range

760-800 nm corresponding to the well known oxygen triplet transitions (as it will be shown below), and in a less extent for the spectral range 931-952 nm.

The influence of the kinetic models is shown in Figure 6.29 for the Case 1 and in Figure 6.30 for the Case 3, where the calculations, obtained for $\alpha = 0$, are compared with the measurements. For the high pressure Case 1, a slight influence to the model, in the non equilibrium region of the flow is observed, confirmed by the reduced departures among the Boltzmann and CR calculations. More pronounced is the sensitivity to the kinetic models in the peak region for the low pressure Case 3, as opposed to the plateau region, where the flow approaches the equilibrium conditions. Also, the peak region is characterized by a strong discrepancies among the measurements and CR predictions, which predict a reduced radiative overshoot and the Boltzmann results that strongly overestimate the peak. The CR calculations obtained using different models, disagree almost by 50% in the peak region and agree in the plateau. The comparison with the experiments suggest that the MODIFIED ABBA, based on updated kinetic models for ionization and excitation processes, can be considered as an improvement. The influence of the model ABBA TCNQ used for the thermal relaxation (see Section 6.3.1) is also presented in Figures 6.29-6.30 and was found to be rather weak for all the cases if compared to the effect of the kinetic models. The overall comparisons show a satisfactory agreement except for Case 3, although the discrepancies with the measurements remain acceptable (less than 50 % for the MODIFIED ABBA calculations). For Case 2, the measurements remain, over the entire spatial range, between the intensity profiles obtained for velocities $v_s - 1.5\%$ and $v_s + 1.5\%$ (corresponding to the experimental uncertainties on the velocity). The measured profile for Case 1 is bounded by the $v_s \pm 1.5\%$ profiles only in the plateau region, whereas some discrepancies are observed in the excitation stage. The calculated intensity profiles for Case 4 are slightly under-predicted, although the profile calculated with $v_s + 1.5\%$ shows a reasonable agreement with the measurements. The intensity burst at about 0.7 cm is not reproduced and it is believed to be an experimental artefact.

The possible reasons for the observed disagreement may have various sources. The influence of the uncertainty of $\pm 1.5\%$ on the velocity measurements has a significant effect as it was shown. The uncertainties on the Einstein coefficients (which remain lower than 10 % for the most important transitions) and on the Stark broadening width (which acts mainly on the pronounced optically thick cases 1 and 2) are not sufficient to explain the disagreement obtained for the low pressure cases. On the contrary the ki-

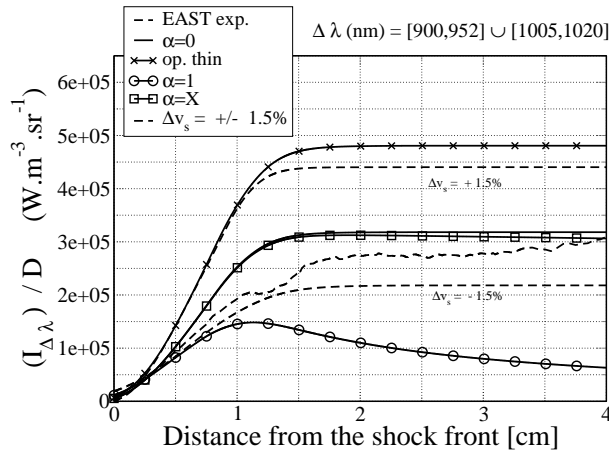


Figure 6.27: Case 2. Shock speed 9880 m/s: comparison among experimental and simulated radiative intensity profiles.

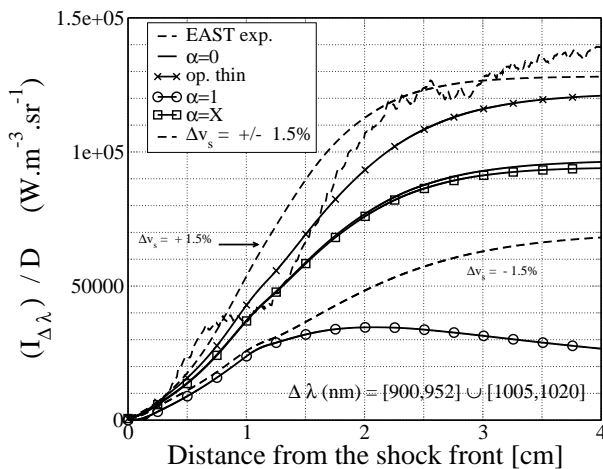


Figure 6.28: Case 4. Shock speed 10340 m/s: comparison among experimental and simulated radiative intensity profiles.

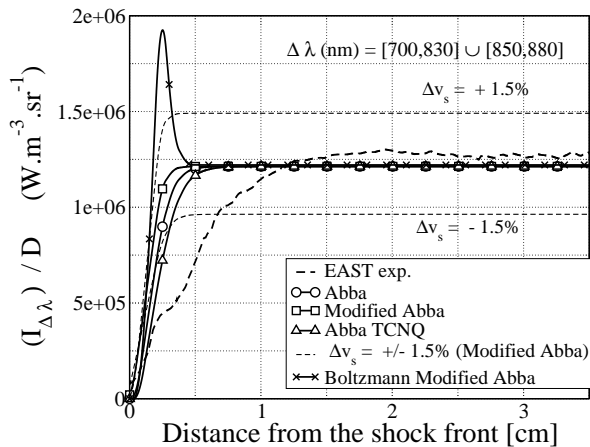


Figure 6.29: Case 1. Shock speed 9165 m/s: comparison among experimental and simulated radiative intensity profiles.

netic models have revealed an important influence on the predictions for the non equilibrium regions.

The impact of the different kinetics models considered (see Section 6.3.1), on the population density of the excited levels is detailed in Figures (6.31-6.32-6.33) for Cases 3 and 4. The intensity profiles predicted in two narrow spectral ranges corresponding to the N(10) and O(6) levels for Case 3 and N(31), O(10) for Case 4 and are also compared to the experiments. The calculations were performed by combining the ABBA baseline model with the various updated kinetic models for the ionization and excitation combinations presented in Table 6.4.

6.3.3.3 Influence of the kinetic model on the results

The impact of the kinetics of elementary processes on the radiative source strength is addressed in the present section, comparing the results obtained with the ABBA kinetic mechanism against the improved MODIFIED ABBA model. The importance of the each single set of rate constant, introduced into the baseline ABBA model, are analyzed in order to assess their influence on the results. Also, the comparison with the experiments are carried out

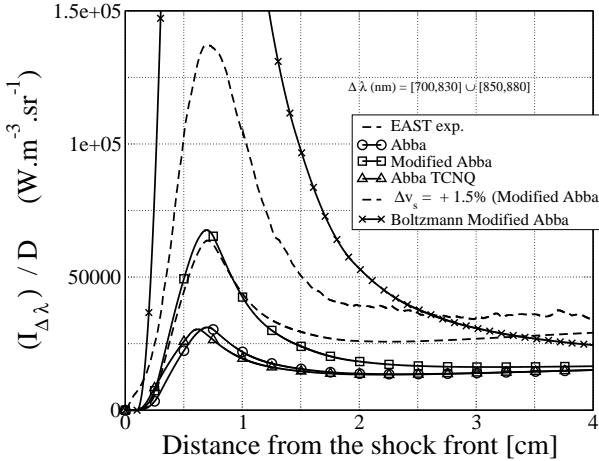


Figure 6.30: Case 3. Shock speed 9989 m/s: comparison among experimental and simulated radiative intensity profiles.

over a reduced wave-length range, to allow a better understanding of the influence of the kinetic processes on the single electronic state population.

The analysis of Case 4, in Figure (6.31), shows rather good agreement with the experimental data. The distance required to reach the plateau is the same for experiments and numerical simulation. The same figure presents results obtained neglecting the self-absorption, leading to the conclusion that the optical thickness of the gas in this spectral range is negligible. The influence of the model for this case are found negligible since all the emission profiles are overlapped for the different kinetic mechanisms. As far as this case is concerned our results seem to match quite well with the prediction given in reference [92], since the departures among the simulated curves and the measured ones are similar.

Figure (6.32)-(6.33) describe the evolution of the radiative signature produced by N(10) and O(6) respectively. We notice a different behavior for the two atomic lines, while the nitrogen atomic line is not strongly self-adsorbed, the O triplet line depicted in Figure (6.33) is strongly self-adsorbed. Focusing our attention on Figure (6.32) we can see that the baseline ABBA model

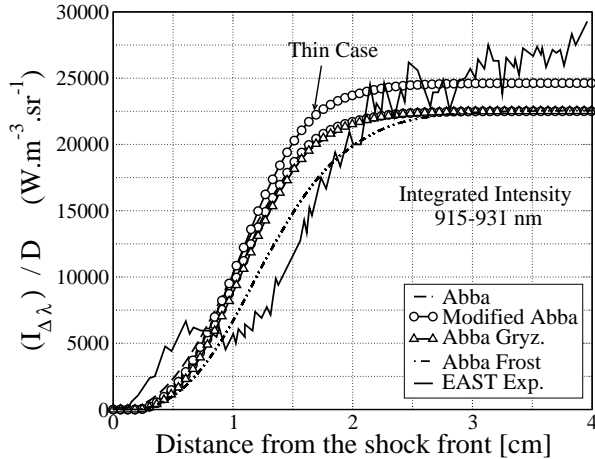


Figure 6.31: Case 4. Comparison among experimental and simulated radiative intensity profiles.

underestimates the peak of radiative intensity by 83%, whereas the MODIFIED ABBA underestimate the peak region by 66%. The improvement is mainly due to the use of rate constants computed by Frost et al. [62], since the use of the Gryzinski's cross sections have a negligible impact on the results. Figure (6.33) shows an excellent agreement with the experimental data for the thin case, when using MODIFIED ABBA model. However when the self-absorption is accounted for the same kind of under-prediction obtained for the other nitrogen line can be observed. As expected Frost's model plays no influence on the results, since it provides rate constant for the excitation of atomic nitrogen only. In this case however the MODIFIED ABBA model can take advantage of the cross sections due to Gryzinski that accounts for the increase of the peak in the radiative intensity.

Globally we can conclude that the MODIFIED ABBA model improves the agreement with the experimental results performed on the EAST facility.

Further insight into this comparison is gained from inferring the number densities of the radiating levels from the measured intensities as explained in Ref. [92]. The results are plotted in Figure (6.34-6.35), where the normal-

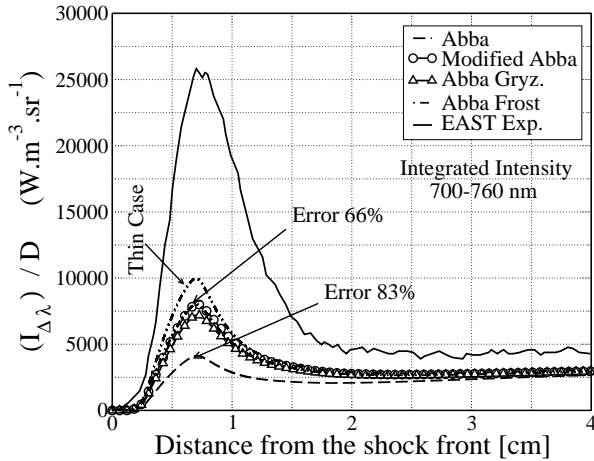


Figure 6.32: Spectral integrated profiles $\Delta\lambda = 700 - 760$: comparison among experimental and simulated radiative intensity profiles.

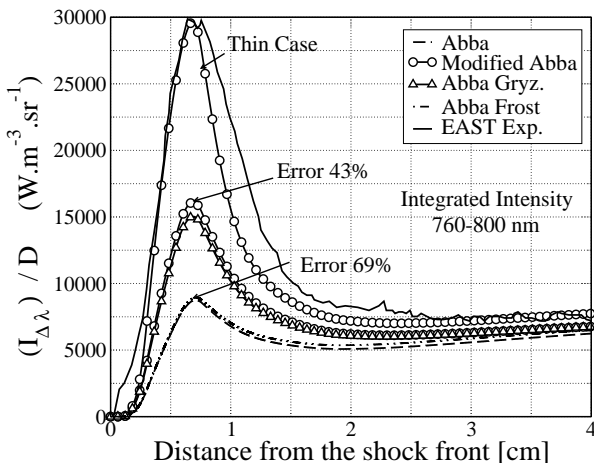


Figure 6.33: Spectral integrated profiles $\Delta\lambda = 760 - 800$: comparison among experimental and simulated radiative intensity profiles.

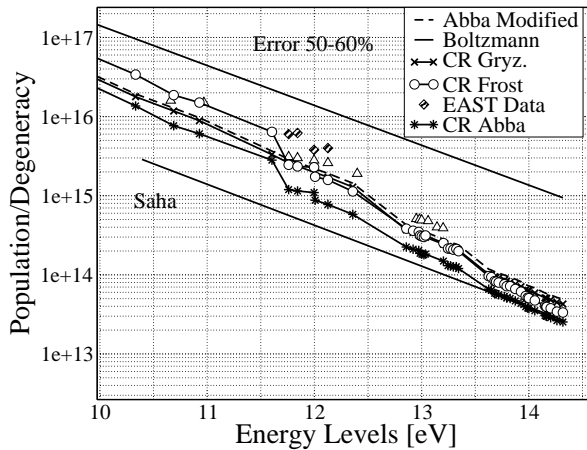


Figure 6.34: Case 3. Normalized population of the electronic states of atomic nitrogen at 0.65 cm from the shock front. Electronic energy level populations [m^{-3}]: CR model ABBA FROST (line with circles), Boltzmann distribution (unbroken line), and Saha distribution (dashed line).

ized population, i.e. the population of the electronic levels divided by the degeneracy of the corresponding level, is depicted as a function of the energy expressed in eV. Figure (6.34) describes the population densities of the electronic states of atomic nitrogen at a distance of 0.65 cm from the shock front and corresponds to the shock condition of Case 3. Figure (6.35) describes the excitation of the atomic nitrogen for the shock conditions of Case 4 and at a location of 1 cm from the shock front. The measurements exhibit a strong depopulation of the excited levels, consistent with the reduced radiative signature of the gas and in good agreement with the numerical predictions. Generally speaking the predicted population densities are underestimated by (50%) for Case 3, whereas the agreement is quite good for Case 4.

As a concluding discussion, the strong influence of the velocity on the radiation, for the low pressure case, is investigated below. For high speed flight conditions, molecules quickly dissociate and radiation is mostly produced by atoms. Atomic radiation depends on the electron density as well as the free-electron temperature (in our case T_V), which are affected by the

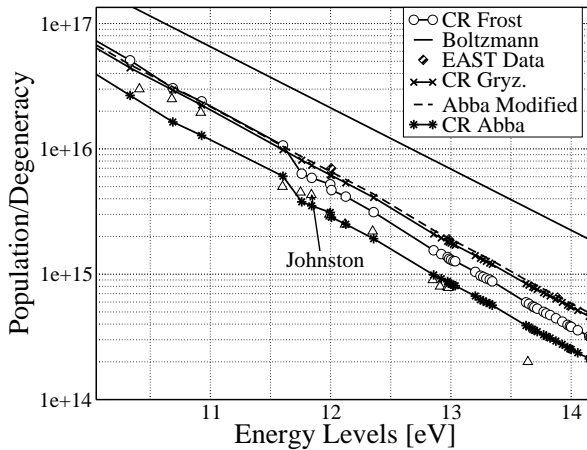


Figure 6.35: Case 4. Normalized population of the electronic states of atomic nitrogen at 1.0 cm from the shock front. Electronic energy level populations [m^{-3}]: CR model ABBA FROST (line with circles), Boltzmann distribution (unbroken line), and Saha distribution (dashed line).

nonequilibrium ionization process [146]. Hence in order to correctly describe the radiation mechanism an accurate description of the ionization process is required.

It is well known [146] that the number of chemical reactions involved in the nonequilibrium ionization processes, occurring in air shock layers, increases with the velocity. At low velocity, the electrons are mainly produced by the associative ionization process, i.e. $\text{N} + \text{O} \rightarrow \text{NO}^+ + \text{e}^-$, since the direct ionization of N and O is forbidden for energy reasons. The efficiency of this process is determined by the decrease in the ionization threshold resulting from the chemical bond energy of the molecular ion [46].

At intermediate velocity (about 8-9 km/s), charge exchange is added to the first process. Let us consider for example the following reaction, $\text{NO}^+ + \text{N} \rightarrow \text{NO} + \text{N}^+$. When the rates for charge exchange are high, a great amount of N^+ is formed, at expenses of NO^+ , formed by associative ionization. NO^+ reacts with N, produced by dissociation of N_2 . In these

conditions, the production of N^+ leads to a decrease of the role of the direct formation of N^+ by electron impact on N, and as a result an increase of the ionization distance can be observed.

For high velocity, the density of the produced electrons becomes sufficient to activate the electronic avalanche through the electron impact ionization $N + e^- \rightarrow N^+ + 2e^-$, leading to the exponential rise of the electron density. It is interesting to note that the impact that this mechanism has on the ionization rate is limited by the loss of the electronic thermal energy during the electron impact ionization process [46, 138, 146]. Indeed a high rate of ionization suppresses the electron thermal energy by this mechanism.

The evolutions of the calculated intensity profiles and electron density, in the velocity range 9-10 km/s, are given in Figures (6.36)-(6.37) respectively, with the MODIFIED ABBA model. The two sets of profiles present similar features: at 9 km/s they are characterized by pronounced peaked shape in the region right after the shock followed by a plateau. Increasing the velocity, it is observed that, the plateau rises much more rapidly than the peak removing the overshoot at about 10 km/s.

Similarities in the evolution of electron density (in Figure (6.37) and population of the excited levels (in Figure (6.25) is justified by the fact that excitation is mainly ruled by the electron-impact processes, owing to the high degree of ionization (excited states are in equilibrium with the free electrons).

This transition from a peaked to a monotonic electron density profile is due to the competition between various processes contributing excitation de-activation of the excited states, mainly occurring because of the inelastic collisions with the free electrons.

The contribution to the net rate of electron production are detailed in Figure (6.36) and Figure (6.37) for 9 km/s and 10 km/s respectively. At 9 km/s, the net rate becomes negative leading consequently to the observed drop of the electron density at about 1 cm, whereas at 10 km/s $\dot{\omega}_e$ it remains positive. For the two cases, the negative value for the associative ionization net rate is due to the importance of the backward reaction, induced by a sufficient chemical depletion of the atomic neutral species N and O.

Increasing the velocity, we observe that this behavior is reduced, and from 9 km/s and 10 km/s the contribution due to the electron-impact ionization increases 5 times whereas the associative ionization contribution is decreased by only 2 times. As a consequence at a certain velocity threshold, where the electron loss by the reverse associative ionization is always compensated the

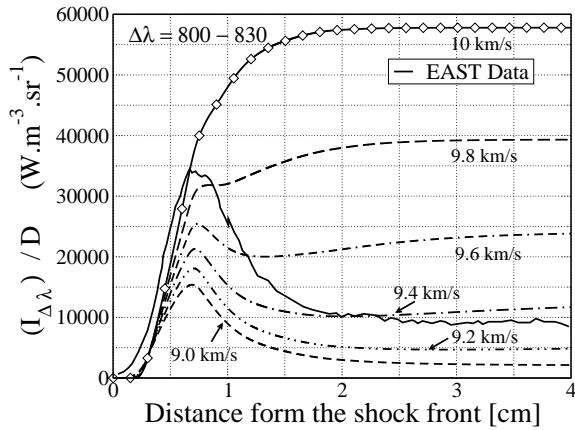


Figure 6.36: Radiative intensity as a function of the shock speed (Ranging from 9 – 10 km/s). Influence of the speed on the radiative intensity profiles.

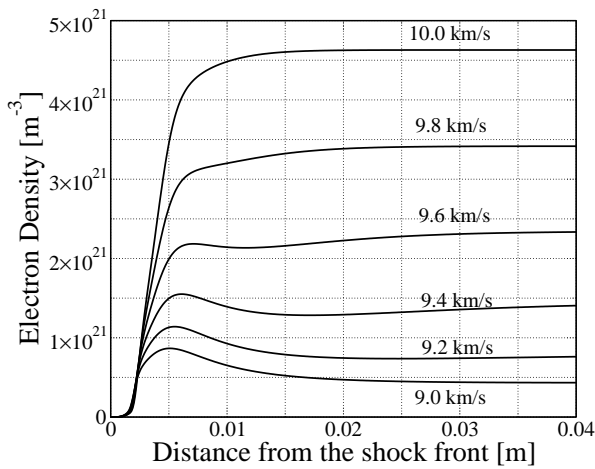


Figure 6.37: Electron density profiles as a function of the shock speed (Ranging from 9 – 10 km/s). Influence of the speed on the radiative intensity profiles.

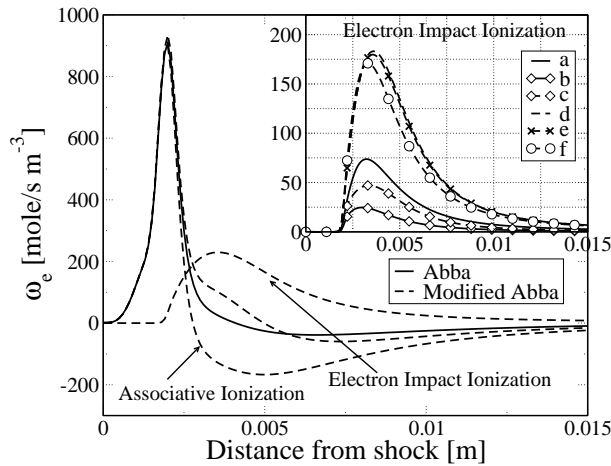


Figure 6.38: Electron production terms 9 km/s. Unbroken lines refer to the ABBA model, whereas dashed lines refer to MODIFIED ABBA Model. Influence of the shock speed on the electron production term [mole /sm⁻³]. Where (a) indicates the contribution given by N for ABBA.(b) indicates the contribution of O for ABBA. (c) Refers to N for MODIFIED ABBA. (d) Refers to O for MODIFIED ABBA. (e) Refers to N for ABBA Gryzinski (f) Refers to N for ABBA FROST.

total net rate remains positive after the shock.

Figures (6.38-6.39) show the influence of the kinetic model on the electron impact ionization process. As shown in the figures the major influence is played by Frost kinetic rates, which affects the production of the electrons due to electron impact ionization (by a factor 4). As a result the electron density is also affected (see Figure 6.25) as well as the radiative intensity profiles.

Conclusions

In this work, we have studied the relaxation of the atomic electronic energy population distributions for one dimensional air flows obtained in a shock-tube. The operating conditions correspond to four test cases taken from the test campaign carried out at NASA Ames. The results have been

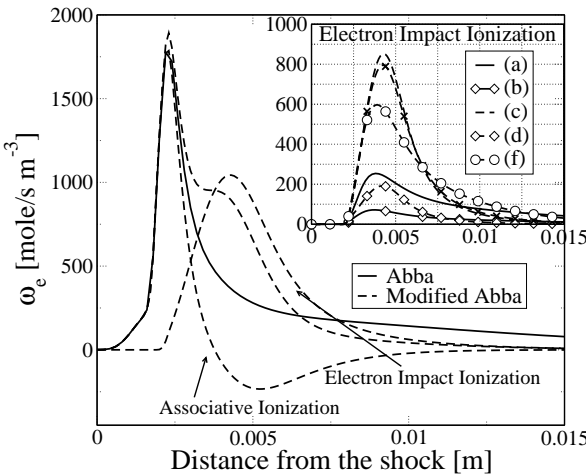


Figure 6.39: Electron production terms 10 km/s. Unbroken lines refer to the ABBA model, whereas dashed lines refer to MODIFIED ABBA Model. Influence of the shock speed on the electron production term [mole /sm⁻³]. Where (a) indicates the contribution given by N for ABBA.(b) indicates the contribution of O for ABBA. (c) Refers to N for MODIFIED ABBA. (d) Refers to O for MODIFIED ABBA. (e) Refers to N for ABBA Gryzinski (f) Refers to N for ABBA FROST.

obtained by means of a multi-temperature fluid model fully coupled with an electronic-specific collisional radiative model. We have compared the radiative intensity profiles with the experimental data of Ref. [92]. We found good agreement for the low pressure run indicated as Case 4 in the manuscript where the flow is in strong nonequilibrium and for the high pressure runs (Case 2 and 3) where the post-shock population density of the excited states follows a Boltzmann distribution.

Differences were found in the results of the comparison for Case 3 where the radiative overshoot is under-predicted by the baseline model tested (ABBA). An alternative set of reaction constants have been proposed for the excitation and ionization of atomic species by electron impact. In particular, the use of the kinetic data compiled by Frost et al. [62] seems to reduce the discrepancies with the experimental data.

Owing to the strong influence of the ionizational nonequilibrium on the radiative properties of the shock layer, we proposed a detailed investigation of the free electron production as a result of three kinetic processes: associative ionization, charge exchange and electron impact ionization. The relative importance of the associative ionization and the electron impact ionization justifies the presence of a maximum in the electron density, which is strongly correlated to the nonequilibrium radiative overshoot described. Also, the influence of the speed on the radiative signature of the gas as well as the free electron production is discussed.

Chapter 7

Collisional radiative model: atoms and molecules

Last chapters describe a simplified version of the ABBA model which allows us to account for nonequilibrium effects in the population of the electronic levels of the atomic species present in air mixture. The present chapter addresses the modeling of the post shock relaxation of atomic and molecular species by means of an electronically specific collisional radiative model.

In the first part of the chapter we discuss the ABBA model for the electronic levels of atoms and molecules. Details concerning mixture, the kinetic and radiative processes involving molecules and the other particles in the flow are discussed in Section 7.1. The modifications to the set of equations to be solved are discussed in Section 7.1.1, together with the additional energy exchange source terms. The second part of the chapter is devoted to the analysis of the behavior of the electronic states of the molecules behind a normal shock. The test conditions are taken from the first point in the trajectory of the FIRE II flight experiment analyzed in Section 6.2.4. A comparison between the ABBA model employed throughout the present analysis and the recently developed Park's model is carried out in Section 7.3.

7.1 Collisional Radiative model: molecules

The population of the electronic levels of the molecules as well as the one of the atoms, may strongly depart from the Boltzmann distribution in the relaxation zone behind a shock. Hence in the course of the present analysis, in analogy with what was done for the atoms, no assumptions are made concerning the electronic distribution functions of molecular species.

Mostly, we restrict ourselves to the analysis of the electronic states below the dissociation limit (of the fundamental states of the molecules), for two

main reasons: firstly the high-lying states are scarcely populated; secondly, and more important, the states above the dissociation limit are likely to be in equilibrium with the associated free states, owing to the large number of states (repulsive and non-repulsive) crossing them [140].

In this study, air is considered as a mixture of N₂, O₂, and their products only. Electronic levels of the atoms are assumed in nonequilibrium as in the previous chapter (§6). Moreover in order to investigate the departures from the equilibrium of the excited states of the molecules, each of their levels is considered as an additional species whose composition is governed by finite rate chemistry. The complete list of species and pseudo-species of the mixture accounts for:

- Neutral species: N₂(1 – 4), O₂(1 – 5), NO(1 – 5), N(1 – 46), and O(1 – 40),
- Charged species: N₂⁺(1 – 4), O₂⁺(1 – 4), NO⁺(1 – 5), N⁺, O⁺, and e⁻.

Forty-six levels for N and 40 levels for O are taken into account as well as a total number of 27 levels for the diatomic species. Coupling of these levels through the different elementary processes (see Sections 6.1.2 and 7.1.0.4) allows the explicit determination of the plasma excitation and its radiative signature without any equilibrium assumption. A list of the electronic levels for molecules and molecular ions is given in Table (7.1). The overall number of species reads 116.

Table 7.1: Species Considered in the present CR model.

Type	Species	State
Molecules	N ₂	X ¹ Σ _g ⁺ , A ³ Σ _u ⁺ , B ³ Π _g , C ³ Π _u
	O ₂	X ³ Σ _g ⁻ , a ¹ Δ _g , b ¹ Σ _g ⁺ , A ³ Σ _u ⁺ , B ³ Σ _u ⁻
	NO	X ² Π, A ² Σ ⁺ , B ² Π, C ² Π, B' ³ Δ
Molecular ions	N ₂ ⁺	X ² Σ _g ⁺ , A ² Π _u , B ² Σ _u ⁺ , C ² Σ _u ⁺
	O ₂ ⁺	X ² Π _g , a ⁴ Π _u , A ² Π _u , b ⁴ Σ _g ⁻
	NO ⁺	X ¹ Σ ⁺ , a ³ Σ ⁺ , b ³ Π, b ³ Σ ⁻ , A ¹ Π

7.1.0.4 Elementary processes: Molecules

The present section addresses the modeling of the kinetic elementary processes due to interaction with electrons and heavy particles, briefly intro-

duced in Section 6.1.2.

As we could appreciate already when discussing the thermodynamic properties of the diatoms, the molecules have a more complicated internal structure than the atoms and, besides electronic levels, they exhibit a ro-vibrational structure that further complicates the modeling of thermodynamics, kinetic and radiative properties.

If we analyze the electron induced processes as they occur among the atoms, we realize that the cross sections of the elementary process depends only on the threshold energy (given by the difference among the two electronic states) and the kinetic energy of the free electron. Thus, for atoms (Section 6.1.2) although the cross section may depend on the possibility of an optical transition among the two excited state, the threshold is well determined and the reaction rates can be easily obtained, if the electron energy distribution is known (it is assumed Maxwellian in this work).

Although the same conclusions hold for excitation/ionization processes among the rovibronic states of the molecular species, i.e. for transitions from the rovibronic state $E_{(i)}(e_1, v_1, J_1)$ to the rovibronic state $E_{(j)}(e_2, v_2, J_2)$, when averaging over the rovibrational levels, the resulting rate depends on the rotational and vibrational temperature.

In other words, in order to use our electronically specific CR model, we need to define rate constants applicable to transitions from molecules characterized by electronic energy $E_e(e_1)$ and generic ro-vibrational energies to molecules having electronic energy $E_e(e_2)$ and whatever rotational and vibrational energy. In this case the threshold energy is not precisely known and it is function of the rovibrational excitation of the molecule in the lower state, thus depending on the rotational and translational temperature [3].

The rate coefficients for excitation, ionization and dissociation of molecular species by electron impact recently calculated by Teulet [170] are used in the present work. Teulet estimated the inelastic rate constants using the method developed by Bacri and Medani (weighted total cross section, WTCS) in Ref. [3–5]. Some modifications were introduced to account for the pre-dissociation of some electronic states of O₂ and NO in the estimation of the dissociation rate coefficients, as suggested by Sarrette [159].

Following the WTCS method, the final expression of the global cross section, for excitation/ionization, from the electronic state E_{e1} to the electronic

state E_{e2} , can be written as

$$\sigma_{e_{e2}}^{e_{e1}} = Q_{INT}^{-1} \sum_{v_1}^{V_{Max}^{(e_1)}} \exp\left(-\frac{\epsilon_v^{(e_1, v_1)}}{k_B T_e}\right) \sum_{J_1}^{J_{Max}^{(e_1, v_1)}} (2J_1 + 1) \exp\left(-\frac{\epsilon_J(e_1, v_1, J_1)}{k_B T_T}\right) \\ \times \sum_{v_2}^{v_{Max}^{(e_2)}} \sum_{J_2}^{J_{Max}^{(e_2, v_2)}} \delta(J_2 - J_1 \pm 2) \int_0^\infty P_{v1}(r) \sigma_{e_1, v_1, J_1}^{e_2, v_2, J_2}(r, \epsilon) \quad (7.1)$$

where δ is the Kronecker symbol and it was introduced in the calculations to respect the selection rules, that limit the transitions among the rotational levels. Indeed given the weak mass of the electrons, the changes in the rotational quantum number is assumed to be limited to ± 2 [140]. The symbol $P_{v1}(r)$ accounts for the radial probability and it is estimated using the harmonic oscillator model. The rovibronic elementary cross section is indicated $\sigma_{e_1, v_1, J_1}^{e_2, v_2, J_2}$ and is estimated using the approximate formulas of Drawin, described in Section 6.1.2.1. The symbol Q_{INT} is the "partial" internal partition function and can be written as

$$Q_{INT} = \sum_{v_1}^{v_{Max}^{(e_1)}} \exp\left(-\frac{\epsilon_v(e_1, v_1)}{k_B T_e}\right) \sum_{J_1}^{J_{Max}^{(e_1, v_1)}} (2J_1 + 1) \exp\left(-\frac{\epsilon_J(e_1, v_1, J_1)}{k_B T_T}\right) \quad (7.2)$$

The method is very similar to the one developed by Park in Ref. [143]. The main difference is the treatment of the radial dependence of the elementary cross section: while Teulet calculated it for each rotational transition and Park uses the Franck Condon factors [140].

The equation 7.1 is written assuming thermal equilibrium among vibration and free-electron energy and among translational temperature (heavy particles) and rotation. However, noticing a weak dependence of the rate constants on the rotational temperature, the final set of rates for excitation/ionization by electron impact was assumed to depend only on the free electron temperature, i.e. T in the equation 7.1 was replaced by T_e .

Sensitivity analysis: N₂ excitation

The rates estimated by Teulet with the WTCS are compared with other kinetic data available in literature. Huo's calculations [88] relies on the same hypotheses made by Park: firstly the Frank-Condon factors were used to account for the radial dependence of the cross section; secondly the electronic transitions are subject to a weak change in the rotational quantum number. The main difference comes from the use of quantum mechanics for the estimation of the cross-sections $\sigma_{e_1, v_1, J_1}^{e_2, v_2, J_2}$. Figure 7.1, shows that, for N₂ excitation from the X to the C state, Teulet's predictions underestimate the rates given by Huo by one order of magnitude, which is a reasonable agreement. Furthermore, Teulet's predictions are between Huo's and Losev's rates for this transition as well as for the transition from the ground to the B state N₂(X → B) (not shown in figure).

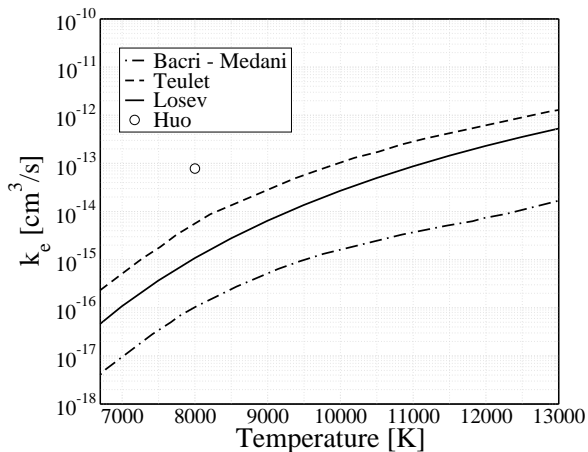


Figure 7.1: N₂. Rate constant for excitation from X to C comparison: (○) Huo [88]; (dashed curve) Teulet's results; (unbroken line) Losev rate and (dash-dotted line) Bacri [5]. Such transition is not included in Park model [140].

Sensitivity analysis: N_2^+ excitation

Figure 7.2 shows the rate constants for the excitation of the ground state of N_2^+ to the (B) state. The radiative transition from this state to the ground state gives origin to the N_2^+ first negative system, which is a major contributor to the molecular component of the radiative heat-flux for high speed earth entries. Hence knowing that the *B* state is mainly populated by collisional processes $\text{X} \rightarrow \text{B}$ (ref. [93]), the accurate estimation of such transition becomes very important.

However, large differences among the predictions from different sources, are shown in Figure 7.2: Park's model [140] yields the larger rate for this transition, overestimating Teulet's prediction by a factor 10. Gorelov [73] rates are many order of magnitude lower, as opposed to the model used by Johnston which is in the middle among all these predictions.

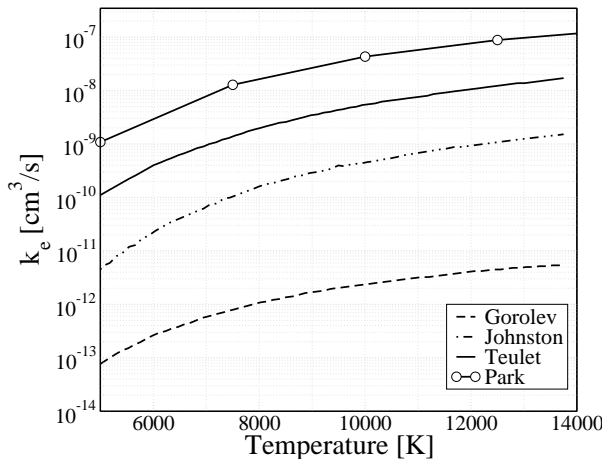


Figure 7.2: N_2^+ . Rate constant for excitation from X to B comparison: Park's model [140] (\circ); Teulet's results (unbroken line); (dashed-dotted) curve Johnston and the dashed line Gorelov.

The large uncertainty on the rate constants suggests the need for more accurate data, based on experiments or more accurate quantum calculations. In the following analysis, a sensitivity study of the influence of the results

of the model chosen for this transition is performed. As we shall see the use of Teulet's rate constant as opposed to the one used by Gorelov (in [73]) leads to a difference of one order of magnitude on the population of the B state of N_2^+ , putting forward the importance of such transition.

The cross section for excitation of molecules under molecular or atomic impact behaves approximately as Lotz[110] therefore this form has been adopted, except in the case when experimental data exist. We have then chosen the rate coefficients compiled by Capitelli[35] and Kossyi[98]. Due to the pressure levels involved in our CR model (which can be employed at high pressure), we have also taken into account the previous processes occurring when a third particle interacts.

Furthermore the kinetic mechanism comprises:

- Dissociation of N_2 , O_2 , and NO by atomic or molecular impact / recombination,
- Dissociation of N_2 by electron impact / recombination,
- Associative ionization / dissociative recombination,
- Radical reactions (including Zel'dovitch reactions),
- Charge exchange.

The model selected for such reactions have been already discussed in Section 6.2.2.1, when describing the simplified ABBA model. The only difference is the treatment of the dissociation and in particular the effects that vibration has on the dissociation rate. Indeed while the foregoing model was completely based on the Park's TT_V model, in the present analysis, we investigate the sensitivity of the model used to couple chemistry and vibration.

We use three different mathematical formulations to correctly describe the influence of the vibration on the dissociation of the molecular species and at the same time account for the influence of the chemistry on the vibrational energy:

- *Park $T - T_V$ model* [138] is the most widely spread and used in the aerospace community due mainly to its simplicity. The geometrical average ($\sqrt{TT_V}$) is used to express the dependence of the rate constant on the vibration, using the modified Arrhenius law. The nature of the

model is purely heuristic and based on the analysis of experimental data coming from the study of the post-shock radiative signature in shock tube facilities. For this model we do not use any preferential dissociation model.

- *Macheret-Fridman model* [111] is based on the corrected forced harmonic oscillator (FHO) approach. The FHO model was successfully applied and culminated in an analytical (or semi-analytical) theory [1, 46, 112]. Such a model with no adjustable parameters produced thermal (equilibrium) dissociation rates in fair agreement with experimental data.
- *Treanor-Marrone model* [116] is based on simple physical concepts firstly introduced by Hammerling [81]. The innovation of the model lies in the introduction of an ad-hoc parameter to change the value of the probability of dissociation among the different energy levels. This results in an increasing dissociation probability with the vibrational level number.

The foregoing models were extensively discussed in Chapter 4.

7.1.0.5 Radiative processes

Atomic coefficients for the atomic line radiation were taken from the NIST database Ref. [117] and are given in appendix in Table A.2. In total, we take into account 45 spontaneous emission lines for N and 24 lines for O to which we add the radiative and dielectronic recombination processes, neglected in the foregoing analysis, and now accounted for. The rate constants for such processes have been taken by Bourdon et al in Ref. [22, 23]. All the details are given in section 6.1.2.4.

As far as the molecules are concerned, some states of species mentioned in Table 7.1 radiate strongly. The β ($B^2\Pi \rightarrow X^2\Pi$) and γ ($A^2\Sigma^+ \rightarrow X^2\Pi$) systems of NO as well as the first positive ($B^3\Pi_g \rightarrow A^3\Sigma_u^+$) and the second positive ($C^3\Pi_u \rightarrow B^3\Pi_g$) systems of N_2 and the first negative system ($B^3\Sigma_u^+ \rightarrow X^2\Sigma_g^+$) of N_2^+ have been considered. Since vibrational equilibrium is assumed for these species the equivalent transition probability for the latter systems is calculated fitting the data calculated by Laux and Kruger[105].

7.1.1 Shock-Tube flow solver

The set of equations in SHOCKING code was modified to account for the non-Boltzmann treatment of the electronic levels of the molecules 6.15.

Firstly, a new set of species conservation equations was added to model the evolution of the excited states of the molecules, governed by their own kinetics. Hence the resulting set of equations to be solved accounts for 116 continuity equations, as opposed to 95 continuity equations for the atomic CR model.

Secondly the separate equation for the free-electron energy (see Section 6.15) was dropped. Hence the relaxation of the electronic energy of the atomic ions N⁺ and O⁺ (assumed to be governed by Boltzmann distribution) and the free electron energy are assumed to be in thermal equilibrium with T_{vN_2} (see equation 6.22).

REMARK. In principle, the use of a separate equation for the free-electron energy is not consistent with the model used to derive macroscopic cross-sections governing the inelastic processes involving electrons. In fact the derivation of those rates was based on the assumption of thermal equilibrium between vibration and free-electron energy. Therefore we substitute the vibrational energy conservation equation of N₂, used in the system of equation (6.15) with equation Section 6.22.

7.1.1.1 Energy relaxation terms: radiative mechanisms

The energy exchange terms have been extensively discussed in the first part of the manuscript. However the introduction of radiative and dielectronic recombination requires to account for energy loss in the free electron energy which is converted in radiation.

Radiative losses are modeled by means of the Q^{Rad} term in the energy equation. This term represents the radiant power emitted per unit volume and is directly given by the expressions

$$Q_I^{Rad} = \sum_{\substack{i,j \in \mathcal{N} \\ j < i}} \alpha_{ij} (E_i - E_j) \mathcal{A}_{ij} N_i + \sum_{\substack{i,j \in \mathcal{O} \\ j < i}} \alpha_{ij} (E_i - E_j) \mathcal{A}_{ij} N_i \quad (7.3)$$

where \mathcal{A}_{ij} is the Einstein coefficient, N_i , the number density of the excited state, and α , the escape factor.

Radiative losses due to radiative recombination and dielectronic recombination reactions are accounted for in approximate manner by the expression

$$\begin{aligned} Q_{II}^{Rad} = & \sum_{j \in \mathcal{N}} (\mathcal{I}_N - E_j) n_e N^+ (\alpha_j^{RR} \kappa_j^{RR} + \alpha_j^{RD} \kappa_j^{RD}) \\ & + \sum_{j \in \mathcal{O}} (\mathcal{I}_O - E_j) n_e O^+ (\alpha_j^{RR} \kappa_j^{RR} + \alpha_j^{RD} \kappa_j^{RD}) \end{aligned} \quad (7.4)$$

This term is to be added to the vibrational energy conservation of N_2 which accounts for free-electron energy conservation.

Following the derivation of Thivet [173], the conservative system of Eqs. (6.15)-(6.19) is transformed into a system of ordinary differential equations easily solved by means of the LSODE [153] library.

7.2 Results

The objective of the present investigation is the characterization of the physico-chemical properties of the weakly ionized air plasma in the shock layer of a re-entry vehicle. The investigation is carried out studying the evolution of temperature and concentration profiles of the different species in the shock layer, focusing our attention on the behavior of the electronically excited states of atoms and molecules. We chose to analyze the point at 1634 second in the re-entry trajectory of the FIRE II flight experiment, extensively discussed in Section 6.2.4. The 1634 point (see Table 6.2), belongs to the early part of the trajectory of the FIRE capsule. Under these flight conditions the relatively low pressure (only few pascals) and the high flow speed drive the flow out of equilibrium.

The analysis of the shock-layer in the same test conditions was conducted in Section 6.2.4 assuming that the electronic levels of the molecules are populated according to the Boltzmann distribution and treating the electronic states of the atoms as pseudo-species. In this chapter, using the complete CR model (atomic and molecular specific), we address the validity of the foregoing assumption, investigating the behavior of the excited states of atoms and molecules. The treatment of the electronic states of the molecules, considered as pseudo-species, allows us a more detailed description the kinetic

and radiative processes occurring in the plasma. The Boltzmann distribution is, in this case, a result of the detailed kinetic processes of the excited states. Indeed the equilibrium among the excited states of the molecules is achieved if the characteristic time of the flow is much smaller than the characteristic time of the elementary processes.

Recently Park, in Ref. [89, 140, 141], proposed an accurate review of literature on the kinetic mechanisms involving the electronic states of the molecules for air plasmas. The model was compiled and included in the Spradian code [140] and it is freely distributed on demand. It is important to note that currently, some of the reaction rate constants are uncertain by several orders of magnitude. Hence a comparison of our predictions with the results obtained using Park's model gives an idea of the sensitivity of the electronic energy distribution function on the model used for the flow conditions studied.

The third and last part of this contribution is devoted to an analysis of different physical phenomenon occurring in the gas after a strong normal shock. We begin the investigation addressing the modeling of the dissociation and the influence that the model used to couple vibration and dissociation has on the temperature field and on the concentration profiles. Particular attention is devoted to the electron density evolution which governs the excitation processes of atoms and molecules.

Also, we investigate the influence of the precursor ionization on the electronic energy distribution function of the atoms and we compare the production of the electrons due to this phenomena with the production of the *prime electrons* due to the interaction with heavy species. The sensitivity of the results to the optical thickness is also addressed varying the escape factors from 0 to 1.

7.2.1 Flowfield results: comparison with atomic CR model

The analysis begins with the discussion of the temperature and composition profiles in the post-shock relaxation area, obtained using the electronically specific CR model coupled with the Park's model for dissociation and the non preferential model of Candler for the vibration-dissociation coupling. In particular in this section we propose a comparison of the results obtained with the ABBA model described in Section 6.2.4 (referred to as *atomic CR model* in the following) and the model described in the present chapter (referred in the following as *molecular CR model*).

Figure (7.3) shows the evolution of the temperature profiles obtained with the molecular CR model. If we compare the profiles with the ones obtained with the atomic CR model in Fig. 6.8, we observe some differences in terms of relaxation of the ro-translational temperature, being the thermal relaxation longer in this case. Such differences are, at least in part due to the use of Park's correction to the Landau Teller formula applied in the molecular CR model. Better is the agreement with the Johnston's results, being the vibrational relaxation slower, thermal equilibrium is reached only at 2 cm from the shock front and the vibrational temperatures do not overshoot the translational one. We remind the reader that the overshoot in the results obtained with the atomic CR model is due to the absence of the preferential dissociation model for the coupling chemistry-vibration and the use of the Landau Teller formula without Park's correction. Figures (7.4-7.5) compare

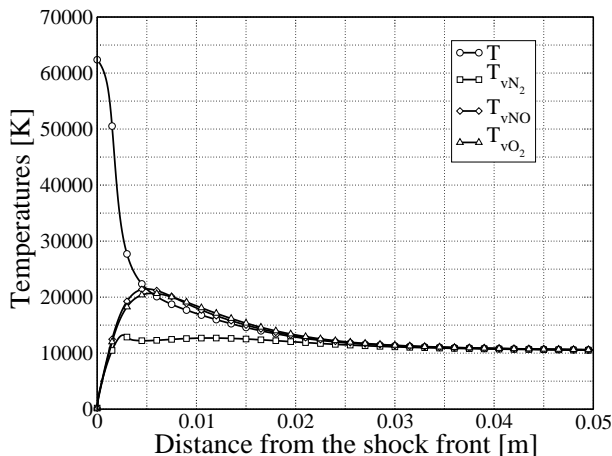


Figure 7.3: Temperature profiles: CR model molecules

species evolution in the post shock area for the CR model for all the species (7.4) and only for atoms (7.5). Strong differences are found in the relaxation of the N_2^+ . The atomic specific CR model predicts a slow relaxation to the equilibrium values as opposed to the detailed ABBA model which exhibits an overshoot right after the shock. The reason of the disagreement is certainly due to the differences in the kinetic mechanism used for the reaction rate

constants. An accurate analysis of the experimental results [66] shows an overshoot in the radiation from the $\text{N}_2^+(1-)$ system and suggests a presence of an overshoot in the N_2^+ population consistent with the results given by the more accurate model. A deeper investigation of the problem is required before driving any conclusion however results from literature [93] also confirm the presence of an overshoot in the population of the excited states after the shock.

The concentration of N_2 is found to be slightly different in the two cases under analysis. The reasons of such discrepancies are due to the differences in the vibrational temperature of N_2 and a different rate constant for the electron impact dissociation. The atomic CR model uses the electron impact dissociation rate proposed by Park which is larger than the value proposed in the ABBA model. Moreover the vibrational temperature of N_2 is also lower in the latter case. The behavior of the remaining species is found to be qualitatively similar although the delay in the relaxation can affect the concentration of the different species.

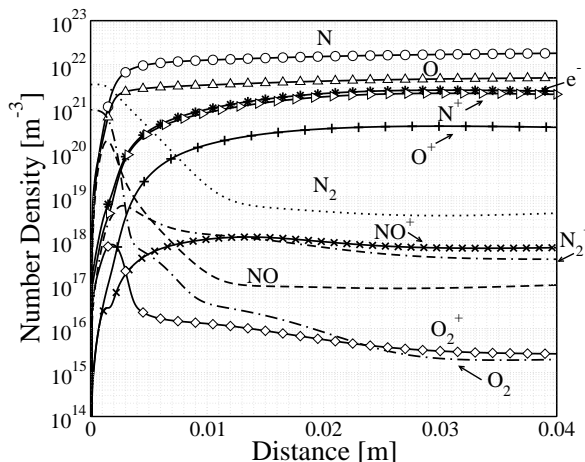


Figure 7.4: 1634 s case. Population profiles obtained with the CR molecules for all species.

No significant differences have been found in the electronic population

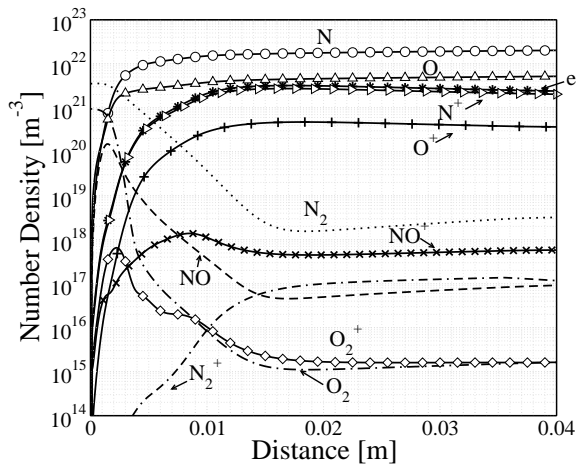


Figure 7.5: 1634 s case. Population profiles obtained with the CR model for the atoms.

distributions of atomic nitrogen and oxygen.

7.2.2 Results: molecules

In this section, the evolution of the composition of the molecular species through the shock layer is presented. Particular attention is given to N_2^+ and N_2 since they contribute to the nonequilibrium radiative signature of the gas under high speed re-entry conditions. The contributions from the NO and O_2 bands are limited, since at these high temperatures they are found almost completely dissociated.

N_2^+ Population

The determination of the N_2^+ composition is important, since it is a strong radiator in the UV part of the spectrum. Its radiative contribution, due to the bound transitions from the N_2^+ ($B^2\Sigma_u^+$) to the N_2^+ ($X^2\Sigma_g^+$), is relevant at speed up to 10 km/s .

Figure (7.6) shows the population profiles of the ground and excited states, comparing them with the equilibrium values for each point of the shock layer. All the levels of the molecule are found to be in equilibrium, con-

firmering the prediction of Ref. [93]. The population of the $B^2\Sigma_u^+$ state is governed by the transitions to and from the ground state due to electron impact. In this work we use the rate constant proposed by Teulet [171],

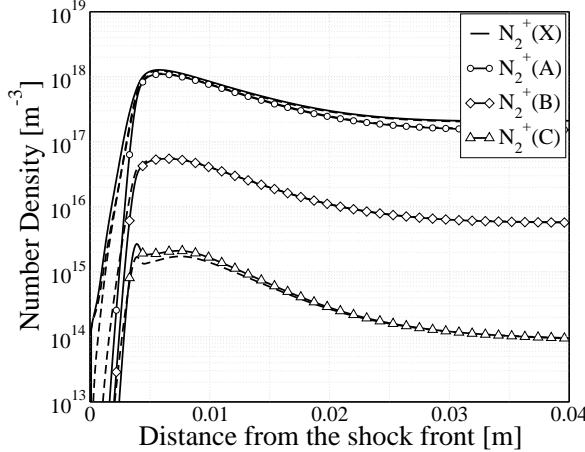


Figure 7.6: 1634 s case. Population profiles of N_2^+ molecules. Dashed lines represent the equilibrium values; unbroken lines correspond to the CR results.

which gives an high value for the kinetic rate compared with other models available in literature (see 7.2). Thus in order to assess the influence to the kinetic model, we decided to replace Teulet's rates with those compiled by Gorelov in Ref. [73]. This model was chosen owing to its underestimation of the rate constants compared to other compilations of rates available in literature [124, 126]. This allows us to draw some bounds in the evolution of the electronic state population of the molecular ion. A comparison of the results obtained with the two models is shown in Figure 7.7. The predictions of the population of the excited states differ significantly and since the results with Teulet's model were found in Boltzmann equilibrium, we can conclude that the Gorelov's model predicts strong departures from equilibrium.

The calculations presented assume that the molecular radiation is optically thin, which means that the radiative transitions have their maximum influence on the depleting processes of the radiating levels. However, the analysis of the results assuming an optically thick medium, does not change

the conclusions concerning the departures of the populations from Boltzmann equilibrium.

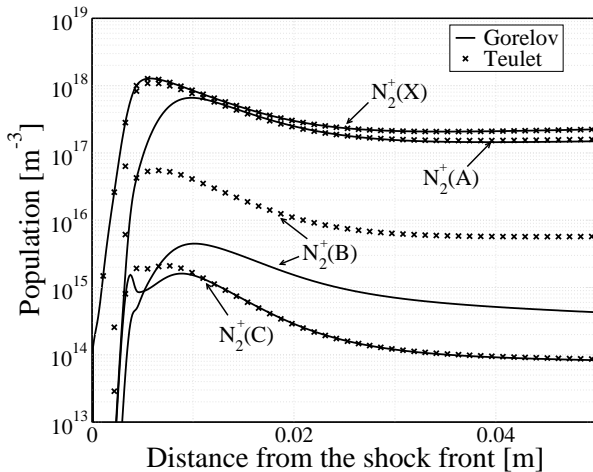


Figure 7.7: Composition evolution of N_2^+ . (Dashed lines) results with Teulet's rates; (unbroken lines) CR results with Gorelov's rates.

It is interesting to note that the $\text{B}^2\Sigma_u^+$ can be formed also through a process known as inverse pre-dissociation [138]. There are indeed several repulsive potentials passing through the B state. In this analysis however, we have found that inverse pre-dissociation is of secondary importance for the population of the $\text{B}^2\Sigma_u^+$ state, being the excitation by electron impact dominant.

N_2 Population

Figure 7.8 compares the equilibrium population of the N_2 molecules versus the nonequilibrium calculation given by the CR model. The $\text{N}_2(\text{A})$ and $\text{N}_2(\text{B})$ states, which are closely spaced in energy, are shown to have similar Boltzmann and non-Boltzmann distributions throughout the shock layer. Departures from the equilibrium distribution are located close to the shock front, where the equilibrium calculations exhibit a sharper peak respect to the non Boltzmann predictions.

Figure 7.9 shows a comparison among the predictions done using the ABBA

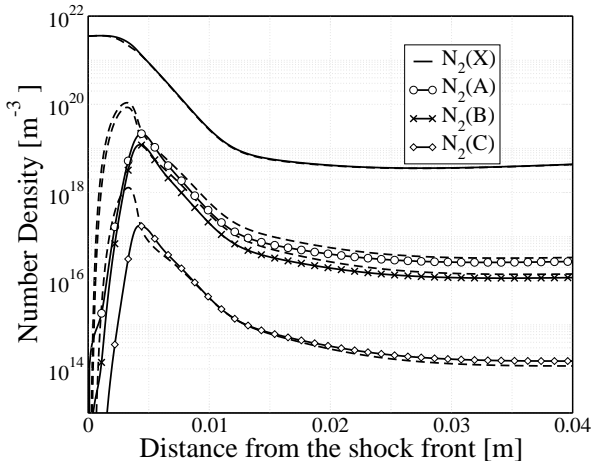


Figure 7.8: 1634 s case. Population profiles of N_2 molecules. Dashed lines represent the equilibrium values; unbroken lines with symbols correspond to the CR results.

model, which rely on the reaction rates of Teulet and the model of Losiev shown in Fig. 7.1. Although the use of the latter model enhances the nonequilibrium effects in the post shock region, the differences are rather small.

NO Population

The number densities for NO obtained with the CR model are presented and compared with the Boltzmann results, in Figure 7.10. Large deviations from a Boltzmann distribution are present for the excited states right after the shock, similarly to the behavior obtained N_2 . The CR model predicts a much lower number density, which implies that the radiative emission is reduced proportionately. NO^+ formed by associative ionization of N and O atoms is found to be very close to equilibrium conditions throughout the shock layer and it is not shown here.

The present analysis puts forward the need for a non-Boltzmann treatment of the N_2 , NO molecules as opposed to the NO^+ , which is found to be close

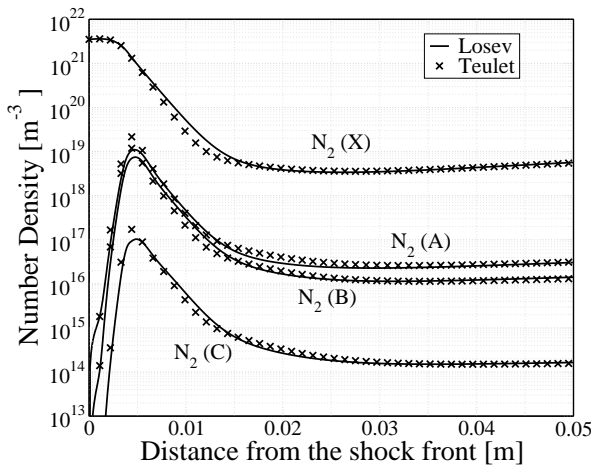


Figure 7.9: N_2 population profiles. (Dashed lines) results with Teulet's rates; unbroken lines the CR results with Losev's rates.

to equilibrium conditions and does not require a state specific treatment of the electronically excited states. The predictions of the population of the electronic states of N_2^+ is more complicated because of the sensitivity of the population to the rates used to model electron impact excitation. We have tested two sets of rates, very different from each other: the set proposed by Teulet and the set compiled used by Gorelov. The two models proposed exhibit rate constants which differ by at least three orders of magnitude. Hence the analysis (even if it is not conclusive) allows us to set some limits to the population of the B state of N_2^+ . Thus we can argue that the population of this state is at most a factor ten lower than the equilibrium values.

7.2.3 Dissociation of the excited states of O_2

The analysis of the population profiles of the molecular oxygen revealed a strong overpopulation of the upper excited states. In some cases the population of such levels exceeds the population of the fundamental state. The reason for such behavior is the lack of a mechanism for the dissociation of the upper state in the ABBA model. Hence the excited molecules are trapped in these states and they can only be depleted by collisional and radiative de-activation processes.

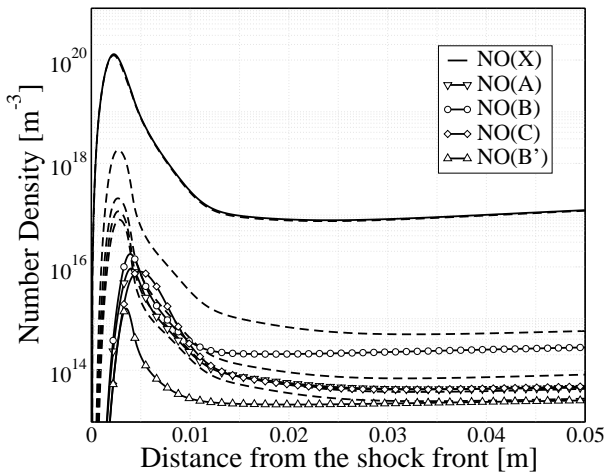


Figure 7.10: Population profiles of NO molecules. Dashed lines are the equilibrium values; unbroken lines the CR results.

In order to investigate the sensitivity of the results to this process, we extend the validity of the dissociation rates used for the ground states to the excited states. By doing so, we underestimate the influence of dissociation processes of the excited states, being the potential well deeper in case of the fundamental state. Figure (7.11) shows the influence of the dissociation on the population of the excited states. Unbroken lines refer to the base line model which does not account for dissociation processes, whereas broken lines refer to the calculation performed assuming that the dissociation rate is the same as the fundamental state. The dissociation processes drastically reduce the population of the $O_2(A)$ and $O_2(B)$ which in the baseline calculation are more populated than the fundamental and the low excited states.

7.3 Park's model

Hereafter we present a comparison among the ABBA model previously described and the model recently developed by Park and described in Ref. [89, 140, 141]. Besides the differences in the model used for the molecular and

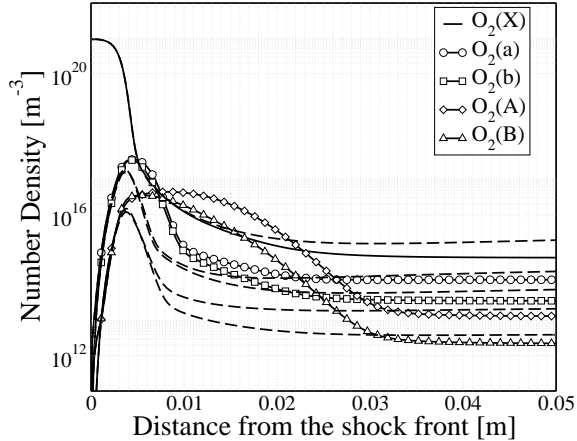


Figure 7.11: 1634 s case. Population profiles of O_2 molecules: (unbroken lines) baseline CR model; (dashed lines) dissociation rates of $O_2(X)$ are used for the excited states.

atomic elementary processes, the two CR models differ in the way they deal with the time integration. Park's model, as it is implemented in the Spradian code, assumes that the QSS condition is reached for the excited states and solves a nonlinear algebraic set of equations. Different is also the coupling with the flow, we propose a fully coupled approach as opposed to the Spradian code which is used in post-processing, totally decoupled from the flowfield calculation. Influences of such assumptions on the results have been thoroughly described in Ref. [136].

7.3.1 Atomic and molecular population distributions: comparison against Park 2008

We now present a comparison of our results with the ones obtained with Park's model in terms of electronic energy distribution of atoms and molecules. Flowfield quantities such as temperatures and composition of the different species, obtained summing the concentrations of all the electronic states, are extracted from the ABBA calculations and fed as input into the Spradian code. The nonequilibrium capabilities of the code are used to predict the

nonequilibrium population of the excited states of the molecules and atoms. The calculations with the ABBA model are carried out under the assumption of optically thin medium, i.e. all escape factors are assumed to be equal to the unity. A sensitivity analysis of the results to such assumption is carried out later on in Section 7.3.2.2.

Figure (7.12) shows the electronic level population of nitrogen atoms at 1 cm from the shock front. It is found that Boltzmann distribution, represented by the unbroken line in the figure, leads to an overestimation of the population of the high-lying excited states up to three orders of magnitude according to our predictions. The same type of depopulation of the excited states is predicted by Park's model even if the populations of the upper levels ($E > 10$ eV) are about one order of magnitude larger. The populations of the ground state ($N(^4S)$), and the two metastable states ($N(^2D)$ and $N(^2P)$) are found to be in Boltzmann equilibrium for the two models.

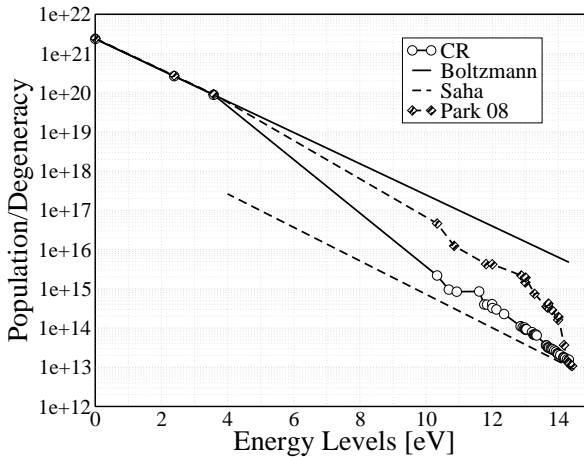


Figure 7.12: Saha diagrams for the excited states of the atomic nitrogen. Park's model (\diamond); ABBA model ($\alpha = 0$) (\circ); unbroken line: Boltzmann equilibrium; broken line: Saha equilibrium.

The perturbation of the electronic energy distribution function is confirmed by an analysis of the radiative heat flux measurements performed

during the re-entry. The values of the heat flux were found to be much lower than the predictions [138, 144] made before flight. Such predictions were based on the assumption of Boltzmann distribution for the populations of excited states. When departures from Boltzmann equilibrium are accounted for, excellent agreement with the experimental values is found [93]. Indeed the strong depopulation of the excited states (Figure 7.12) drastically influences the radiative signature of the gas which is dominated by atomic line radiation at these flight conditions.

As the vehicle approaches the lower parts of the atmosphere the pressure rises and the importance of the collision processes with respect to the radiative processes becomes larger and larger. In fact the collisional processes scale with p^2 as opposed to the radiative effects which scale with p , then in the lower parts of the atmosphere, the distributions are found to be Boltzmann as shown in Ref. [136].

N_2^+ and N_2 : comparison of population distributions

An accurate comparison in terms of population of excited states between Park and ABBA model is shown in Figures 7.13-7.14 for the molecular species. For N_2^+ the two models are in good agreement and predict equilibrium distributions for the excited states. Conversely, Figure 7.13 shows discrepancies between both models for the concentration of the excited species of the N_2 molecules. Park's model predicts a sharp overshoot of the population of the excited levels approaching the equilibrium values, while our results show a smoother relaxation towards the equilibrium region.

7.3.2 Detailed physico-chemical analysis

In this part, we analyze the influence of the modeling of dissociation, radiation and ionization on the distribution function of atomic nitrogen. All these effects are believed to affect the physico-chemical properties of the plasma in the shock layer. Hence in this section we try to have a quantitative idea (when possible) of their effective influence on the electronic excitation of the atoms.

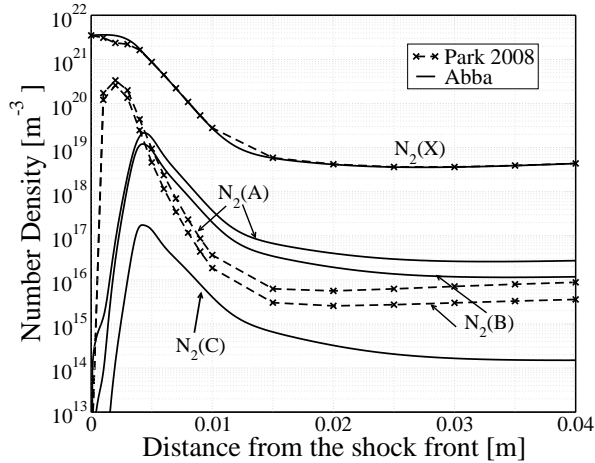


Figure 7.13: Population profiles of N_2 molecules comparison:(\times) Park; unbroken lines ABBA.

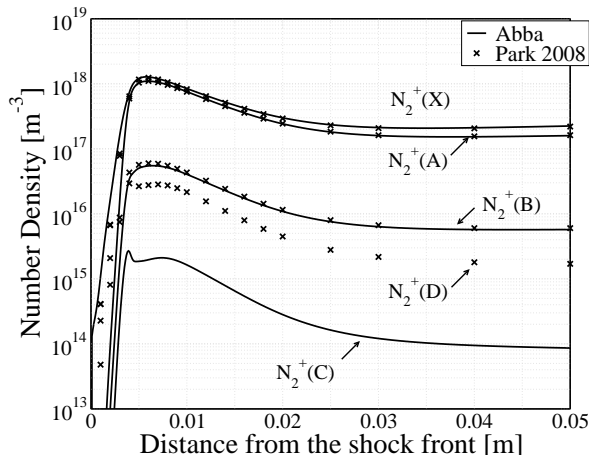


Figure 7.14: Population profiles of N_2^+ molecules comparison:(\times) Park's model; unbroken lines ABBA.

7.3.2.1 Influence of the dissociation model on the results

The mechanism of production of free electrons is governed by the associative ionization reaction and in a lesser extent by the direct ionization of the atomic species. Both these two processes depend on the dissociation that creates the atomic species needed for this reactions to occur. We therefore propose a sensitivity analysis of the results to the model used to describe the dissociation and in particular its coupling with vibration.

Figures 7.15- 7.16 shows a direct comparison of the evolution of the temperatures in the post-shock region for Macheret and Treanor model. The behavior of the temperatures through the shock layer is very similar and they both strongly differ from the predictions obtained by means of the Park's model. The main difference lies in the absence of the overshoot in the NO and O₂ vibrational temperatures. The reason of such a difference is to be sought in the vibration-dissociation coupling, which in the Treanor or Macheret model is based on the preferential dissociation assumption as opposed to the baseline model, which uses a non-preferential model. Thus, by allowing the molecules to dissociate at the higher vibrational levels, the energy removal due to dissociation processes, exceeding the average vibrational energy, tends to lower the post-shock vibrational temperatures. In other words the Ω^{CV} source term in the preferential dissociation models is higher than the corresponding source term in the non-preferential dissociation model (see Chapter 4).

The differences in the evolution of the vibrational temperatures have an impact on the composition. Both models based on the preferential dissociation predict the same evolution for the composition of the main molecular species. As expected some differences are found when we compare these results with the non-preferential dissociation model, which predicts a faster dissociation of molecules, as described in figure 7.17. The effects on the electron density are shown in Figure 7.18. A delay in the production of the free-electrons, present when using Treanor and Macheret model, causes a slight displacement of the peak in the electron density.

In conclusion, although the preferential dissociation models lead to a less effective dissociation of the molecules and in general lower vibrational energies through the shock-layer, such effects are small for the analyzed flow conditions. Hence, in the following we propose to adopt a non-preferential dissociation model.

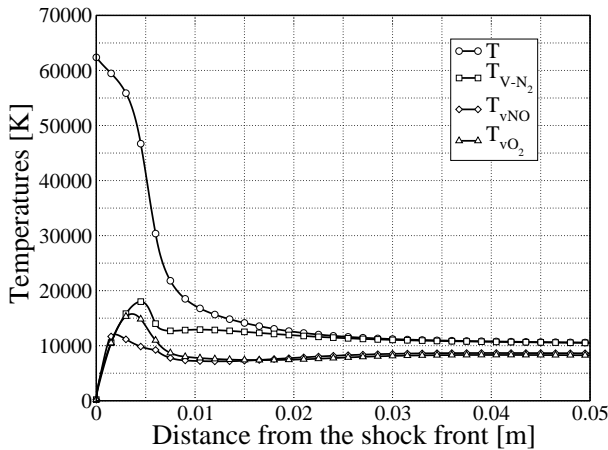


Figure 7.15: Temperature profiles obtained with Macheret's model.

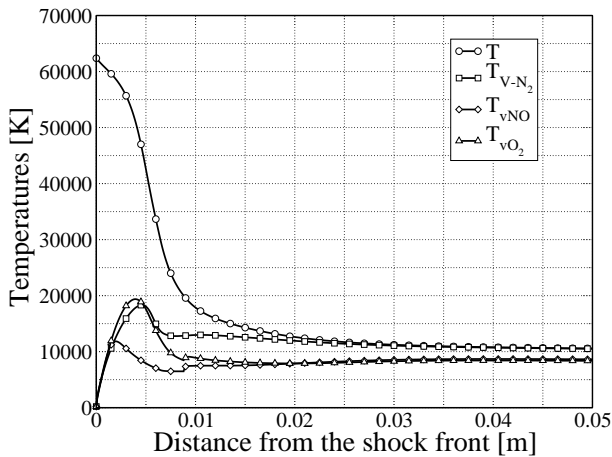


Figure 7.16: Temperature profiles obtained with Treanor's model. The U parameter was set to $(T_D/3)$.

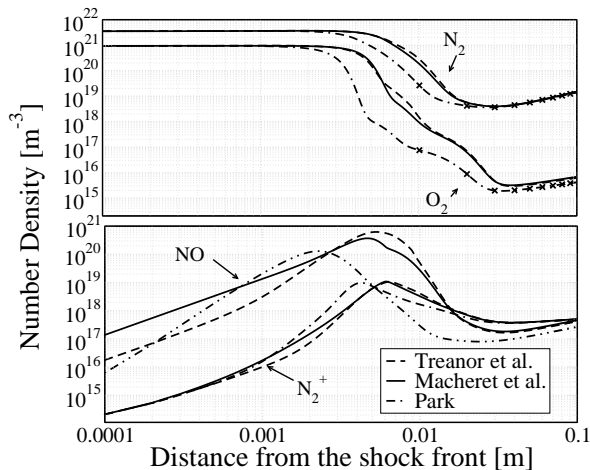


Figure 7.17: 1634 s case. Comparison of population profiles obtained with: Treanor model (dashed lines); Macheret's model (unbroken lines); and Park's model (dot-dashed lines).

7.3.2.2 Influence of the optical thickness and the ionization precursor on the results

So far, the gas has been considered optically thin, which means that all the radiation emanated in the shock layer was supposed to leave the computational domain, without interacting with the atoms and molecules present in the gas. We now try to assess the influence of the optical thickness of the medium on the population of the electronic excited states of the atomic species, varying the value of the escape factors of some lines. It is well-known that the resonance lines tend to be self-absorbed affecting the internal distribution function of atomic nitrogen and oxygen. In order to account for this phenomenon we set the escape factor of the VUV lines to zero and 1 for other radiative transitions.

The results are shown in figure (7.19). The low lying excited states (strongly radiating in the VUV part of the spectrum) are found to be overpopulated with respect to the previous predictions with the ABBA model and are then closer to the results obtained with Park's model.

Furthermore Figure 7.20 shows that the electron density evolution is

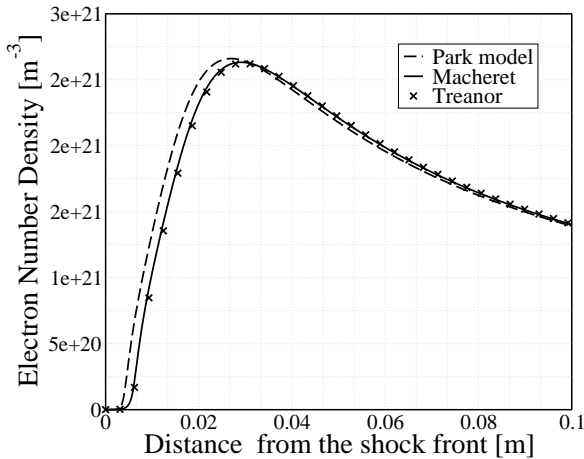


Figure 7.18: Free electron density plots obtained with: Treanor model (\times); Macheret's model (unbroken line); and Park's model (dashed line).

strongly affected: while in the case of optically thin medium its evolution presents a maximum followed by a monotonic decrease, now the population exhibits an monotonically increasing behavior followed by a plateau region. The reason of such behavior is the radiation cooling, which removes energy from the flow, lowering the temperature of the free electrons that recombine. The influence of a radiation on the ionization degree for low temperature plasmas was discussed in details in Ref. [133]

When considering the thickness of the plasma, the radiation generated within the shock layer can propagate ahead of the shock and interacting with the cold gas, can be re-adsorbed. Such interaction produces ionization, dissociation and the excitation of the internal energy modes. This phenomenon is know with the name of *precursor*. An accurate modeling of this physical mechanism would require the solution of the radiative heat transfer equation fully coupled with the flow solver. Such treatment is out of the scope of the present manuscript and we limit ourselves to a approximate modeling of these precursor effects, using experimental data extracted from shock tubes in the same range of operating conditions.

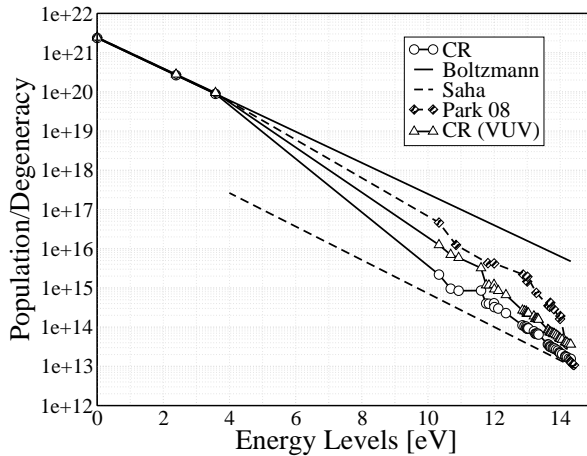


Figure 7.19: Population profiles of N at 1 cm from the shock front comparison: Park's model (\diamond); ABBA model $\alpha = 0$ (\circ); (\triangle) ABBA model with the VUV lines which are self-adsorbed.

Thus, in order to assess the influence of the precursor ionization on the results, we assume that a certain amount of electrons are present right after the shock. The choice of the initial electron density is based on the experimental analysis carried out by Gorelov [72]. Analyzing a large number of experiments he found the dependence of the ionization density as a function of a shock speed and pressure. The results of such analysis are summarized in Figure 7.21 (taken from Ref. [72]) which describes the electron densities as a function of the distance ahead of the shock wave. The value chosen for the electron density is of $10^{19} \text{ [m}^{-3}\text{]}$ which corresponds to the maximum value of the electron density in the plot in Figure 7.21. We have also assumed that the temperature of free electrons is about 8000 K in order to maximize the precursor effects.

Results of such analysis, are depicted in Figure 7.22, where the electronic distribution function of the atomic nitrogen considering the precursor effects is compared with the original distribution (without precursor). Although, the presence of the free-electrons in the pre-shock region enhances the excitation of the atomic nitrogen, which is found to be a closer to the Boltzmann equilibrium, the differences with respect to the former case are considered

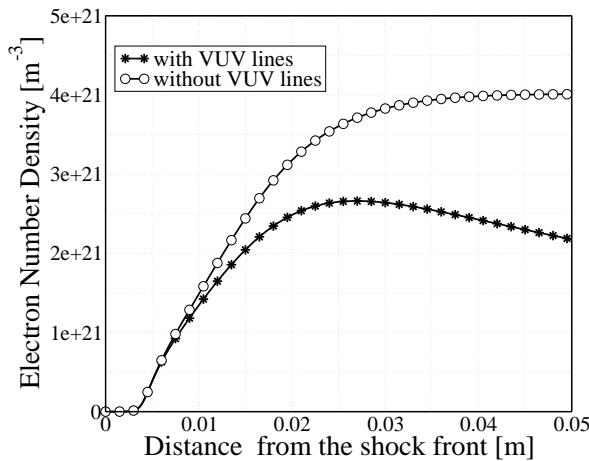


Figure 7.20: Electron density profiles. (*) indicates the ABBA model ($\alpha = 0$) and (o) is the ABBA model with the VUV lines which are self-adsorbed.

small. Hence the effects of precursor can be considered limited.

7.3.2.3 Influence of the heavy particles impact excitation on ionization

As a rule, ionization by electron impact proceeds step-by-step. It is a ladder climbing process, in which the electrons are first excited and then ionize, when they are close enough to the ionization limit. In fact, since in our case the kinetic energy of the free electrons is much smaller than the ionization potential, i.e. ($\mathcal{I} \gg kT_e$), (where \mathcal{I} is the ground atomic state ionization energy) the atomic ionization occurs mainly from the upper excited states with the ionization energy equal to ($\mathcal{I} - kT_e$). Therefore, ionization processes are strongly affected by the degree of excitation of the electronic states population.

The present section investigates the influence of the inelastic collisions among heavy particles on the ionization process. It is commonly believed that the excitation of electronic energy modes of atoms is dominated by the interaction with the free electrons [138, 178] except right after the shock, where the electron density is scarce and the molecules are the only mean of

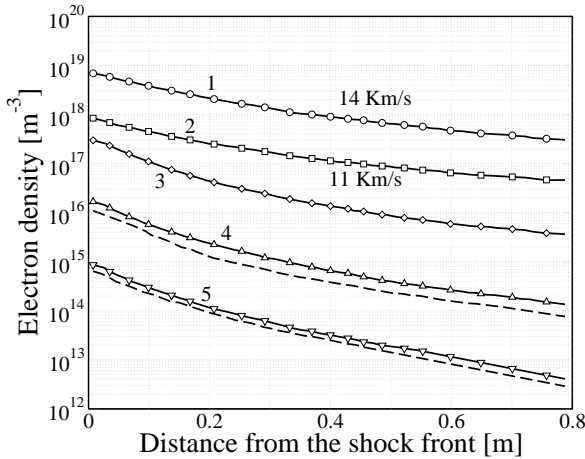


Figure 7.21: Electron population distributions ahead a shock wave. $p = 0.5$ torr: 1 - $V_s = 8.0$ km/s ; 2- $V_s = 7.5$ km/s ; 3- $V_s = 9.5$ km/s; $p_1 = 0.2$ torr: 4- $V_s = 11.3$ km/s; 5 - $V_s = 14.0$ km/s; broken lines - calculated results. Experimental results taken from Ref. [72].

excitation [120, 176]. Figure 7.23 shows the effect of the individual processes on the electron number density. The different curves in the plot represent respectively: the electron density profile obtained neglecting all the inelastic processes of atoms with heavy particles (unbroken line); the electron density profile, when inelastic collisions of the atoms with the molecules are considered (dashed line); the electron density profile, when inelastic processes due to the atom-atom and atom-molecules (dot-dashed line) interaction are accounted for.

We observe a different evolution of the electron density after the shock if heavy particle excitation and ionization is taken into account. These processes contribute to the formation of the first electrons in the post-shock region. In particular the processes involving molecular species tend to produce electrons very close to the shock, as opposed to the atoms that can contribute to the formation of the electrons only when a significant amount of dissociation has taken place. However the amount of electrons produced, is fairly small and does not affect the excitation processes. If we compare the electron density produced by the interaction with the heavy particles

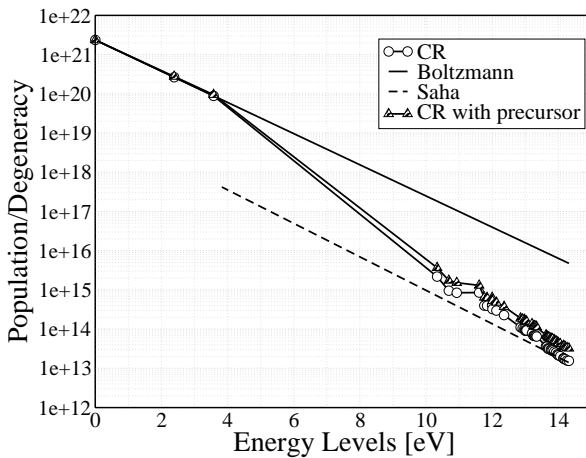


Figure 7.22: Population profiles of N at 1 cm from the shock front. (\diamond) Park's model; (\circ) is the ABBA model ($\alpha = 0$). Unbroken line is the Boltzmann and Saha is the dashed line. \triangle accounts for the precursor effects.

with the one of figure 7.21, we can see that the radiation emitted in the shock layer interacting with atoms and molecules in the pre-shock region produce more electrons. Therefore the importance of the heavy particles excitation is reduced if the interaction of the radiative field and the flowfield is correctly accounted for.

Summary

We study the behavior of the excited electronic states of atoms in the relaxation zone of one-dimensional air flows obtained in shock-tube facilities. A collisional radiative model is developed, accounting for thermal nonequilibrium between the translational energy mode of the gas and the vibrational energy mode of individual molecules. The electronic states of atoms and molecules are treated as separate species, allowing for non-Boltzmann distributions of their populations. We apply the model to a trajectory point of the FIRE II flight experiment. In the rapidly ionizing regime behind strong shock waves, the electronic energy level populations depart from Boltzmann distributions since the high lying bound electronic states are depleted. In

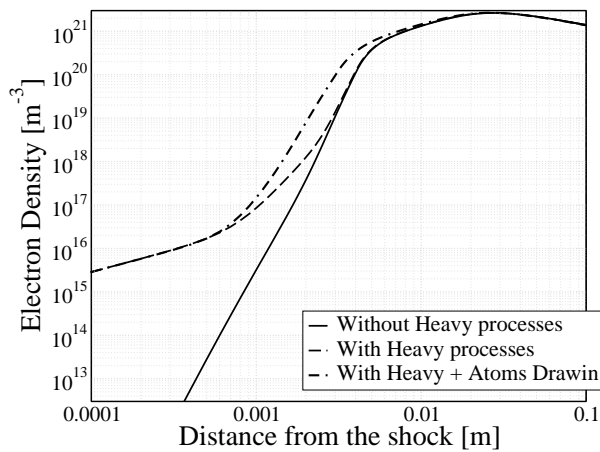


Figure 7.23: 1634 s case. Influence of the heavy particles processes on ionization.

order to quantify the extent of this nonequilibrium effect, we compare the results obtained by means of the collisional radiative model with those based on Boltzmann distributions. For the molecules the behavior is different and departures from the Boltzmann equilibrium are limited to a narrow zone close to the shock front. A comparison with the more recent model of Park reveals a rather good agreement for predictions involving molecules as opposed to the predictions involving the populations of the electronic levels of atoms which show discrepancies.

The analysis presented here allowed us to understand the relative importance of different physical phenomena occurring in the shock layer of a spacecraft at high re-entry speed. The influence of the vibration-dissociation coupling is found to have a small influence on the results also because at high speed the dissociation does occur from all the vibrational levels and it is not restricted to the upper vibrational levels. In other words there is no preferential way for the molecules to dissociate.

The influence of the optical thickness on the results puts forward the need for a coupling of radiation and flowfield calculation, given the influence of the radiative processes on the electron energy distribution function and on the

thermo-physical properties of the plasma. This would allow us to account for precursor phenomena in a physically consistent manner and to have a more reliable estimation of the influence of such processes on the thermo-physical state of the shock layer. According to our approximate estimations, however it seems that precursor phenomena have a little influence on the results.

Processes involving the excitation of the heavy particles are found negligible respect to the interaction with the free-electrons and be neglected in a simplified model.

Chapter 8

Detailed chemistry in expanding flows

The study of the ionizing flows in shock tubes has led us to the conclusion that nonequilibrium ionization effects may cause deviations from equilibrium in the distribution of the electronic energy levels of atoms and molecules. As a consequence the reduced nonequilibrium electron density with respect to the equilibrium number density, brings about a depletion of the population of the high lying excited levels. Different is the situation in expansion, where the ionized plasma flows, while recombining, provoke an overpopulation of the electron density. Hence, owing to the strong collisional coupling among high-lying excited states and free electrons, the nonequilibrium electron density results in an overpopulation of the excited states [106].

The behavior of the internal energy levels in expanding flows was extensively studied by the Capitelli's group at IMIP in Bari and the results of such investigation are thoroughly presented in Ref. [35]. Colonna in Ref. [47], presents a self-consistent kinetic model for nitrogen plasmas to describe an expansion through a converging-diverging conic nozzle. In particular, he investigates the role of electronically excited states of nitrogen-molecules and free electrons and he shows that the strong coupling among these two systems affects not only the kinetic processes but also macroscopic quantities such as Mach number and temperature profiles.

In the present chapter, we propose an analysis of the air plasma flow generated by an electromagnetic discharge, taking place in the inductively coupled plasma torch of the Von Karman Institute (VKI) Minitorch. Air plasmas are intrinsically more complicated than nitrogen plasmas owing to the large number of species (and pseudo-species) produced. The behavior of the electronically excited states of atoms and molecules is discussed, seeking for possible deviations from equilibrium distribution function of the electronic levels. A thorough description of the CR model used, is presented in Chapter 7.

Reservoir Conditions	
Temperature [K]	10000.0
Pressure [Pa]	101325.0
Mass-Flow [g/s]	0.55
N_e [m^{-3}]	1.72493E+22
Composition	L.T.E.

Table 8.1: Flowfield quantities inside the torch of the Minitorch.

The chapter is divided in two main parts: in Section 8.1.3, we analyze the thermo-physical state of the plasma, disregarding the radiative transitions and considering the medium optically thick; in Section 8.1.5 we discuss the effects of the radiative transitions on the electronic energy distribution function, comparing with the optically thick results. This allow us to separate the two different effects that kinetic and radiative processes have on the thermo-physical state of the plasma.

8.1 Analysis of the VKI Minitorch

High pressure ICP sources are used in numerous applications, in particular for the testing of thermal protection materials used to protect space (re-)entry vehicles. The planetary gas is injected in a swirling, annular way into a heat-resistant quartz tube, surrounded by an inductor. A radio-frequency electric current runs through the inductor and induces a secondary current through the gas inside the tube, which heats up by means of Ohmic dissipation. Such an ICP torch (Fig. 8.1) typically produces a low Mach number plasma jet, which can possibly be accelerated to supersonic flow conditions by a nozzle [53].

The plasma produced in the torch, initially in equilibrium conditions at atmospheric pressure, is expanded in a converging-diverging nozzle, placed at the outlet of the torch. The reservoir conditions are written in Table 8.1.

The nozzle geometry composed of a converging part of 2.85 cm and a conical diverging part of 1.35 cm, with an semi-opening angle of 3 degrees, is depicted in Figure 8.2. The converging part of the nozzle is usually found in equilibrium conditions up to the throat, as opposed to the region close to the

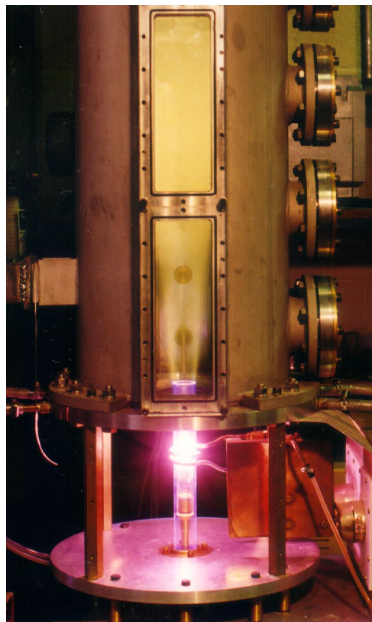


Figure 8.1: VKI pilot ICP facility in operation.

nozzle exit, where the flow may freeze. The two points under investigations are the nozzle throat and the nozzle outlet, located at respectively 2.85 cm and 4.2 cm from the inlet. The part of the flowfield among these two points is characterized by strong nonequilibrium effects and justifies the choice of the points of analysis.

8.1.1 Model description

The nozzle code, presented in Chapter 2 and validated against literature in Chapter 5, is applied to the analysis of the expanding flow taking place in the nozzle of the VKI Minitorch facility. The electronic specific CR model accounts for the modeling of the electronic energy, whereas the vibrational energy levels are assumed to be populated accordingly to the Boltzmann distribution. Furthermore the free electrons follow a Maxwellian distribution at a temperature T_e and their evolution is governed by a separate equation.

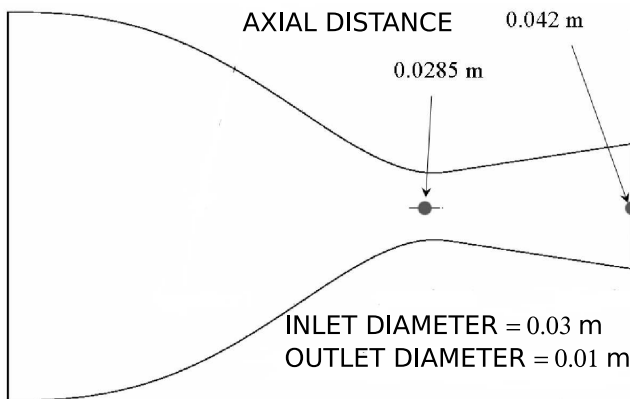


Figure 8.2: Geometry of the nozzle of the VKI Minitorch.

The mixture used, accounts for the species and pseudo-species listed in the preceding chapters: the forty six levels of atomic nitrogen and forty levels of the atomic oxygen can be found in Tab. A.1; the electronic states considered for the molecular species are presented in Tab. 7.1. All the details concerning radiative and kinetic process can be found in Chapter 6. The set of equations was discussed in Chapter 2 and the modifications introduced, owing to the state specific treatment of the electronic levels, were discussed in Chapter 6. The TT_V model of Park is used in order to account for the vibration-dissociation coupling and the non-preferential model of Candler has been used to account for the influence of chemistry on vibration. In the following calculations the optical thickness of the medium has been considered by making use of the escape factors. Ranging their value from 0 to 1, we change the thickness of the gas from *thick* to *thin*.

REMARK: Recent experiments conducted at Stanford University [65] have shown that the vibrational levels of certain electronic states (in particular $B^3\Pi$ of N_2), can strongly depart from the Boltzmann distribution when the concentration of atomic nitrogen is higher than its equilibrium value. Vibrational nonequilibrium models have been developed for nitrogen plasmas in Ref. [150–152] in order to account for departures from Boltzmann distribution.

Since the hypothesis of Boltzmann distribution among the vibrational energy levels may not hold, the first steps to extend the collisional radiative model to account for vibrational nonequilibrium effects have been carried out. A thorough description work done is given in Ref. [25] and the kinetic data-set is detailed in [40, 90].

8.1.2 Flowfield characterization

The knowledge of pressure, temperatures and electron number density inside the nozzle is of primary concern to characterize important features of the physico-chemical state of the plasma. An accurate investigation of the evolution of these flow quantities is presented here.

The pressure, depicted in Figure 8.3, has a strong influence on the thermo-physical and chemical state of the plasma, since it influences the response time of the gas to the changes in the thermodynamic properties occurring along the expansion. Since most of the expansion in the flow takes place in the diverging part, the converging part of the nozzle is characterized by high pressure and low velocity keeping the plasma to equilibrium conditions. However, as the gas moves downstream, towards the throat and the nozzle exit, the first nonequilibrium effects begin to appear since the pressure is low and the flow velocity is maximum.

Temperature profiles are shown in Figure 8.4. The vibrational temperature of molecular nitrogen and the free-electron translational temperature are strongly coupled to each other thanks to EV exchanges and reach a state of partial equilibrium among each other in the diverging part of the nozzle. Different is the behavior of molecular oxygen and nitric-oxide whose vibrational temperatures stay close to equilibrium values and show small departures from the ro-translational temperature.

In Table 8.2, we summarize the characteristic quantities of the flow at the nozzle exit and in particular, we indicate two different values of the electron number density: n_e , n_{eEQ} .

The first value refers to the computed number density at the outlet, given by the nozzle code, the second value represents the equilibrium number density expected at 6000 K and 3000 Pa, respectively the free-electron temperature¹ and static pressure at the outlet.

¹Since the flow is not in equilibrium we decided to use the free electron temperature since it rules the ionization-recombination processes.

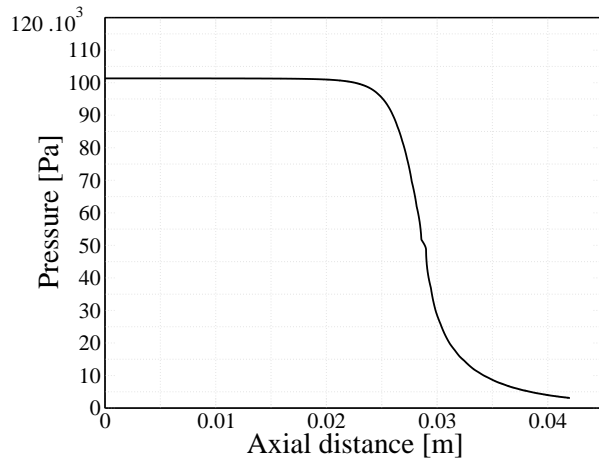


Figure 8.3: VKI Minitorch. Pressure profile along the axis of the nozzle.

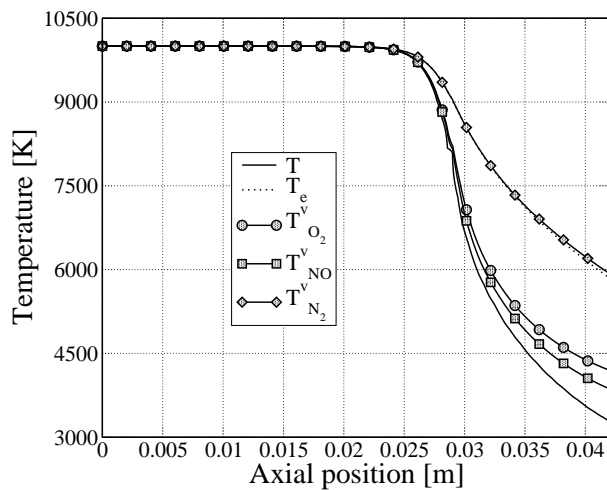


Figure 8.4: VKI Minitorch. Evolution of the temperatures along the axis of the nozzle. Optically thick medium.

Outlet Conditions	
T [K]	3283.
T_{vN_2} [K]	5851.
T_{vNO} [K]	3865.
T_{vO_2} [K]	4198.
T_e [K]	5930.
Pressure [Pa]	3093.
n_e [m^{-3}]	1.14091E+21
n_{eEQ} [m^{-3}]	1.65602E+19

Table 8.2: VKI Minitorch. Flowfield quantities in correspondence of the torch outlet.

We observe a strong nonequilibrium of the free electrons density which, as we shall see in the next section, causes an overpopulation of the electronically excited states of the atoms and molecules, since free electrons are very efficient as collision partner for electronic excitation.

8.1.3 Analysis of the atomic distribution function

The converging part of the nozzle is characterized by high values of the static pressure and the distribution of the excited states tends to follow a Maxwell-Boltzmann distribution. Therefore the knowledge of pressure and temperature allows us to accurately describe the physico-chemical state of the plasma. However, as we approach the nozzle throat, the gas rapidly expands, the temperature of atoms and molecules decreases, and the ions and atoms tend to recombine to reach chemical equilibrium corresponding to the local temperature. In this condition, the collisional processes may not be efficient enough to maintain the equilibrium among the electronic levels of atoms and molecules.

Figure 8.5 shows the electronic distribution function of atomic nitrogen at the throat. It is interesting to observe that at this location the population is very close to a Boltzmann distribution, although vibrational nonequilibrium effects are already present, as shown in Figure 8.4. The atomic oxygen exhibits the same type of behavior in correspondence of the throat and is found to be in Boltzmann equilibrium. At the outlet of the nozzle, Fig-

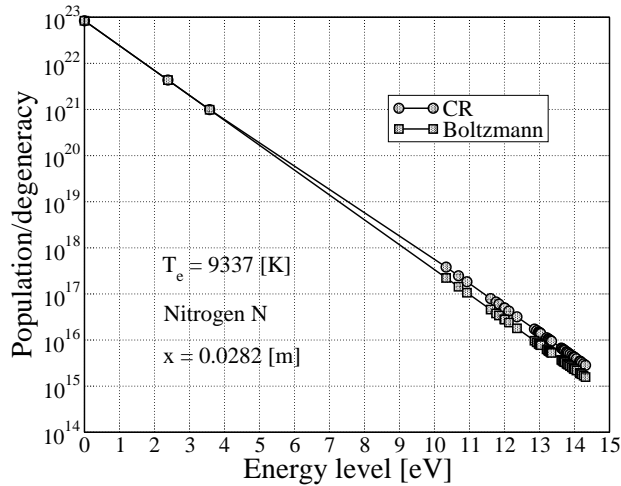


Figure 8.5: Throat. Normalized Population plots: comparison with equilibrium.

ure 8.6 shows a strong overpopulation of the excited states. In recombining plasmas, the high-lying bound electrons tend to behave like free electrons. Thus, the electronic levels of the upper states are found in Saha equilibrium (at T_e) with the free-electrons and they are not in thermal equilibrium with the ground electronic state [106]. The same physical phenomena have been observed experimentally in argon plasmas produced by electromagnetic discharges in Ref. [9, 71, 127]. The importance of such phenomenon is underlined in Ref. [127] where the influence of the non-Boltzmann distribution of the excite states on the temperature measurements is discussed. Only by accounting for the non-Boltzmann distribution of excited states it is possible to find agreement among spectroscopic measurements, based on the analysis of the atomic line radiation and an independent calorimetric energy balance. In molecular gases however, those effects may be reduced for two reasons. Firstly, in air, electrons are strongly coupled with N_2 vibration (and to a lesser extent, also with O_2 vibration) [87]. Since vibrational temperature thermalizes with the translational energy of heavy particles by means of VT exchanges, finally the translational temperature of free electrons is cooled and the ionization degree is lower. Secondly, the mechanism of recombination of free-electrons is due to dissociative recombination, a

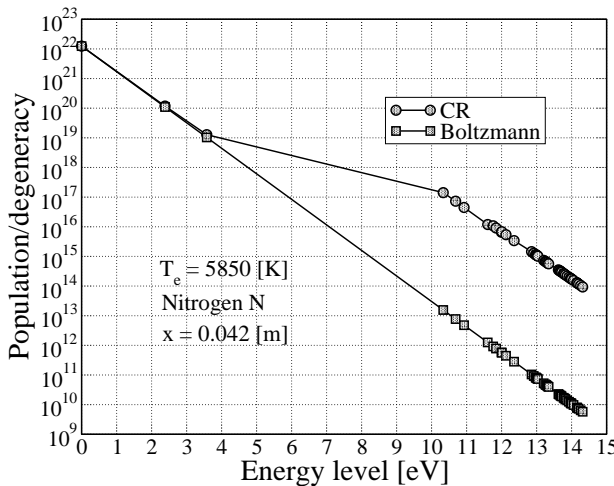


Figure 8.6: Outlet. Normalized population plots of atomic nitrogen: comparison with equilibrium.

two body process which is much faster than the three-body recombination taking place in atomic plasmas [65].

In conclusion, the analysis of the population of the electronic levels of atomic species demonstrates the importance of the use of a state specific approach in order to capture the deviation from equilibrium from the electronic energy distribution function. If neglected, such effects may lead to a misinterpretation of the experimental results as indicated in Ref. [127].

8.1.4 Analysis of the electronic states of the molecules

The analysis of the evolution of the electronic states of the molecules in a post-discharge environment is addressed in numerous contributions [61, 65, 107, 152]. The general tendency shows an overpopulation of excited states of the electronic levels, which is confirmed by the spectroscopic measurements [65]. In this section we compare the population of the excited states, produced by the CR calculation, against the corresponding equilibrium value. This allows us to quantify the extent of nonequilibrium of the electronic states of the molecular species.

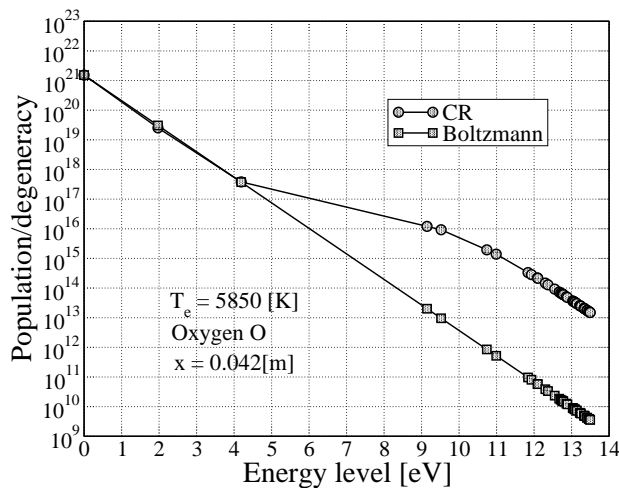


Figure 8.7: Outlet. Normalized population plots of atomic oxygen: comparison with equilibrium.

Figure 8.8 shows the behavior of the ground and the excited states of molecular nitrogen. A comparison is carried out with the corresponding equilibrium values at each location along the nozzle axis. Equilibrium calculations (dashed lines) have been carried out extracting number density and temperatures of the individual molecule under analysis, assuming that the excited states are populated according to Boltzmann distribution.

Figure 8.8 shows how the population of N_2 , which is supposed to be in equilibrium in the reservoir, stays in equilibrium throughout all the expansion, although a slight overpopulation of $N_2\text{C}$ state is present at the nozzle outlet. Similar behavior can be observed for the excited states of N_2^+ in Figure 8.9 where the overpopulation of the $N_2^+\text{B}$ is rather limited. The excitation processes of the B state of N_2^+ are modeled using rate constants estimated by Teulet in Ref. [171]. However a comparison of those rates with others found in literature [73], shows large discrepancies. Therefore the conclusions concerning the state of degree of nonequilibrium of N_2^+ may be substantially different, owing to the sensitivity of the electronic population to the model used for the kinetic processes.

Different is the behavior of NO, NO^+ and O_2 which are found to depart from equilibrium in proximity of the nozzle exit. In Figure 8.10 the popula-

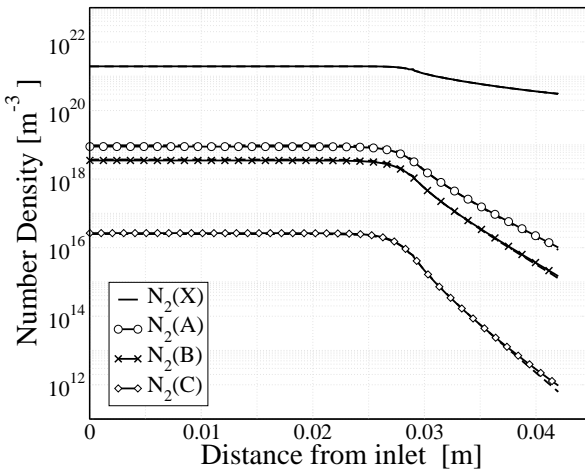


Figure 8.8: N_2 excited states of populations [m^{-3}] along the nozzle axis. Dashed lines: equilibrium value; unbroken lines CR model results.

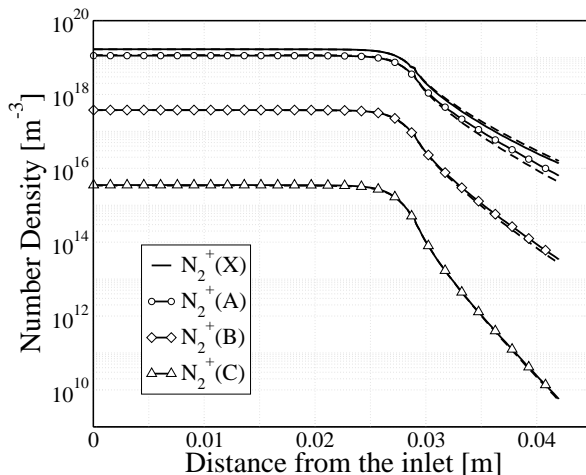


Figure 8.9: N_2^+ excited states of populations [m^{-3}] along the nozzle axis. Dashed lines: equilibrium value; unbroken lines CR model results.

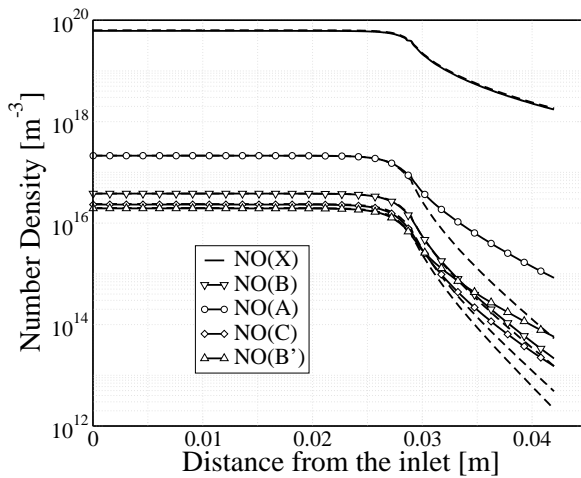


Figure 8.10: NO excited states of populations [m^{-3}] along the nozzle axis. Dashed lines: equilibrium value; unbroken lines CR model results.

tion of exited states of NO is found to be overpopulated by more than one order of magnitude, with a consequent enhancement of the radiative signature, e.g. $\beta(\text{B}^2\Pi \rightarrow \text{X}^2\Pi)$ $\gamma(\text{A}^2\Sigma \rightarrow \text{X}^2\Pi)$ systems. Similar is the behavior of NO^+ and O_2 molecules where the excited states follow the same trend of NO.

In conclusion, according to the analysis carried out in this section, the populations electronic states of N_2 and N_2^+ can be described by a temperature as they are in Boltzmann equilibrium at the free-electron temperature. Different is the behavior of the other molecular species, which are found strongly overpopulated at the nozzle outlet.

8.1.5 Influence of the optical thickness on the results

In this section, the influence of radiative transitions on the thermo-chemical state of the plasma is addressed. The analysis, carried out within the crude approximation of optically thin medium, begins with the investigation of the radiative effects on the flowfield quantities.

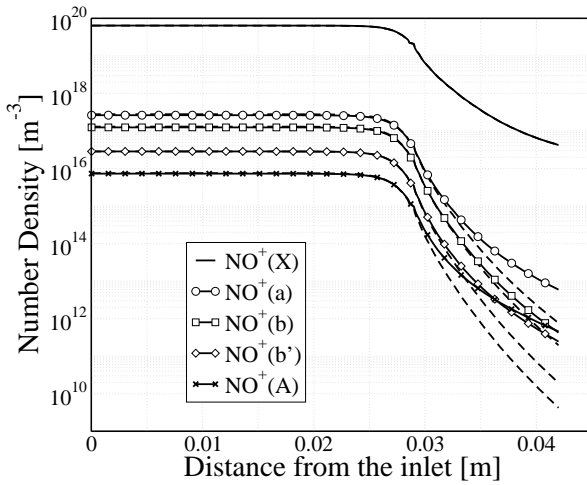


Figure 8.11: NO⁺ excited states of populations [m⁻³] along the nozzle axis. Dashed lines: equilibrium value; unbroken lines CR model results.

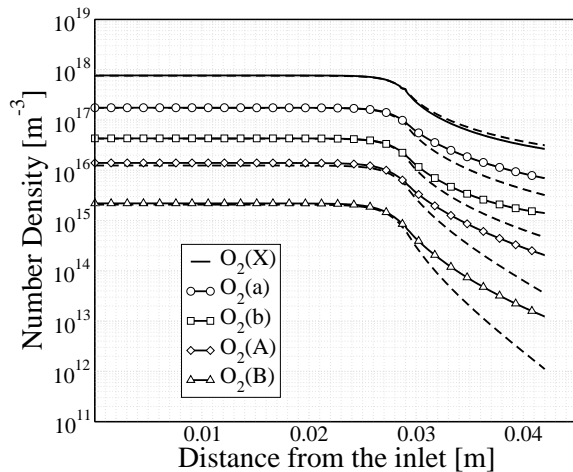


Figure 8.12: NO⁺ excited states of populations [m⁻³] along the nozzle axis. Dashed lines: equilibrium value; unbroken lines CR model results.

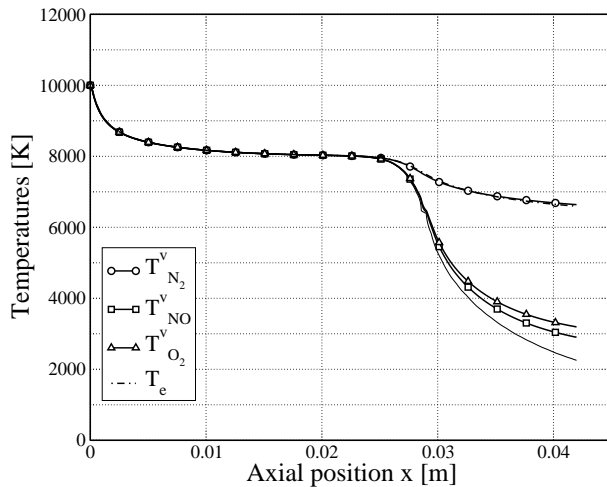


Figure 8.13: Temperature profiles along the nozzle axis: optically thin medium.

Comparing the temperature profiles in Figure 8.13 (optically thin) and Figure 8.4 (optically thick), we notice the absence of a plateau in the converging part of the nozzle, being the temperatures generally lower than the optically thick case. Such effect is due to a decreasing of the total enthalpy of the gas, owing to the radiative cooling. Indeed since we assume that all the radiation escapes, the gas cools down and the temperature profiles exhibit a monotonically decreasing behavior. Particularly strong are the effects in the converging part of the nozzle, where pressure and temperature are high. The behavior of the free-electron temperature, depicted in the same figure exhibits larger departures from the heavy particles translational temperature, if compared to the optically thick case. The reason is to be sought in the reduced density of the charged particles due to radiative cooling, which makes the elastic exchanges among light and heavy particles less efficient. Furthermore, since the analysis does not include radiative and dielectronic recombination, the radiative losses do not influence directly the temperature of free electrons.

The behaviors of the atomic and molecular electronic distribution functions, depicted in Figures 8.14-8.17 strongly depend on the relative impor-

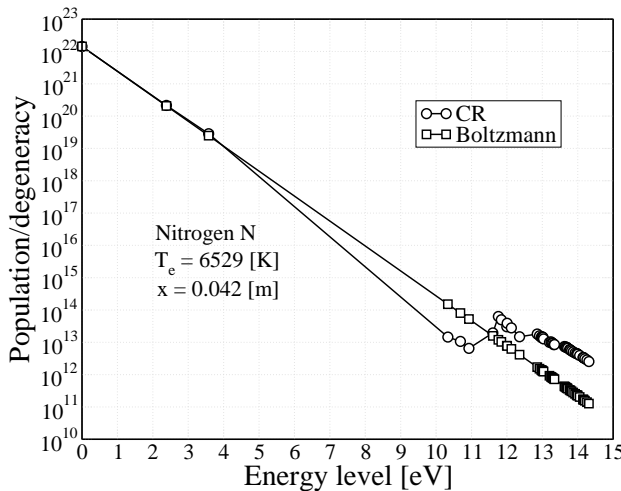


Figure 8.14: Outlet. Normalized population plots of atomic nitrogen: comparison with equilibrium.

tance of radiative and collisional processes. If we consider for example the excitation from a level i to a level j (with $i < j$) of a generic molecule or atom

$$\frac{dA(j)}{dt} = k_{i \rightarrow j} A(i) e^{-}$$

we see that the excitation rate $\frac{dA(j)}{dt}$ scales with p^2 as opposed to radiative processes which scale with p . Hence, at high pressure the rate of collisional excitation and de-excitation tends to be much faster than the radiative processes and the flow is found in equilibrium. However, as the pressure is lowered, radiation may have an important effect on the population and de-population of the electronically excited levels.

The effects of radiative transitions on the electronic population of the atomic nitrogen can be observed in Figure 8.14. Radiative transitions tend to deplete the low lying excited levels, which, in some cases, are found to be depopulated respect to the Boltzmann prediction. The high-lying levels, which do not radiate as much, are very closely coupled by kinetic processes with the emitting levels and their population is also lowered.

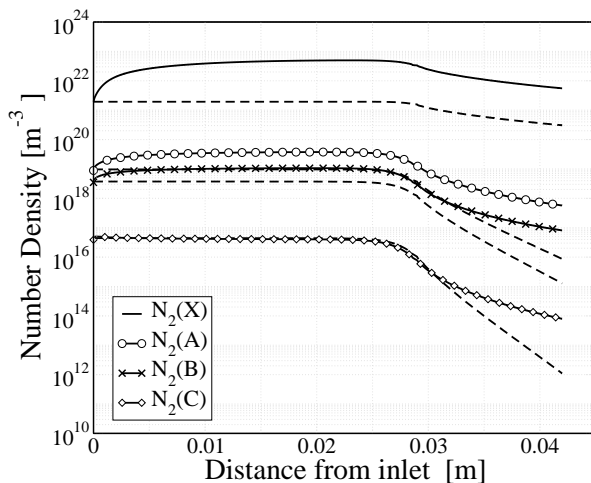


Figure 8.15: N_2 excited states of populations [m^{-3}] along the nozzle axis: comparison optically thin (unbroken lines) and optically thick results (dashed lines).

The behavior of molecular nitrogen is strongly affected by the cooling of the gas. Figure 8.15 compares the number densities of the optically thick case with the optically thin case. The drop of the temperature in the converging part of the nozzle, enhancing the recombination of atoms and ions, brings about an increase of the density of the molecular species in the ground and excited states. The overpopulation of the excited states mostly comes from the recombination of the ionic molecules, which are found to be underpopulated, as shown in Figure 8.16. The analysis of the departure from equilibrium conditions confirms the results discussed in the optically thick case: N_2 and N_2^+ are found in equilibrium throughout the all computational domain. In Figure 8.16 the equilibrium results, shown only for few locations have been estimated extracting number density and free electron temperature from the optically thin calculations and therefore these values differ from the values estimated in the optically thick case. The analysis of the other molecules present in the mixture, shows the same increase in the population of the ground state and excited states of the neutral molecules due to radiative cooling, as discussed in the case of molecular nitrogen. However a direct comparison of extent of nonequilibrium in Figure 8.17 with the

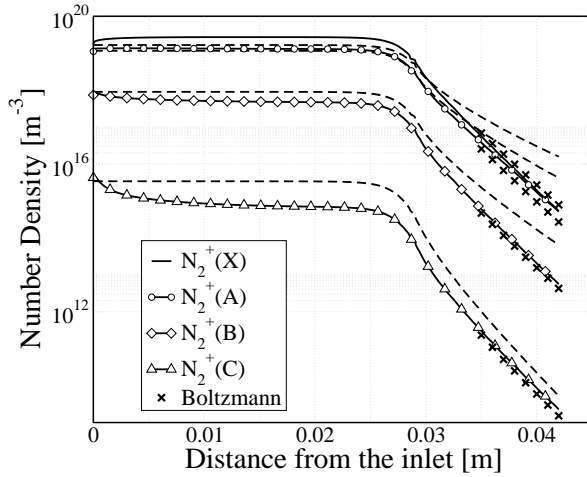


Figure 8.16: N_2^+ excited states of populations [m^{-3}] along the nozzle axis: comparison optically thin (unbroken lines) and optically thick results (dashed lines). Equilibrium results (\times).

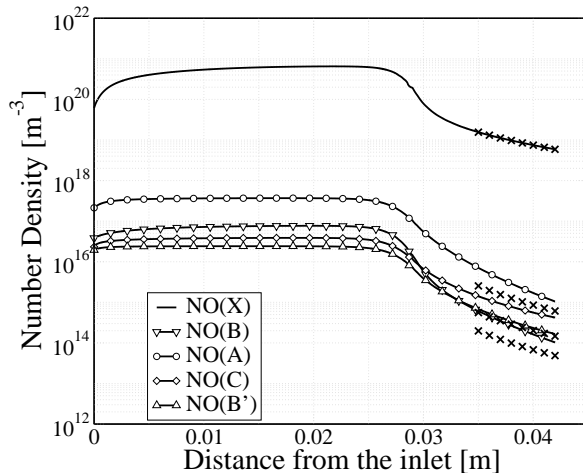


Figure 8.17: Normalized population plots of NO: comparison optically thin (unbroken lines) and equilibrium results (\times).

corresponding optically thick case in Figure 8.10 shows a reduction of the overpopulation of the excited states due to radiative processes.

Summary and conclusions

In this chapter the expansion of the plasma in the nozzle of the VKI Minitorch facility was studied using an electronically specific collisional radiative model for air plasmas. The collisional-radiative model accounts for thermal nonequilibrium between the ro-translational and vibrational energy modes of individual molecular species and deals with electronic states of atoms and molecules as separate species. Therefore, non-Boltzmann distributions of the electronic state populations of atoms and molecules are allowed. A separate temperature characterizes the energy contained in the translational mode of the free electrons. Radiative processes are accounted for using escape factors and the influence of the optical thickness of the medium on the results has been also discussed.

In order to quantify the extent of departure from equilibrium of the electronic state populations, our results have been compared with those obtained assuming a Boltzmann distribution. Departures of the electronic state distribution function of atoms and molecules from the Maxwell-Boltzmann distribution are found at the outlet of the nozzle. The radiative losses in the plasma have been accounted for by means of escape factors. The optically thick results revealed a strong overpopulation of the electronically excited states of the atoms and for all the molecular species with the exception of N_2 , N_2^+ . When the radiative effects are accounted for, the overpopulation of the excited states of atoms is drastically reduced as opposed to the behavior of excited states of the molecules, which show a small reduction of the nonequilibrium effects in particular for NO , NO^+ and O_2 . Moreover the effect of the radiative cooling leads to a strong overpopulation in the density of the molecular species owing to the recombination of atoms and ions.

Chapter 9

Toward a simplified model

The collisional radiative models, discussed in the previous chapters, describe the evolution of the electronically excited states of atoms and molecules, solving a large number of equations. The practical implementation of such models in multi-dimensional Navier-Stokes solvers, would require prohibitive computational resources and is therefore not applicable. Nowadays this problem is overcome adopting the loosely coupled QSS approach, extensively discussed in Chapter 6. This approach may give reasonable results, but it is not general, since it requires ad hoc assumptions for the flowfield calculations (§ 6.2.5.3). Gally in Ref. [64] proposed an innovative method assuming that the metastable states are populated according to a Boltzmann distribution and the upper levels are in a Saha equilibrium with the free state. Gally's model, although very appealing, owing to the analytical expressions for the electronic distributions, which makes it computationally efficient, was proven to give inaccurate results [93].

In this work, the detailed CR models previously described, are used to derive an approximate model, which is significantly simpler, given the reduced number of levels accounted for. The model is designed for its direct application to conventional 2D-3D CFD solvers (as shown in Chapter 10) and it accounts for a combination of "real" and lumped electronic state of the atoms, allowing for an explicit determination of the electronic distribution function. An accurate description of the number of electronic levels considered, is given in Section 9.1, while the formulation adopted to model the elementary processes is discussed in Section 9.2. The results obtained are nearly as accurate as the detailed CR model at predicting the resulting nonequilibrium populations, as confirmed by the comparison among the two models presented in details in Section 9.3.

Grouped states	Effective state N	Energy [eV]	State O	Energy [eV]
1	1	0.	1	0.
2	2	2.38	2	1.97
3	3	3.58	3	4.19
4	4-6	10.69	4-6	9.52
5	7-13	12.	7-13	12.09
6	14-21	12.98	14-21	12.78
7	22-27	13.27	22-27	13.05
8	28-46	13.68	28-40	13.464

Table 9.1: Nitrogen and Oxygen. Grouped states simplified ABBA model.

9.1 Lumping of the states of the atomic species

To create a simplified Collisional-Radiative model, we first need to define the energy states. An accurate analysis of the results presented in Section 6.2.5 suggests the possibility of reducing the number of levels to be considered in the CR model, by grouping the high lying excited levels of the atomic species. Indeed many electronic levels, owing to a reduced energy spacing, are likely to be in equilibrium among each other, thanks to the collisional coupling. Moreover the levels located close to the continuum are in chemical equilibrium (Saha equilibrium) with the free electrons and their population can be easily estimated by means of the Saha equation. Therefore the description of the detailed kinetic processes for these electronic states, results in an increase of the computational effort, without improving the accuracy of the model.

Substantially different is the behavior of the metastable states, which tend to be in equilibrium with the ground state. The different kinetics of the metastable and high lying excited states requires a separate grouping. Furthermore among the high lying excited states we can distinguish two additional group of levels: the ones close to the ionization limit, which do not radiate significantly and are in Saha equilibrium; and the lower excited levels close to the metastable states, which strongly radiate in the VUV part of the spectrum and are less efficiently coupled by collisions, owing to the larger energy barrier among each other. The three macroscopic groups of levels have been subdivided as indicated in Table 9.1. The ground and the metastable states are not grouped together, since, as observed in Sec-

tion 6.2.5.4, their populations may depart from the Boltzmann distribution. Furthermore an accurate estimation of their population is crucial, since they are highly populated and strongly contribute to the excitation of the upper states [99]-[100]. The second macroscopic group of levels, has been subdivided including in the same group the levels having nearly the same slope in Figure 6.12.

Another important constraint, when coupling the energy states is given by the radiative transitions: it is important to avoid that two major radiative transitions of interest are lost as a consequence of a poor choice of level grouping [31]. Hence the grouping of the levels is chosen avoiding to include the major radiative transitions within the same grouped state.

9.2 Elementary processes of grouped levels

To describe the evolution of the plasma, once defined the energy states to consider, we have to model the way these levels evolve with time, expressing the rates at which each single level is populated or depleted. A description of the elementary processes requires a modification of the kinetic and radiative processes introduced in chapter 6 to account for the grouping of the levels.

The radiative processes within the same grouped level have been discarded, since they do not affect the population of the level. In principle we could account for their contribution to the radiation cooling, however given the low energy content, such contribution was considered negligible.

The elementary process involving inelastic collisions of atoms and electrons, i.e. the excitation and ionization processes, require the average of the reaction rate constants, due to the grouping of the levels. The averages are based on the Boltzmann distribution and are outlined in the following sections. The same type of averaging is required for the inelastic excitation involving heavy particles. However, given their reduced influence on the excitation as well as the ionization processes (§ 7), such induced processes have been neglected.

Ionization for grouped levels

The ionization rate coefficients, from the L^{th} grouped level, is obtained averaging the rates of each un-grouped state over the Boltzmann distribution.

Therefore we can write:

$$\mathcal{K}_f^{L \rightarrow c} = \sum_i^{N_L} \frac{N_i}{N_{TOT}} k_{i,f}^{i \rightarrow c} \quad (9.1)$$

where N_L indicate the number of levels included in the lumped group, N_{TOT} is the total number density of the lumped level and $k_{i,f}$ refers to the rate constant for electron impact ionization of the single state.

Substituting the Boltzmann distribution function in 9.1 we retrieve:

$$\mathcal{K}_f^{L \rightarrow c} = \frac{\sum_i^{N_L} g_i k_{i,f}^{i \rightarrow c} \exp\left(-\frac{E_i}{k_B T_e}\right)}{\sum_k^{N_L} g_k \exp\left(-\frac{E_k}{k_B T_e}\right)} \quad (9.2)$$

where $\mathcal{K}_f^{L \rightarrow c}$ is the desired averaged rate constant.

Excitation for grouped levels

The grouping procedure requires the averaging of the reaction rate constants for the excitation processes. Indicating with L^* the lower grouped level and with L^{**} the final state, the averaged rate constants reads:

$$\mathcal{K}_f^{L^* \rightarrow L^{**}} = \sum_i^{N_{L^*}} \frac{N_i}{N_{TOT}^*} \sum_j^{N_{L^{**}}} \frac{N_j}{N_{TOT}^{**}} k_f^{i \rightarrow j} \quad (9.3)$$

where N_{TOT}^* is the number density of the lower grouped state and N_{TOT}^{**} is number density of the upper grouped state. The index i and j indicates respectively the un-grouped states of the lower and upper excited states. The rate coefficient for the electron impact excitation from the generic level i to the level j is indicated with $k_f^{i \rightarrow j}$. Assuming the Boltzmann population of the grouped states equation 9.3 becomes:

$$\mathcal{K}_f^{L^* \rightarrow L^{**}} = \frac{\sum_i^{N_{L^*}} \sum_j^{N_{L^{**}}} g_i g_j k_f^{i \rightarrow j} \exp\left(-\frac{E_i + E_j}{k_B T_e}\right)}{\sum_k^{N_L^*} \sum_l^{N_L^{**}} g_k g_l \exp\left(-\frac{E_k + E_l}{k_B T_e}\right)} \quad (9.4)$$

In a similar manner the excitation rate constants from the ground and the metastable states to the lumped states (indicated with L) are estimated.

$$\mathcal{K}_f^{i \rightarrow L} = \frac{\sum_j^{N_L} g_j k_f^{i \rightarrow j} \exp\left(-\frac{E_j}{k_B T_e}\right)}{\sum_l^{N_L} g_l \exp\left(-\frac{E_l}{k_B T_e}\right)} \quad (9.5)$$

Where i represents the index of ground, first or second metastable state for nitrogen or oxygen atoms.

9.3 Comparison approximate and accurate CR models

A needed step, before a full implementation of the approximate CR model in a multidimensional CFD solver, is the validation against the accurate model presented in the foregoing chapters. The mixture used in the present investigation accounts for neutral and charged species and includes a detailed treatment of the electronic states of nitrogen, N(1 – 8) and oxygen, O(1 – 8) atoms. The molecular species are assumed to be populated according to Boltzmann distribution. Such hypothesis may not hold, as discussed in Chapter 7, however since the main objective of the present work is the application of the model to CFD solvers, the detailed description of the nonequilibrium population of the atoms is considered sufficient at this stage.

The set of equations solved and the models used for the missing radiative and kinetic processes are detailed in Section 6.2.3 . The shock tube operating conditions are chosen to match the flight conditions of the FIRE II testcase at the 1634 second from the launch. The comparison among the two CR models is performed analyzing the Boltzmann diagrams at 1 cm from the shock front.

For the populations of the atomic nitrogen levels, Figure 9.1 shows that the differences among the two models are limited to small departure in the population density in the intermediate energy range. High lying excited states close to the continuum as well as the metastable states are very well described by the few states of the simplified model. In order to improve the agreement among the intermediate states, the number of grouped levels could be increased, increasing the accuracy and computational time.

Computational efficiency of the model is easily demonstrated if we consider that a full simulation requires only a couple of seconds, as opposed to

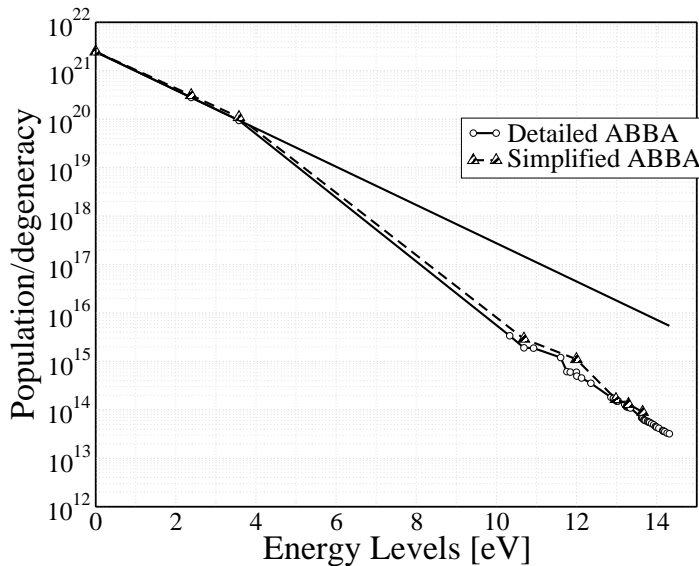


Figure 9.1: 1634 sec. Comparison among the detailed ABBA model (\circ) and the simplified CR approach (\triangle) for atomic nitrogen. The location is 1 cm from the shock front.

the full model which requires about 5 minutes.

From the present analysis concerning the non-Boltzmann modeling of atomic species, for the high speed re-entry applications, the simplified model provides a sufficiently accurate prediction of the electronic distribution function of the atoms, being computationally more efficient than the detailed models. The eight grouped levels used by this model for nitrogen and oxygen (listed in Table 9.1) can substitute respectively, the 46 and 40 levels for nitrogen and oxygen, allowing the implementation in more sophisticated flow solvers.

Summary

A simplified CR model, obtained using the more complete and elaborated model detailed in Chapters 6-7 is presented and validated. The use of group

of levels allows to drastically reduce the computational time, given the limited number of equations to be solved. In Table 9.1 all the levels considered for nitrogen and oxygen atoms are listed.

In conclusion, the eight grouped levels used by this model for nitrogen and oxygen (listed in Table 9.1) can substitute respectively, the 46 and 40 levels for nitrogen and oxygen, allowing the implementation in more sophisticated flow solvers.

Part III

Application to CFD: COOLFluiD Hypersonic

Chapter 10

Computational Fluid Dynamics

In the present chapter the physical models, developed in the first and second part of the manuscript, are applied to a multi-dimensional Navier-Stokes solver. All the results to be presented have been obtained using a parallel unstructured solver, COOLFLUID, an object-oriented high-performance framework for multi-physics written in C++, extensively described in [103, 104]. COOLFLUID was extended to thermochemical nonequilibrium, in the framework of this project and thanks to the fruitful collaboration with Dr. A. Lani, who took care of the practical implementation of the numerical methods, needed to solve the governing equations detailed in Chapter 2. The techniques employed for the discretization and the solution of the equations are detailed in Section 10.1.

The chapter is organized as follows: We first discuss the 2D results obtained for high speed re-entry conditions, analyzing the shock layer of the FIRE II flight experiment, for the flight condition 1636, and comparing our Navier-Stokes results with the one produced by the LAURA code, aiming at validating the code, for high speed re-entry conditions.

We move then, in Section 10.3, to the detailed investigation of the flight condition 1634. As previously shown, the analysis of such case requires the use of a CR model to account for the non-Boltzmann effects, in the electronic energy distribution function. To this end we use the simplified CR model presented, in section 9.

The last part of the Chapter 10.2, is devoted to the full 3D simulation of the flow around the EXPERT vehicle, in the early part of its trajectory, where thermal and chemical nonequilibrium effects are strong (§10.4).

10.1 Numerical methods

When coming to the practical solution of the governing equations discussed in Chapter 2, the present research project could benefit from the work, carried out by A. Lani in the development of numerical algorithms for conservation laws [102]. Therefore in this section, we limit ourselves to a brief description of the techniques used.

10.1.1 Numerical discretization

The governing equations for the nonequilibrium flow are now written in a form that is more suitable for the derivation of the numerical method. Notice that in the following the diffusive part of the heat flux is written explicitly.

$$\mathbf{U} = (\rho_s, \rho \vec{u}, \rho E, \rho e_m^V, \rho E_e)^T \quad (10.1)$$

The convective and diffusive fluxes are given by:

$$\mathbf{F}_i^c = \begin{pmatrix} \rho_s \vec{u} \\ \rho \vec{u} \vec{u} + p \hat{I} \\ \rho \vec{u} H \\ \rho \vec{u} e_m^V \\ \rho \vec{u} H_e \end{pmatrix}, \quad \mathbf{F}_i^v = \begin{pmatrix} -\rho_s \vec{V}_s \\ \bar{\tau} \\ \bar{\tau} \vec{u} - \vec{q}_c - \sum_s \rho_s h_s \vec{V}_s \\ -\sum_s \rho_s h_s^V \vec{V}_s - \vec{q}_v \\ -\sum_{s \in \mathcal{H}} \rho_s h_s^E \vec{V}_s - \rho_e h_e \vec{V}_e - \vec{q}_e^c \end{pmatrix}. \quad (10.2)$$

and the vector of source terms

$$\mathbf{S} = \begin{pmatrix} \dot{\omega}_s \\ \mathbf{0} \\ -Q_I^{Rad} \\ \dot{\Omega}_m^{CV} + \dot{\Omega}_m^{VT} + \dot{\Omega}_m^{VV} - \dot{\Omega}_m^{EV} \\ -p_e \nabla \cdot \vec{u} + \sum_{i \in \mathcal{E}} M_i \dot{\omega}_i e_i^E - \dot{\Omega}^I + \dot{\Omega}^{ET} + \dot{\Omega}^{EV} - Q_{II}^{Rad} \end{pmatrix} \quad (10.3)$$

The non-conservative term in the electron and electronic excitation energy equation $-p_e \nabla \cdot \vec{u}$, may poses problems in presence of discontinuity.

Alternatives are being sought as recently discussed in [113].

The solution of the partial differential equations, previously discussed, is obtained using a finite volume technique. We consider the system of governing equations written in integral conservation form:

$$\frac{\partial}{\partial t} \int_{\Omega} \mathbf{U} d\Omega + \oint_{\Sigma} \mathbf{F}^c \cdot \mathbf{n} d\Sigma + \oint_{\Sigma} \mathbf{F}^v \cdot \mathbf{n} d\Sigma = \int_{\Omega} \mathbf{S} d\Omega \quad (10.4)$$

where F^c and F^v are respectively the convective and diffusive fluxes and \mathbf{S} is the reaction term. We apply a conventional cell centered Finite Volume space discretization with weighted least square reconstruction [7], yielding second order accuracy. Oscillation free solutions are obtained with the multidimensional limiters of Barth-Jespersen [7] or Venkatakrishnan (our preferred choice in 3D) [175]. The numerical convective flux is computed by means of the Liou-Steffen AUSM scheme [109], appropriately extended to deal with thermo-chemical non equilibrium, which offers a good compromise between robustness and accuracy, while being not prone to the carbuncle phenomenon (at least we did not experience it in any of our calculations). We rewrite the system Eqs. (10.4) as follows:

$$\tilde{R}(P) = \frac{dU}{dt} + R^{FV}(U) = 0 \quad (10.5)$$

where $\tilde{R}(P)$ is a ‘pseudo-steady’ residual and $P = [\rho_s, \vec{V}, T, T_{vi}, T_e]$ is the vector of primitive variables, in which the governing equations are ‘explicitly closed’ and which is therefore the most logical choice for storing the solution. The choice of a Backward Euler time integrator leads to the following expression for $\tilde{R}(P)$:

$$\tilde{R}(P) = \frac{U(P) - U(P^n)}{\Delta t} + R^{FV}(U(P)), \quad (10.6)$$

where the relation $U = U(P)$ is an explicit analytical relation, i.e. the transformation from primary to conservative variables. The application of a one step Newton method yields the following linear system:

$$\left[\frac{\partial \tilde{R}}{\partial P} (P^n) \right] \Delta P^n = -\tilde{R}(P^n), \quad (10.7)$$

where the jacobian matrix $\frac{\partial \tilde{R}}{\partial P}$ is computed numerically. The GMRES algorithm with an ILU preconditioner serves to solve the corresponding linear systems arising from Newton linearizations.

The update is also performed in primitive variables:

$$P^{n+1} = P^n + \Delta P^n. \quad (10.8)$$

This scheme can effectively be applied with an arbitrarily convenient choice for the variables P , but also leaving freedom to the users in the choice of the implicit time integrator, e.g. Crank-Nicholson or Three Point Backward if time accuracy is required.

10.2 Multitemperature model: 1636 s case

The analysis to be presented shortly, concerns the nonequilibrium simulation of the flowfield in the shock layer of the FIRE II vehicle. The forthcoming results will allow us to verify the validity of the multitemperature model, comparing our results with the predictions given in Ref. [83].

Even if COOLFLUID is an unstructured solver, we found that structured meshes, carefully aligned with the shock, give better results in hypersonic regimes. Indeed any minor misalignment of the grid with the bow shock wave, can generate errors in the stagnation region, which can degenerate in the well-known carbuncle phenomena [32]. The use of unstructured grids is therefore avoided when possible.

Figure 10.1 shows a snapshot of the grid and the geometry of the heat shield from the symmetry axis (stagnation line) to the shoulder. Only half of the shock-layer is simulated, being the body symmetric and at zero incidence. The structured mesh accounts for 28841 elements, and was designed to contain the bow shock wave, for different points in the trajectory of the FIRE II experiment.

Although we recognize the importance of an accurate modeling of the gas-surface interaction [44, 45, 154, 174], for sake of simplicity, we consider the surface isothermal (at $T = 800$ K) and non-catalytic.

The AUSM+ scheme is used in the simulations, since it is exceptionally robust and it is carbuncle free even at these very high velocities. Second order accuracy has been achieved by means of the least square reconstruction in combination with the Venkatakrishnan [175] limiter.

As far as the physical model is concerned, the 2-temperatures TT_V model is used to describe the post shock thermal relaxation and Park's kinetic



Figure 10.1: Fire 2 vehicle. Axisymmetric grid composed of 28841 elements.

mechanism was employed to account for the chemistry taking place in the flow. Furthermore Ω^I , as modeled by Johnston and the non-preferential Ω^{CV} source terms are adopted.

In Ref. [102] a validation of COOLFLUID with the models implemented in the framework of this project is presented comparing our predictions against experimental data and different CFD results. In Figure 10.2, translational and vibrational temperatures are compared against the results provided from literature. The shock is located on the left as opposed to the boundary layer which is located at a distance of 5 cm from the shock front. The stand off distance is very similar for the different predictions. The maximum translational temperature, predicted by COOLFLUID, exceeds the values given by the reference codes. In particular, LAURA's predictions are slightly higher than 30 000 K as opposed to our results, which reach 45 000 K. The calculations have been performed on different grids and comparing the thickness of the shocks, we may infer that LAURA's results are more dissipative in the shock region. A possible explanation is given by lack of grid refinement in correspondence of the shock, which may justify the lowering of the maxi-

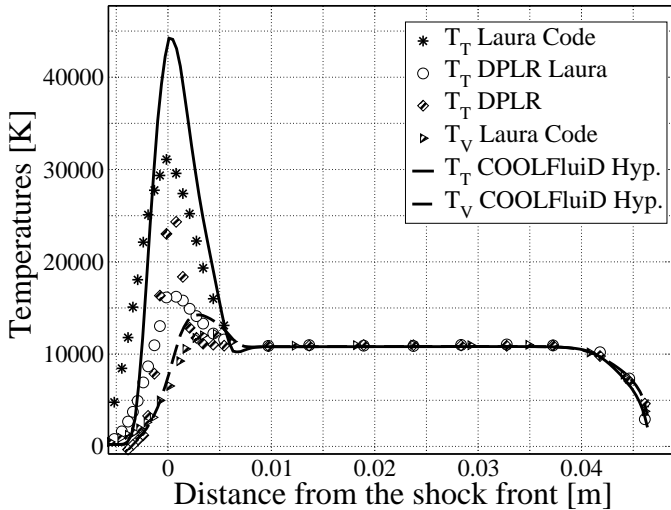


Figure 10.2: 1636 s. Temperature profiles: comparison with literature Ref. [83].

mum temperature.

Also, the reasons of the discrepancies in the vibrational temperature profiles are to be sought in a different modeling of the VT term. The use of an-harmonic oscillators in the expression of the Landau-Teller formula in the reference results, as opposed to the harmonic oscillator expression used throughout this work, may partially accounts for the differences shown in the picture. Furthermore the constants used in the Millikan and White formulas to express the relaxation times are slightly different: we use the constants given by Park in Ref. [146] as opposed to the other codes, whose relaxation time constants are given in Ref. [83].

In Figure 10.3, the number density of N , O and e^- are compared with results obtained with LAURA code and kindly provided by C. Johnston. The concentration profiles are in rather good agreement with LAURA's prediction in the post shock area as well as in the equilibrium region. Differences are found in correspondence of the boundary layer (right side of the picture), owing to the different assumption concerning the catalytic properties of the

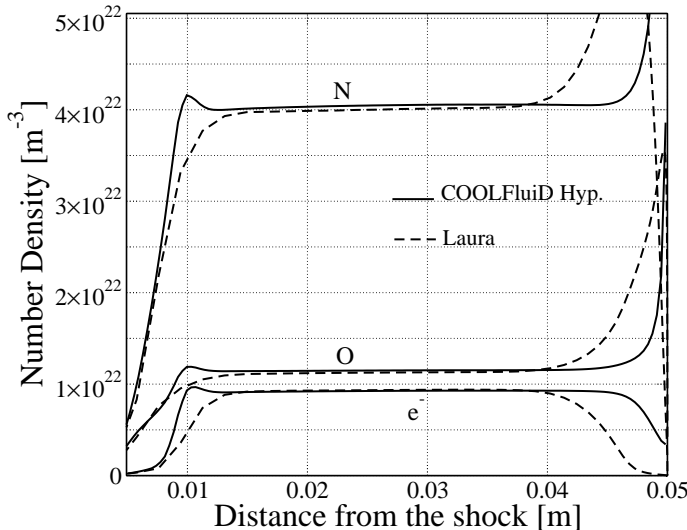


Figure 10.3: 1636 s. Number density profiles for N, O, e^- . Comparison literature: (unbroken lines) COOLFLUID Hypersonic; (dashed) LAURA code.

wall. We have assumed non-catalytic wall as opposed to LAURA's predictions which are based on the fully catalytic assumption. A detailed discussion on the influence of the catalytic activity of the wall on the results may be found in Ref. [6, 154].

It is interesting to compare the predictions given by COOLFLUID, with the ones of SHOCKING depicted in Figure 5.3. The better agreement, shown by COOLFLUID when compared with literature, is due to the influence of the viscous effects, neglected in SHOCKING. The vibrational temperature just after the shock in the viscous calculation (Figure 10.2) is higher than the free-stream value (which is the value assumed by SHOCKING) and promotes the dissociation of the molecular species. Also, in the area close to the shock, the steep gradients in temperature pressure and composition enhance the diffusion of the different species and in particular electrons, which can react with the incoming N_2 and O_2 molecules. All these effects constitute the so called *conduction precursor* [119] and have to be accounted for, since they may affect the chemistry.

Generally speaking the comparison of temperature and composition profiles shows a reasonable agreement with the solutions provided in literature.

10.3 Simplified Collisional-Radiative model: COOLFluiD hypersonic

To investigate the influences of the non-Boltzmann electronic distribution function on the physico-chemical properties of the plasma, we use the simplified CR model, discussed in chapter 9. The forthcoming results investigates the strong nonequilibrium effects, which characterize the shock layer of the FIRE II vehicle in the early part of its re-entry trajectory (1634 s).

As previously discussed, the approximate model was explicitly designed for its application to multidimensional flow solver and was proven to provide results in good agreement with the detailed CR model. Owing to the large number of equations to be solved, we decided to restrict our analysis to the atomic nitrogen, assuming that the electronic states of atomic oxygen are populated according to Boltzmann distribution. A common temperature, referred in the following as T_V , describes the vibrational and electronic excitation of the species in the mixture. Also, the effect of radiation on the flowfield is modeled in crude manner, using the escape factors and including radiation cooling effects. The resulting set of equations consists of twenty partial differential equations to be solved on the structured grid depicted in Figure 10.1.

The large nose radius of FIRE II, designed to reduce the effects of the convective heating, is responsible for the high temperatures and low convection speeds within the shock layer. Vibrational and translational temperatures in the stagnation region are depicted in Figure 10.4, assuming that the medium is optically thin ($\alpha = 1$). The upper part of the plot represents T , whereas the lower part is related to T_V . The temperatures seem to be rather uniform in radial direction, being the gradients very small because of the blunted nose, which strongly stagnates the flow. The evolution along the stagnation line is depicted in Figure 10.5. As expected the translational temperature strongly rises in the post shock region, as opposed to the vibrational temperature, which stays much lower. An important difference, with respect to the one dimensional results, is given by the post shock vibrational

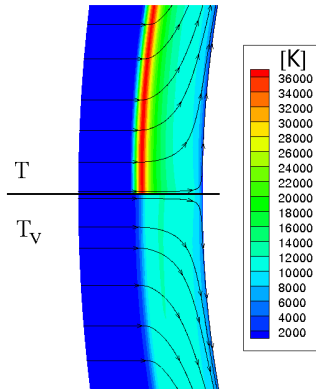


Figure 10.4: 1634 s. Temperature plots in the stagnation region. Upper part: Translational temperature T . Lower part: Vibrational temperature T_V .

temperature, which is defined as the temperature in correspondence of the peak in translational temperature. In the foregoing chapters, when dealing with onedimesional shock tube calculations, we imposed the freezing of the internal energy modes across the shock, assuming that the post-shock vibrational temperature was the same as the free-stream temperature. However, as demonstrated in Figure 10.5, the combined effects of viscosity and thermal conductivity lead to a finite thickness shock inducing vibrational excitation within the shock. The use of a shock slip condition [93] would allow to correct such discrepancies in the one dimensional calculations.

Figure 10.6 shows that the electron number density exhibits a strong dependence on optical thickness of the shock layer. In Figure (10.6) the upper part of the contour represents the optically thick case, whereas the optically thin results are shown in the lower part of the plot. As expected, the optically thin case exhibits lower electron densities, owing to the effects of the radiation cooling.

10.3.1 Detailed analysis: atomic nitrogen

The population of the excited states of atomic nitrogen, governed by the detailed kinetics, is compared with the corresponding equilibrium values, in order to characterize the extent of nonequilibrium within the shock layer. To this end we define the *nonequilibrium factor*, (χ), as the ratio of the pop-

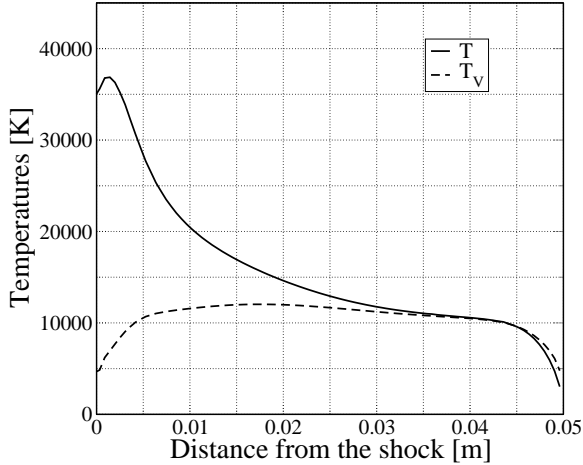


Figure 10.5: 1634 s. Temperature profiles along the stagnation line: T translational temperature; T_V vibrational temperature.

ulation provided by the CR calculations and the corresponding equilibrium density, given by the Boltzmann distribution at the temperature T_V . The evolution of χ for the grouped level N(4), (composed of N(4), N(5), N(6) ungrouped levels) is depicted in Figure 10.7. The upper part of the plot, shows the value of the nonequilibrium factor for the optically thick case ($\alpha = 0$), as opposed to the lower part, which displays results obtained assuming an optically thin medium.

Within the shock layer, we can observe a different behavior of the nonequilibrium parameter, as a function of the optical thickness of the medium: when radiative effects are accounted for, the value of χ is found to be far below one, with the exclusion of the boundary layer region, where the overpopulation factor is larger than one. When instead, the radiative processes are discarded, we observe a higher value of the nonequilibrium factor, owing to the absence of the radiative transitions, which bring about a depletion of the high lying states.

The comparison of the normalized populations ¹ predicted by the COOLFLUID, at 1 cm from the shock, and the predictions obtained using the one dimensional solver are shown in Figures 10.8. The results provided by the

¹The population divided by the degeneracy.

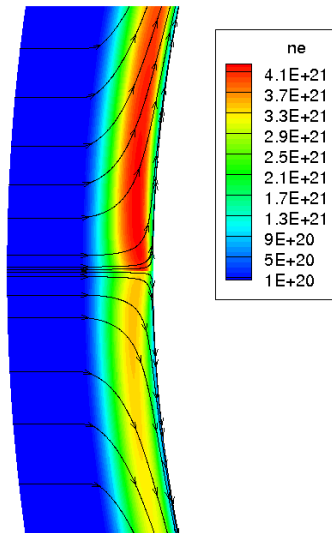


Figure 10.6: 1634 s. Comparison of the free electron number density: optically thick case (upper part); the optically thin case (lower part).

simplified CR model are in reasonable agreement with the prediction delivered by SHOCKING, when using the detailed model. Although the population predicted by COOLFLUID, exhibits a larger extent of nonequilibrium, the main features of the electronic distribution function are reproduced. The reasons for the small discrepancies are in part due to the finite thickness of the shock, which introduces an uncertainty in the relative location of the point under analysis, with respect to the one dimensional case.

As we move towards the wall the collisional processes tend to equilibrate the electronic levels, approaching the Boltzmann distribution as shown in Figure 10.9. As already demonstrated in section 6.2.5.3, the complete equilibration of the electronic states is not possible due to the optically thin assumption, which causes deviation of the equilibrium distribution.

Boundary layer:

The value of the nonequilibrium factor, χ was found everywhere lower than one, except in the boundary layer. Indeed, as the plasma approaches

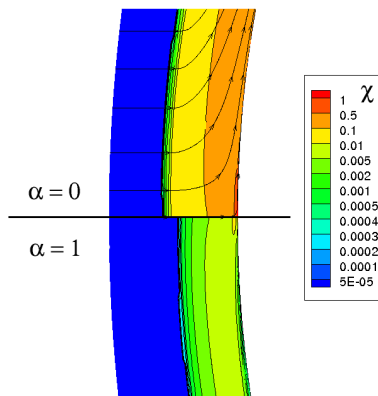


Figure 10.7: 1634 s. Nonequilibrium factor ($\chi = N(4)/N(4)_{EQ}$) as a function of the optical thickness: (upper part) optically thick case; (lower part) optically thin case.

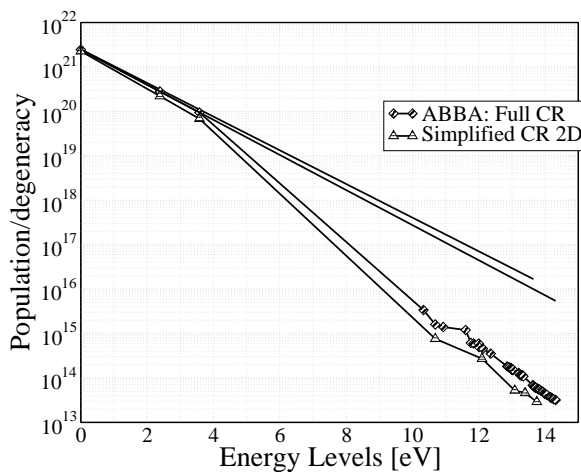


Figure 10.8: 1634 s. Boltzmann diagram: N. Located at 1 cm from the shock along the stagnation line.

the wall, the translational and vibrational temperatures drop, provoking the freezing of the internal energy modes. The situation is similar to the expanding flows, discussed in chapter 8.

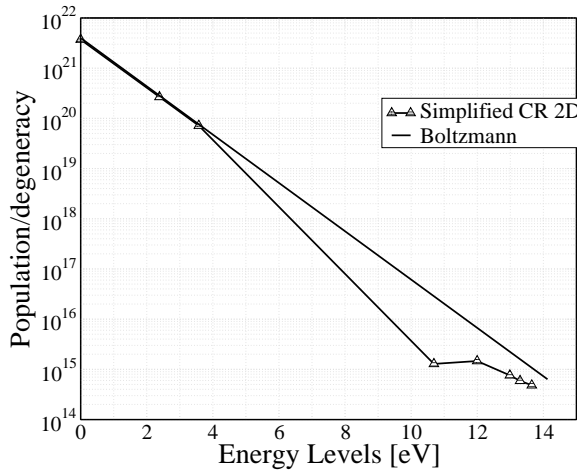


Figure 10.9: 1634 s. Boltzmann plot atomic nitrogen in correspondence of the boundary layer edge.

If we observe the behavior of the nonequilibrium factor in Figure 10.10, we may notice a sudden increase of χ close to the wall. Such increase is mainly due to the drop in the equilibrium value of $N_{EQ}(4)$ caused by the sudden reduction of T_V . Different is the behavior of the population of the excited states predicted by the CR model, which is insensitive to the cooling in the boundary layer.

As expected the effects of radiation tend to reduce the overpopulation within the boundary layer as shown in the same figure. The value of χ is found to be two orders of magnitude larger for the optically thick case than for the thin case.

In conclusion we observed a strong under-population of the excited states of atomic species in the earlier part of the shock layer, which is in agreement with the predictions obtained using the detailed model described in part II of the manuscript. Also, the use of COOLFLUID hypersonic allow to investigate the behavior of the electronic levels within the boundary layer. The results of such analysis demonstrate a strong overpopulation of the excited states, suggesting that the assumption of equilibrium among vibrational and electronic levels is not adequate to describe the behavior of the electronic

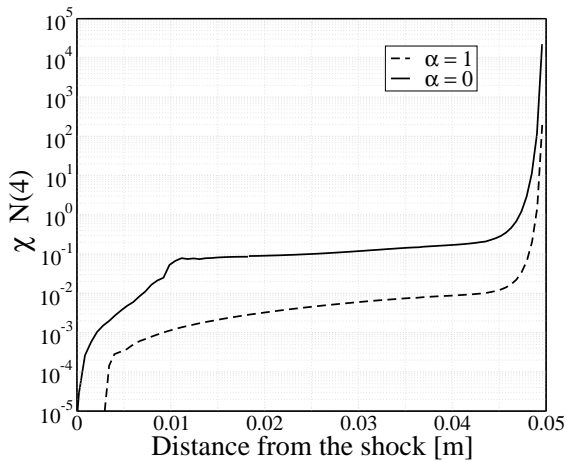


Figure 10.10: 1634 s. Nonequilibrium (χ) factor profile along the stagnation line: $N(4)$ grouped state.

states within the boundary layer.

REMARKS In the preceding analysis the collision integrals for the estimation of transport properties of the pseudo-species, have been assumed equal to the ground state value. The accurate modeling of the transport properties for excited species is discussed in Ref. [37].

10.4 3D simulations: Expert vehicle

In the following section, we briefly investigate effects of non-equilibrium in the shock layer around the EXPERT vehicle. The aim of the section is to show the 3D capabilities of the COOLFLUID Hypersonic solver. A more detailed analysis of the testcase to be presented can be found in Ref. [130].

The European re-entry vehicle EXPERT (EXPERimental Re-entry Testbed) [123] is part of the ESA's research program aiming at designing a low cost hypersonic flight experiment aerothermodynamic phenomena and thus provide real flight database for the validation of the numerical codes.

The conventional multi-temperature approach(T, T_{vN_2}, T_{vO_2}) with a separate temperature for N_2 and O_2 molecules will be employed to simulate the non equilibrium relaxation. The need for additional temperatures is due to the different vibrational relaxation characteristics of the different molecules considered. For instance, nitric oxygen quickly equilibrate[75] with the translational temperature as opposed to molecular nitrogen, which needs longer time.

Also, in order to better describe the influence of the vibration on the chemical kinetics, we introduce the model of Knab[95]. It is important to stress that this model accounts for the influence of vibration on the dissociation reactions and on other reactions such as exchange reactions.

A 5-species air mixture was employed due to computational constraints, and the macroscopic kinetic model of Park [146] was selected to account for the reactions taking place within the shock layer.

The results to be presented shortly, concern the investigation of a point in the early part of the trajectory followed by EXPERT during the re-entry phase. This point has been chosen in order to investigate flow conditions characterized by a strong thermal and chemical nonequilibrium. The flight conditions relative to the point in the trajectory are shown in Tab.(10.1).

Table 10.1: Flight conditions.

Mach	18.4
Pressure [Pa]	2
Speed [m/sec]	5040.0
Temperature [K]	186.4
Wall Temperature [K]	1650

This 3D computation was run in parallel on a 3.3 million hexaedra mesh (generated by Fabio Pinna), on up to 316 AMD64 processors on KU Leuven cluster. The surface mesh is presented in Figure 10.11-10.12b.

The full three dimensional temperature fields are shown in Figures 10.13 to 10.15. The peak in translational temperature (Figure 10.13), slightly higher than 12100 K, is justified by the low speed conditions which charac-

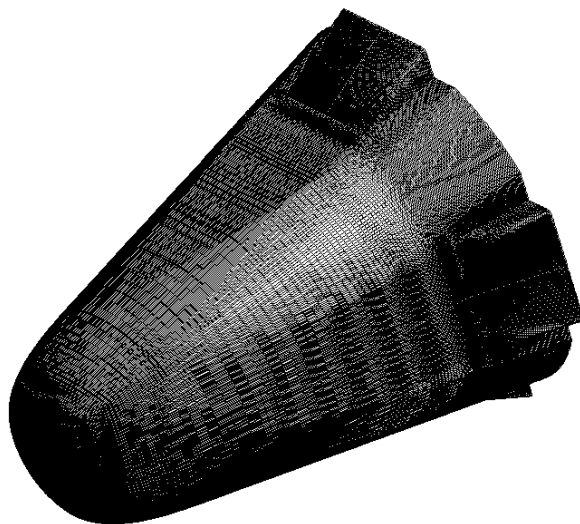
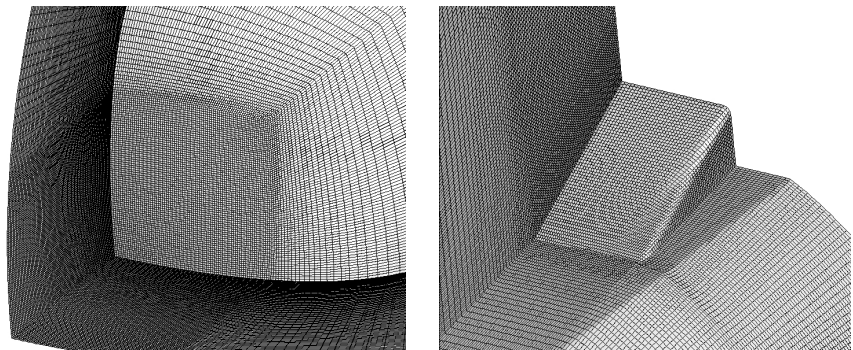


Figure 10.11: Global view of the wall surface mesh for the EXPERT vehicle.



(a) Zoom on the wall and mirror mesh surfaces near the nose

(b) Zoom on the wall and mirror mesh surfaces near one flap

Figure 10.12: Detailed views on the surface mesh for the EXPERT vehicle.

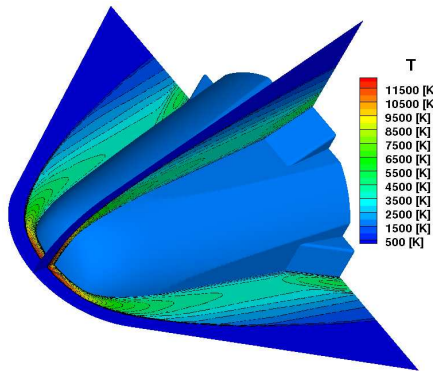


Figure 10.13: Ro-translational temperature on the EXPERT vehicle.

terized the flight condition under investigation. Nevertheless owing to the extremely low pressure, strong thermal nonequilibrium effects are present in the shock layer. The analysis of the contours and isolines of vibrational temperature of N_2 in Figure 10.14 reveals the strong nonequilibrium with the translational energy mode. The maximum in the post-shock vibrational temperature of N_2 is about 6300 K, exceeds the corresponding value in the vibrational temperature of O_2 , presented in Figure 10.15, which exhibits a maximum of 5100 K.

The flight conditions extrapolated from the reentry trajectory of the EXPERT vehicle have been analyzed by means of a 3D Navier Stokes calculation, in order to highlight the thermal and chemical nonequilibrium effects. The results presented clearly demonstrate the 3D capabilities of the COOLFLUID Hypersonic solver, whose development was one of the goal of the present project.

Summary

The chapter discusses an application of simplified Collisional Radiative model, developed in Chapter 9, to the flow surrounding the FIRE II vehicle in the early part of re-entry trajectory, using COOLFLUID Hypersonic, a Navier Stokes solver extended in the framework of this project, to the simulation of chemically reacting flows. The detailed analysis of the characteristic flow-

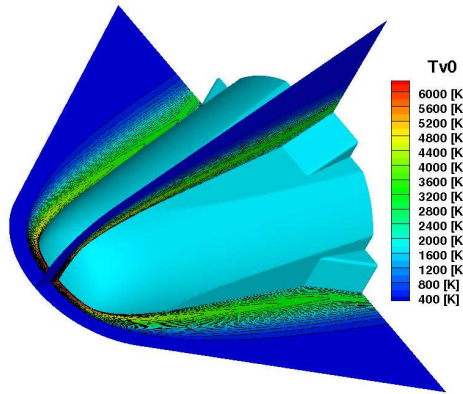


Figure 10.14: Vibrational temperature of N_2 field on the EXPERT vehicle.

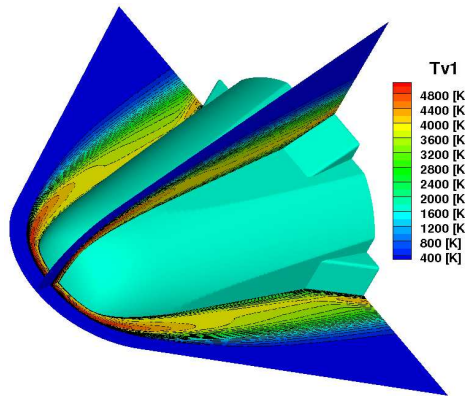


Figure 10.15: Vibrational temperature of O_2 field on the EXPERT vehicle.

field quantities is complemented by a more detailed investigation of the electronic energy distribution function of the atomic nitrogen.

The investigation shows a strong depopulation of the excited states of atomic nitrogen in the post shock region, as opposed to the boundary layer area which exhibits a strong overpopulation of the atomic excited states.

Also, a validation of the multitemperature model with the results produced by LAURA code and a brief analysis of the 3D flowfield in the shock layer of the EXPERT vehicle are presented. In particular the latter analysis demonstrate the 3D capabilities of the Navier Stokes solver when applied to low speed re-entry cases.

Chapter 11

Conclusions and future research

In this last chapter, the achievements, the contributions to the field as well as the recommendations for future research are discussed.

The numerical modeling of the chemical reacting flows, requires the solution of the well known Navier-Stokes equations, complemented by additional conservation equations. The number of equations needed, in general, depends on the assumptions made and on the degree of approximation used in the modeling of the physical phenomena and can be large in sophisticated approaches such as in state to state or collisional radiative [38, 107, 151] models, or significantly reduced as in multitemperature models [24, 33, 138].

Following the historical evolution of the models for the description of nonequilibrium high enthalpy flows, the first part of the manuscript gives a review of the state of the art multitemperature models, with particular attention to the interaction of kinetics and excitation of the internal energy modes. Also, two simplified flow solvers are presented and used as a benchmark to test the physical models studied: SHOCKING, which simulates the thermal and chemical relaxation behind a strong normal shock; nozzle code, which reproduces the physical and chemical effects in the relaxing flow in a nozzle, within the quasi-one dimensional approximation.

Owing to their computational efficiency, these models have demonstrate to be invaluable tools for the testing of the more sophisticated and advanced collisional radiative models, analyzed in the second part of the manuscript. Although based on very simple physical representation of dynamics of the flow, which neglects the viscous nature of the fluid, SHOCKING has shown to be capable of reproducing the most complicated non-Boltzmann effects occurring in strong nonequilibrium flows as well as the radiative signature of shock heated air, generated in high enthalpy shock tubes, allowing for a validation of the physical models.

The insights gained thanks to the detailed analysis of the nonequilibrium flows, allowed to synthesize an approximate CR model, drastically reducing the computational effort and keeping the accuracy of the more sophisticated CR models. The final step in the project consists in the implementation of the simplified collisional radiative and multitemperature models in the multidimensional CFD solver, which allow for a more realistic representation of the flow features. To this end, COOLFLUID Hypersonic, a multitemperature unstructured 3D-Navier-Stokes code, has been successfully developed and validated against results available in literature.

MUTATION-2.0

Mutation is an electronic library developed for the estimation of the thermodynamic, transport properties and chemistry, of thermal plasmas and was written by T. Magin [114]. In the framework of this work MUTATION was extended to the modeling of nonequilibrium plasmas, within the multitemperature or state to state approximation. The state-of-the-art multitemperature models have been successfully implemented, tested and validated against literature and experimental results. The detailed and approximate electronic CR models have been included in the library, which can account for non-Boltzmann effects in air mixture as well as CO₂ and Titan mixture, given the flexibility of the implementation.

Also, an accurate thermodynamic model for the partitioning of the internal energy into vibrational, rotational, and electronic contributions, consistently accounting for the non-separable nature of the various energy modes, was also included in the library.

Accomplishments

Part 1: multitemperature models

Nonequilibrium plasma flows are often described by means of multitemperatures models. Under non equilibrium, the internal energy modes do not have time to equilibrate among each other and one temperature is not sufficient to describe the state of the gas. Thus, assuming that the populations of internal energy states follow a Boltzmann distribution, different temperatures are employed to model the relaxation of the energy modes to a common temperature. The system of governing equations, describing gases under

thermal and chemical nonequilibrium, requires the definition of the thermodynamic, transport properties, chemical reaction rates and energy exchange terms of the studied gas mixture.

Thermodynamic properties

Thermodynamic properties of individual species are computed by means of the semi-classical statistical mechanics. In particular, when describing the thermodynamic properties of diatomic species, two different approaches can be followed: a first approach, referred to as *approximate model* in the following, based on the simplifying assumption of rigid rotor and harmonic oscillator and a second model, more accurate, termed *accurate model* in the following, which accounts for anharmonicity effects and coupling between vibration and rotation. Both formulations are general and can be used in equilibrium as well as in non equilibrium situations. The limit of validity of these models is dictated by the limit of applicability of the multitemperature approaches and it is restricted therefore to small departures from equilibrium, when distributions of the internal modes are still Boltzmann. When performing calculations with the accurate model, a special treatment of the thermodynamic properties is required due to the fact that internal energy modes are strictly coupled to each other and are relaxing according to different temperatures, as prescribed by Jaffe in Ref. [91]. This formulation leads to a definition of internal energies which are dependent on all internal temperatures, accounting in this way for the influence of the modes on each other. The computational effort needed to use this formulation in CFD solvers, is cumbersome and thus it was used only for validation purposes.

Although a direct comparison of the approximate model with the more accurate model, for a range of temperatures compatible with hypersonic entry calculations (i.e. 300–50 000 K), revealed strong differences in terms of specific heats and enthalpy of the diatoms, the effects of such discrepancies on the characteristic flowfield quantities, assessed using simplified flow-solvers, was found to be negligibly small. Hence since the approximate model offers better performances in terms of computational efficiency, it has been used in the present study.

Energy exchanges

In the present work, particular emphasis was given to the modeling of the exchange mechanisms between the internal energy modes. An accurate re-

view of the different models present in literature was performed and a series of tests for different flow typologies were carried out in order to assess their reliability and in particular their range of applicability.

Thermal nonequilibrium models are distinguished by the way they describe the interaction among the excitation of the internal energy modes and the macroscopic kinetic mechanisms employed. Particular attention was paid to the modeling of the mutual interaction among dissociation and vibration. In the literature two different classes of models can be identified: *preferential* and *non-preferential* dissociation models. The models of Treanor [116], Knab [96], Macheret [111] fall into this category, whereas Candler's model [33] constitutes one example of non-preferential dissociation model. The analysis performed led us to the conclusion that the vibration-chemistry interaction based on the preferential dissociation model causes a reduction of the thermal and chemical relaxation rate, with respect to the non preferential dissociation models.

Part 2: collisional radiative models

The effects of non-Boltzmann distribution of the atomic and molecular electronic levels have been accounted for by means of collisional-radiative model. The model adopted combines a state specific approach to determine the population of the electronic energy levels and multitemperature approach for the rotational and vibrational energy modes. The nonequilibrium models developed, used in fully coupled manner with the three different flowfield solver, have been applied to the FIRE II flight experiment, the EAST experimental campaign and nozzle of the VKI Minitorch, aiming to study the effects of the non-Boltzmann population distributions.

FIRE II: *atoms*

The departures of the atomic electronic energy populations from Boltzmann distributions for one dimensional air flows obtained in a shock-tube, have been investigated. The operating conditions are taken from three points in the trajectory of the FIRE II flight experiment at 1634 s, 1636 s, and 1643 s elapsed time from the launch. We have found that, for the first two points of the trajectory (1634 s and 1636 s), the electronic energy level populations of the N and O atoms depart from Boltzmann distributions since the high lying bound electronic states are depleted. The analysis of the last trajectory point (1643 s) reveals instead a Boltzmann distribution among the electronic

levels. An analysis of the state of the flow for the first flight condition (1634 s) led us to the conclusion that the excited species of atoms satisfy the quasi-steady-state assumption, except for the two metastable states. As a consequence, the global rate coefficients and free electron energy loss terms could be derived in the steady state based on our model, considering however the metastable states as separate pseudo-species governed by their own chemical-kinetic mechanism.

Moreover, the validity of the standard QSS approach widely used by the aerospace community has been tested; the results obtained by means of our full CR model and the standard QSS model are found in good agreement. It is important to mention that the full CR model is more general, since the parameters governing the free-electron energy losses by electron impact ionization are obtained from the expressions for the reaction rates intrinsic to the model, without any a priori hypothesis.

Finally, we have shown that the populations of high-lying excited states of atoms obtained by using the rates of Park [138] for electron-impact excitation and ionization reactions are up to two orders of magnitude higher than the populations obtained by using the rates of Bultel et al. [27], consistent with the result of Johnston [93].

Shock Tube experiments: EAST

This study was committed to the partial validation of the collisional-radiative model against recent experimental data. The behavior of the electronically excited states of the atoms in the one dimensional air flows obtained in a shock-tube, has been discussed. The operating conditions have been taken from the test campaign carried out at NASA Ames on the EAST facility. We have compared the radiative intensity profiles with the experimental data provided in Ref. [92]. We found good agreement for the low pressure runs (0.1 torr), where the flow is in strong nonequilibrium and for the high pressure runs (0.3 torr), where the post-shock population density of the excited states follows a Boltzmann distribution.

Differences have been found for one of the low pressure tests, where the radiative overshoot was under-predicted by the baseline model tested (ABBA). An alternative set of reaction constants, partially based on the work of Frost et al. [62], have been proposed for the excitation and ionization of atomic species by electron impact. The use of the improved kinetic model have reduced the discrepancies with the experimental data, being the differences in the most unfavorable case less than 50%.

FIRE II: atoms and molecules

The analysis of the early part of the trajectory of the FIRE II flight experiment was carried out with detailed CR model for atomic and molecular species. The behavior of the atomic species showed strong departures from the population of the excited states as previously discussed. Departures in the population of the electronic states of the molecules were in general limited to a narrow zone close to the shock front, although the extent of nonequilibrium was found to be strongly dependent on the set of kinetic mechanisms selected, for some key electronic transitions. For instance, the use of Teulet's rate constants [171] led to small departure from equilibrium distribution, as opposed to the model of Gorelov [73], which predicted a strong depletion of the population of the excited states. Furthermore a comparison with the more recent model of Park revealed a rather good agreement for predictions involving molecules as opposed to the results related to the electronic levels of the atoms, which show discrepancies.

Also, several physical phenomena occurring in the shock layer of a space-craft re-entering at high re-entry speed were investigated. The main conclusions are listed hereafter:

- The vibration-dissociation coupling was found to have a small influence on the results, since at high speed the dissociation does occur from all the vibrational levels and it is not restricted to the upper vibrational levels. In other words there is not a preferential way for the molecules to dissociate.
- The influence of the optical thickness of the medium on the results, modeled in a crude manner making use of escape factors, put forward the need for a coupling of radiation and flowfield calculation, given the influence of the radiative processes on the electron energy distribution function and on the thermo-physical properties of the plasma.
- The influence of the precursor phenomena on the thermo-physical state of the shock layer, was found to be negligible for the typical lunar entry conditions. Similar are the conclusions concerning the processes involving the excitation of the heavy particles, which were found negligible respect to the interaction with the free-electrons.

VKI Minitorch

The analysis of the plasma during the expansion in the nozzle of the VKI Minitorch facility was studied using an electronically specific collisional radiative model for air plasmas. Departures of the electronic state distribution function of atoms and molecules from the Maxwell-Boltzmann distribution were found at the outlet of the nozzle. Also, the use of escape factors for the modeling of the optical thickness of the plasma, has shown the relevance influence of radiation on the results. When the medium was considered optically thick the electronic states of the atoms and molecules were found strongly depopulated. However when the medium was assumed optically thin, a strong reduction of the over-population of the electronic levels was shown. In particular the population of some electronic states of atomic species, from which the highly energetic atomic lines originates, were found underpopulated with respect to the Boltzmann population.

Approximate CR model

The proper modeling of the radiative and kinetic processes occurring in nonequilibrium plasmas, requires the use of a large number of equations, restricting the use of CR model to 1D or 0D calculations. To this end an efficient and accurate model for the simulation of the nonequilibrium plasma flows was developed, in order to account for non-Boltzmann distribution in multidimensional CFD solver, preserving the computational efficiency of the multitemperature models. The approximate model, for the electronic levels of the atomic species was developed, lumping the excited states in macroscopic groups, with a consequent drastic reduction of pseudo-species to be accounted for. A direct comparison against the detailed CR model has demonstrated the accuracy of the model.

Part 3: COOLFluiD hypersonic

The approximate CR model previously discussed, was successfully applied to COOLFLUID Hypersonic. The extension of the multitemperature models did not require any major change in the solver, being the modifications limited to the inclusion of additional conservation equations for the pseudo-species.

The hybrid CR/Multitemperature models developed in the framework of this work allowed to successfully model the strong nonequilibrium effects,

present in the early part of the FIRE II trajectory, accounting for the de-population of the excited states of the atomic species, due to ionizational nonequilibrium effects. Also, the computational efficiency of the multitemperature models, was successfully combined with the accuracy of the collisional radiative model.

Future work

The recommendations for future research are discussed.

Coupling with radiation

Radiation may have a strong influence on the state of the gas and the accurate coupling with flowfield solver is desirable in case of high speed re-entries. The coupling with radiation would allow to accurately define the escape factors in the master equations and the source term Q^{Rad} in the energy conservation equation, which account for the radiative cooling effects. The radiative transport equation is to be solved fully coupled with the master equations for the kinetics, momentum and energy conservation equations. Owing to the large computational resources needed to estimate the radiative properties of the medium, i.e. adsorption and emission coefficients, the radiative transport equation is to be solved in a loosely coupled manner as indicated in Ref. [82].

Nitrogen dissociation

In the past, physical models for nonequilibrium phenomena have been developed, based on experimental data obtained in high enthalpy facilities, such as shock-tube wind-tunnels, for specific flight conditions. The problem with this methodology is that the models can contain many uncertainties that can be extremely difficult to quantify. Recently, the computational chemists have embarked on an alternate solution, namely the characterization of nonequilibrium chemistry from first principles. The implementation of this set of reaction rates into a one dimensional fluid code is a necessary step towards the future development of simplified mechanisms for three dimensional simulations of atmospheric entry flows.

The work carried out at Stanford in the framework of the CTR summer program and published in Ref. [25], constitutes a first step toward the devel-

opment of a simplified mechanism for 3-D simulations of atmospheric entry flows.

Appendix

Appendix A

Collisional Radiative model: data

A.1 Electronic levels

The electronic levels for the atomic species are listed in Table A.1, indicating the energy E_k , degeneracy g_k and the second quantum number l_k to distinguish the optically forbidden and allowed transitions. The list of the states was taken by Ref. [22, 23].

Table A.1: Index, energy, degeneracy, and secondary quantum number for the N and O electronic energy states considered.

k for N(k)	E_k (eV)	g_k	l_k	k for O(k)	E_k (eV)	g_k	l_k
1	0.000	4	1	1	0.000	9	1
2	2.384	10	1	2	1.970	5	1
3	3.576	6	1	3	4.190	1	1
4	10.332	12	0	4	9.146	5	0
5	10.687	6	0	5	9.521	3	0
6	10.927	12	1	6	10.740	15	1
7	11.603	2	1	7	10.990	9	1
8	11.759	20	1	8	11.838	5	0
9	11.842	12	1	9	11.930	3	0
10	11.996	4	1	10	12.090	25	2
11	12.006	10	1	11	12.100	15	2
12	12.125	6	1	12	12.300	15	1
13	12.357	10	0	13	12.370	9	1
14	12.856	12	0	14	12.550	15	0
15	12.919	6	0	15	12.670	5	0

k for N(k)	E_k (eV)	g_k	l_k	k for O(k)	E_k (eV)	g_k	l_k
16	12.972	6	2	16	12.710	3	0
17	12.984	28	2	17	12.740	5	0
18	13.000	26	2	18	12.760	25	2
19	13.020	20	2	19	12.770	15	2
20	13.035	10	2	20	12.780	56	3
21	13.202	2	1	21	12.860	15	1
22	13.245	20	1	22	12.890	9	1
23	13.268	12	1	23	13.030	5	0
24	13.294	10	1	24	13.050	3	0
25	13.322	4	1	25	13.080	40	2
26	13.343	6	1	26	13.087	56	3
27	13.624	12	0	27	13.130	15	1
28	13.648	6	0	28	13.140	9	1
29	13.679	90	2	29	13.220	5	0
30	13.693	126	3	30	13.230	3	0
31	13.717	24	1	31	13.250	168	2
32	13.770	2	1	32	13.330	5	0
33	13.792	38	1	33	13.340	3	0
34	13.824	4	1	34	13.353	96	2
35	13.872	10	1	35	13.412	8	0
36	13.925	6	1	36	13.418	40	2
37	13.969	18	0	37	13.459	8	0
38	13.988	60	2	38	13.464	40	2
39	13.999	126	3	39	13.493	3	0
40	14.054	32	1	40	13.496	40	2
41	14.149	18	0				
42	14.160	90	2				
43	14.164	126	3				
44	14.202	20	1				
45	14.260	108	0				
46	14.316	18	0				

Table A.2: Probability $A_{i \rightarrow j}$ for $\text{N}(i) \rightarrow \text{N}(j < i) + h\nu$ and $\text{O}(i) \rightarrow \text{O}(j < i) + h\nu$ spontaneous emission.

i for $\text{N}(i)$	j for $\text{N}(j)$	$A_{i \rightarrow j} (\text{s}^{-1})$	i for $\text{O}(i)$	j for $\text{O}(j)$	$A_{i \rightarrow j} (\text{s}^{-1})$
6	1	2.30×10^8	5	1	3.80×10^8
4	1	5.40×10^8	9	1	1.77×10^8
5	2	5.50×10^8	11	1	0.38×10^8
5	3	2.00×10^8	14	1	2.30×10^8
13	2	4.60×10^8	19	1	6.77×10^7
13	3	0.52×10^8	17	2	4.50×10^8
10	6	4.05×10^6	6	4	0.34×10^8
17	2	8.60×10^3	12	4	3.26×10^5
18	2	0.65×10^8	7	5	0.28×10^8
20	2	0.47×10^8	13	5	6.60×10^5
16	3	1.30×10^8	8	6	2.72×10^7
18	3	5.80×10^3	10	6	4.19×10^7
20	3	1.30×10^8	15	6	0.71×10^7
15	2	1.10×10^8	18	6	7.01×10^6
15	3	0.20×10^8	23	6	3.05×10^6
22	6	0.25×10^6	25	6	1.23×10^6
23	6	0.37×10^6	9	7	1.88×10^7
25	6	0.43×10^6	11	7	2.35×10^7
28	2	0.33×10^8	14	7	2.90×10^7
8	4	0.19×10^8	16	7	0.62×10^7
9	4	2.28×10^7	19	7	3.25×10^6
10	4	3.18×10^7	24	7	2.34×10^6

A.2 Einstein coefficients

We have taken into account 45 spontaneous emission lines for N and 24 for O with an Einstein probability higher than $5 \cdot 10^{-3} \text{ s}^{-1}$ for N and $3 \cdot 10^5 \text{ s}^{-1}$ for O. The data are taken from NIST.

i for N(i)	j for N(j)	$A_{i \rightarrow j}(s^{-1})$	i for O(i)	j for O(j)	$A_{i \rightarrow j}(s^{-1})$
11	5	2.17×10^7	12	8	4.50×10^6
12	5	2.86×10^7	12	10	4.70×10^5
31	5	1.70×10^6			
31	13	1.59×10^7			
22	4	0.02×10^8			
23	4	0.73×10^7			
25	4	0.25×10^7			
21	5	2.34×10^6			
16	7	2.56×10^7			
17	8	3.73×10^7			
19	8	9.92×10^6			
17	9	7.46×10^4			
18	9	6.30×10^6			
19	9	2.48×10^7			
18	10	5.72×10^6			
18	11	1.16×10^7			
20	11	0.06×10^8			
14	8	1.47×10^7			
14	9	0.76×10^7			
27	8	3.89×10^6			
27	9	2.12×10^6			
38	7	2.30×10^5			
37	9	6.10×10^5			

Table A.3: Nitrogen. Rate constant for electron impact excitation $K_{i \rightarrow j}$.

i for N(i)	j for N(j)	A	η	T_x
1	2	$3.30e - 08$	-0.109	39452.44
1	3	$8.77e - 09$	-0.084	43417.07
1	4	$2.79e - 04$	-0.876	123410.45
1	5	$3.45e - 09$	-0.091	125411.13
1	6	$1.12e - 07$	-0.224	127800.78
1	7	$6.62e - 09$	-0.234	139453.98
1	8	$1.28e - 08$	-0.138	137729.63
1	9	$1.71e - 10$	0.206	138658.06
1	10	$8.47e - 10$	0.205	142252.22
1	11	$1.85e - 08$	-0.239	144791.64
1	12	$2.75e - 08$	-0.320	148734.44
1	13	$1.24e - 10$	-0.041	144053.49
1	16	$6.80e - 10$	-0.074	154418.32
1	17	$3.39e - 09$	-0.089	154637.63
1	18	$2.75e - 11$	0.260	154754.30
1	19	$9.70e - 10$	-0.020	155288.94
1	20	$5.39e12$	-4.517	205389.51
1	30	$8.11e - 10$	0.031	165586.16
1	36	$1.05e - 10$	0.128	168085.09

A.3 Rate coefficients

Frost et al. in Ref. [62] compiled a new set of inelastic cross sections for atomic and ionized nitrogen. The data-set was obtained using the R-matrix method and it validated using spectroscopic measurements in the visible and Vacuum Ultra Violet (VUV) wavelength range using low pressure arc plasmas. The inelastic transitions studied involve the excitation from the ground state and two metastable states to the first 23 states of atomic nitrogen.

The rate constants provided by Frost have been fitted in Arrhenius form using a least squared method and are available in Table A.3. *Do not use the rates for free electron temperatures larger than 20 000 K.*

i for N(i)	j for N(j)	A	η	T_x
2	3	$1.11e - 06$	-0.376	25119.09
2	4	$8.31e - 07$	-0.538	94851.73
2	5	$5.21e - 09$	0.029	96963.27
2	6	$5.21e - 06$	-0.661	104196.28
2	7	$4.08e - 06$	-0.808	110316.60
2	8	$1.38e - 08$	-0.194	111609.39
2	9	$3.41e - 08$	-0.319	113259.37
2	10	$1.11e - 07$	-0.526	118210.59
2	11	$4.52e - 09$	0.092	112224.58
2	12	$1.11e - 11$	0.425	113569.51
2	13	$4.42e - 10$	0.266	115515.53
2	16	$6.51e - 11$	0.138	125342.31
2	17	$4.70e - 09$	-0.154	126137.38
2	18	$3.25e - 10$	0.275	125733.55
2	19	$7.05e - 09$	-0.258	126669.46
2	20	$1.59e - 10$	0.226	126307.33
2	30	$8.36e - 09$	0.008	136402.69
2	36	$7.24e - 08$	-0.393	144960.52
3	4	$3.54e - 07$	-0.442	80525.13
3	5	$5.10e - 09$	0.046	82469.90
3	6	$1.43e - 05$	-0.744	90736.93
3	7	$1.64e - 08$	-0.353	98613.73
3	8	$6.25e - 07$	-0.530	97954.63
3	9	$2.83e - 07$	-0.494	98276.46
3	10	$3.22e - 09$	-0.295	100461.21
3	11	$1.63e - 09$	0.023	97855.92
3	12	$9.40e - 10$	0.264	101459.10
3	13	$2.09e - 09$	0.064	104494.52
3	16	$1.10e - 10$	0.310	111505.82
3	17	$1.98e - 09$	-0.086	112538.98
3	18	$6.95e - 10$	0.078	112118.80
3	19	$5.52e - 09$	-0.151	112649.10
3	20	$3.31e - 10$	0.312	112386.89
3	30	$1.17e - 08$	-0.204	125641.08
3	36	$2.78e - 09$	0.097	124619.59

Bibliography

Each reference is followed by the list of the pages where it is cited.

- [1] V. I. Adamovich, S. O. Macheret, W. J. Rich, and C. E. Treanor. Vibrational energy transfer rates using a forced harmonic oscillator model. *Journal of Thermophysics and Heat Transfer*, 2(1):57–65, 1998. 170
- [2] R. Allen, P. Rose, and J. Camm. Nonequilibrium and equilibrium radiation at super-satellite re-entry velocities. *AVCO Research Report*, 156, 1962. 102
- [3] J. Bacri and A. Medani. Electron diatomic molecule weighted total cross section calculation. *Phisica*, 101(C):399–409, 1980. 165
- [4] J. Bacri and A. Medani. Electron diatomic molecule weighted total cross section calculation II. application to the nitrogen molecule. *Phisica*, 101(C):410–419, 1980.
- [5] J. Bacri and A. Medani. Electron diatomic molecule weighted total cross section calculation III. main inelastic processes for N_2 and N_2^+ . *Phisica*, 112(C):101–118, 1982. 165, 167, 289
- [6] P. F. Barbante. *Accurate and Efficient Modeling of High Temperature Nonequilibrium Air Flows*. PhD thesis, von Karman Institute, Rhode-Saint-Genèse, Belgium, 2001. 26, 231
- [7] T. Barth and D. Jespersen. The design and application of upwind schemes on unstructured meshes. Technical Paper 89-0366, AIAA, Reno, Nevada, January 1989. 227
- [8] D. Bates, A. Kingston, and R. McWhirter. Recombination between electrons and atomic ions. i. optically thin plasmas. *Proceedings of the Royal Society, Series A*, 1:297–312, 1962. 6
- [9] D. A. Benoy, J. A. M. van der Mullen, and D. C. Schram. Radiative energy loss in a non-equilibrium argon plasma. *Journal of Physics D: Applied Physics*, 26:1408–1413, 1993. 204

- [10] A. Berrington, P. Burke, and W. Robb. The scattering of electrons by atomic nitrogen. *Journal of Physics B: Atomic and Molecular Physics*, 8(15):2500–2511, 1975. 112, 113
- [11] A. Bhatia and S. Kastner. The neutral oxygen spectrum. I. collisionally excited level populations and line intensities under optically thin conditions. *The Astrophysical Journal Supplement Series*, 96:325–341, 1995. 102, 106, 286
- [12] G. A. Bird. *Molecular Gas Dynamics and the Direct Simulation of Gas Flows*. Oxford University Press, New York, 1994. 17
- [13] D. Bose and G. Candler. Thermal rate constants of the $\text{N}_2 + \text{O} \rightarrow \text{NO} + \text{O}$ reaction using ab initio 3 a and 3 a potential-energy surfaces. *Journal of Chemical Physics*, 104(8):2825, 1996. 114
- [14] D. Bose and G. Candler. Thermal rate constants of the $\text{O}_2 + \text{N} \rightarrow \text{NO} + \text{O}$ reaction using ab initio 3 a and 3 a potential-energy surfaces. *Journal of Chemical Physics*, 107(16):6136, 1997. 114
- [15] D. Bose, M. Wright, D. Bogdanoff, G. Raiche, and G. A. Allen. Modeling and experimental assessment of CN radiation behind a strong shock wave. *Journal of Thermophysics and Heat Transfer*, 20:220, 2006. 93, 138
- [16] D. Bose, M. J. Wright, D. W. Bogdanoff, G. A. Raiche, and G. A. Allen. Modeling and experimental assessment of CN radiation behind a strong shock wave. *Journal of Thermophysics and Heat Transfer*, 20(2):220–230, 2006. 143
- [17] D. Bose, E. McCorkle, C. Thompson, D. Bogdanoff, D. Prabhu, G. Allen, and J. Grinstead. Analysis and model validation of shock layer radiation in air. In *AIAA*, pages AIAA 2008–1246, Reno, Nevada, January 2008. 111, 137, 139
- [18] B. Bottin. *Aerothermodynamic Model of an Inductively-Coupled Plasma Wind Tunnel*. PhD thesis, von Karman Institute, Rhode-Saint-Genèse, Belgium, 1999. 33
- [19] B. Bottin, D. Vanden Abeele, M. Carbonaro, G. Degrez, and G. S. R. Sarma. Thermodynamic and transport properties for inductive plasma modeling. *Journal of Thermophysics and Heat Transfer*, 13:343–350, 1999. 33

- [20] A. Bourdon and A. Bultel. Detailed and simplified kinetic schemes for high enthalpy air flows and their influence on catalycity studies. In *Experiment, modeling and simulation of gas surface interaction for reactive flows, VKI-LS Rhode-Saint-Genèse, Belgium, February 6-9 2006*, 1:60, 2006. 4, 108, 112
- [21] A. Bourdon and P. Vervisch. Electron-vibration exchange models in nitrogen flows. *Physical Review E*, 55(4):4634, 1997. 68
- [22] A. Bourdon and P. Vervish. Three body recombination rates of atomic nitrogen in low pressure plasma flows. *Physical Review E*, 54(2):1888–1898, 1996. 96, 108, 170, 257
- [23] A. Bourdon, Y. Térésiak, and Vervisch. Ionization and recombination rates of atomic oxygen in high temperature air plasma flows. *Physical Review E*, 57(4):4684–4692, 1996. 96, 170, 257
- [24] A. Bourdon, A. Leroux, P. Domingo, and P. Vervisch. Experiment-modeling comparison in a nonequilibrium supersonic air nozzle flow. *Journal of Thermophysics and Heat Transfer*, 13(1):68–75, 1999. 5, 18, 79, 84, 86, 87, 88, 89, 245, 285
- [25] A. Bourdon, M. Panesi, A. Brandis, T. Magin, G. Chaban, W. Huo, R. Jaffe, and D. W. Schwenke. Simulation of flows in shock-tube facilities by means of a detailed chemical mechanism for nitrogen excitation and dissociation. *Center for Turbulence Research, Proceedings of the Summer Program 2008*, 2008. 59, 63, 64, 201, 252, 284
- [26] A. Bultel, B. van Ootegem, A. Bourdon, and P. Vervisch. Influence of Ar_2^+ in an argon collisional-radiative model. *Physical Review E*, 65:046406, 2002. 98, 106, 114
- [27] A. Bultel, B. Chéron, A. Bourdon, O. Motapon, and I. Schneider. Collisional-radiative model in air for earth re-entry problems. *Physics of Plasmas*, 13(4):11, 2006. 6, 12, 94, 98, 110, 111, 112, 113, 114, 136, 137, 139, 249, 281
- [28] J. L. Cambier. Numerical methods for TVD transport and coupled relaxing processes in gases and plasmas. In *AIAA 21st Fluid Dynamics, Plasma Dynamics and Lasers Conference*, pages AIAA-90-1574, June 18-20, Seattle, WA 1989. 6

- [29] J. L. Cambier. Numerical simulations of a nonequilibrium argon plasma in a shock-tube experiment. In *AIAA 22nd Fluid Dynamics, Plasma Dynamics & Lasers Conference*, pages AIAA-91-1464, June 24-26, Honolulu, Hawaii 1991. 6
- [30] J. L. Cambier and G. P. Manees. A multi-temperature TVD algorithm for relaxing hypersonic flows. In *AIAA 9th Computational Fluid Dynamics Conference*, pages AIAA-89-1971, June 13-15, Buffalo, NY 1989. 6
- [31] J. L. Cambier and S. Moreau. Simulations of a molecular plasma in collisional-radiative nonequilibrium. In *AIAA 24th Plasmadynamics & Lasers Conference*, pages AIAA-1993-3196, July 6-9, Orlando, FL 1993. 6, 96, 217
- [32] G. Candler and I. Nompelis. Computational fluid dynamics for atmospheric entry. *RTO-EN-AVT-162 VKI lecture series*, 1(1), 2008. 228
- [33] G. V. Candler and MacCormack. Computation of weakly ionized hypersonic flows in thermochemical nonequilibrium. *Journal of Thermophysics and Heat Transfer*, 5(11):266, 1991. 4, 67, 71, 116, 245, 248
- [34] M. Capitelli, G. Gorse, S. Longo, N. Dyatko, and K. Hassouni. Non-maxwell behavior of electron energy distribution functions in expanding nitrogen arcs. *Journal of Thermophysics and Heat Transfer*, 12 (4):478–481, 1998. 8
- [35] M. Capitelli, C. Ferreira, B. Gordiets, and A. Osipov. *Plasma kinetics in Atmospheric Gases*. Springer, Berlin, 2000. 6, 8, 98, 107, 114, 169, 197
- [36] M. Capitelli, G. Colonna, D. Giordano, L. Marraffa, A. Casavola, P. Minelli, D. Pagano, L. Pietanza, and F. Taccogna. Tables of internal partition functions and thermodynamic properties of high-temperature Mars-atmosphere species from 50 K to 50000 K. Technical notes ESA STR-246, ESA, ESTEC, Noordwijk, The Netherlands, October 2005. 35, 36, 37, 38, 41, 42, 283
- [37] M. Capitelli, D. Bruno, G. Colonna, C. Catalfamo, and A. Laricchiuta. Electronically excited states and their role in affecting thermodynamic

- and transport properties of thermal plasmas. *RTO-EN-AVT-162 VKI lecture series*, 1(1), 2008. 238
- [38] M. Capitelli, , G. Colonna, and I. Armenise. State-to-state electron and vibrational kinetics in one dimensional nozzle and boundary layer flows. In *Physico-chemical models for high enthalpy and plasma flows*, 1:21, Rhode-Saint-Genèse, Belgium, July 4-7 2002. 4, 6, 94, 245
 - [39] D. L. Cauchon. Radiative heating results from FIRE II flight experiment at a reentry velocity of 11.4 km/s. ,Technical Report NASA TM X-1402, Ames Research Center, Moffet Field, Moffet Field, 1967. 110
 - [40] G. Chaban, R. Jaffe, D. Schwenke, and W. Huo. Dissociation cross sections and rate coefficients for nitrogen from accurate theoretical calculations. In *AIAA*, pages AIAA 2008-1209, Reno, Nevada, January 2008. 63, 69, 201
 - [41] S. Chauveau, M. Y. Perrin, P. Riviere, and A. Soufiani. A contribution of diatomic molecular electronic systems to heated air radiation. *Journal of Quantitative Spectroscopy and Radiative*, 72:503–530, 2002. 137, 140, 141
 - [42] S. Chauveau, C. Deron, M. Y. Perrin, P. Riviere, and A. Soufiani. Radiative trasfer in lte air plasmas for temperatures up to 15000 K. *Journal of Quantitative Spectroscopy and Radiative*, 77:113–130, 2003. 137, 140, 141
 - [43] S. M. Chauveau, C. Laux, J. D. Kelley, and C. Kruger. vibrationally-specific collisional-radiative model for non-equilibrium air plasmas,. *33th AIAA Plasmadynamics and Lasers Conference*, 2002. Maui, HW. 6, 94
 - [44] O. Chazot. Hypersonic stagnation point aerothermodynamics in plasmatron facilities. *VKI LS Course on hypersonic entry and cruise vehicles, Palo Alto, California, USA.*, 2008. 4, 228
 - [45] O. Chazot, H. Krassilchikoff, and J. Thömel. TPS ground testing in plasma wind tunnel for catalytic properties determination. In *46th AIAA Aerospace Sciences Meeting and Exhibit*, pages AIAA 2008-1252, 7-10 January 2008, Reno, Nevada 2008. 228
 - [46] S. A. Chernyi, G. G.and Losev, S. O. Macheret, and B. V. Potapkin. *Physical and Chemical processes in gas dynamics: physical and*

- chemical kinetics and thermodynamics of gases and plasmas.* AIAA, Reston, Virginia, 2004. 98, 157, 158, 170
- [47] G. Colonna and M. Capitelli. Self-consistent model of chemical, vibrational, electron kinetics in nozzle expansion. *Journal of Thermophysics and Heat Transfer*, 15(3):308–316, 2001. 6, 197
 - [48] G. Colonna, M. Tuttafesta, and D. Giordano. Numerical methods to solve euler equations in one-dimensional steady nozzle flow. *Computer Physics Communications*, 138:213–221, 2001. 29
 - [49] G. Colonna, M. Capitelli, and D. Giordano. State to state electron and vibrational kinetics in supersonic nozzle air expansion: An improved model. In *AIAA*, pages AIAA 2002–2163, Maui, Hawaii, May 20-23 2002. 94
 - [50] G. Colonna, F. Esposito, and M. Capitelli. The role of rotation in state-to-state vibrational kinetics. In *AIAA*, pages AIAA 2006–3423, San Francisco, California, 5-8 June 2006 2006. 59
 - [51] M. L. Da Silva, V. Guerra, and J. Loureiro. Two-temperature models for nitrogen dissociation. *Chemical Physics*, 342:275–287, 2007. 61
 - [52] C. Deron, P. Riviere, M. Y. Perrin, and A. Soufiani. Modelling of radiative properties of lte atmospheric plasmas. In *Proceedings of the 15th international conference on gas discharges and their applications*, Toulouse, 2004. 137, 140
 - [53] J. Diebel, T. Magin, M. Panesi, and J. Degrez. Simulation of supersonic flows in inductively coupled plasma tunnels. *3rd International Conference on Computational Fluid Dynamics, ICCFD3*, Toronto, 12-16 July, 2004. 13, 198
 - [54] H. Drawin. Zur formelmaßigen darstellung des ionisierungsquerschnitts fur den atom-atomstoss und über die ionen-elektronen-rekombination im dichten neutralgas. *Zeitschrift für Physik*, page 404:417, 1968. 98, 112, 139
 - [55] H. Drawin. Atomic cross sections for inelastic collisions. *Report*, pages EUR-CEA-FC 236, 1963. 98, 112, 139
 - [56] H. W. Drawin and F. Emard. Atom-atom excitation and ionization in shock waves of the noble gases. *Physics Letters A*, 43:333–335, Mar. 1973. 106

- [57] K. S. Drellishak, D. P. Aeschliman, and A. B. Cambel. Partition functions and thermodynamics properties of nitrogen and oxygen plasmas. *Phys. Fluids*, 8(9):1590–1600, 1965. 37, 42
- [58] M. G. Dunn and S. W. Kang. Theoretical and experimental studies of reentry plasmas. NASA NTRS CR-2232, NASA, 1973. 94, 110
- [59] F. Esposito, I. Armenise, and M. Capitelli. N-N₂ state to state vibrational relaxation and dissociation rates based on quasiclassical calculations. *Chemical Physics*, 331:1–8, 2006. 69
- [60] J. H. Ferziger and H. G. Kaper. *Mathematical Theory of Transport Processes in Gases*. North-Holland, Amsterdam, 1972. 7, 24, 27
- [61] D. Fletcher. Measurement tecniques for high enthalpy and plasma flows. NATO RTO-EN 8, von Karman Institute for Fluid Dynamics, St.-Genesius-Rode, Belgium, October 1999. 205
- [62] R. M. Frost, P. Awakowicz, H. P. Summers, and N. R. Badnell. Calculated cross-sections and measured rate coefficients for electron impact excitation of neutral and singly ionized nitrogen. *Journal of Applied Physics*, 84(6):2989, 1998. 101, 139, 140, 154, 161, 249, 261
- [63] C. Fryer and A. Bultel. Thermodynamique. Technical report, Université de Rouen, CORIA CNRS UMR 6614, Haute Normandie, Juin 2006 2006. 37
- [64] T. A. Gally. *Development of engineering methods for nonequilibrium radiative phenomena about aeroassisted entry vehicles*. PhD thesis, Texas A&M Univ., College Station., 1992. 215
- [65] R. J. Gessman, C. Laux, and C. Kruger. Experimental study of kinetic mechanisms of recombining atmospheric pressure air plasmas,. *28th AIAA Plasmadynamics and Lasers Conference*, 1997. AIAA-1997-2364. 200, 205
- [66] J. Ginstead, M. Wilder, J. Olejniczak, D. Bogdanoff, G. Allen, K. Dang, and M. Forrest. A comparison of the east shock-tube data with a new air radiation model. In *AIAA*, pages AIAA 2008–1244, Reno, Nevada, January 2008. 137, 143, 175
- [67] D. Giordano. Hypersonic-flow governing equations with electromagnetic fields. *RTO-EN-AVT-162 VKI lecture series*, 1(1), 2008. 17, 18

- [68] D. Giordano. Impact of the born-oppenheimer approximation on aerothermodynamics. *Journal of Thermophysics and Heat Transfer*, 12(3):172–179, 2007. 7, 32
- [69] P. A. Gnoffo, R. N. Gupta, and J. L. Shinn. Conservation equations and physical models for hypersonic air flows in thermal and chemical non-equilibrium. Technical Paper 2867, NASA, 1989. 4, 17, 51, 72, 140
- [70] F. J. Gordillo-Vazquez and J. Kunc. Diagnostics of plasmas with substantial concentrations of atomic oxygen. *Physical Review E*, 51: 6010–6015, 1995. 102, 103, 105, 106, 286
- [71] M. H. Gordon. *Nonequilibrium Effects in a Thermal Plasma*. PhD thesis, Stanford University, San Francisco, CA, February 1992. 204
- [72] V. Gorelov, L. Kildushova, and A. Kireev. Ionization particularities behind intensive shock waves in air at velocities of 8-15 km/s. In *AIAA*, pages AIAA 94–2051,, June 1994. 190, 192, 291
- [73] V. A. Gorelov, M. K. Gladyshev, A. Y. Kireev, I. V. Yegorov, Y. A. Plastinin, and G. F. Karabadzhak. Experimental and numerical study of nonequilibrium ultraviolet NO and N_2^+ emission in shock layer. *Journal of Thermophysics and Heat Transfer*, 12:172–179, 1998. 168, 169, 177, 206, 250
- [74] B. Graille, E. T. Magin, and M. Massot. Kinetic theory of plasmas: translational energy. *Math. Models Methods Appl. Sci.*, 2008. accepted for publication. 17
- [75] B.-D. Green, G. E. Caledonia, R. E. Murphy, and F. X. Robert. The vibrational relaxation of NO($v = 1 - 7$) by O₂. *Journal of Chemical Physics*, 76(5):2441–2448, 1982. 239
- [76] J. H. Grinstead, J. Olejniczak, M. C. Wilder, M. W. Bogdanoff, G. A. Allen, and R. Lilliar. Shock-heated air radiation measurements at lunar return conditions: Phase I east test report. In *NASA REPORT*, 2007. NASA EG-CAP-07-142. 143
- [77] M. Gryzinski. Classical theory of electronic and ionic inelastic collisions. *Physical Review*, pages n2–115:374–382, 1958. 99, 100, 139, 140

- [78] S. Guberman. Electron-vibration exchange models in nitrogen flows. *Kluwer, Dordrecht.* 114
- [79] R. N. Gupta, J. M. Yos, R. A. Thompson, and K. P. Lee. A review of reaction rates and thermodynamic and transport properties for an 11-species air model for chemical and thermal non-equilibrium calculations to 30 000 K. Reference Publication 1232, NASA, August 1990. 94
- [80] L. Gurvich, I. Veyts, and C. Alcock. Thermodynamic properties of individual substances. *Hemisphere Publishing Corporation,* 1, 1989. 38, 41, 115
- [81] P. Hammerling, J. D. Teare, and B. Kivel. Theory of Radiation from Luminous Shock Waves in Nitrogen. *Physics of Fluids,* 2:422–426, July 1959. 61, 170
- [82] L. Hartung, R. Mitcheltree, and P. Gnoffo. Coupled radiation effects in thermochemical nonequilibrium shock capturing flowfield calculation. In *27th Thermophysics Conference*, pages AIAA–1992–2868, Nashville, TN, July 6–8, 1992 1992. 252
- [83] D. Hash, J. Olejniczak, M. Wright, D. Prabhu, M. Pulsonetti, B. Hollis, P. Gnoffo, P. Barnhardt, I. Nompelis, and G. Candler. FIRE II calculations for hypersonic nonequilibrium aerothermodynamics code verification: DPLR, LAURA, and US3D. In *AIAA*, page 4634, Reno, Nevada, January 2007. 111, 130, 131, 132, 136, 228, 230, 287, 292
- [84] G. Herzberg. *Spectra of Diatomic Molecules.* John Wiley & Sons, New York, 1950. 33, 38
- [85] J. O. Hirschfelder, C. F. Curtiss, and R. B. Bird. *Molecular theory of gases and liquids.* John Wiley and Sons, New York, 1954. 18
- [86] M. W. Huo. Electron impact excitation and ionization in air. *RTO-EN-AVT-162 VKI lecture series,* 1(1), 2008. 11, 97, 98, 102, 104, 107, 112, 286
- [87] W. Huo. Private communication, September 2008. 204
- [88] W. M. Huo and V. McKoy. The production of excited molecular species by electron impact in high temperature nonequilibrium air. In *AIAA- 22nd Thermophysics Conference*, pages AIAA 87–1634, June 8–10, 1987/Honolulu, Hawaii 1987. 167, 289

- [89] S. Y. Hyun, C. Park, and K. S. Chang. Rate parameters for electronic excitation of diatomic molecules, III. CN radiation behind a shock wave. In *AIAA*, pages AIAA 2008–1276, Reno, Nevada, January 2008. 173, 181
- [90] R. Jaffe, D. Schwenke, G. Chaban, and W. Huo. Vibrational and rotational excitation and relaxation of nitrogen from accurate theoretical calculations. In *AIAA*, pages AIAA 2008–1208, Reno, Nevada, January 2008. 63, 201
- [91] R. L. Jaffe. The calculation of high-temperature equilibrium and nonequilibrium specific heat data for N₂, O₂ and NO. In *AIAA-22nd Thermophysics Conference*, pages AIAA 87–1633, June 8–10, 1987/Honolulu, Hawaii 1987. 11, 32, 43, 46, 247
- [92] C. Johnston. A comparison of the east shock-tube data with a new air radiation model. In *AIAA*, pages AIAA 2008–1245, Reno, Nevada, January 2008. 111, 137, 139, 143, 144, 146, 148, 153, 154, 161, 249, 281
- [93] C. O. Johnston. *Nonequilibrium Shock-Layer Radiative Heating for Earth and Titan Entry*. PhD thesis, Virginia Polytechnic Institute and State University, Virginia, 2006. 6, 51, 79, 80, 81, 89, 93, 94, 101, 102, 103, 107, 110, 111, 117, 119, 121, 124, 125, 126, 127, 128, 130, 131, 132, 136, 137, 138, 139, 140, 141, 168, 175, 177, 184, 215, 233, 249, 285, 286, 287
- [94] Y.-K. Kim and J.-P. Desclaux. Ionization of carbon, nitrogen and oxygen by electron impact. *Physical Review A*, 66:012708, 2002. 112, 113
- [95] O. Knab, H. Frühauf, and E. Messerschmid. URANUS/CVCV model validation by means of thermochemical nonequilibrium nozzle airflow calculations. *Proceeding of the 2nd European Symposium on Aerothermodynamics for Space Vehicles, ESA Publication Div., Noordwijk, The Netherlands*, page 129, 1994. 5, 18, 67, 239
- [96] O. Knab, H. Freuhauf, and E. Messerschmid. Theory and validation of the physically consistent coupled vibration-chemistry-vibration model. *Journal of Thermophysics and Heat Transfer*, 9(2):219–226, 1995. 62, 70, 86, 248

- [97] O. Knab, H.-H. Fruhauf, and S. Jonas. Multiple temperature descriptions of reaction rate constants with regard to consistent chemical-vibrational coupling. In *AIAA*, July 6-8, 1992/Nashville, TN. AIAA 92-2947. 73
- [98] I. Kossyi, A. Kostinsky, A. Matveyev, and V. Silakov. Kinetic scheme of the non-equilibrium discharge in nitrogen-oxygen mixtures. *Plasma Sources Science and Technology*, -(1):207, 1992. 114, 169
- [99] J. A. Kunc and W. H. Soon. Collisional-radiative non-equilibrium in partially- ionized atomic nitrogen. *Physical Review A*, 40:5822, 1989. 217
- [100] J. A. Kunc and W. H. Soon. Thermal nonequilibrium in partially ionized atomic oxygen. *Physical Review A*, 41:825–843, 1990. 217
- [101] J. M. Lamet, Y. Babou, P. Riviere, M. Y. Perrin, and A. Soufiani. Radiative trasfer in gases under thermal and chemical nonequilibrium conditions: Application to earth atmospheric re-entry. *Journal of Quantitative Spectroscopy and Radiative*, 1:235–244, 2008. 140, 141
- [102] A. Lani. *An Object-Oriented and High-Performance Platform for Aerothermodynamics Simulation*. PhD thesis, von Karman Institute, Rhode-Saint-Genèse, Belgium, 2008. 226, 229
- [103] A. Lani, T. Quintino, D. Kimpe, H. Deconinck, S. Vandewalle, and S. Poedts. The coolfluid framework: Design solutions for high-performance object oriented scientific computing software. In *Computational Science - ICCS 2005*, 2005. 225
- [104] A. Lani, T. Quintino, D. Kimpe, H. Deconinck, S. Vandewalle, and S. Poedts. Reusable object-oriented solutions for numerical simulation of pdes in a high performance environment. *Scientific Programming*, 2007. 225
- [105] C. Laux and C. Kruger. Arrays of radiative transition probabilities for the N₂ first and second positive, NO beta and gamma, N₂⁺ first negative and O₂ schumann-runge band systems. *Journal of Quantitative Spectroscopy and Radiative Transfer*, 1992. also AIAA paper 1998-2664. 170
- [106] C. O. Laux. *Optical Diagnostics and Radiative Emission of Air Plasmas*. PhD thesis, Stanford University, San Francisco, CA, August 1993. 11, 197, 204

- [107] C. O. Laux. Radiation and nonequilibrium collisional radiative models. in *Physico-chemical models for high enthalpy and plasma flows*, 1:55, Rhode-Saint-Genèse, Belgium, July 4-7 2002. 4, 205, 245
- [108] J. H. Lee. Basic governing equations for the flight regimes of aeroassisted orbital transfer vehicles. Technical Paper 84-1729, AIAA, Snowmass, Colorado, June 1984. 17, 68
- [109] M.-S. Liou and C.-J. Steffen. A new flux splitting scheme. *Journal of Computational Physics*, 107:23–39, 1993. 227
- [110] W. Lotz. Electron-impact ionization cross sections and ionization rate coefficients for atoms and ions from hydrogen to calcium. *Zeitschrift fur Physik*, page 216(3):241, 1968. 101, 107, 169
- [111] S. Macheret, A. A. Fridman, I. V. Adamovich, J. W. Rich, and C. E. Treanor. Mechanisms of nonequilibrium dissociation of diatomic molecules. In *AIAA, 1994,Colorado Springs, CO. 94-1984*. 63, 76, 170, 248
- [112] S. O. Macheret and I. V. Adamovich. N-N₂ semiclassical modeling of state-specific dissociation rates in diatomic gases. *Chemical Physics*, 17:113, 2000. 170
- [113] E. T. Magin, B. Graille, and M. Massot. Kinetic theory of plasmas. *RTO-EN-AVT-162 VKI lecture series*, 1(1), 2008. 7, 24, 25, 227
- [114] T. Magin. *A Model for Inductive Plasma Wind Tunnels*. PhD thesis, von Karman Institute for Fluid Dynamics, Rhode-St-Genese, Belgium, June 2004. 18, 24, 26, 246
- [115] T. E. Magin, L. Caillault, A. Bourdon, and C. O. Laux. Nonequilibrium radiative heat flux modeling for the huygens entry probe. *Journal of Geophysical Research - Planets*, 111:E07S12, 2006. 94, 138
- [116] P. V. Marrone and C. E. Treanor. Chemical Relaxation with Preferential Dissociation from Excited Vibrational Levels. *Physics of Fluids*, 6:1215–1221, Sept. 1963. 61, 170, 248
- [117] W. C. Martin, J. R. Fuhr, D. R. Kelleher, A. Masgrove, J. Sugar, and W. L. Wiese. Nist atomic spectra database (version 2.0). Available from: <http://physics.nist.gov/asd2> Gaihersburg, 1999. 96, 108, 137, 142, 170

- [118] B. McBride, M. J. Zehe, and S. Gordon. Nasa glenn coefficients for calculating thermodynamic properties of individual species. Technical Report NASA TP-2002-211556, NASA, 2002. 51
- [119] D. Mihalas and B. Mihalas. *Foundation of Radiation Hydrodynamics*. Oxford University Press, New York, 1984. 231
- [120] M. Mitchner and C. Kruger. *Partially ionized gases*. John Wiley and Sons, New York, 1973. 139, 192
- [121] O. Motapon, M. Fifirig, A. Florescu, F. Waffeu-Tamo, O. Crumeyrolle, G. Varin-Breant, A. Bultel, J. Vervisch, P.; Tennyson, and I. Schneider. Reactive collisions between electrons and NO⁺ ions: rate coefficient computations and relevance for the air plasma kinetics. *Plasma sources science and technology*, 15(1):23–32, 2006. 114
- [122] A. Munafo, M. Panesi, and O. Chazot. Non-equilibrium flow in nozzle expansion and post-shock relaxation zone by means of quasi 1d flow approximation. VKI-SR 2008-17, von Karman Institute for Fluid Dynamics, St.-Genesius-Rode, Belgium, 2008. 29, 82, 87
- [123] J. Muylaert and L. Walpot. Preparing for reentry with expert: the esa in flight atd research program. Bremen, Germany, 2003. 54th International Congress of the International Astronautical Federation, the International Academy of Astronautics, and the International Institute of Space Law. 238
- [124] O. Nagy. Excitation cross-sections of N₂⁺ molecular ion by electron impact and the vibrational energy levels of the three target states. *Chemical Physics*, 286:109–114, 2003. 177
- [125] D. Olynick, W. D. Henline, L. Hartung, and G. Candler. Comparisons of coupled radiative Navier-Stokes flow solutions with the project FIRE II flight data. In *AIAA*, pages AIAA 94–1955, Colorado Springs, CO, June 20-23 1994. 110
- [126] A. E. Orel. Theoretical study of electron-impact excitation of N₂⁺. *Physical Review*, 42:5292–5297, 1990. 177
- [127] T. G. Owano, M. H. Gordon, and C. H. Kruger. Measurements of the radiation source strength in argon at temperatures between 5000 and 10 000 K. *Phys. Fluids B*, 2(12):3184–3190, 1990. 204, 205

- [128] M. Panesi and O. Chazot. Thermodynamic properties of diatoms. VKI tecnical notes, von Karman Institute for Fluid Dynamics, St.-Genesius-Rode, Belgium, October 2008. 33, 39, 41, 42, 283
- [129] M. Panesi, P. Rini, G. Degrez, and O. Chazot. Analysis of chemical non-equilibrium and elemental demixing in the VKI plasmatron. In *37th AIAA Plasmadynamics and Lasers Conference*, pages AIAA–2006–2896, San Francisco, California, June 5–8 2006. 13
- [130] M. Panesi, A. Lani, T. Magin, F. Pinna, O. Chazot, and H. Deconinck. Numerical investigation of the non equilibrium shock-layer around the expert vehicle. In *AIAA Paper 2007-4317*, Miami (Florida), Jun 2007. 38th AIAA Plasmadynamics and Lasers Conference. 238
- [131] M. Panesi, T. Magin, A. Bourdon, A. Bultel, and O. Chazot. Simulation of nonequilibrium reentry air plasmas by means of a collisional-radiative model. *38th AIAA Plasmadynamics and Lasers Conference*, June 2007. 13, 137, 138, 141, 144, 288
- [132] M. Panesi, P. Rini, G. Degrez, and O. Chazot. Analysis of chemical non-equilibrium and elemental demixing in the VKI plasmatron. *Journal Thermophysics and Heat Transfer*, 21(1):57–66, 2007. 4, 13
- [133] M. Panesi, Y. Babou, and O. Chazot. Predictions of nonequilibrium radiation: analysis and comparison with east experiments. In *40th Thermophysics Conference*, pages AIAA–2008–3812, Seattle, Washington, June 23–26 2008. 13, 189
- [134] M. Panesi, T. Magin, A. Bourdon, A. Bultel, and O. Chazot. Analysis of the Fire II flight experiment by means of a collisional-radiative model. In *46th AIAA Aerospace Sciences Meeting and Exhibit*, Reno, Nevada, January 2008. 13, 110, 137, 138, 144, 288
- [135] M. Panesi, T. Magin, A. Bourdon, A. Bultel, and O. Chazot. Collisional radiative modeling in flow simulation. *RTO-EN-AVT-162 VKI lecture series*, 1(1), 2008. 13
- [136] M. Panesi, T. Magin, A. Bourdon, A. Bultel, and O. Chazot. Analysis of the Fire II flight experiment by means of a collisional radiative model. *Journal of Thermophysics and Heat Transfer*, 2009. Accepted for publication. 12, 13, 137, 182, 184

- [137] C. Park. nonequilibrium air radiation (neqair) program : user's manual. ,Technical Report NASA TM86707, Ames Research Center, Moffet Field, Moffet Field, 1985. 94, 101
- [138] C. Park. *Nonequilibrium Hypersonic Aerothermodynamics*. John Wiley and Sons, New York, 1989. 4, 5, 6, 18, 19, 43, 60, 67, 85, 93, 94, 100, 102, 107, 125, 126, 136, 140, 158, 169, 178, 184, 191, 245, 249
- [139] C. Park. Thermochemical relaxation in shock tunnels. *Journal of Thermophysics and Heat Transfer*, 20(4):689, 2006. 6, 93, 94
- [140] C. Park. Rate parameters for electronic excitation of diatomic molecules - electron-impact processes. In *AIAA*, pages AIAA 2008-1206, Reno, Nevada, January 2008. 164, 166, 167, 168, 173, 181, 289
- [141] C. Park. Rate parameters for electronic excitation of diatomic moleculesa - heavy particle-impact processes. In *AIAA*, pages AIAA 2008-1206, Reno, Nevada, January 2008. 173, 181
- [142] C. Park. Collisional ionization and recombination rates of atomic nitrogen. *AIAA Journal*, -(7):1653, 1969. 101
- [143] C. Park. Calculation of nonequilibrium radiation in AOTV flight regimes. In *AIAA 22nd Aerospace Sciences Meeting*, pages AIAA-1984-0306, January 9-12, 1984/Reno, Nevada 1984. 166
- [144] C. Park. Radiation enhancement by nonequilibrium in Earth's atmosphere. *Journal of Spacecraft and Rackets*, 22:27-36, 1985. 184
- [145] C. Park. Problems of rates chemistry in the flight regimes of aeroassisted orbital transfer vehicles. *Thermophysical Aspects of Re-entry Flows edited by J. N. Moss and C. D. Scott AIAA*, New York, 1969. 94, 131
- [146] C. Park. Review of chemical-kinetic problems of future NASA mission, I: Earth entries. *Journal of Thermophysics and Heat Transfer*, 7(3):385, 1993. 66, 68, 72, 86, 110, 116, 157, 158, 230, 239
- [147] C. Park and J. Lee. Validation of multitemperature nozzle flow code. *Journal of Thermophysics and Heat Transfer*, 9(1):9-16, 1995. 79, 84, 85, 89, 285

- [148] C. Park, R. Jaffe, and H. Partridge. Chemical-kinetic parameters of hyperbolic Earth entry. *Journal of Thermophysics and Heat Transfer*, 15(1):76, 2001. 111, 113, 119, 121, 126, 127, 128, 286, 287
- [149] M. Perrin, P. Riviere, and A. Soufiani. Radiation database for Earth and Mars entry. *RTO-EN-AVT-162 VKI lecture series*, 1(1), 2008. 108
- [150] L. Pierrot. Chemical kinetics and vibrationally specific collisional radiative models for nonequilibrium nitrogen plasmas. ESA report, Stanford University, July 1999. 6, 200
- [151] L. Pierrot, C. Laux, and C. Kruger. Vibrationally-specific collisional-radiative model for non-equilibrium nitrogen plasmas,. *29th AIAA Plasmadynamics and Lasers Conference*, 1998. also AIAA paper 1998-2664. 245
- [152] L. Pierrot, L. Yu, R. J. Gessman, C. O. Laux, and C. Kruger. Collisional-radiative modeling of non-equilibrium nitrogen plasmas. Technical Paper 99-3478, AIAA, Norfolk, Virginia, June-July 1999. 6, 200, 205
- [153] K. Radhakrishnan and A. Hindmarsh. Description and use of LSODE the livermore solver for ordinary differential equations. *NASA reference publication*, 1:124, 1993. 28, 172
- [154] P. Rini. *Analysis of differential diffusion phenomena in high enthalpy flows*. PhD thesis, von Karman Institute for Fluid Dynamics, Rhode-St-Genese, Belgium, March 2006. 228, 231
- [155] P. Rini, M. Panesi, G. Degrez, and O. Chazot. Non equilibrium and elemental demixing analysis of CO₂ flows inside icps. In *45th AIAA Aerospace Sciences Meeting and Exhibit*, pages AIAA-2007-1356, Reno, Nevada, January 8-11 2007. 13
- [156] P. Rivière. Systematic semi-classical calulations of stark broadening parameters of N_I, O_I, N_{II} and O_{II} multiplet for modelling radiative transfer in atmospheric air mixture plasmas. *Journal of Quantitative Spectroscopy and Radiative Transfer*, 73:91–110, 2002. 140, 142
- [157] T. P. Roberts. Implementation into TINA modelling for electron-electronic energy equation. In *Thermophysics Conference*, New Orleans, LA, June 1996. 68, 116

- [158] G. S. R. Sarma. Physico-chemical modeling in hypersonic flow simulation. *Progress in Aerospace Sciences*, pages 281–349, 1958. 5, 18
- [159] J.-P. Sarrette, J. Gomes A.-M., Bacri, C. Laux, and C. Kruger. Collisional-radiative modeling of quasi-thermal air plasmas with electronic temperatures between 2000 and 13000 K. *Journal of Quantitative Spectroscopy and Radiative Transfer*, 1:53–125, 2001. 6, 94, 165
- [160] T. Schwartzenruber. *A modular particle-continuum numerical algorithm for hypersonic non-equilibrium flows*. PhD thesis, University of Michigan, 1301 Beal Ave, Ann Arbor, MI, 48109-2122, June 2007. 18
- [161] D. Scutaru, L. Rosenmann, and J. Taine. Approximate intensities of CO₂ hot bands at 2.7, 4.3, and 12 microns for high temperature and medium resolution applications. *Journal of Quantitative Spectroscopy and Radiative Transfer*, 52:765–781, Dec. 1994. 140
- [162] S. P. Sharma and C. Park. Operating characteristics of a 60- and 10-cm electric arc driven shock tube - part I : the driver. *Journal of Thermophysics and Heat Transfer*, 4(3):259–265, 1990. 142
- [163] S. P. Sharma and C. Park. Operating characteristics of a 60- and 10-cm electric arc driven shock tube - part II : the driven. *Journal of Thermophysics and Heat Transfer*, 4(3):266–272, 1990. 142
- [164] Q. Sun, I. D. Boyd, and G. V. Candler. A hybrid continuum/particle approach for modeling subsonic, rarefied gas flows. *J. Comput. Phys.*, 194(1):256–277, 2004. ISSN 0021-9991. 17
- [165] S. Surzhikov. Electronic excitation in air and in carbon dioxide gas. *RTO-EN-AVT-162 VKI lecture series*, 1(1), 2008. 98
- [166] S. Surzhikov, O. Rouzaud, T. Soubrie, V. Gorelov, and A. Kireev. Prediction of non-equilibrium and equilibrium radiation for reentry conditions. In *AIAA*, pages AIAA 2006–1188, Reno, Nevada, January 2006. 5, 18
- [167] S. Surzhikov, I. Sharikov, M. Capitelli, and G. Colonna. Kinetic model of nonequilibrium radiation of strong air shock waves. In *AIAA*, pages AIAA 2006–586, Reno, Nevada, January 2006. 5, 18
- [168] H. Tawara and M. Kato. Electron impact data for atoms and ions: up-dated in 1998. *NIFS Data Serie S*, 51:256P, 1975. 112, 113

- [169] S. Tayal. Effective collision strengths for electron impact excitation of n. *Atomic Data and Nuclear Data Tables*, 76(1):191–212, 2000. 102
- [170] P. Teulet, J.-P. Sarrette, and A.-M. Gomes. Calculation of electron impact inelastic cross sections and rate coefficients for diatomic molecules. *Journal of Quantitative Spectroscopy and Radiative*, 1:69–549, 1999. 165
- [171] P. Teulet, J.-P. Sarrette, and A.-M. Gomes. Collision-radiative modeling of one- and two- temperature air and air-sodium plasmas at atmospheric pressure with temperatures of 2000 - 12000 K. *Journal of Quantitative Spectroscopy and Radiative*, 1:70–159, 2001. 6, 94, 114, 177, 206, 250
- [172] I. The Opacity Project Team. The opacity project. *Institute of Physics Publishing, Bristol, Philadelphia*, 1, 1995. 141
- [173] F. Thivet. *Modeling and computation of hypersonic flows in chemical and thermodynamic nonequilibrium (in French)*. PhD thesis, Ecole Cent. Paris, Chatenay-Malabry, France, 1992. 28, 71, 172
- [174] D. Vanden Abeele. *An Efficient Computational Model for Inductively Coupled Air Plasma Flows under Thermal and Chemical Non-Equilibrium*. PhD thesis, von Karman Institute, Rhode-Saint-Genèse, Belgium, 2000. 25, 68, 228
- [175] V. Venkatakrishnan. Convergence to steady state solutions of the euler equations on unstructured grids with limiters. *Journal of Computational Physics*, 118:120–130, 1995. 227, 228
- [176] W. Vincenti and C. Kruger. *Introduction to Physical Gas Dynamics*. John Wiley and Sons, New York, 1965. 7, 8, 9, 17, 19, 24, 32, 33, 58, 59, 192
- [177] O. Zatsarinny and S. Tayal. Electron collisional excitation rates for O_I using the B-spline R-matrix approach. *The Astrophysical Journal Supplement Series*, 148:575–582, 2003. 102, 105, 106, 286
- [178] Y. Zeldovich and Y. Raizer. *Physics of Shock Waves and High Temperature Hydrodynamic Phenomena*. ACADEMIC PRESS INC., Berkley Square House, London, 1966. 98, 108, 191

List of Tables

3.1	v_{max} for different excited state of molecular nitrogen.	39
3.2	Electron density and influence of the thermodynamic models.	53
4.1	Recommendation for multiple temperature rate constants for different types of reactions.	66
4.2	Shock-tube flow characteristic quantities.	72
5.1	Shock-tube flow characteristic quantities.	80
6.1	Parameters A , α and θ for the calculation of the rate coefficient (in $m^3 s^{-1}$) given by Eq.(6.14) for the transition $i \rightarrow j$ induced by electron collision. θ is expressed in K . (Taken from Ref. [27])	113
6.2	Shock-tube flow characteristic quantities.	118
6.3	Kinetic models used in the investigation.	141
6.4	Operating conditions for the EAST shock-tube experiments considered here (see Ref. [92]).	144
7.1	Species Considered in the present CR model.	164
8.1	Flowfield quantities inside the torch of the Minitorch.	198
8.2	VKI Minitorch. Flowfield quantities in correspondence of the torch outlet.	203
9.1	Nitrogen and Oxygen. Grouped states simplified ABBA model.	216
10.1	Flight conditions.	239
A.1	Index, energy, degeneracy, and secondary quantum number for the N and O electronic energy states considered.	257
A.2	Probability $A_{i \rightarrow j}$ for $N(i) \rightarrow N(j < i) + h\nu$ and $O(i) \rightarrow O(j < i) + h\nu$ spontaneous emission.	259
A.3	Nitrogen. Rate constant for electron impact excitation $K_{i \rightarrow j}$	261

List of Figures

1.1	Schematic of the flowfield surrounding a capsule during the (re-)entry phase in a planetary atmosphere: (red line) recombination, (black line) ionization (courtesy of NASA).	5
1.2	Electronic population distribution in ionizing (black curve) and recombining plasmas (red curve).	10
3.1	N_2 . Non-dimensional specific heat at constant pressure. The broken line refers to the calculation of Capitelli <i>et al</i> [36]. The unbroken lines represent the results obtained with the simplified models, for increasing number of electronic levels considered.	36
3.2	Potential curve (Morse) for N_2 ground state for different centrifugal distortions	40
3.3	N_2 . Non dimensional enthalpy. (x) refers to the calculation performed by Panesi at al. [128]. The unbroken line refers to the work of Capitelli <i>et al</i> [36] and the broken line represents the results obtained with the simplified models.	42
3.4	N_2 first partition method. Nonequilibrium specific heat at constant pressure as a function of T_V and T . The values of the specific heat have been non-dimensionalized dividing by \mathcal{R}	47
3.5	N_2 second partition method. Nonequilibrium specific heat of vibration at constant pressure as a function of T_V and T . The values of the specific heat have been non-dimensionalized dividing by \mathcal{R}	48
3.6	N_2 relative error. Nonequilibrium specific heat of vibration at constant pressure as a function of T_V and T . Influence of the partitioning method.	49
3.7	N_2 first partition method. Nonequilibrium specific heat of rotation at constant pressure as a function of T_V and T . The values of the specific heat have been non-dimensionalized dividing by \mathcal{R}	50

3.8	N_2 second partition method. Nonequilibrium specific heat of rotation at constant pressure as a function of T_V and T . The values of the specific heat have been non-dimensionalized dividing by \mathcal{R}	51
3.9	N_2 relative error. Nonequilibrium specific heat of rotation at constant pressure as a function of T_V and T . Influence of the partitioning method.	52
3.10	EAST case. Temperature profiles. Unbroken lines indicate the first method of partitioning and the broken lines represent the results obtained adopting the second method of partitioning.	53
3.11	EAST case. Composition profiles. (\times) indicate the first method of partitioning and the unbroken lines represent the results obtained adopting the second method of partitioning.	54
3.12	1634 s. Comparison of the temperature profiles along the stagnation line. Unbroken lines refer to results obtained with the accurate model for thermodynamics. Dashed lines refer to the simplified model.	55
4.1	$N_2 - N$. Comparison of the dissociation reaction rate constants in thermal nonequilibrium: (\circ) NASA Ames chemists Ref. [25]; (dash-dotted line) Treanor and Marrone's model; (unbroken line) Park TT_V model; (dashed line) Knab's model; (\times) Macheret's model.	64
4.2	Temperature profiles. Comparison among the preferential dissociation model of Treanor and Marrone (unbroken lines) and the non-preferential dissociation model of Park-Candler (dashed lines).	73
4.3	Temperature profiles. The preferential dissociation model of Knab is used in this figure. The symbol (\square) represents the vibrational temperature of N_2 ; we indicate the vibrational temperature of O_2 with the symbol (\triangle). Translational temperature is indicated with the symbol (\circ) in the figure.	74
4.4	Temperature profiles. The preferential dissociation model of Macheret is used in this figure. The symbol (\square) represents the vibrational temperature of N_2 ; we indicate the vibrational temperature of O_2 with the symbol (\triangle). Translational temperature is indicated with the symbol (\circ) in the figure.	74

4.5	Temperature profiles. The preferential dissociation model of Treanor is used in this figure. The symbol (\square) represents the vibrational temperature of N_2 ; we indicate the vibrational temperature of O_2 with the symbol (\triangle). Translational temperature is indicated with the symbol (\circ) in the figure.	75
4.6	Composition profiles for preferential dissociation methods. Unbroken line indicates Knab's model; dashed lines represent Treanor's model and the dotted lines indicate the results obtained with Macheret's model.	75
4.7	Comparison of the composition profiles obtained with Knab's model (unbroken lines) and the non-preferential model of Park-Candler (dashed lines).	76
5.1	1634 s. Temperature profiles comparison with Ref. [93] (unbroken lines). (\times) results obtained with assuming a prescribed value of Ω^I . The dash-dot lines refers to the classical expression for Ω^I	80
5.2	FIRE II -1634 s. Number density profiles: Johnston's results (unbroken line);(\times) our results obtained with a prescribed value of Ω^I ; (dashed lines) classical approach Ω^I	82
5.3	1636 s. Temperature profiles: Johnston's results (unbroken line); results obtained with a prescribed value of Ω^I (dashed lines).	83
5.4	1634 s. Number density profiles (Park-Candler). Johnston's (unbroken line). (dashed lines) results obtained with a prescribed value of Ω^I	83
5.5	Temperature profiles in arc-jet wind tunnel (AEDC): comparison with Ref. [147].	85
5.6	Composition evolution in the contoured nozzle of the TT1 arcjet facility: comparison with Ref. [24]	87
5.7	Ro-translational temperature in the contoured nozzle of the TT1 arcjet facility: comparison with Ref. [24]	88
5.8	Vibrational temperature of N_2 in the contoured nozzle of the TT1 arcjet facility: comparison with Ref. [24]	88
6.1	Nitrogen. Rate constant electron impact excitation $N(1) \rightarrow N(4)$. Comparison among Drawin model (dashed line), Gryzinski (unbroken line), Park (\times) and Frost (dash-dotted line).	103

6.2	Nitrogen. Rate constant electron impact excitation $\text{N}(2) \rightarrow \text{N}(5)$. Comparison among Drawin model (unbroken line), Van Regmorter (dashed line), Park (dashed with two dots) and Frost (dash with one dot). Tayal (\times)	104
6.3	Oxygen. Rate constant electron impact excitation $\text{O}(1) \rightarrow \text{O}(10)$. Comparison among Drawin model (dashed line), Gordillo Kunc [70] (dash and two dots), Park (\times) Gryzinski (+), Zatsarinny and Tayal [177] (unbroken line), Allen (dash-dotted line)	105
6.4	Oxygen. Rate constant electron impact excitation $\text{O}(1) \rightarrow \text{O}(10)$. Comparison among Drawin model (dashed line), Gordillo Kunc [70] (+), Allen (\times) Gryzinski (dash-two dots), Zatsarinny and Tayal [177] (unbroken line), Bathia and Kastner [11] (dash-dotted line)	106
6.5	Comparison rate constants for electron impact ionization processes of N: (dashed lines) Huo's results Ref. [86]; (unbroken lines) Drawin rate constants Ref. [93].	107
6.6	1634 s case. Temperature profiles. Comparison between the five temperature model with $T_{v\text{N}_2} \neq T_e$ (unbroken line) and the four temperature model with $T_{v\text{N}_2} = T_e$ (dashed line).	120
6.7	Electronic energy level populations for atomic nitrogen [m^{-3}] : CR model at 0.2 cm, 0.4 cm, and 0.6 cm; Boltzmann distribution at 0.4 cm. Comparison between the five temperature model with $T_{v\text{N}_2} \neq T_e$ (unbroken line) and the four temperature model with $T_{v\text{N}_2} = T_e$ (dashed line).	120
6.8	1634 s case. Temperature profiles: CR model (unbroken line); Johnston's results [93] (dashed line).	121
6.9	1634 s case. Electron number density profiles: CR model with escape factor values of 0, 0.1, 0.25, 0.5, and 1 (unbroken line); simplified kinetic mechanism of Park et al. [148] (line with circles).	121
6.10	1634 s case, Species number density profiles.	122
6.11	1634 s case, number density profiles: $\text{N}(1)$, $\text{N}(2)$, $\text{N}(3)$, $\text{N}(4)$, $\text{N}(10)$, $\text{N}(20)$, $\text{N}(30)$, $\text{N}(40)$	123
6.12	1634 s case. Electronic energy level populations for atomic nitrogen at 0.7 cm from the shock front [m^{-3}]: CR model (line with circles), Boltzmann distribution (unbroken line), Saha distribution (dashed line), and Johnston's results [93] (black diamonds)	124

6.13 1634 s case. Electronic energy level populations for atomic nitrogen at 2.5 cm from the shock front [m^{-3}]: CR model (line with circles), Boltzmann distribution (unbroken line), Saha distribution (dashed line), and Johnston's results [93] (black diamonds)	125
6.14 1634 s case, 0.7 cm from the shock front. Electronic energy level populations for atomic nitrogen [m^{-3}]: full CR model (dotted line), QSS ABBA model (line with diamonds), QSS Park et al. model [148] (crosses), Boltzmann distribution (unbroken line), and Johnston's results [93] (black diamonds)	128
6.15 1634 s case. Electronic energy level populations for atomic nitrogen [m^{-3}]: simplified CR model (line with circles), full CR model (line with diamonds), Boltzmann distribution (dashed line).	130
6.16 1636 s case. Temperature profiles: comparison with results from literature Refs. [83]-[93]. CR model with escape factor values of 0 and 1 (unbroken line), LAURA code (diamonds), DPLR code [83] (circles), and Johnston's results [93] (dashed line).	131
6.17 1636 s case. Ionization degree profiles: CR model with escape factor values of 0 and 1 (unbroken line), LAURA code [83] (line with diamonds), and Johnston's results [93] (line with triangles).	132
6.18 1636 s case, 0.5 cm from the shock front. Electronic energy level populations of atomic nitrogen [m^{-3}]: CR model (line with circles), Boltzmann distribution (unbroken line), and Saha distribution (dashed line).	133
6.19 1636 s case, 0.5 cm from the shock front. Electronic energy level populations of atomic oxygen [m^{-3}]: CR model (line with circles), Boltzmann distribution (unbroken line), and Saha distribution (dashed line).	134
6.20 1643 s case. Temperature profiles with escape factor values of 0 and 1.	135
6.21 1643 s case. Electronic energy level populations for atomic nitrogen [m^{-3}]: CR model (line with circles) and Boltzmann distribution (unbroken line), 0.5 cm from the shock front.	135

6.22 High resolution emission coefficient predicted for Case 1 at 4 cm downstream from the shock. The considered spectral ranges $\Delta\lambda$ are detailed. The corresponding main contributing electronic levels are indicated using the nomenclature of Ref. [131, 134].	144
6.23 Case 3-4. Temperature profiles [K]. Dashed line profiles correspond to flight conditions of case 3. Unbroken lines refer to case 4.	145
6.24 Case 3. Evolution of the composition in the post shock area.	146
6.25 Case 3. Populations of electronically excited states of atomic nitrogen. N(10) (unbroken line), O(6) (dashed line), N(9) (dotted line), N(8) (circle) and N(12) (dash-dotted line) . . .	147
6.26 Influence of the model on the population densities of O(6) and N(10) electronic states.	147
6.27 Case 2. Shock speed 9880 m/s: comparison among experimental and simulated radiative intensity profiles.	151
6.28 Case 4. Shock speed 10340 m/s: comparison among experimental and simulated radiative intensity profiles.	151
6.29 Case 1. Shock speed 9165 m/s: comparison among experimental and simulated radiative intensity profiles.	152
6.30 Case 3. Shock speed 9989 m/s: comparison among experimental and simulated radiative intensity profiles.	153
6.31 Case 4. Comparison among experimental and simulated radiative intensity profiles.	154
6.32 Spectral integrated profiles $\Delta\lambda = 700 - 760$: comparison among experimental and simulated radiative intensity profiles.	155
6.33 Spectral integrated profiles $\Delta\lambda = 760 - 800$: comparison among experimental and simulated radiative intensity profiles.	155
6.34 Case 3. Normalized population of the electronic states of atomic nitrogen at 0.65 cm from the shock front. Electronic energy level populations [m^{-3}]: CR model ABBA FROST (line with circles), Boltzmann distribution (unbroken line), and Saha distribution (dashed line).	156
6.35 Case 4. Normalized population of the electronic states of atomic nitrogen at 1.0 cm from the shock front. Electronic energy level populations [m^{-3}]: CR model ABBA FROST (line with circles), Boltzmann distribution (unbroken line), and Saha distribution (dashed line).	157

6.36 Radiative intensity as a function of the shock speed (Ranging from 9 – 10 km/s). Influence of the speed on the radiative intensity profiles.	159
6.37 Electron density profiles as a function of the shock speed (Ranging from 9 – 10 km/s). Influence of the speed on the radiative intensity profiles.	159
6.38 Electron production terms 9 km/s. Unbroken lines refer to the ABBA model, whereas dashed lines refer to MODIFIED ABBA Model. Influence of the shock speed on the electron production term [mole /sm ⁻³]. Where (a) indicates the contribution given by N for ABBA.(b) indicates the contribution of O for ABBA. (c) Refers to N for MODIFIED ABBA. (d) Refers to O for MODIFIED ABBA. (e) Refers to N for ABBA Gryzinski (f) Refers to N for ABBA FROST.	160
6.39 Electron production terms 10 km/s. Unbroken lines refer to the ABBA model, whereas dashed lines refer to MODIFIED ABBA Model. Influence of the shock speed on the electron production term [mole /sm ⁻³]. Where (a) indicates the contribution given by N for ABBA.(b) indicates the contribution of O for ABBA. (c) Refers to N for MODIFIED ABBA. (d) Refers to O for MODIFIED ABBA. (e) Refers to N for ABBA Gryzinski (f) Refers to N for ABBA FROST.	161
7.1 N ₂ . Rate constant for excitation from X to C comparison: (o) Huo [88]; (dashed curve) Teulet's results; (unbroken line) Losev rate and (dash-dotted line) Bacri [5]. Such transition is not included in Park model [140].	167
7.2 N ₂ ⁺ . Rate constant for excitation from X to B comparison: Park's model [140] (o); Teulet's results (unbroken line); (dashed-dotted) curve Johnston and the dashed line Gorelov.	168
7.3 Temperature profiles: CR model molecules	174
7.4 1634 s case. Population profiles obtained with the CR molecules for all species.	175
7.5 1634 s case. Population profiles obtained with the CR model for the atoms.	176
7.6 1634 s case. Population profiles of N ₂ ⁺ molecules. Dashed lines represent the equilibrium values; unbroken lines correspond to the CR results.	177

7.7	Composition evolution of N_2^+ . (Dashed lines) results with Teulet's rates; (unbroken lines) CR results with Gorelov's rates.	178
7.8	1634 s case. Population profiles of N_2 molecules. Dashed lines represent the equilibrium values; unbroken lines with symbols correspond to the CR results.	179
7.9	N_2 population profiles. (Dashed lines) results with Teulet's rates; unbroken lines the CR results with Losev's rates.	180
7.10	Population profiles of NO molecules. Dashed lines are the equilibrium values; unbroken lines the CR results.	181
7.11	1634 s case. Population profiles of O_2 molecules: (unbroken lines) baseline CR model; (dashed lines) dissociation rates of $O_2(X)$ are used for the excited states.	182
7.12	Saha diagrams for the excited states of the atomic nitrogen. Park's model (\diamond); ABBA model ($\alpha = 0$) (\circ); unbroken line: Boltzmann equilibrium; broken line: Saha equilibrium.	183
7.13	Population profiles of N_2 molecules comparison:(\times) Park; unbroken lines ABBA.	185
7.14	Population profiles of N_2^+ molecules comparison:(\times) Park's model; unbroken lines ABBA.	185
7.15	Temperature profiles obtained with Macheret's model.	187
7.16	Temperature profiles obtained with Treanor's model. The U parameter was set to $(T_D/3)$	187
7.17	1634 s case. Comparison of population profiles obtained with: Treanor model (dashed lines); Macheret's model (unbroken lines); and Park's model (dot-dashed lines).	188
7.18	Free electron density plots obtained with: Treanor model (\times); Macheret's model (unbroken line); and Park's model (dashed line).	189
7.19	Population profiles of N at 1 cm from the shock front comparison: Park's model (\diamond); ABBA model $\alpha = 0$ (\circ); (\triangle) ABBA model with the VUV lines which are self-adsorbed.	190
7.20	Electron density profiles. (*) indicates the ABBA model ($\alpha = 0$) and (\circ) is the ABBA model with the VUV lines which are self-adsorbed.	191
7.21	Electron population distributions ahead a shock wave. $p = 0.5$ torr: 1 - $V_s = 8.0$ km/s ; 2- $V_s = 7.5$ km/s ; 3- $V_s = 9.5$ km/s; $p_1 = 0.2$ torr: 4- $V_s = 11.3$ km/s; 5 - $V_s = 14.0$ km/s; broken lines - calculated results. Experimental results taken from Ref. [72].	192

7.22 Population profiles of N at 1 cm from the shock front. (◊) Park's model; (○) is the ABBA model ($\alpha = 0$). Unbroken line is the Boltzmann and Saha is the dashed line. Δ accounts for the precursor effects.	193
7.23 1634 s case. Influence of the heavy particles processes on ionization.	194
8.1 VKI pilot ICP facility in operation.	199
8.2 Geometry of the nozzle of the VKI Minitorch.	200
8.3 VKI Minitorch. Pressure profile along the axis of the nozzle. .	202
8.4 VKI Minitorch. Evolution of the temperatures along the axis of the nozzle. Optically thick medium.	202
8.5 Throat. Normalized Population plots: comparison with equi- librium.	204
8.6 Outlet. Normalized population plots of atomic nitrogen: com- parison with equilibrium.	205
8.7 Outlet. Normalized population plots of atomic oxygen: com- parison with equilibrium.	206
8.8 N_2 excited states of populations [m^{-3}] along the nozzle axis. Dashed lines: equilibrium value; unbroken lines CR model results.	207
8.9 N_2^+ excited states of populations [m^{-3}] along the nozzle axis. Dashed lines: equilibrium value; unbroken lines CR model results.	207
8.10 NO excited states of populations [m^{-3}] along the nozzle axis. Dashed lines: equilibrium value; unbroken lines CR model results.	208
8.11 NO^+ excited states of populations [m^{-3}] along the nozzle axis. Dashed lines: equilibrium value; unbroken lines CR model results.	209
8.12 NO^+ excited states of populations [m^{-3}] along the nozzle axis. Dashed lines: equilibrium value; unbroken lines CR model results.	209
8.13 Temperature profiles along the nozzle axis: optically thin medium.	210
8.14 Outlet. Normalized population plots of atomic nitrogen: com- parison with equilibrium.	211
8.15 N_2 excited states of populations [m^{-3}] along the nozzle axis: comparison optically thin (unbroken lines) and optically thick results (dashed lines).	212

8.16	N_2^+ excited states of populations [m^{-3}] along the nozzle axis: comparison optically thin (unbroken lines) and optically thick results (dashed lines). Equilibrium results (\times)	213
8.17	Normalized population plots of NO: comparison optically thin (unbroken lines) and equilibrium results (\times)	213
9.1	1634 sec. Comparison among the detailed ABBA model (\circ) and the simplified CR approach (Δ) for atomic nitrogen. The location is 1 cm from the shock front.	220
10.1	Fire 2 vehicle. Axisymmetric grid composed of 28841 elements.	229
10.2	1636 s. Temperature profiles: comparison with literature Ref. [83].	230
10.3	1636 s. Number density profiles for N, O, e^- . Comparison literature: (unbroken lines) COOLFLUID Hypersonic; (dashed) LAURA code.	231
10.4	1634 s. Temperature plots in the stagnation region. Upper part: Translational temperature T. Lower part: Vibrational temperature T_v .	233
10.5	1634 s. Temperature profiles along the stagnation line: T translational temperature; T_v vibrational temperature.	234
10.6	1634 s. Comparison of the free electron number density: optically thick case (upper part); the optically thin case (lower part).	235
10.7	1634 s. Nonequilibrium factor ($\chi = N(4)/N(4)_{EQ}$) as a function of the optical thickness: (upper part) optically thick case; (lower part) optically thin case.	236
10.8	1634 s. Boltzmann diagram: N. Located at 1 cm from the shock along the stagnation line.	236
10.9	1634 s. Boltzmann plot atomic nitrogen in correspondence of the boundary layer edge.	237
10.10	1634 s. Nonequilibrium (χ) factor profile along the stagnation line: $N(4)$ grouped state.	238
10.11	Global view of the wall surface mesh for the EXPERT vehicle.	240
10.12	Detailed views on the surface mesh for the EXPERT vehicle.	240
10.13	Ro-translational temperature on the EXPERT vehicle.	241
10.14	Vibrational temperature of N_2 field on the EXPERT vehicle.	242
10.15	Vibrational temperature of O_2 field on the EXPERT vehicle.	242